DESIGN AND PERFORMANCE TESTING OF A NOVEL CEILING PANEL FOR SIMULTANEOUS HEAT AND MOISTURE TRANSFER TO MODERATE INDOOR TEMPERATURE AND RELATIVE HUMIDITY

A Thesis Submitted to the College of

Graduate Studies and Research

in Partial Fulfillment of the Requirements

for the Degree of Doctor of Philosophy

in the Department of Mechanical Engineering

University of Saskatchewan

Saskatoon

By

Melanie Fauchoux

PERMISSION TO USE

In presenting this thesis in partial fulfillment of the requirements for a Postgraduate degree from the University of Saskatchewan, I agree that the Libraries of this University may make it freely available for inspection. I further agree that permission for copying of this thesis in any manner, in whole or in part, for scholarly purposes may be granted by the professors who supervised my thesis work or, in their absence, by the Head of the Department or the Dean of the College in which my thesis work was done. It is understood that any copying, publication, or use of this thesis or parts thereof for financial gain shall not be allowed without my written permission. It is also understood that due recognition shall be given to me and to the University of Saskatchewan in any scholarly use which may be made of any material in my thesis.

Requests for permission to copy or to make other use of material in this thesis in whole or in part should be addressed to:

Head of the Department of Mechanical Engineering

University of Saskatchewan

Saskatoon, Saskatchewan, S7N 5A9

ABSTRACT

An important aspect in the design of buildings is the comfort of the occupants inside the building. Although many factors can affect comfort, the factor of particular interest in this research is the indoor humidity level. High indoor humidity levels can make the indoor air feel stuffy at warm temperatures and reduce the amount of moisture that can be removed from a person's body, making a person feel warm. On the other hand, low indoor humidity levels can cause health problems such as dry eyes and sore throats. In addition to the comfort implications of improperly maintaining indoor humidity levels, the building itself can suffer from mould growth and rotting materials at high humidity levels.

This thesis presents the first research on a novel panel that can simultaneously transfer heat and moisture to/from an occupied space. The panel is referred to as a heat and moisture transfer panel (HAMP). A HAMP is similar in design to a radiant ceiling panel, but uses a liquid desiccant as the heat and moisture transfer medium and the surface of the panel is made of a semi-permeable membrane. A HAMP can be installed into a space and heat and moisture will be transferred between the liquid desiccant and the space air, through the membrane. The main objectives of this thesis are to design a prototype HAMP and to measure the performance of the HAMP under different operating conditions.

The performance of the HAMP is quantified by the sensible and latent effectivenesses, as well as the total heat and mass flux between the HAMP and the air in the test section. The results of the experiments show that the HAMP is able to simultaneously transfer heat and moisture with the air in the test section under all operating conditions. The sensible and latent effectivenesses of

the HAMP are higher when the air in the test section becomes unstable, due to the natural convection in the duct ($\varepsilon_{sensible} \approx 15\%$, $\varepsilon_{latent} \approx 40\%$). These include cases of cooling and/or dehumidification. The sensible and latent effectivenesses of the HAMP are lower when forced convection is dominant in the test section ($\varepsilon_{sensible} \approx 5\%$, $\varepsilon_{latent} \approx 25\%$). This occurs during cases of heating and/or humidification. The presence of natural convection in the test section is confirmed with flow visualization photographs. The photographs show laminar boundary layer flow during the stable airflow cases, and the presence of convection roll cells during the unstable airflow cases.

The total heat flux increases with an increase in the temperature difference between the panel and the air and the mass flux increases with an increase in the humidity ratio difference between the panel and the air. For a temperature difference of 10°C, the prototype HAMP can provide ~4 W/m^2 of cooling. This is small compared to the actual cooling loads that would be required in a space. The HAMP is able to provide enough moisture transfer to remove the moisture generated by one person (~70 g_w/hr), with ~2 m^2 of panel surface area. Although the rate of heat transfer between the HAMP and the airflow is limited, the moisture transfer rates are very good.

An analysis of standard heat exchanger correlations typically used to predict the effectiveness of a heat exchanger shows that these methods are not applicable for a HAMP. Instead, new correlations must be developed to predict the sensible and latent effectivenesses of a HAMP. These correlations are not determined in this thesis, but an analysis of the experimental data is presented to show that the effectivenesses are functions of several design parameters such as the number of heat transfer units (NTU_{exp}), the number of mass transfer units ($NTU_{m,exp}$), the

effective Rayleigh number of the air (Ra^+), the operating condition factor (H^*) and the ratio of $NTU_{exp}/NTU_{m,exp}$.

The experimental results presented in this thesis show that a HAMP can be used to simultaneously transfer heat and moisture with the air in a space, and may be used as a ceiling panel in a space to simultaneously control the temperature and relative humidity of the air. The performance of a HAMP can be determined using two parameters: NTU_{exp} and $NTU_{m,exp}$. Determining these two parameters is very complicated and involves analysis of several design parameters, such as NTU_{theo}, $NTU_{m,theo}$, H^*, Ra^+ and the ratio $NTU_{exp}/NTU_{m,exp}$. The experimental data collected in this thesis was used to analyze the relationships between NTU_{exp} and $NTU_{m,exp}$ and these design parameters and is a starting point for future research on developing a correlation for predicting the performance of a HAMP.

ACKNOWLEDGEMENTS

I would like to thank the following people for their help and support throughout my Ph.D. research:

- My supervisors – Dr. Carey Simonson and Dr. David Torvi for their continued support and guidance,
- My committee members – Prof. Robert Besant, Dr. Greg Schoenau and Dr. Lope Tabil for their guidance,
- Chris James, Dave Deutscher and Rick Retzlaff for their guidance and assiatance setting up my test facility and their continued support throughout the testing phase of my research
- Dr. Prabal Talukdar for performing CFD modeling of my experiments
- My fellow grad students – Mohit Bansal, Mike Larson, Conrad Iskra, David Beriault, Mohammad Afshin, Alireza Vali, Khizir Mahmud, Ramin Namvar, Howard Hemingson, Soheil Akbari, Radia Eldeeb
- To my family for their support and encouragement throughout my studies, and
- The University of Saskatchewan, NSERC and my supervisors for financial support.

DEDICATION

This thesis is dedicated to my late Grandmother, who was the greatest teacher I have known and inspired me in many ways. Also to my husband and family who have supported me throughout my time as a graduate student.

TABLE OF CONTENTS

LIST OF FIGURES

LIST OF TABLES

NOMENCLATURE

ACRONYMS

AWG	American wire gauge
HVAC	heating, ventilating and air-conditioning
HAMP	heat and moisture transfer panel
LiCl	lithium chloride

SYMBOLS

A	used to calculate the partial pressure of water vapour of a salt solution
A	area [m^2]
A_i	coefficient used to calculate the concentration of a salt solution
B	used to calculate the partial pressure of water vapour of a salt solution
B	reduced length of the starting section
B_x	total bias uncertainty at 95% confidence level
b_x	bias uncertainty at 68% confidence level
C	concentration (mass fraction) [kg_w/kg_{air} or kg_{salt}/kg_{sol}]
C	used to calculate the partial pressure of water vapour of a salt solution
C_8, C_9, C_{10}, C_{11}, C_{12}, and C_{13}	coefficients used to calculate the saturated pressure of water vapour
c_p	specific heat [J/(kg·K)]
Cr	heat capacity rate of an energy exchanger [-] $\left((\dot{m}c_p)_{min}/(\dot{m}c_p)_{max}\right)$
D	binary diffusion coefficient of water vapour in a fluid [m^2/s]
D	used to calculate the partial pressure of water vapour of a salt solution
D_h	hydraulic diameter [m]
D_i	parameter used in calculating dynamic viscosity of salt solution [-]
$\dot{E}$	rate of energy transfer [W]
F	view factor for radiation calculation [-]
f_1, f_2	functions used to calculate the specific heat of a salt solution
g	acceleration due to gravity [m/s^2]
Gr	Grashof number [-]
h	enthalpy [kJ/kg_{air}]

h	heat transfer coefficient [$W/(m^2 \cdot K)$]
h_m	convection mass transfer coefficient [$kg_{air}/(m^2 \cdot s)$ based on W]
h_{fg}	heat of vaporization [kJ/kg_w]
H	height of the duct [m]
H^*	operating condition factor [-] ($2500\Delta W/\Delta T$)
I	ionic strength of salt solution [$mol_{solute}/kg_{solvent}$]
J	diffusion flux used in the numerical model [$kg/(m^2 \cdot s)$]
K	electrolyte parameter for lithium chloride[-]
k	thermal conductivity [$W/(m \cdot K)$]
k_1, k_2	constants used in natural convection heat transfer correlation
L	characteristic length [m]
Le	Lewis number [-] (Sc/Pr or $k/\rho c_p D$)
M	molecular weight [kg/mol]
m	mass [kg]
m	molality of salt solution [$mol_{solute}/kg_{solvent}$]
$\dot{m}$	mass flow rate [kg/s]
$\dot{m}''$	mass flux [$kg/(m^2 \cdot s)$]
$\Delta mass$	change in mass of the liquid desiccant inside the HAMP [kg_{sol}]
N	buoyancy ratio [-] defined by Yan (1996)
N	number of data points in a sample, for uncertainty calculations
NTU	number of heat transfer units of an energy exchanger [-] $\left(UA_{surface}/\left(\dot{m}c_p\right)\right)$
NTU_m	number of mass transfer units of an energy exchanger[-] ($U_m A_{surface}/\dot{m}$)
Nu	Nusselt number [-] (hD_h/k)
P	pressure [Pa]
Pr	Prandtl number [-] ($\mu c_p/k$)
q	heat transfer rate[W]
$\dot{q}''$	heat flux [W/m^2]
Q	volume flow rate [L/min]
R	calculated result, used in the uncertainty analysis
R	resistance to vapour diffusion [s/m]
R	universal gas constant of air [$J/(kg_{air} \cdot K)$]

Ra	Rayleigh number [-] (Gr_hPr or Gr_mSc)
Ra^+	effective Rayleigh number [-] (Lin et al., 1992b) ($Ra_h + Ra_m$)
Re	Reynolds number [-] ($\rho V D_h/\mu$)
RH	relative humidity [% RH]
Ri	Richardson number [-] ($(Ra/Pr)/Re^2$)
s_x	precision uncertainty at 68% confidence level
Sc	Schmidt number [-] (ν/D)
Sh	Sherwood number [-] ($h_m^W D_h/(\rho_{air} \cdot D)$)
t	time [s]
T	temperature [°C or K]
TC	thermocouple
U	overall heat transfer coefficient [$W/(m^2 \cdot K)$]
U_m	overall mass transfer coefficient [$kg_{air}/(m^2 \cdot s)$ based on W]
U_x	total uncertainty at 95% confidence level
V	velocity [m/s]
W	humidity ratio [g_w/kg_{air}]
X	concentration of water vapour
X_{sol}	ratio of the mass of water to the mass of salt in the solution [kg_w/kg_{salt}]
x,y,z	coordinate system for CFD model
Z	length of the heat transfer surface [m]
Z	valence number [-]
z	charge of the ionic species [-]

GREEK SYMBOLS

β	coefficient of thermal expansion [1/K]
γ	concentration of salt solution as a fraction [kg_{salt}/kg_{sol}]
Δ	difference between two values
δ	thickness [m]
δ	fluctuations in measurements
ε	effectiveness [%]
ε	emissivity of a surface [-]

Θ	parameter used to calculate specific heat of salt solution
μ	dynamic viscosity [Pa·s]
ν	kinematic viscosity [m^2/s]
ν	number of moles [mol]
ρ	density [kg/m^3]
σ	Stefan-Boltzmann constant [$W/(m^2 \cdot K^4)$]
ϕ	relative humidity, expressed as a fraction [-]
$\phi_x^{1/3}$	constant used in forced convection heat transfer correlation [-]
χ	variable used in calculation of P_w for a salt solution [-]

SUBSCRIPTS

air	properties of air
avg	properties at the average temperature and humidity ratio of the air
atm	atmospheric conditions
bulk	properties at the bulk temperature and humidity ratio of the flow
C	cold fluid stream
c	cross-sectional
conv	convection
cr	critical
dry air	properties of the dry airflow
DOWNSTREAM	measurements taken in the airflow downstream of the HAMP
eff,air	effective heat transfer coefficient of the air
exp	experimental results
forced	forced convection
H	hot fluid stream
h	heat transfer
HAMP	measurements taken in the liquid desiccant inside the HAMP
HAMP,surf	surface of the HAMP on the liquid desiccant side
humid	properties of the humid airflow
in	inlet
j, J	indices used in uncertainty calculations

latent	latent moisture transfer
lm	log mean
m	mass transfer
max	maximum value
membrane	properties of the semi-permeable membrane
min	minimum value
mixed	mixed convection
natural	natural convection
out	outlet
r	radiation
salt	properties of the salt in liquid desiccant solution
sensible	sensible heat transfer
sol	properties of the liquid desiccant solution
storage	storage in the control volume
surface	surface of the HAMP
theo	theoretical results
total	total energy transfer (latent and sensible)
UPSTREAM	measurements taken in the airflow upstream of the HAMP
w	properties of water or water vapour
ws	saturated water vapour
+	cation
-	anion
1	surface 1
2	surface 2

SUPERSCRIPTS

C	properties calculated based on concentration
W	properties calculated based on humidity ratio

CHAPTER 1 – INTRODUCTION

In climates such as those experienced in some North American cities, people spend the majority of their time inside buildings. Inside these buildings, there are various sources which can add heat, moisture and contaminants to the indoor air; including people, computers and other types of equipment. In order to make the indoor space comfortable for occupants, heat and moisture must be added to or removed from the space, to maintain an appropriate temperature and moisture content within the space air. One element required for occupant comfort, and to maintain an acceptable indoor air quality (by removing air contaminants) is fresh outdoor air, which must be supplied to the space so occupants have fresh air to breathe. Depending on the outdoor climate, however, the outdoor air may not be suitable to supply to the space, as it may be too hot, too cold, too humid or too dry. In addition to the heat and moisture that must be added to or removed from the space, the ventilation air will also require the addition or removal of heat and moisture to make it acceptable to supply to the space.

The heating, ventilating and air-conditioning (HVAC) industry utilizes many different types of equipment and technologies to handle the addition or removal of heat and moisture to the space and ventilation air. Some technologies, such as all-air systems, handle both the space air and ventilation air at once, while other systems, such as radiant ceiling panels, separate the space air loads and the ventilation air loads between different types of equipment. Each of these systems has its advantages and disadvantages. Currently, the typical equipment used to add or remove

heat and moisture from the space and ventilation air consume a large amount of energy. A United States Department of Energy report (2010) stated that 39% of energy consumed by residential and commercial buildings was used for heating, cooling and ventilating. Many researchers are currently working on developing and enhancing new technologies that can help to reduce energy consumption by HVAC equipment, while still handling the necessary heat and moisture addition or removal in buildings.

This thesis investigates a new device that will have the ability to simultaneously add or remove heat and moisture directly within the space. The research presented in this thesis is the first work performed on this novel device, referred to as a heat and moisture transfer panel or a HAMP. A HAMP is a panel, which can be built directly into a space, similar to a radiant ceiling panel. A HAMP can simultaneously transfer both heat and moisture with the space air, thus maintaining the indoor relative humidity as well as the indoor temperature at acceptable levels. Since a HAMP is designed similar to a radiant ceiling panel, it will share many of the advantages radiant ceiling panels have over typical all-air HVAC systems. This chapter provides some background information on indoor thermal comfort and radiant ceiling panels to highlight the advantages of a HAMP. The main objectives of this thesis are to design and measure the performance of a prototype HAMP and to determine if this concept will work. In addition, the effects of several design parameters on the performance of a HAMP are investigated. A literature review relating to these parameters is also included in this chapter.

1.1 THERMAL COMFORT

It is important to ensure that indoor environments are comfortable for the occupants inside. The term 'comfort' indicates an occupant's satisfaction with the indoor environment and can be divided into two categories: general comfort and thermal comfort. *General comfort* refers to the overall comfort of a person which is affected by a number of factors within the space. *Thermal comfort* refers to the comfort of a person with respect to the temperature of the air in the space. It is impossible to satisfy comfort conditions for all the occupants in a building, however, because comfort is entirely subjective and will vary from one person to another. ASHRAE Standard 55 (2010) outlines the factors that affect thermal comfort and gives guidelines to achieve satisfactory thermal comfort for 80% of occupants.

The main factor that affects thermal comfort is the temperature of the air in the space. People naturally generate heat, which must be removed from the body in order to make the person feel comfortable. If the temperature of the space is too high, not enough heat will be removed from the body but if the temperature of the space is too low, too much heat will be removed, making the person uncomfortable. Another factor that can affect thermal comfort is thermal radiation, between an occupant and the various surfaces within a space. A person sitting near a cold window may be less comfortable than a person sitting on the other side of the room, because of the excess heat lost to the window surface. A third factor that can affect thermal comfort is the speed of the air in the space. Excessive drafts in a space can make a person feel cool because too much heat is being removed from their body. These three factors are dependent on the indoor environment and will be similar for the majority of occupants within a space, depending on their proximity to windows and air diffusers.

Two additional factors that can affect thermal comfort are the metabolic rate of a person, which depends on the type of activity the person is performing and the type of clothing the person is wearing. These factors are specific to each person and will vary from one person to another. Occupants that are performing more labour intensive tasks will produce more heat than occupants performing sedentary tasks and will feel warmer under similar thermal conditions. Clothing provides some insulation between the body and the space air, which will affect the amount of heat transfer to/from the occupants.

The guidelines suggested by ASHRAE Standard 55 (2010) to achieve 80% satisfaction among occupants are based on a metabolic rate for a light, sedentary activity and use typical clothing levels for each season (light clothing for summer, heavier clothing for winter). During the summer, an indoor temperature between 25.0°C and 28.5°C is recommended. In the winter, the recommended range is 21.5°C to 26.5°C. The standard recommends an air speed of less than 0.2 m/s in the space.

1.2 INDOOR HUMIDITY LEVELS

One of the factors that was not mentioned in the above discussion on thermal comfort was the humidity level of the space air. The body cools itself through perspiration and respiration, where excess moisture (water vapour) on the skin and in the respiratory tract evaporates into the space air, leaving the body cooler. The amount of water vapour that evaporates from the skin and therefore, the amount of cooling that occurs, is dependent on the concentration of water vapour in the space air. If the air has a higher concentration of water vapour than the skin, the amount of

evaporation that can occur is limited, which prevents the body from adequately cooling itself. ASHRAE Standard 55 (2010) suggests the indoor humidity ratio (the ratio of water vapour to dry air by mass) should be maintained at or below 12 g_w/kg_{air} (60% RH at 25°C) to achieve good thermal comfort. There is no lower limit suggested because low humidity levels do not affect thermal comfort, which is the purpose of the standard. Both high and low indoor humidity levels, however, can affect the overall comfort of a person, as shown by several researchers.

In addition to limiting the amount of moisture removed from the body, high indoor humidity levels can lead to respiratory problems such as coughing, wheezing and asthma (Bornehag et al. (2004), Fisk et al. (2007)). Spaces with high humidity are also thriving environments for bacteria and dust mites, which can result in allergies and other problems. Toftum et al. (1998a) studied the effect of increased humidity on warm respiratory discomfort and determined that humidity and temperature both have a large impact on perceived thermal sensation, freshness and acceptability of indoor air. They conclude that the discomfort is related to insufficient evaporative and convective cooling of the mucous membranes. Fang et al. (1998a, 1998b) studied the acceptability of air in relation to the enthalpy of the air and found that the acceptability decreases as the enthalpy increases. High indoor humidity levels can also lead to a build-up of moisture on the skin, due to the limited evaporation of the water vapour from the skin. Toftum et al. (1998b) found that an excess of moisture can result in an increase in friction between the skin and clothing which can also cause discomfort. Kosonen and Tan (2004) studied the effects of high humidity on the productivity rate of workers. For a test at 25°C they found productivity decreased by 2% when the relative humidity was increased from 50% RH to

75% RH (an increase in humidity ratio of 4.1 g_w/kg_{air}). At 27°C the productivity decreased by 5% for the same relative humidity increase (an increase in humidity ratio of 4.6 g_w/kg_{air}).

In addition to the reduced comfort of occupants, high indoor humidity levels can also cause problems within the structure of the building. Excess water vapour in the air will be absorbed into, or condense onto, the surfaces in a space. This can lead to mold growth, rot and deterioration of the building materials (Hutcheon (1971), Chen et al. (2004), Moon and Yoon (2010)). It is important to maintain the indoor humidity at moderate levels to avoid these problems.

Although low indoor humidity levels do not affect thermal comfort in the same manner as high indoor humidity levels, low humidity levels can affect an occupant's overall comfort. Low indoor humidity levels cause an excess of water vapour to be removed from the surfaces of the body, such as eyes, nose and throat. This can lead to dry skin and eyes and cause irritation of the mucous membranes of the body. Wyon et al. (2006) studied the effects of low humidity levels on occupant comfort by measuring the dryness of different areas of test subjects and determined that there was evidence of negative effects caused by low humidity levels (less than 15% RH at 22°C). Wyon et al. also found that the productivity of office workers was lower when the humidity level was lower. Reinikainen et al. (1992) conducted a trial in an office building, where occupants were exposed to low humidity levels and high humidity levels at different times. The study showed that the increase in relative humidity reduced the frequency of dry skin and allergic reactions among subjects. Another problem caused by low humidity levels is the spread of infections such as influenza. Ogasawara et al. (2011) showed that the survival rate of

influenza particles in the air is strongly related to the humidity ratio of the air, with a significant increase in the survival rate at low humidity ratios.

The amount of moisture in the indoor air can be affected by the people in the building, who give off moisture through breathing and sweating, the humidity level of the ventilation air supplied to the space, as well as the humidity level of outdoor air entering through infiltration. In order to maintain the indoor humidity ratio at acceptable levels, moisture needs to be added to or removed from the space air, as well as the ventilation air supplied to the space. In dry climates, the low humidity ratio of the ventilation air can be helpful, as the dry air can be used to remove excess moisture from within a space, if needed. In moderate and humid climates, however, the ventilation air is often too humid and cannot be used to remove excess moisture from within a space. In these cases, additional equipment must be used to moderate the amount of moisture in a space.

There are many types of equipment that can be used to add or remove moisture in the ventilation air; including evaporator coils, enthalpy wheels, condenser reheat coils and dedicated preconditioning direct-expansion systems (Witte and Henninger (2010)). All of these units are located outside of the space and condition the ventilation air to a desired humidity level before it is supplied to the space. Fauchoux et al. (2007, 2009) showed that an enthalpy wheel, used to transfer heat and moisture between the outdoor air and the exhaust air of a building, could maintain the indoor humidity levels within acceptable limits. In a humid climate, the energy wheel was able to reduce the simulated peak indoor relative humidity by 14% RH in an office building and 36% RH in a school while maintaining the same indoor temperature. In a cold, dry

climate, the peak relative humidity was reduced by 10% RH in the summer months and increased by 5% RH in the winter.

The indoor humidity levels can be maintained by placing dehumidifying/humidifying equipment directly inside the space, such as a dehumidifier. A dehumidifier works by cooling the air past its dew point temperature, causing the moisture in the air to condense inside the unit. Although dehumidifiers work well at maintaining the indoor humidity levels for small spaces, they are not ideal for large spaces, such as open floor plan offices. Another drawback is the fact that the device takes up floor space and needs to be connected to a drain system to remove the condensed water. Most commercial dehumidifiers also consume a lot of energy, when run regularly, although newer low energy models are becoming more common (McWhinney et al. (2005)). Another disadvantage of this type of device is that they are generally designed to either dehumidify the air or humidify the air, and are not able to do both.

Another method for maintaining adequate indoor humidity levels directly within the space is the use of hygroscopic materials in the space. Hygroscopic materials can be present in the walls, ceiling or floor of a space or in the furniture inside a space. Wood and gypsum are examples of commonly used hygroscopic building materials. If the air in the space has a higher vapour pressure than the hygroscopic material, the hygroscopic material will absorb moisture from the air, lowering the humidity ratio of the air. The hygroscopic material will store the moisture until the vapour pressure of the air drops below the vapour pressure of the hygroscopic material, at which point the moisture will be released back into the space, humidifying the air. In this manner, the hygroscopic materials can be used to both humidify and dehumidify the space air as

needed. Research has shown that hygroscopic materials used in buildings shows that these materials can lower the peak relative humidity in a space, under constant temperature conditions (Simonson et al. (2002, 2004a, b, c), Kurnitski et al. (2007)).

Each of the methods discussed for moderating indoor humidity levels has some advantages, but also some disadvantages. Hygroscopic materials have been shown to work well in bedrooms, but the ability to absorb moisture is greatly reduced if the materials are painted with a latex paint, which has a high resistance to moisture transfer. All-air systems, such as the enthalpy wheel system discussed, consume large amounts of energy due, in part, to the large fans required to move the supply air around the buildings. There is a need for a new technology, which has the ability to either humidify or dehumidify the space air when required, which also consumes less energy than all-air systems.

1.3 RADIANT CEILING PANELS

When considering the sensible load of a space, one way to reduce the energy consumption of the HVAC system is to use equipment that can add or remove heat directly in the space, such as a radiant ceiling panel. A radiant panel consists of a temperature controlled surface which is mounted flush with the floor, ceiling or wall of a space. A schematic of a radiant ceiling panel is shown in Figure 1.1. This example consists of pipes mounted between two sheets of metal, with insulating foam surrounding the pipes. The panel is mounted into a surface in the space and air flows past the steel surface. Water, which has been either heated or cooled, is circulated through the pipes, causing the steel surface of the panel to heat up or cool down. Heat is then transferred between the panel and the space air. Heat transfer occurs mainly through thermal radiation

between the panel and the various surfaces in the space, but also through convection between the panel and the air in the space.

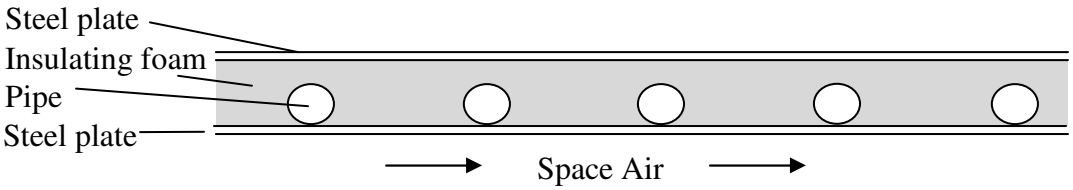

FIGURE 1.1. A schematic of a radiant ceiling panel.

Radiant ceiling panels have been studied by many researchers and have a number of advantages over traditional all-air systems. ASHRAE (2012) lists 25 advantages to using radiant panels to heat/cool buildings. Feustel and Stetiu (1995) and Simmonds (1997) also give summaries of the many advantages of radiant cooling panels, a few of which will be discussed here.

The first set of advantages, which fit the motivation of this thesis, involve thermal comfort for occupants. As mentioned, radiant panels transfer heat with the surfaces in the space through radiation, and with the space air through convection. This means that the air temperature and the mean radiant temperature of the space (related to the temperature of all the surfaces in the space) are both affected by the radiant panel. The use of radiant ceiling panels results in good thermal comfort, as there are no surfaces in the space at drastically different temperatures from the air temperature, such as hot or cold windows. In addition to the heat transfer between the panel and the surfaces in the space, there is also direct transfer between the panel and the occupants, which helps to improve comfort. Finally, the amount of air supplied to the space is less when using radiant panels than for an all-air system, which helps to reduce drafts in the space, and improve comfort for the occupants. Improved thermal comfort using radiant panels has been shown by

several researchers both experimentally and through computer simulations (Vangtook and Chirarattananon (2006, 2007), Kim et al. (2005), Mieriel et al. (2002), Imanari et al. (1999)).

In addition to improved thermal comfort, radiant ceiling panels consume less energy than other systems. Since radiant ceiling panels can maintain both the indoor air temperature and the mean radiant temperature of the space, the design air temperature can be lowered by a few degrees and the mean radiant temperature increased by a few degrees during the heating season, while maintaining the same indoor conditions. Similarly, in the cooling season, the design air temperature can be raised by a few degrees and the mean radiant temperature lowered, without affecting thermal comfort. This results in less energy being used by the heating and cooling equipment to condition the indoor air temperature. Radiant panels also use less energy than all-air systems because they supply heated or cooled water to the space instead of all-air systems which supply heated or cooled air. It takes less energy to pump water around the space than to move the amount of air that would be needed to achieve the same amount of heat transfer. Vangtook and Chirarattananon (2006, 2007), Miriel et al. (2002) and Sodec (1999) found that energy consumption was reduced when using radiant panels as opposed to all-air systems. Eldeeb (2012) performed computer simulations on a one-storey office building with an all air-system and with a radiant ceiling panel in conjunction with a dedicated outdoor air system. Looking at annual energy consumption, the radiant ceiling panel system used 35% less energy than the all-air system.

Although there are many advantages to using radiant panels, ASHRAE (2012) also lists some disadvantages. Most of these relate to improper design and control of the panels, such as, a slow

response time if the controls are not properly designed and installed. A slow response time means it will take a long time for the panel to adjust to the conditions in the room. The disadvantage of interest in this thesis, however, is the inability of the panels to add or remove moisture from a space, as radiant panels can only perform sensible heating or cooling within a space. In addition to the reasons discussed previously for the importance of moderating indoor humidity levels, there is also the added risk of condensation forming on the panels when they are used for cooling. To avoid these problems, panels are often coupled with stand-alone dehumidifiers in the space, or the latent load is handled by the ventilation air, by drying the air before it enters the building. From this disadvantage comes the motivation for the new heat and moisture transfer panel (HAMP) that is the topic of this thesis.

1.4 HEAT AND MOISTURE TRANSFER PANEL (HAMP)

A HAMP is designed to simultaneously add or remove heat and moisture from the space air. Similar to a radiant panel, a HAMP is mounted flush with any surface in a space, and is heated or cooled to a desired set point. Figure 1.2 shows a schematic of a prototype HAMP, as a ceiling panel, which consists of a semi-permeable membrane, mounted to an acrylic tray. A liquid desiccant flows through channels in the tray, directly in contact with the membrane. Heat and moisture are transferred between the liquid desiccant and the space air, through the semi-permeable membrane.

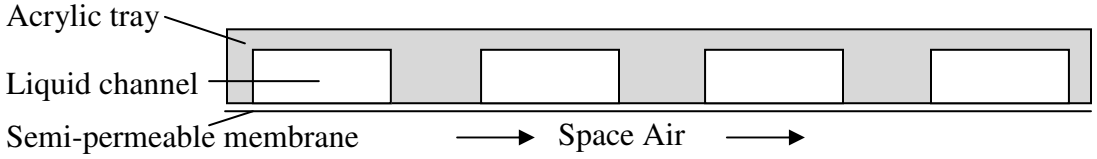

FIGURE 1.2. Schematic of the proposed prototype heat and moisture transfer panel.

1.4.1 Semi-permeable Membranes

A semi-permeable membrane is a material that is permeable to water vapour but impermeable to liquid water. This means that the liquid desiccant inside a HAMP can be in direct contact with the semi-permeable membrane and the liquid desiccant will not leak through the membrane. Semi-permeable membranes are commonly used for making breathable clothing (e.g. outerwear, rain jackets) and building materials (e.g. house wraps) which prevent rain or liquid water from passing through the material, but allow water vapour to pass through. Using a semi-permeable membrane allows for moisture transfer between the space air and the liquid desiccant.

1.4.2 Liquid Desiccants

In order for moisture transfer to occur through the semi-permeable membrane, a concentration gradient must exist across the thickness of the membrane. A HAMP is designed to have air on one side of the membrane and a liquid on the other side of the membrane. When the concentration of water vapour in the air is low, and humidification is required, the liquid must have a higher concentration of water vapour than the air, in order to add moisture to the air. When the air has a high concentration of water vapour, and dehumidification is required, the concentration of water vapour in the liquid must be lower than the air, in order to remove moisture from the air. A liquid desiccant is used, as it has the ability to both humidify and dehumidify the airflow.

Liquid desiccants are liquid solutions that have the ability to absorb water vapour and are often used in the HVAC industry to dehumidify air without having to cool the air to dew point. Liquid desiccants also have the ability to humidify air, as needed. An example of a liquid desiccant is a

mixture of salt and water. A salt solution has a lower surface vapour pressure than pure water, which results in a lower surface humidity ratio than water. At a temperature of 20°C, water has a surface humidity ratio of 14.7 g_w/kg_{air} (100% RH). At the same temperature, a saturated sodium chloride solution has a surface humidity ratio of 11.0 g_w/kg_{air} (75% RH), a saturated magnesium chloride solution has a surface humidity ratio of 4.8 g_w/kg_{air} (33% RH) and a saturated lithium chloride solution has a surface humidity ratio of 1.6 g_w/kg_{air} (11% RH) (ASTM Standard E104 (2007)). If the concentration of the salt solution is below saturation, then the surface humidity ratio (and relative humidity) will be higher than the reported saturated solution values. Different concentration gradients can be created across the membrane by choosing different salts or by using solutions of different concentrations.

1.4.3 Liquid Desiccant Membrane Based Energy Exchangers

Energy exchangers that utilize liquid desiccants and semi-permeable membranes are an emerging type of technology that are being studied by several research groups. One example is a liquid-to-air energy exchanger, which can be used to add or remove heat and moisture from an airflow, before the air is supplied to a space. Zhang (2011), Zhang and Huang (2011) and Zhang et al. (2012) have studied a counter flow hollow fiber membrane exchanger, which consists of airflow around a bed of fibers. The fibers are made of a semi-permeable membrane and a liquid desiccant flows inside the fibers, similar to a shell and tube heat exchanger. Bergero and Chiari (2011) have studied a similar liquid-to-air exchanger with the liquid flow through fibers, but in a cross-flow configuration. Both research groups performed experimental and numerical work on their exchangers.

Another type of liquid-to-air membrane energy exchanger that is used to pre-condition the supply air, has been developed at the University of Saskatchewan (Vali et al. (2009), Mahmud et al. (2010), Hemingson et al. (2011), Akbari et al. (2012)). This energy exchanger was a cross-counter flow exchanger which consisted of multiple semi-permeable membranes, separated by alternating air channels and liquid desiccant channels. Similar exchangers that use alternating air channels and liquid desiccant channels, separated by semi-permeable membranes have been studied by Bergero and Chiari (2010) and Huang et al. (2012). The difference between the liquid-to-air membrane exchangers discussed and a HAMP is that the other exchangers have been used to pre-condition an airflow that was supplied to a space to maintain the indoor temperature and relative humidity, whereas the HAMP would be installed in a space to add or remove heat and moisture from the space air directly.

Lowenstein (2008), Kozubal et al. (2011), and Dieckmann et al. (2011) summarized present liquid desiccant dehumidification systems. According to Dieckmann (2011), liquid desiccant membrane systems typically use 50-90% less energy than other cooling systems, such as direct expansion systems. Kozubal et al. (2011) found that liquid desiccant membrane systems are able to reduce the relative humidity in a space, keeping the peak relative humidity below 50% RH, which provides suitable comfort for the occupants and reduces the risk of mold in the space.

1.5 PERFORMANCE OF THE HAMP

In order to measure the performance of the newly designed prototype HAMP, a test facility was designed, which will be discussed in Chapter 2. ASHRAE Standard 84 (2008) sets out guidelines for testing and obtaining performance data for air-to-air heat and/or energy

exchangers. The scope of this standard includes heat and/or water vapour transfer from one air stream to another, which is different than a HAMP, which transfers heat and water vapour between an air stream and a liquid stream. However, the basic procedures outlined in ASHRAE Standard 84 (2008) can be applied to study a HAMP. The main parameter used to define the performance of any energy exchanger is the effectiveness (ε) of the exchanger.

Effectiveness is a ratio of the actual transfer that occurs in an exchanger to the maximum possible transfer that can occur. Since a HAMP will be used to transfer both heat and moisture, it will have both a sensible and latent effectiveness, as well as a total effectiveness. Sensible effectiveness is a ratio of the actual heat transfer to the total heat transfer and is calculated from temperature, based on the equation

$$\varepsilon_{sensible} = \frac{T_{air,out} - T_{air,in}}{T_{HAMP} - T_{air,in}} \tag{1.1}$$

where $T_{air,in}$ is the temperature of the air as it comes into the exchanger, $T_{air,out}$ is the temperature of the air as it leaves the exchanger and T_{HAMP} is the temperature of the liquid desiccant inside the HAMP [°C or K].

Latent effectiveness is a ratio of the actual moisture transfer to the maximum possible moisture transfer and is calculated from the humidity ratio, based on the equation

$$\varepsilon_{latent} = \frac{W_{air,out} - W_{air,in}}{W_{HAMP} - W_{air,in}} \tag{1.2}$$

where $W_{air,in}$ is the humidity ratio of the air as it enters the exchanger, $W_{air,out}$ is the humidity ratio of the air as it leaves the exchanger and W_{HAMP} is the surface humidity ratio of the liquid desiccant inside the HAMP. All humidity ratios are given in [g_w/kg_{air}].

Total effectiveness is a measure of the actual total energy transfer to the maximum possible total energy transfer and is calculated from the enthalpy, based on the equation

$$\varepsilon_{total}=\frac{h_{air,out}-h_{air,in}}{h_{HAMP}-h_{air,in}} \tag{1.3}$$

where $h_{air,in}$ is the enthalpy of the air as it enters the exchanger, $h_{air,out}$ is the enthalpy of the air as it leaves the exchanger and h_{HAMP} is the enthalpy of the liquid desiccant inside the HAMP. All enthalpies are given in [kJ/kg_{air}]. Appendix A gives a detailed list of all the equations used in this thesis, for easy reference. The equations in Appendix A are given with more specific descriptions relating to locations inside the test facility where measurements are taken.

The equations discussed above can be used to calculate the sensible, latent and total effectivenesses of a HAMP, when the temperature, humidity ratio and enthalpy of the inlet air, outlet air and of the liquid desiccant inside the HAMP are known. These values can be measured in an experiment, as will be described in this thesis, for the prototype HAMP. In practice however, these values are not always known. As such, the effectiveness of an energy exchanger is commonly calculated using correlations, such as the effectiveness–NTU method.

The effectiveness–NTU method relates the number of heat transfer units (NTU) of an energy exchanger to the sensible effectiveness of the exchanger. ASHRAE (2009) presents correlations for exchangers with different flow configurations. The number of heat transfer units of an energy exchanger is dependent on the overall convection heat transfer coefficient of the exchanger (U). For a HAMP, the overall convection heat transfer coefficient will include the

convection and radiation heat transfer coefficients in the air, the thermal conductivity of the membrane and the convection heat transfer coefficient in the liquid desiccant.

The latent effectiveness of an energy exchanger can also be determined from these correlations by substituting the number of mass transfer units (NTU_m) in place of the number of heat transfer units. The number of mass transfer units is dependent on the overall convection mass transfer coefficient (U_m), which includes the convection mass transfer coefficient in the air, the permeability of the membrane and the convection mass transfer coefficient in the liquid desiccant inside the HAMP.

In order to determine the number of heat and mass transfer units for the prototype HAMP, the heat and mass transfer coefficients in the air and liquid desiccant, and the thermal conductivity and permeability of the membrane must be known. The properties of the membrane can be measured, and are presented for the semi-permeable membrane used in the prototype HAMP by Larson (2006). The convection heat and mass transfer coefficients are dependent on the flow characteristics inside the test section, such as the geometry of the flow and the mode of convection that is dominant in the test section.

Typically, heat transfer correlations from the literature are used to determine the convection heat transfer coefficients and the heat and mass transfer analogy is used to determine the convection mass transfer coefficients for an energy exchanger. In this thesis, the number of heat and mass transfer units are calculated both theoretically from the heat transfer correlations and experimentally from the measured data. As there are many possible flow configurations and

many research papers on each flow configuration, the literature review presented will be confined to those that are the closest to the flow configuration in the test facility used to study the prototype HAMP. The following section summarizes the important aspects of the flow configuration and the relevant literature.

1.6 CONVECTION HEAT TRANSFER COEFFICIENTS

The current literature on convection heat transfer coefficients is quite extensive. For heat transfer in ducts, the convection heat transfer coefficients are dependent on several parameters, including the geometry and orientation of the duct and the boundary conditions (constant temperature or heat flux) on the walls of the duct. Convection heat transfer coefficients are also dependent on the fluid flow inside the duct; whether it is laminar or turbulent, hydrodynamically fully developed or developing flow. In order to present a summary of the literature that is relevant to this study, a summary of the characteristics of the test facility is first presented here. The test facility will be described in detail in Chapter 2 of this thesis. The important parameters of the test facility are:

- the test section is a horizontal, rectangular duct, with an aspect ratio (width/height) of 1.5,
- the airflow is laminar (Reynolds number is approximately 65 for each test),
- the boundary conditions are assumed to be constant temperature and concentration on one surface (the HAMP) and adiabatic, impermeable conditions on the other three surfaces and
- the airflow is hydrodynamically fully developed (the velocity profile is not changing in the direction of the flow).

The following literature review is not a comprehensive list, but a summary of the pertinent literature for the test facility used in this study.

1.6.1 Literature Review for Heat Transfer in a Rectangular Duct

The case of convection heat transfer in rectangular ducts has been well studied. There are three convection regimes that need to be considered: forced convection, where the air motion is caused by an external force, natural convection, where the air motion is caused by buoyancy forces and mixed convection, where both forced and natural convection occur. The correlations found in the literature are given in terms of the Nusselt number (Nu), which is a dimensionless form of the convection heat transfer coefficient. The Nusselt number makes it possible to compare convection heat transfer coefficients for ducts of different geometry and size.

Forced Convection

When forced convection is the dominant mode of convection in a duct, the heat transfer coefficient is affected by the Reynolds number of the flow, the aspect ratio of the duct, the length of the heat transfer surface, and the hydraulic diameter of the duct. Several researchers, including Kooijman (1973), Shah and London (1974 and 1978), Shah and Bhatti (1987) and Kays and Perkins (1985) have presented average Nusselt numbers for rectangular ducts with a constant surface temperature on all four walls, for both thermally fully developed and thermally developing flows.

Lyczkowski et al. (1981) presented a numerical analysis of heat transfer in a rectangular duct with different aspect ratios with a constant surface temperature on one, two, three and all four

walls. The average Nusselt numbers are presented for fully developed flow for four aspect ratios. Krishnamurty and Sambasiva Rao (1967) presented analytical expressions which can be used to calculate the local and average Nusselt number in a rectangular duct with a constant surface temperature on one wall (the bottom) and on all four walls.

Natural Convection

When natural convection is dominant, the flow can be characterized by the Grashof number (Gr) and the heat transfer by the Rayleigh number (Ra) which relates the strength of the buoyancy forces to the viscous forces in the duct. Ou et al. (1974) and Cheng et al. (1972) performed numerical analyses on natural convection flows through rectangular ducts with high Prandtl numbers and multiple aspect ratios. Ou et al. used a constant surface temperature boundary condition on all four walls and Cheng et al. used a constant surface heat flux boundary condition. Both present local Nusselt numbers for different Rayleigh number flows.

Catton (1978) and Raithby and Hollands (1985) presented reviews of natural convection in enclosures, including rectangular ducts with a constant temperature on one surface. When the heated surface is on the top of the duct, the heat transfer in the duct is by conduction and the Nusselt number is equal to one, independent of Rayleigh number. When the heated surface is on the bottom of the duct, heat transfer by convection occurs. Raithby and Hollands (1985) presented a correlation for Nusselt number as a function of Rayleigh number which compares within 10% to experimental data for gas and liquid flows through ducts with aspect ratios between 1 and 10.

Mixed Convection

Mixed convection will occur in the duct when both the forced and natural convection forces are large, which occurs when the Richardson number is approximately equal to one. A mixed convection flow is dependent on both the Reynolds number and Rayleigh number of the flow. Ou et al. (1976) and Morcos et al. (1986) studied mixed convection through inclined rectangular ducts. Ou et al. performed a numerical analysis with a constant surface temperature on all sides and various aspect ratios. The results show that the Nusselt number is greatly affected by the inclination angle of the duct. Morcos et al. (1986) performed experiments with hydrodynamically and thermally developing flow through a duct with a constant surface temperature on all sides. The results show that the Nusselt number increases with increasing Rayleigh number and with increasing aspect ratio.

A constant heat flux boundary condition was used on all walls by Savino and Siegel (1964) and Abou-Ellail and Morcos (1983) to numerically study mixed convection in a horizontal rectangular duct with different aspect ratios. Their results also show that the Nusselt number increases with Rayleigh number and aspect ratio. Mixed convection in rectangular ducts with constant surface temperature on all four walls has also been studied numerically (Chou and Hwang (1984), Lin and Chou (1989) and Chou (1990)). These studies incorporated various aspect ratios as well as various Prandtl number flows. Results of local Nusselt number for different Rayleigh numbers were presented.

The research presented for mixed convection up to this point has been for constant boundary conditions on all four walls. A numerical study by Narusawa (1993) investigated mixed

convection in a duct with an aspect ratio of 10, with only the top wall cooled and the bottom wall heated. The focus of the Narusawa study was the length required to reach thermally developed conditions. Nyce et al. (1992) also studied flow in a duct with the top wall cooled and the bottom wall heated, with an aspect ratio of two. The study by Nyce et al. focused on the effects of different Reynolds numbers on the velocity profiles in the duct, for a Rayleigh number of 22,200.

Lin and Lin (1996) and Chiranjivi and Parabrahmachary (1972) performed experiments with mixed convection in horizontal rectangular ducts with only the bottom wall heated. Chiranjivi and Parabrahmachary based their experiments on the work of Krishnamurty and Sambasiva Rao (1967) discussed in the forced convection section but expanded it to include the effects of buoyancy. They derived an equation based on their results, which can be used to calculate the heat transfer coefficients for different Reynolds and Grashof numbers.

1.7 SIMULTANEOUS HEAT AND MASS TRANSFER

The preceding discussion has been on heat transfer in horizontal, rectangular ducts. The focus of the research in this thesis, however, is on simultaneous heat and mass transfer between a HAMP and an air stream. Since the heat and mass transfer are coupled, one will have an effect on the other and the correlations found in the literature for heat transfer may not be applicable for simultaneous heat and mass transfer. A summary of some of the current research on heat and mass transfer in a rectangular duct is presented here.

1.7.1 Literature Review of Heat and Mass Transfer in a Rectangular Duct

Lin et al. (1992a) and Yan (1994, 1996) studied heat and mass transfer in a rectangular duct, using numerical simulations. Lin et al. modeled a thin film of water on the bottom of the duct at constant temperature, whereas Yan modeled a uniform temperature and concentration on all four walls of the duct. Both studied laminar, mixed convection airflow through the duct. The results of both studies showed that the combined effects of thermal and mass diffusion can significantly affect heat transfer characteristics in the duct. The Nusselt and Sherwood numbers were enhanced when the buoyancy forces due to the species diffusion assisted the buoyancy forces due to the heat transfer.

To quantify the ratio of mass transfer to heat transfer, Lin et al. (1992a) defined a ratio which relates the energy transport from the species diffusion to that from the thermal diffusion. In a similar manner, Yan (1996) defined a buoyancy ratio (N) which relates the amount of mass transfer to the amount of heat transfer in the duct. A ratio of zero refers to the case of all heat transfer (no mass transfer) and a ratio of one refers to the case of equal heat and mass transfer. A positive ratio indicates the heat and mass transfer are acting in the same direction (assisting each other) and a negative ratio means the heat and mass transfer are acting in the opposite direction (opposing each other).

Both Lin et al. and Yan presented the local Nusselt numbers for the length of their ducts for various buoyancy forces. Figure 1.3 shows the local Nusselt and Sherwood numbers for various Rayleigh numbers, with a buoyancy ratio equal to one, presented by Yan (1996). This graph showed how the Nusselt and Sherwood numbers in the duct changed across the length of the heat

and mass transfer surface. The Nusselt and Sherwood numbers were approximately the same at the inlet and outlet of the duct, independent of the Rayleigh number. In between the inlet and outlet, the Nusselt and Sherwood numbers increased with increasing Rayleigh number. This meant the buoyancy forces had a significant impact on the heat and mass transfer in the duct.

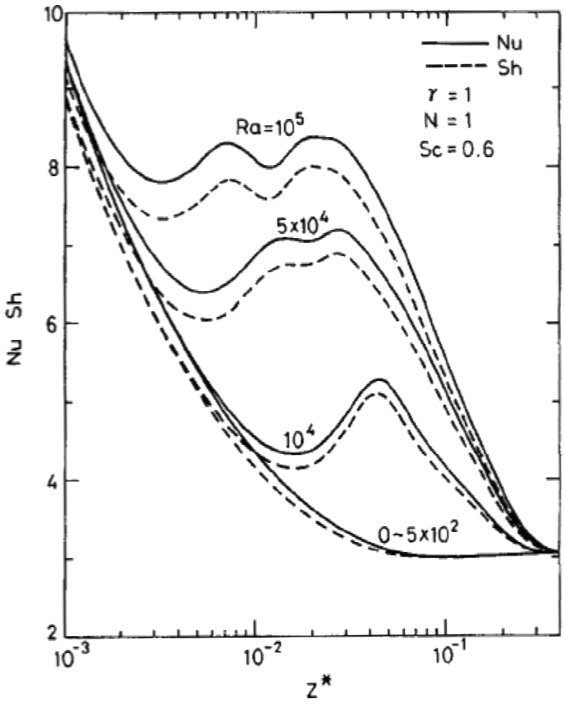

FIGURE 1.3. Axial variation of local Nusselt and Sherwood numbers for Rayleigh numbers ranging from 0 to 10^5, where Z^* is the dimensionless axial length of the duct, γ is the aspect ratio of the duct and N is the buoyancy ratio (Yan, 1996)*.

Figure 1.4 shows the effect of the buoyancy ratio on the Nusselt and Sherwood numbers for one Rayleigh number, from Yan (1996). The middle curve represents a buoyancy ratio of zero, which is the case of heat transfer only. When the buoyancy ratio was positive (assisting gradients) the Nusselt and Sherwood numbers were larger than the case of heat transfer only.

* Reprinted from International Journal of Heat and Mass Transfer, 69, W.M. Yan, Combined buoyancy effects of thermal and mass diffusion on laminar forced convection in horizontal rectangular ducts, pg 1479-1488, 1996, with permission from Elsevier.

This indicated that the concentration gradient helped to increase the heat transfer. When the buoyancy ratio was negative (opposing gradients) the Nusselt and Sherwood numbers were lower than the heat transfer only case. As the magnitude of the buoyancy ratio increased, the values of the Nusselt and Sherwood numbers also increased.

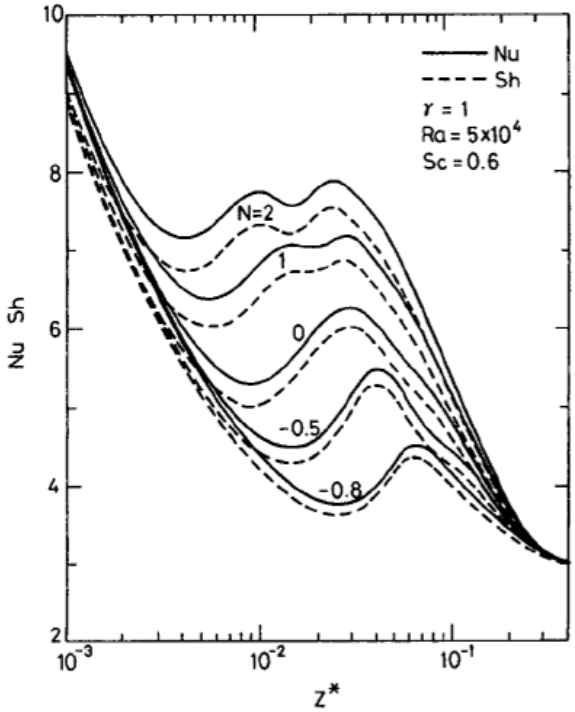

FIGURE 1.4. Axial variation of local Nusselt and Sherwood numbers for buoyancy ratios ranging from -0.8 to 2, where Z^* is the dimensionless axial length of the duct and γ is the aspect ratio of the duct (Yan, 1996)[†].

The range of Rayleigh numbers presented by Lin et al. (1992a) and Yan (1996) were quite small compared to the Rayleigh numbers that would exist in an actual room with a cooled ceiling. In an actual space, the important length scale would be the height of the room, which would be much larger than the length scale used in their studies, or in the test facility used in the current

[†] Reprinted from International Journal of Heat and Mass Transfer, 69, W.M. Yan, Combined buoyancy effects of thermal and mass diffusion on laminar forced convection in horizontal rectangular ducts, pg 1479-1488, 1996, with permission from Elsevier.

research. The Rayleigh numbers that are studied in this thesis have a magnitude in the range of 10^6, based on the height of the duct in the test facility.

One of the objectives of this thesis is to increase the amount of experimental data available in the literature on heat and mass transfer, so a summary of the current data available, based on Rayleigh number and Reynolds number is presented in Figure 1.5 and Table 1.1. In Figure 1.5, the range of experimental data points studied in this thesis is highlighted by the shaded area marked 'present work.' The graph shows the experimental work done by Chang et al. (1997), Lin and Lin (1996), Morcos et al. (1986) and Nyce et al. (1992) as well as the numerical work done by Narusawa (1993), Ou et al. (1976) and Abou-Ellail and Marcos (1983). The papers that presented ranges of Rayleigh numbers or Reynolds numbers instead of specific points are marked with shaded areas that cover the range of data points studied.

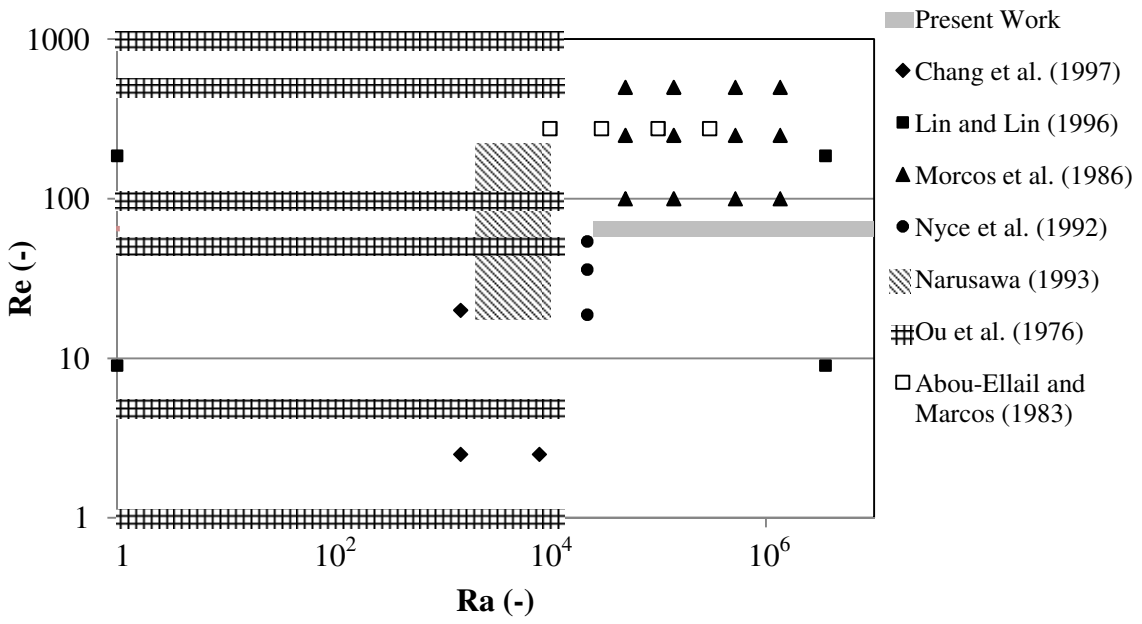

FIGURE 1.5. Range of Rayleigh (Ra) and Reynolds (Re) numbers studied in literature presented in this thesis.

For studies that focused on natural convection flows, or mixed convection flows, the Reynolds number of the flow was not always presented so the data could not be presented in Figure 1.5. Table 1.1 summarizes the range of Rayleigh numbers studied in the remainder of the literature reviewed in this chapter. All of these studies were numerical simulations of either heat transfer, or heat and mass transfer.

TABLE 1.1. Range of Rayleigh numbers studied in the literature presented in this thesis.

Author	Rayleigh Number Range
Heat Transfer	
Cheng (1972)	$1x10^3 – 3x10^5$
Ou et al. (1974)	$\sim0 – 5x10^5$
Lin and Chou (1989)	$\sim0 – 2x10^5$
Chou (1990)	$\sim0 – 1x10^5$
Heat and Mass Transfer	
Lin et al. (1992a)	$4.5\ x10^4 – 9.4\ x10^4$
Yan (1994)	$\sim0 – 1\ x10^5$
Yan (1996)	$\sim0 – 1\ x10^5$
Present Work	$-4.2\ x10^6 – -0.6x10^5$
	$0.5\ x10^5 – 6.4\ x10^6$

1.7.2 Review of Heat and Mass Transfer through a Semi-permeable Membrane

In addition to the liquid desiccant membrane exchangers that were discussed in Section 1.4.3, semi-permeable materials have been the subject of many other research studies. Djongyang et al. (2009) performed an analytical study to predict coupled heat and mass transfer in semi-permeable building materials. Olutimayin and Simonson (2005) studied one-dimensional transient heat and moisture transfer in a semi-permeable cellulose insulation. Qin

and Belarbi (2005) and Qin et al. (2006) used analytical methods involving a transfer function method to model heat and moisture transfer in semi-permeable building materials such as fibrous insulation.

Iskra (2007) measured the heat and mass transfer between a pan of water placed in the bottom of a duct and the air flowing over the pan. He performed these experiments with and without a semi-permeable membrane covering the pan. The purpose of Iskra's research was to measure the convection heat and mass transfer coefficients in the airflow. A numerical model of Iskra's research was created by Talukdar et al. (2008). The test facility they used is similar to the test facility described in this thesis, with the main difference being the height of the duct. In their work, the height of the duct was very small and buoyancy effects were negligible in the duct. The test facility designed to test a prototype HAMP in this thesis, has a larger height to better model a room. The results will show that in some situations, the buoyancy forces are very important to the performance of a HAMP.

1.8 FLOW VISUALIZATION

In the research presented in this thesis, the presence of buoyancy forces in the duct will be demonstrated through the use of flow visualization. Many researchers have done flow visualization of fluid flow through channels of various geometries, but this section will be limited to examples of research on flow through rectangular channels.

As part of a study on flat plate heat exchangers with louvered fins, Huisseune (2012) performed flow visualization of a forced convection flow, by injecting a dye into water flowing through the

exchanger. The visualizations showed that at low Reynolds number, no vortices were formed in the flow and there was very little recirculation in the exchanger. As the Reynolds number increased, vortices appeared and the flow became unstable. These experiments were compared to numerical results, predicting the performance of the heat exchanger.

Almeida and Naylor (2011) studied free convection between two rectangular window panes with blinds between the planes. The airflow in this case was vertical and both side walls were heated or cooled. The steady-state flow patterns were captured using an interferometer. The effects of buoyancy on the flow patterns was studied. Incropera et al. (1987) used a dye injected into water, in a horizontal rectangular channel, to determine the distance from the inlet to the onset of buoyancy in a simultaneously developing flow, with a constant temperature on all four walls.

Lin and Lin (1996) performed flow visualization on a mixed convection airflow in a rectangular duct, with the bottom wall heated. A thin sheet of smoke was injected into the test section along the bottom wall and the flow patterns caused by the buoyancy forces were captured. Chang et al. (1997) also studied mixed convection flow through a rectangular duct, with the bottom wall heated. The object of this research was to study the vortex rolls that formed in the duct.

1.9 OBJECTIVES

The first objective of this Ph.D. thesis is to design and build a prototype of a device that can simultaneously transfer heat and moisture with air in a space (a HAMP). The second objective is to determine if this device has the capability to transfer heat and moisture under various operating conditions (heating, cooling, dehumidification or humidification). This is

accomplished by measuring the performance of the HAMP under different operating conditions. The performance of the HAMP is quantified by the sensible and latent effectivenesses, as well as by the total heat and mass fluxes between the HAMP and the air in the test facility. The final objective of this thesis is to provide general relationships between the performance of the HAMP and several design parameters based on the experimental data collected, which can be used in the future to develop correlations for predicting the sensible and latent effectivenesses of a HAMP. The specific design parameters investigated are the operating condition factor (H^*) of the HAMP, the effective Rayleigh number (Ra^+) of the flow and the ratio $NTU_{exp}/NTU_{m,exp}$.

1.10 THESIS OVERVIEW

To complete the objectives outlined in Section 1.9, the following specific tasks were performed and are presented in the following chapters:

Chapter 2

- A prototype HAMP was designed and built and
- A test facility to measure the performance of the prototype HAMP was designed and built.

Chapter 3

- The test facility was commissioned, by performing a steady-state analysis of preliminary results, an uncertainty analysis and energy and mass balances.

Chapter 4

- The important energy exchanger design parameters were determined for each test case.

Chapter 5

- The change in temperature and relative humidity of the airflow, caused by the heat and moisture transfer between the prototype HAMP and the airflow under different operating conditions were measured,
- The sensible and latent effectivenesses of the prototype HAMP were determined for different operating conditions,
- The effects of Ra^+ on the sensible and latent effectivenesses were determined,
- The effects of natural convection on the induced airflow patterns in the duct were determined, through the use of flow visualization and
- The total heat and mass fluxes between the HAMP and the air in the test section were determined for different operating conditions.

Chapter 6

- Standard methods used to predict the sensible and latent effectivenesses of an energy exchanger were investigated for their relevance to a HAMP,
- The sensible and latent effectivenesses of a HAMP were determined to be functions of the experimental NTU and NTU_m values of the HAMP and
- The general relationships between the design parameters and NTU_{exp} and $NTU_{m,exp}$ were determined.

1.11 CONTRIBUTIONS

The specific contributions of this work are summarized below.

- Design the first prototype of a device that has the ability to simultaneously transfer heat and moisture with air in a space (a HAMP), with transfer in any direction,

- Determine the performance of a HAMP under different combinations of cooling, heating, humidification and dehumidification,
- Provide experimental data relating the performance of an energy exchanger with combined heat and mass transfer to specific design parameters (NTU_{exp}, $NTU_{m,exp}$, H^*, Ra^+ and $NTU_{exp}/NTU_{m,exp}$),
- Provide flow visualization data for forced convection and natural convection in an energy exchanger with combined heat and mass transfer for different temperature and concentration gradients,
- Provide an understanding of general heat and moisture transfer between a laminar airflow (with and without buoyancy) and a liquid desiccant separated by a semi-permeable membrane.

CHAPTER 2 – TEST FACILITY AND INSTRUMENTATION

To measure the performance of a prototype HAMP, a test facility was constructed in the Fluid Mechanics Laboratory at the University of Saskatchewan. The facility was designed to pass air across the surface of a small prototype HAMP and measure the change in the temperature and relative humidity of the airflow, as well as the moisture transfer rate from the liquid desiccant inside the HAMP. The design of the prototype HAMP and test facility and the instrumentation used to take each measurement are discussed in detail in this chapter.

2.1 APPARATUS

The test facility used to measure the performance of the prototype HAMP, shown in Figure 2.1, consisted of four sections. The first section was used to control the temperature, relative humidity and volume flow rate of the air stream. Section 2 was used to precondition the airflow to ensure that it was hydrodynamically fully developed when it entered the test section. The temperature and relative humidity of the air were measured in this section. The airflow then passed into the test section (section 3) where heat and moisture were exchanged between the prototype HAMP and the air. The temperature and density of the liquid desiccant inside the HAMP were measured in this section. Finally, the airflow passed into the mixing section (section 4), where the downstream temperature and relative humidity of the airflow were measured. This section was designed to reduce the area of the duct so the air was well mixed and bulk measurements could be taken at the outlet.

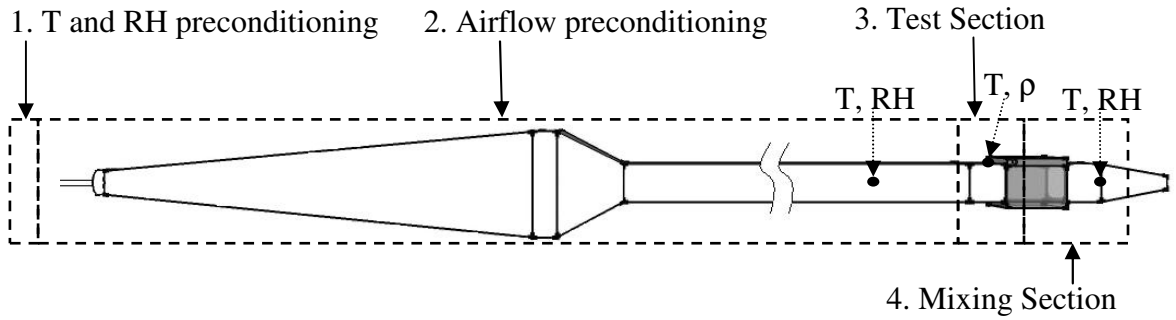

FIGURE 2.1. Schematic of the test facility used to measure the performance of the prototype HAMP.

2.1.1 Temperature and Relative Humidity Preconditioning (section 1)

The temperature and relative humidity preconditioning section was designed to control the upstream temperature and relative humidity of the air to the desired conditions. The inlet was connected to a compressor which supplied dry air to the test facility at approximately 4% RH and 23°C, through a tube with an inside diameter of 9.5 mm (3/8 in). Figure 2.2 shows a schematic of the equipment used in the preconditioning section. The air entered the test facility through a tube, on the left side of the diagram and was then divided into two streams.

One of the air streams was passed through a tank of water. The air was forced into the bottom of the tank and then bubbled up to the top of the tank. Humid air was drawn out of the tank through the shorter hose at the top of the tank. The tank was rigid and well sealed, to ensure that the mass flow rate of the humid air drawn out of the top of the tank was equal to the mass flow rate of the dry air that entered the bottom of the tank. The second air stream bypassed the tank and was then mixed with the humid air from the water tank. The humidity of the airflow was set by mixing appropriate amounts of the dry and humid air.

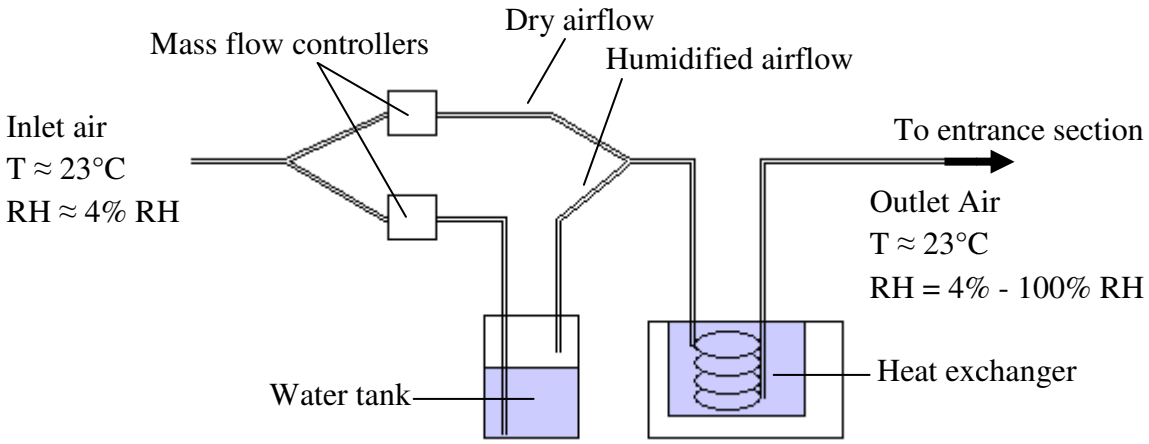

FIGURE 2.2. Schematic of the preconditioning section of the test facility.

After the air had been humidified it was passed through a heat exchanger. The purpose of the heat exchanger was to keep the temperature of the air at a constant value. The temperature of the airflow was dependent on the temperature of the air in the laboratory. Depending on the time of the testing, the temperature changes in the laboratory could cause the temperature of the airflow to change by as much as ±2°C. The heat exchanger was able to keep the airflow at approximately 23°C with fluctuations of less than ±0.1°C during all tests. The heat exchanger could also be used in future tests to heat or cool the upstream airflow as desired.

2.1.2 Airflow Preconditioning (section 2)

After the air was set to the desired temperature and relative humidity, it passed into the airflow preconditioning section. The purpose of this section was to ensure the airflow that entered the test section was hydrodynamically fully developed, laminar flow. Figure 2.3 shows the duct used to create a smooth transition between the inlet hose and the test section. The location of the temperature and relative humidity sensor for the upstream measurements is also shown.

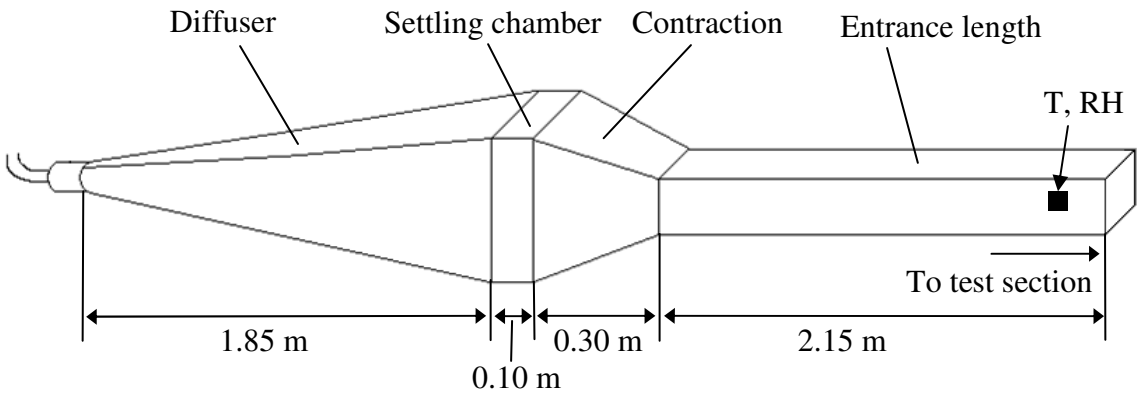

FIGURE 2.3. Schematic of the expansion section of the test facility.

The design of the preconditioning section was based on Mehta (1979), who described methods for proper aerodynamic design of an open circuit wind tunnel. This section consisted of four main parts. The first part was a diffuser, which changed the duct from a round cross-section with a diameter of 9.5 mm (3/8 in) to a rectangular cross-section with dimensions 43 cm (17 in) by 51 cm (20 in). The diffuser was designed to gradually change the cross-sectional area of the duct to ensure the airflow expanded smoothly and did not separate from the inside walls, creating a uniform airflow through the duct. The diffuser had an area ratio (ratio of outlet area to inlet area) of 27.0 and a diffuser angle (the angle between the two lines joining the inlet and outlet) of approximately 10°. The diffuser was made of galvanized steel with a smooth inner surface.

To ensure there was no flow separation in the diffuser, three perforated metal screens (with open area ratios of 0.45) were located at distances of 0.5 m (20 in), 1.1 m (43 in) and 1.65 m (65 in) from the beginning of the diffuser. The screens helped make the velocity profile uniform and reduced the boundary layer thickness along the walls of the diffuser. The second part of the preconditioning section was a settling chamber. The settling chamber was 10 cm (4 in) long and

was filled with sheets of corrugated plastic stacked together to form a honeycomb. The settling chamber helped to straighten the flow and ensure a uniform airflow going into the test section.

The third part of the preconditioning section was a contraction section which reduced the cross-sectional area of the duct to the desired area of the test section. According to Mehta (1979), a contraction or nozzle immediately upstream of the test section can greatly improve the uniformity of the air flow. The contraction had an area ratio (the ratio of the inlet area to outlet area) of 6.3. The contraction was also made of galvanized steel and had a smooth inner surface.

The final part of the preconditioning section was the entrance length. The entrance length had the same cross-sectional area as the test section (15.2 cm (6 in) high by 22.9 cm (9 in) wide) and allowed the airflow to become hydrodynamically fully developed before the air entered the test section. According to Idelchik (1986) the required entrance length for laminar flow through a circular pipe or rectangular duct with an aspect ratio between 0.7 and 1.5, is equal to $B*Re*D_h$ where B is the reduced length of the started section, taken from the literature to be 0.065, Re is the Reynolds number of the flow and D_h is the hydraulic diameter of the duct. For the test facility designed to measure the performance of the prototype HAMP, the required entrance length was 0.012*Re. The entrance length chosen was 2.15 m (7 ft) which was adequate for flows with $Re < 180$. For turbulent flow, Idelchik states that the required entrance length is considerably shorter than for laminar flow. The thermal and concentration boundary layers will begin to develop at the inlet of the test section and will continue to develop over the length of the prototype HAMP.

2.1.3 Test Section (section 3)

The test section was the main part of the test facility. This was where the prototype HAMP was located and where heat and moisture were transferred between the HAMP and the air. A photograph of the test section is shown in Figure 2.4. The test section had a cross-section of 15.2 cm (6 in) high by 22.9 cm (9 in) wide with a hydraulic diameter (D_h) of 18.3 cm. Air entered the test section from the left and exited to the right. The test section was made of clear acrylic, which allowed the user to see into the test section while tests were being performed. This was necessary for the flow visualization tests, which will be discussed in more detail later in this chapter. During other tests, the test section was insulated with 2.5 cm (1 in) thick extruded polystyrene.

The bottom and sidewalls of the test section (in the orientation shown in Figure 2.4) were made from one piece of acrylic. The prototype HAMP fit snug on top of this piece and the seams were covered with aluminum foil tape, to minimize leaks through the seams. The test section was symmetrical top to bottom so the whole section could be inverted without having to make any changes to the duct. By designing the test section in this way, the HAMP could be tested as a floor panel, ceiling panel or wall panel. Specific details of the HAMP will be discussed in Section 2.2.

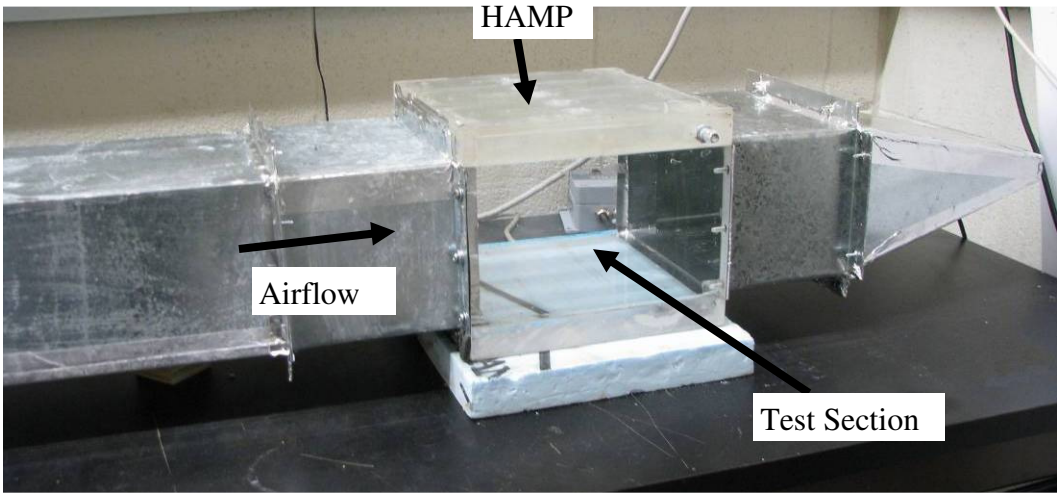

FIGURE 2.4. Photograph of the test section where the heat and moisture transfer occurs.

2.1.4 Mixing Section (section 4)

The final section of the test facility was the mixing section. The purpose of this section was to allow measurements of the bulk temperature and relative humidity of the airflow downstream of the test section to be taken. During testing, temperature and concentration gradients form across the height of the duct. In order to take the bulk measurements, the air must be well mixed before it reaches the sensor. The cross-sectional area of the duct was reduced using a converging nozzle. The sensor was placed near the exit of the nozzle, as shown in Figure 2.5.

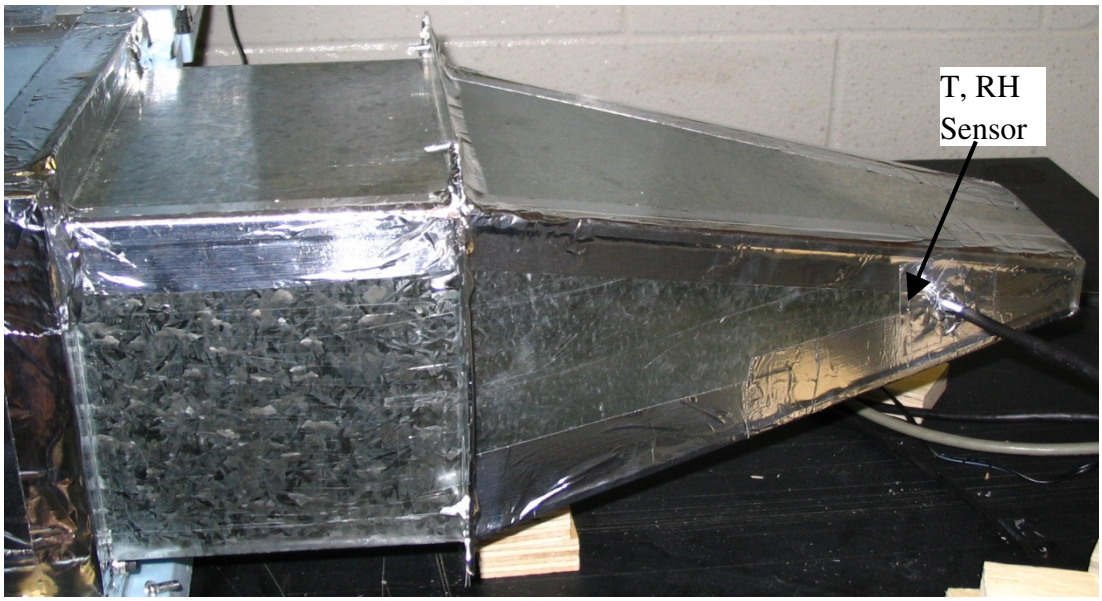

FIGURE 2.5. Photograph of the mixing section of the test facility where downstream temperature and relative humidity measurements are taken.

To ensure that the air was well mixed after leaving the test section, the height of the duct was reduced from 15.2 cm (6 in) to 2.5 cm (1 in) and the width of the duct from 22.9 cm (9 in) to 10.2 cm (4 in), over a length of 30.4 cm (12 in), as shown in Figure 2.6(a). The outlet of the duct was further reduced to an area 2.5 cm (1 in) high by 2.5 cm (1 in) wide, which forces the airflow towards the center of the duct. The Reynolds number of the airflow at the outlet was increased to approximately 500.

The temperature and relative humidity sensor was placed 2.5 cm (1 in) from the outlet, as shown in Figure 2.6(b). The entire sensor head was 6 cm long, with a diameter of 1 cm. The part of the sensor that measured the temperature and relative humidity was 3 cm and was centered in front of the outlet of the duct. The design of the duct, and the size of the sensor head compared to the size of the outlet of the duct ensured that the airflow was well mixed and accurate bulk temperature and relative humidity measurements were being taken.

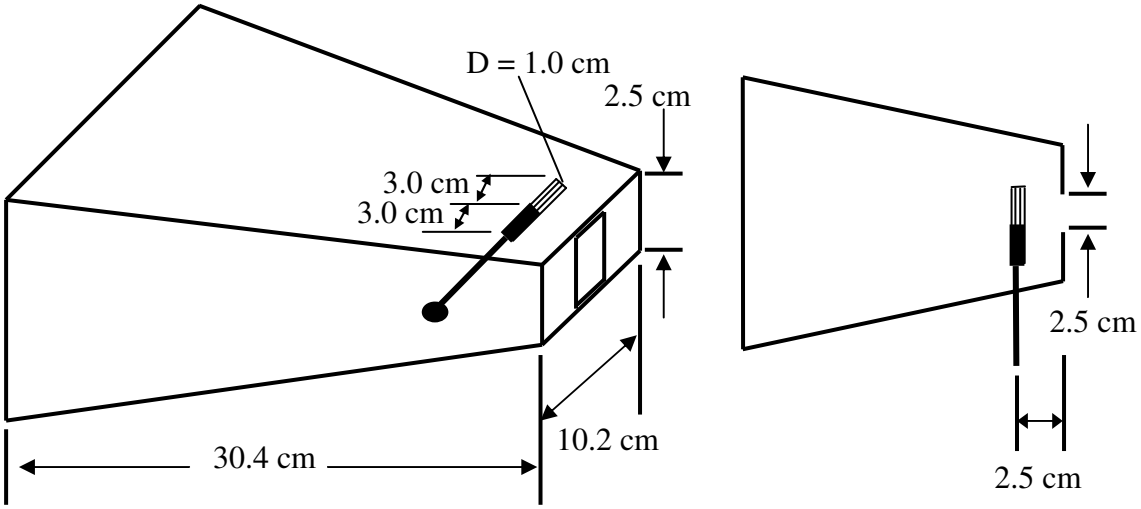

FIGURE 2.6. Schematics of a) an orthogonal view and b) the top view of the mixing section and the sensor, with dimensions shown.

2.2 DESCRIPTION OF THE PROTOTYPE HAMP

As discussed in Chapter 1, a HAMP is a new type of heat and moisture exchanger that has not been studied previously. In order to measure the performance of a HAMP, a prototype needed to be designed and built. The details of the prototype are discussed in this section. The prototype HAMP was made of an acrylic tray with an inlet and an outlet for the liquid desiccant flow, in opposite corners, as shown in Figure 2.7. The acrylic tray was divided into five channels, which allowed the liquid desiccant to flow evenly from the inlet to the outlet. A thermocouple was installed in each of the five channels, to measure the temperature of the liquid desiccant.

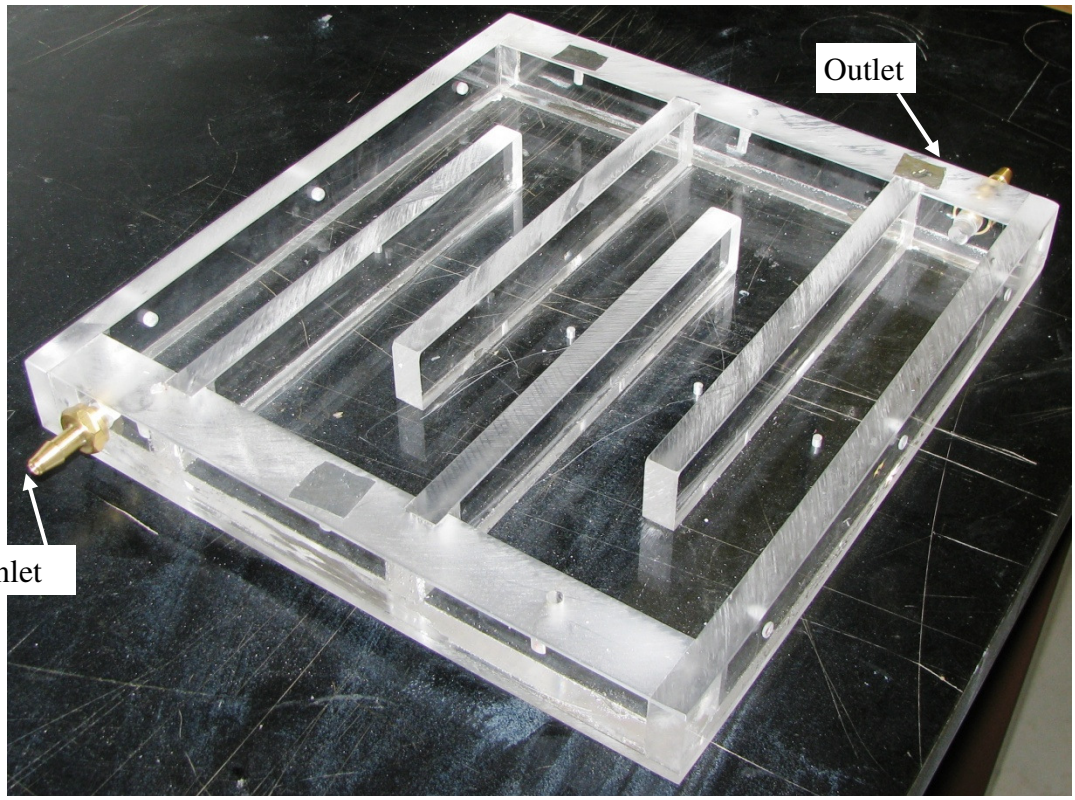

FIGURE 2.7. Photograph of the acrylic tray used to make the prototype heat and moisture transfer panel with the inlet and outlet of the liquid desiccant flow marked.

A semi-permeable membrane was attached to the top of the acrylic tray using a spray adhesive. A photograph of the prototype HAMP with the membrane attached is shown in Figure 2.8. The prototype HAMP had outer dimensions of 27.9 cm (11 in) by 25.4 cm (10 in) by 3.2 cm (1 1/4 in) high. The inner dimensions of the HAMP surface (the area available for heat and moisture transfer) were 22.9 cm (9 in) by 22.9 cm (9 in). The baffles, which divided the HAMP into five channels, each had a surface area of 17.8 cm (7 in) by 1.3 cm (1/2 in), as shown in Figure 2.8. The effective surface area of the HAMP for heat and moisture transfer (total surface area minus surface area of the baffles) was 0.043 m^2. The height of the liquid desiccant flow was 2.5 cm (1 in).

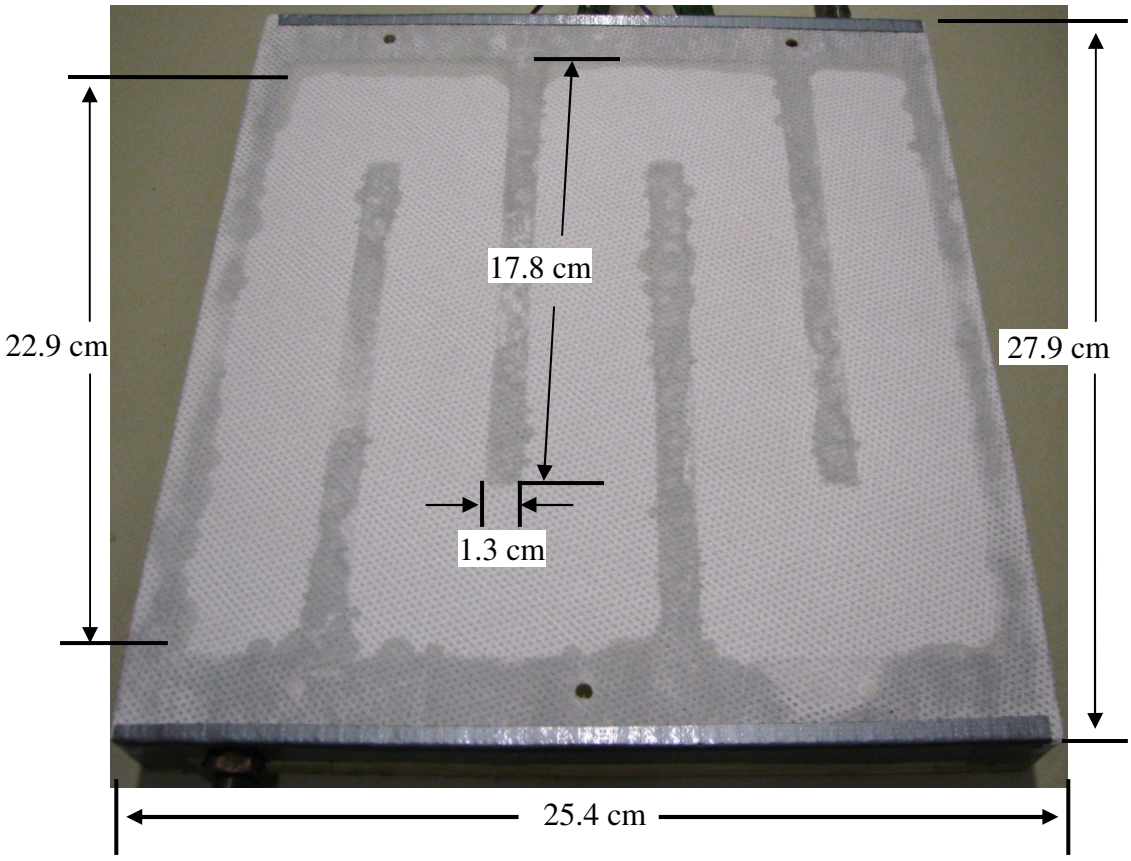

FIGURE 2.8. Photograph of the prototype HAMP with dimensions shown.

The prototype HAMP was placed into the test section, as previously discussed in Section 2.1.3 and air was passed across the surface of the semi-permeable membrane. The direction of the air and liquid desiccant flows are shown in Figure 2.9. The prototype HAMP functioned as a combination of a cross flow and a counter flow energy exchanger. By orienting the two flows in this manner, there was a consistent temperature difference between the liquid desiccant and the air across the whole surface of the HAMP.

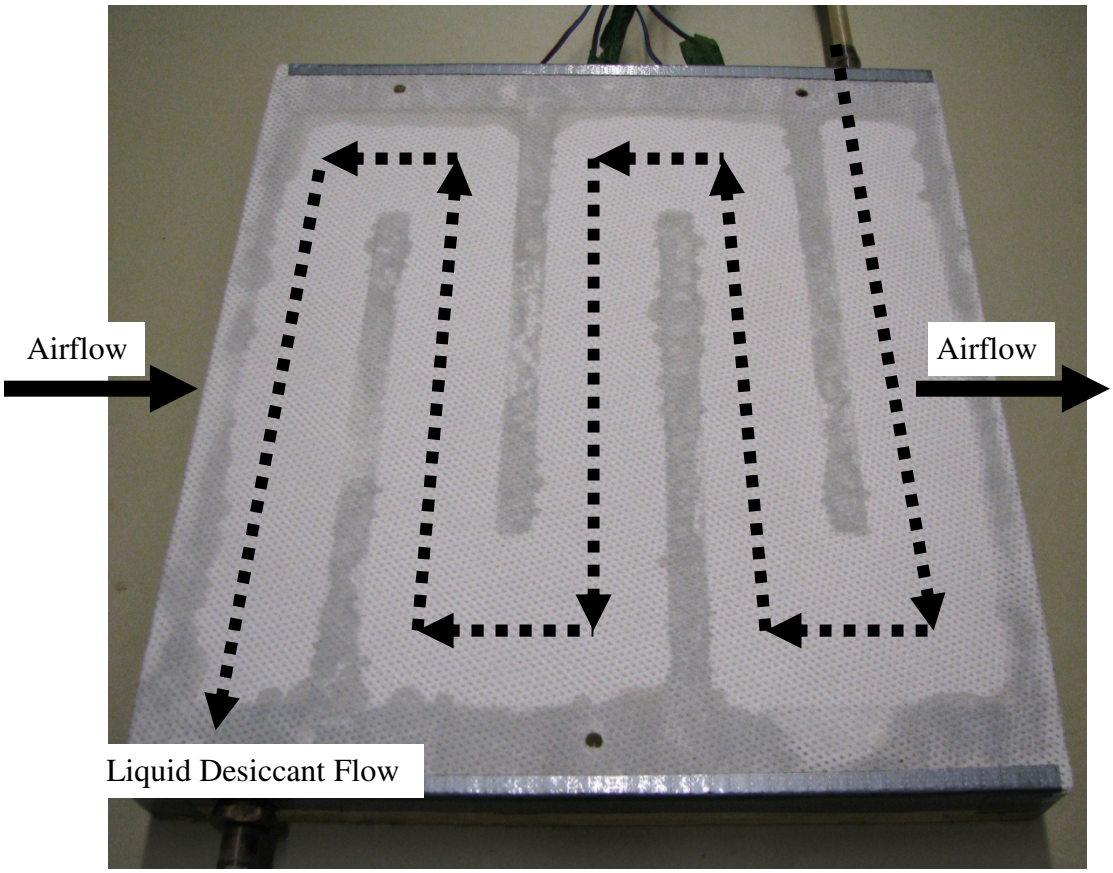

FIGURE 2.9. Photograph of the prototype HAMP with directions of air and liquid desiccant flows shown.

2.2.1 The Semi-permeable Membrane

The surface of the prototype HAMP was covered with a semi-permeable membrane to allow water vapour to transfer between the air and the liquid desiccant. For this study, Propore™ (3M™; St. Paul, Minnesota) was chosen for the semi-permeable membrane. The choice to use Propore™ was based on the work of Larson (2006), who studied many possible membranes, including Tyvek® and Propore™, for use in a prototype run-around membrane energy exchanger. His study focused on these two materials as they are less expensive than other possible materials and are therefore more suitable for use in prototype exchangers. Larson found, when compared to Tyvek®, Propore™ has a lower vapour diffusion resistance (more moisture transfer through

the membrane), a higher airflow resistance (less air passing through the membrane) and a higher liquid penetration pressure (the pressure at which liquid will leak through the membrane).

Typical uses for Propore™ include light duty rainwear, medical packaging and disposable mattress and pillow covers used in hospitals and care homes. Propore™ is a micro-semi-permeable polypropylene membrane, which is affixed to a non-woven polypropylene fabric. The non-woven fabric provides support to the membrane as it is highly elastic. Figure 2.10 shows the microstructure of the Propore™ membrane (Larson 2006).

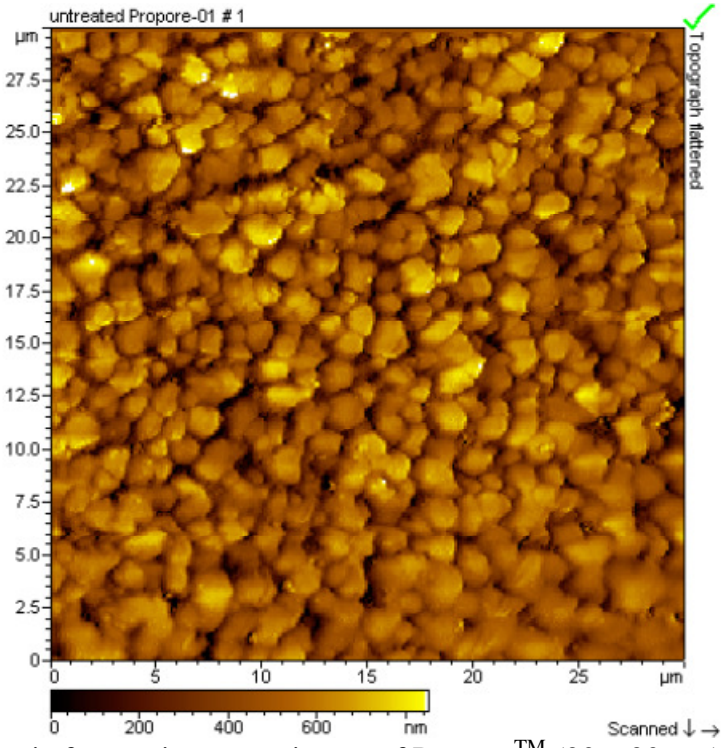

FIGURE 2.10. Atomic force microscope image of Propore™ (30 x 30 µm) (Larson (2006))‡.

To create the prototype HAMP, the semi-permeable membrane was attached to the acrylic tray using a high strength spray adhesive (Hi-Strength 90 Spray Adhesive, 3M™) which can be used

‡ Used with permission from the author.

for permanently bonding materials such as polyethylene and propylene plastics. The membrane was attached to the sides of the tray and tops of the baffles, to ensure a tight seal around the tray. Table 2.1 lists the thermodynamic properties of Propore™ that are required for analysis in this thesis. The values are taken from Larson (2006).

TABLE 2.1. Thermodynamic Properties of Propore™ required for analysis (Larson (2006)).

Property	Value
Thickness [mm]	0.22
Thermal Conductivity [W/(m·K)]	0.334
Resistance to moisture [s/m]	125

2.2.2 The Liquid Desiccant

The liquid desiccant used in the prototype HAMP was a salt solution consisting of water and lithium chloride (LiCl). The concentration of a salt solution is defined by

$$C_{salt} = \frac{m_{salt}}{m_{salt} + m_w} * 100 \tag{2.1}$$

where m is the mass [kg] of either the salt or the water, depending on the subscript, in the salt solution. The concentration can be expressed as a percentage (C_{salt}) or a fraction (γ_{salt}). When mixed with water at 20°C, a saturated lithium chloride solution ($C_{salt} \approx 50\%$) results in a surface relative humidity of approximately 12% RH (ASTM Standard E104, 2007), which corresponds to a humidity ratio of 1.7 g_w/kg_{air}. By varying the concentration of the salt solution, the surface relative humidity of the HAMP can be controlled between 12% RH and 100% RH (pure water). To avoid the problem of crystallization of the salt on the surface of the membrane, the concentration was kept well below the saturation concentration level. Lithium chloride was

chosen because it can be used to create a wide variety of surface humidity conditions, without the problem of crystallization of the salt. If the salt were to crystallize on the surface of the membrane, it would clog the pores of the membrane. This would increase the resistance (decrease the permeability) of the membrane, which would reduce the effectiveness of the HAMP (Afshin (2010)).

Salt solutions are corrosive and can have harmful effects on ductwork and other parts of the test facility. Adequate safety measures must be taken when working with lithium chloride. According to the Material Safety Data Sheet, lithium chloride is harmful if swallowed and can cause irritation of the respiratory tract, eyes and skin. Lithium chloride must also be properly disposed of, as it may contaminate the sewer water.

The surface relative humidity and humidity ratio of the liquid desiccant were calculated from the measured temperature and density using correlations from Cisternas and Lam (1991). These correlations are presented in Appendix B. Figure 2.11 shows how the surface humidity ratio of the salt solution varies with temperature and concentration. The solid line on the graph is the 100% RH line, which corresponds to a salt concentration of 0% (pure water). The graph shows lines of constant concentration from 10% up to 45% in increments of 5%. For a constant temperature, the surface humidity ratio decreases as the concentration increases. For a constant concentration, the surface humidity ratio increases as the temperature increases. The lines of constant concentration nearly follow the lines of constant relative humidity.

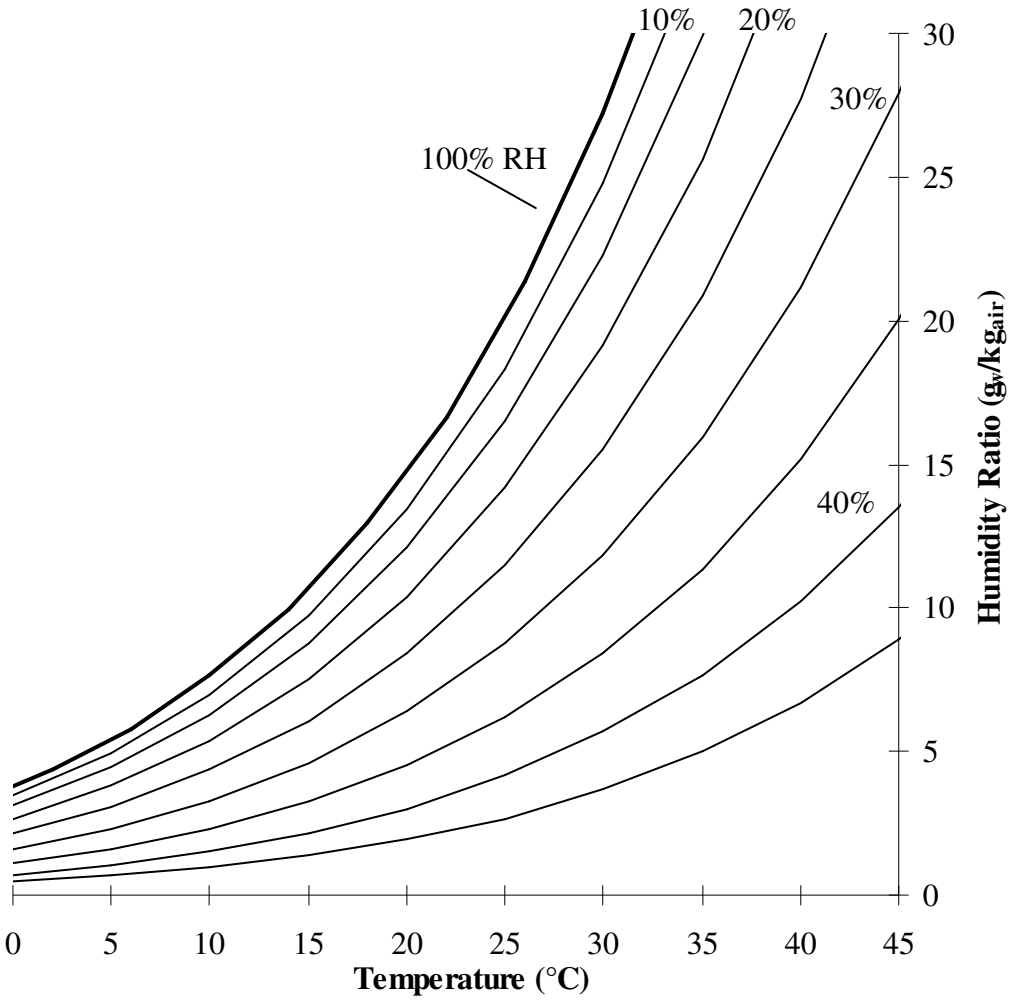

FIGURE 2.11. Surface humidity ratio of an aqueous lithium chloride solution.

The thermodynamic properties of a salt solution will also vary with the temperature and concentration of the solution. Table 2.2 lists the thermodynamic properties of a lithium chloride solution at 20°C for various concentrations. These values were calculated from correlations given by Zaytsev and Aseyev (1992) and Conde-Petit (2009), which are presented in Appendix B.

TABLE 2.2. Properties of an Aqueous Lithium Chloride Solution at 20°C.

Property	Concentration (%)			
	10	**20**	**30**	**40**
Thermal conductivity [W/(m·K)]	0.58	0.56	0.54	0.52
Specific heat [kJ/(kg_{sol}·K)]	3.64	3.22	2.92	2.67
Dynamic viscosity [mPa·s]	1.49	2.23	3.33	4.97
Diffusion coefficient [m^2/s] x10^{-9}	1.67	1.03	0.60	0.36

2.2.3 Configuration of the HAMP

The focus of this research is on testing the prototype HAMP as a ceiling panel, as shown in Figure 2.12(a), however, it can also be used as a floor panel, as shown in Figure 2.12(b). In the ceiling panel configuration, the prototype HAMP was located in the top of the test section, with the airflow underneath the membrane and the liquid desiccant above the membrane. In the floor panel configuration, Figure 2.12(b), the HAMP was located on the bottom of the test section, with the airflow above the membrane and the liquid desiccant underneath the membrane. The test section was symmetrical, so it was easily converted from ceiling panel to floor panel configuration. The majority of tests performed in this thesis were with the HAMP in the ceiling panel configuration.

(a)

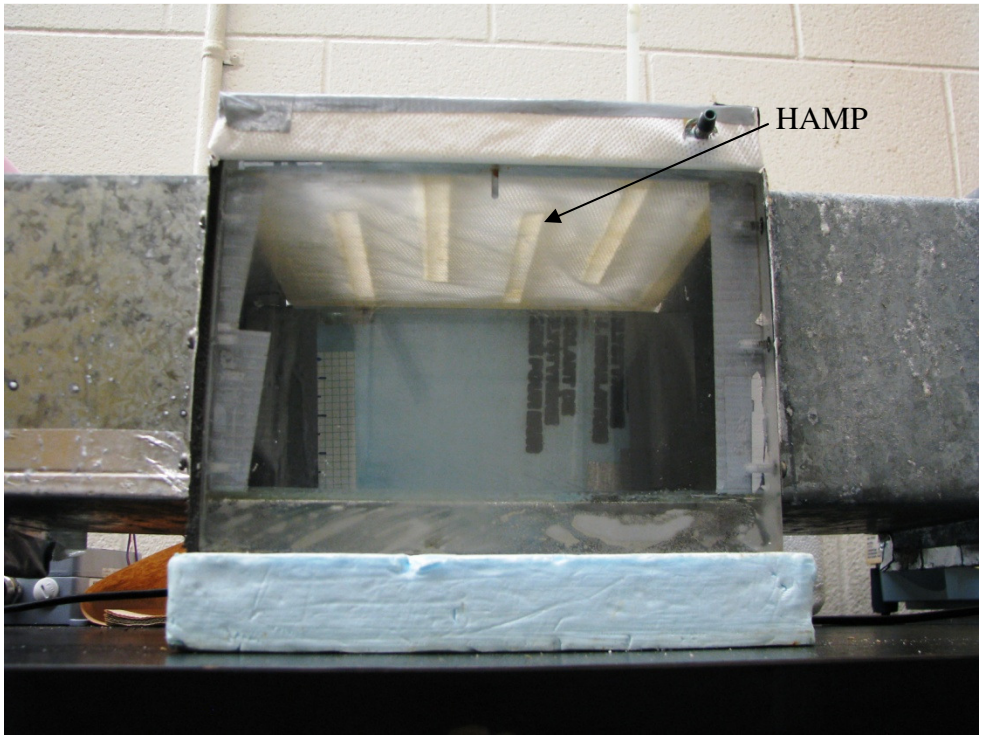

(b)

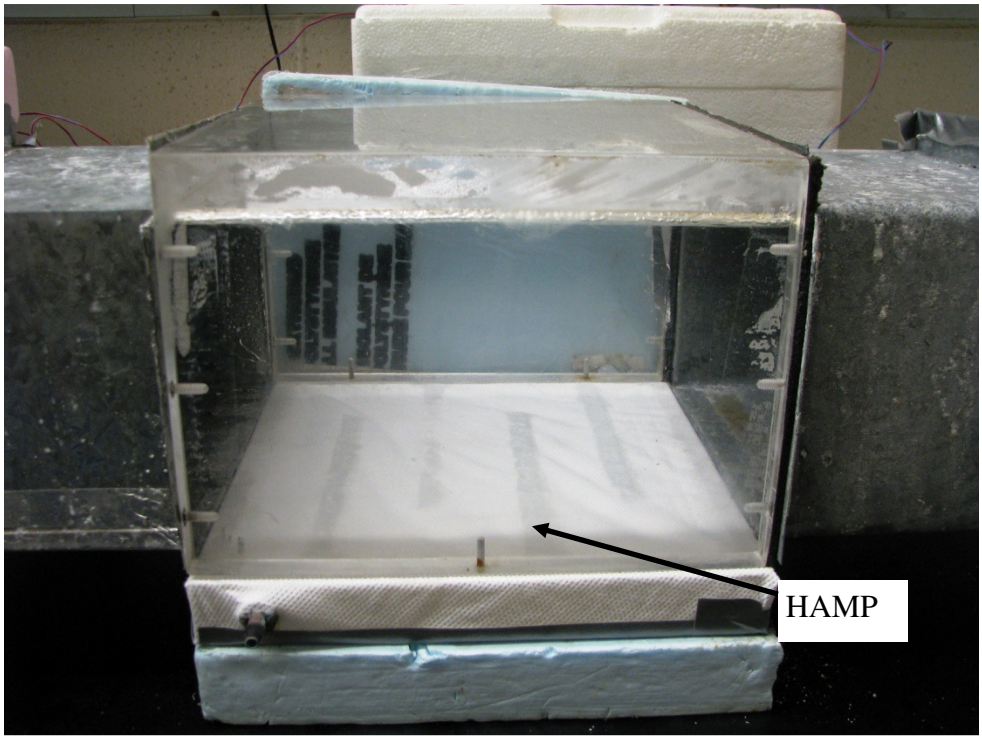

FIGURE 2.12. Photographs of the prototype HAMP in (a) the ceiling panel configuration and (b) the floor panel configuration.

2.3 INSTRUMENTATION AND CALIBRATION

The performance of the prototype HAMP can be quantified by its sensible and latent effectivenesses. The sensible effectiveness (equation 1.1) is calculated from the temperature that was measured in the air, upstream and downstream of the test section and the temperature of the liquid desiccant inside the HAMP as

$$\varepsilon_{sensible}=\frac{T_{DOWNSTREAM}-T_{UPSTREAM}}{T_{HAMP}-T_{UPSTREAM}}. \quad (2.2)$$

The latent effectiveness (equation 1.2) of the prototype HAMP is calculated from the humidity ratio in the upstream air, downstream air and inside the HAMP, from the equation

$$\varepsilon_{latent}=\frac{W_{DOWNSTREAM}-W_{UPSTREAM}}{W_{HAMP}-W_{UPSTREAM}}. \quad (2.3)$$

The humidity ratio at each location was calculated from the measured temperature and relative humidity in the air upstream and downstream of the test section, and from the temperature and density of the liquid desiccant inside the prototype HAMP.

When performing experiments, it is important to calibrate each sensor that is used, to ensure the results reported are accurate. Calibration was performed by comparing the readings of each sensor to a transfer standard which has a high accuracy. This section details the instrumentation and calibration equipment used for each measurement.

2.3.1 Data Acquisition

All measurements taken during testing were recorded using a SCXI 1000 chassis (National Instruments; Austin, Texas) connected to a 16-bit acquisition card. The data was recorded using LabView® 7.1 (National Instruments), a graphical development software package. This program

continuously displayed measurements on the computer and recorded the data to a text file at desired intervals.

2.3.2 Volume Flow Rate of Air

The volume flow rate of the air was controlled using two 1559A Mass-Flo® Controllers (MKS Instruments; Andover, Massachusetts). One controller set the volume flow rate of the dry airflow and the other set the volume flow rate of the humidified airflow. The two airflows were then mixed and the total volume flow rate of the air entering the test section (dry air and water vapour) was the sum of the two volume flow rates. For the majority of the tests, the total volume flow rate of the air was 11.1 L/min, which relates to an air velocity of 0.005 m/s inside the test section. This corresponds to a Reynolds number of approximately 65. Each of the flow controllers has an accuracy of ±1% of the full scale measurement. The bias uncertainties at 68% confidence in the volume flow rates were ±0.3 L/min for the dry airflow and ±0.1 L/min for the humidified airflow. The precision uncertainties in the volume flow rates were ±0.01 L/min. The uncertainty analysis will be shown in more detail in Section 3.3.

2.3.3 Temperature and Relative Humidity of the Airflow

The temperature and relative humidity of the air stream were measured using two HMP 233 sensors (Vaisala; Helsinki, Finland), one located upstream of the test section and one downstream. The sensors used a thin polymer film that absorbed water molecules, changing the capacitance of the film, which was then converted into a relative humidity. The temperature was measured with a platinum resistance thermometer. The sensors have a measuring range of -40°C

to 80°C and 0% RH to 100% RH with an accuracy of ±0.1°C and ±1% RH (for the range of 0% RH to 95% RH).

The Vaisala sensors were calibrated for temperature with a 9107 Dry-well calibrator (Hart Scientific Inc.; American Fork, Utah) and for relative humidity with a 1200 Mini Humidity Generator (Thunder Scientific Corporation; Albuquerque, New Mexico). The sensors were calibrated over the range of 20°C to 30°C and 10% RH to 90% RH. The upstream air sensor had bias uncertainties of ±0.2°C and ±0.6% RH and precision uncertainties of ±0.006°C and ±0.014% RH. The downstream air sensor had bias uncertainties of ±0.2°C and ±0.4% RH and precision uncertainties of ±0.007°C and ±0.014% RH.

2.3.4 Temperature of the Liquid Desiccant

The temperature of the liquid desiccant inside the prototype HAMP was measured using five thermocouples. The thermocouples were inserted into holes drilled in the base of the acrylic tray. The holes around the thermocouples were filled with an epoxy glue so liquid did not leak from the HAMP during testing. The thermocouples were made of 24 AWG (0.51 mm diameter) T-type thermocouple wire. T-type thermocouple wire has a range of -270°C to 400°C and performs well when moisture is present (Omega Engineering, (2011)).

Since the thermocouples are placed into the liquid desiccant inside the HAMP, the liquid must flow around the thermocouples, which may disturb the flow. If the width of the thermocouples is large compared to the width of each channel, the flow will be disturbed, which will have an impact on the conditions measured inside the HAMP. To avoid this problem, a fine gauge

thermocouple wire was chosen, which had a much smaller diameter than the width of the channels. The magnitude of the flow disturbance was negligible and is not expected to have had an impact on the test conditions.

The five thermocouples used to measure the temperature of the liquid desiccant were also calibrated using the 9107 Dry-well calibrator. The thermocouples were calibrated over a range of 0°C to 50°C. Although the thermocouples were used to measure the temperature of the liquid desiccant, they were calibrated in air. The different fluids will have different heat transfer coefficients and so the thermocouples will have different response times for each fluid. The steady-state temperature measured by the thermocouples will be the same for the two fluids, but the time to reach steady state will be different. This problem is overcome by ensuring that the thermocouples reach steady state during both calibration and testing. Therefore, the use of a different fluid for calibration is not expected to have an effect on the results of the calibration process.

The five thermocouples each had a bias uncertainty of ±0.1°C and precision uncertainties ranging from ±0.004°C to ±0.008°C. The temperature of the liquid desiccant inside the HAMP presented in the results is the average of the five thermocouple readings. The uncertainty in the temperature of the liquid desiccant was calculated using the propagation method, which will be described in Section 3.3.2. The bias uncertainty in the liquid desiccant temperature was ±0.1°C and the precision uncertainty was ±0.003°C.

2.3.5 Density of the Liquid Desiccant

In order to calculate the latent effectiveness of the prototype HAMP, the humidity ratio of the liquid desiccant inside the prototype HAMP is needed. For a salt solution, the humidity ratio was calculated from the concentration of salt in the solution. The concentration was calculated from the measured density and temperature of the mixture using correlations by Cisternas and Lam (1991), which are given in Appendix B. The density of the liquid desiccant was measured using a DMA 4500 M density meter (Anton Paar; Graz, Austria).

The density meter was calibrated by comparing the densities measured by the density meter for ten samples of salt solution, to the density calculated by measuring the mass and volume of those samples. The density meter has a range of 0 kg/m^3 to 3000 kg/m^3 with a repeatability of 0.01 kg/m^3. The bias uncertainty of the meter, given by the manufacturer, is dependent on the type of fluid being tested, but they do not list any salt solutions in the manual. Instead, the bias uncertainty of the density measurements (at 68% confidence) was calculated from the calibration data, to be ±5.9 kg/m^3 and the precision uncertainty was ±0.2 kg/m^3.

Unlike the temperature and relative humidity measurements which were taken every 30s, the density measurements were taken less frequently. The density meter measures the density of a sample, which is injected into the machine. This required a sample of the liquid desiccant be drawn out of the HAMP and put into the density meter. Initially measurements were taken before, during and after each test to determine how the density changed throughout each test. The typical change in density seen during one test was approximately 0.2 kg_{sol}/m^3. A change of 3 kg_{sol}/m^3 in the density of the liquid desiccant results in a change of approximately 1% RH in

the surface relative humidity of the mixture, so a change of 0.2 kg_{sol}/m^3 resulted in a very small change in relative humidity. Since the density did not change significantly during each test, only one density measurement was taken at the beginning of each test.

2.3.6 Volume Flow Rate of the Liquid Desiccant

The liquid desiccant was pumped through the HAMP using an 18.6 W continuously running pump (Franklin Electric Co.; Oklahoma City, Oklahoma). The pump has a flow rate of 20 L/min. A screw clamp was used to reduce the flow rate of the liquid desiccant before it entered the HAMP. This allowed the liquid flow rate inside the HAMP to be adjusted from no flow, up to a maximum of 20 L/min. The flow rate of the liquid was measured by diverting the liquid flow into a jar. The time required to fill the jar was measured and the jar was weighed to determine the mass of the liquid. This was done periodically before testing, to ensure the liquid flow rate was the same during all tests.

Table 2.3 provides a summary of the bias and precision uncertainties at 68% confidence and the total uncertainties at 95% confidence of each measurement. A more detailed uncertainty analysis will be presented in Section 3.3.

TABLE 2.3. Summary of the bias, precision and total uncertainties in each sensor and their confidence levels.

Measurement	Bias (68%)	Precision (68%)	Total (95%)
$T_{UPSTREAM}$ [°C]	0.2	0.006	0.3
$RH_{UPSTREAM}$ [% RH]	0.6	0.014	1.1
$T_{DOWNSTREAM}$ [°C]	0.2	0.007	0.3
$RH_{DOWNSTREAM}$ [% RH]	0.4	0.014	0.8
T_{HAMP} [°C]	0.1	0.003	0.1
ρ_{HAMP} [kg_{sol}/m^3]	5.9	0.19	11.7
Q_{dry} [L/min]	0.3	0.01	0.6
Q_{humid} [L/min]	0.1	0.01	0.2

2.4 FLOW VISUALIZATION SETUP

Flow visualization is a qualitative technique used to determine patterns of fluid motion. In this study, smoke was injected into the air stream, upstream of the test section, to make the motion of the air visible. Figure 2.13 shows the view of the test section where the flow visualization photographs were taken. The test section was lit from above with a 100 W light bulb and the bottom and back wall were covered with black paper to highlight the smoke particles inside the test section. A Canon PowerShot S5IS digital camera, placed on a tripod in front of the test section, was used to take the photographs. The camera was set to an ISO speed of 1600 to reduce the effects of the moving smoke, an aperture setting of F8.0 to ensure the whole test section is in focus and a shutter speed of 1/3200 s.

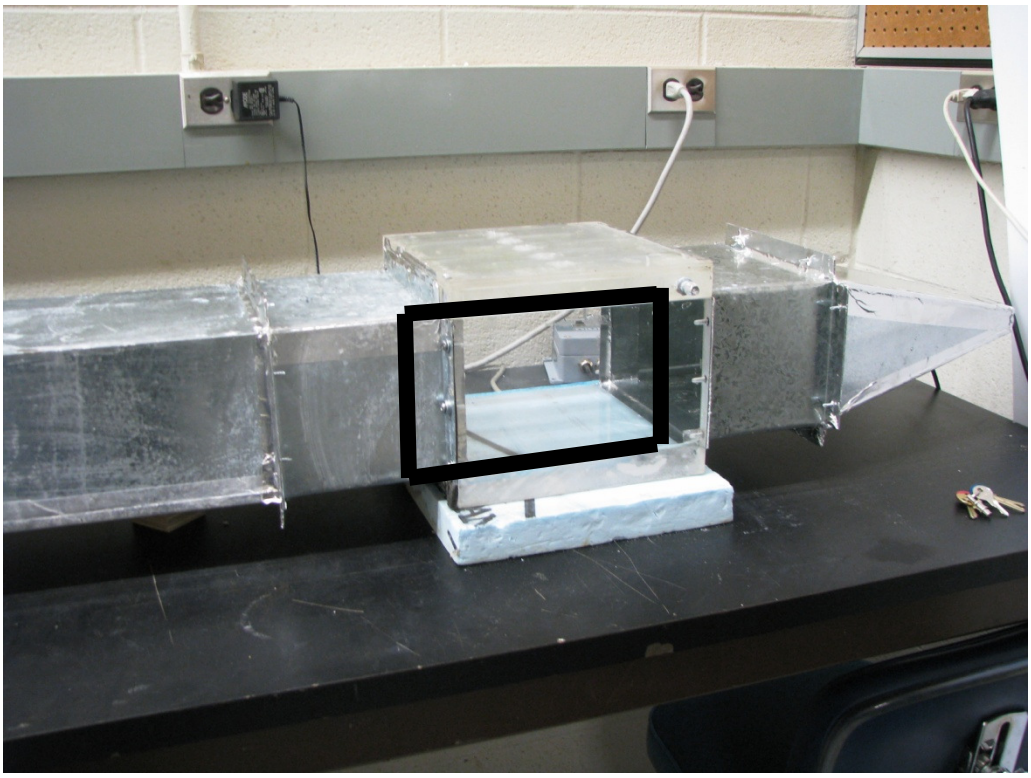

FIGURE 2.13. View of the test section where the flow visualization photographs are taken.

2.5 SUMMARY

This chapter described the design of a prototype ceiling panel which can simultaneously transfer heat and moisture. The test facility designed to measure the performance of the prototype HAMP was also discussed. The instrumentation used to take each measurement and the bias and precision uncertainty in each instrument were presented. This test facility can be used for further research on this particular HAMP prototype, or expanded to include variations in the HAMP, such as different membranes or liquid desiccants, and different orientations of the prototype HAMP in the test section.

CHAPTER 3 –COMMISSIONING AND UNCERTAINTY ANALYSIS

One of the main objectives of this research is to measure the performance of the newly designed prototype HAMP. This is accomplished using the test facility and instrumentation presented in Chapter 2. Before the experimental results can be presented, however, an analysis is performed, to ensure that these results were reliable. First, the transient data will be presented, which shows the time it took for the test facility to reach steady state. Each measurement will then be presented for the full length of a 60 min test for one test case, to confirm that the data was at steady state, and that the results of the tests were as expected. An uncertainty analysis is then presented for each of the measurements taken, as well as for the calculated results that are used in this thesis. Finally, energy and mass balances are performed on the data to ensure that mass and energy were conserved within acceptable uncertainty limits for the test facility. This chapter will discuss these analyses for one test case, to confirm that the measurements taken with this test facility were reliable.

The conditions for the test case that will be used throughout this chapter are presented in Figure 3.1 on a psychrometric chart. The psychrometric chart shows temperature and humidity ratio, as well as lines of constant relative humidity. In this test, the prototype HAMP was used to cool and dehumidify the airflow. The upstream air was set at room temperature and a high humidity ratio, while the liquid desiccant was set at a low temperature and a high concentration, to obtain a low humidity level.

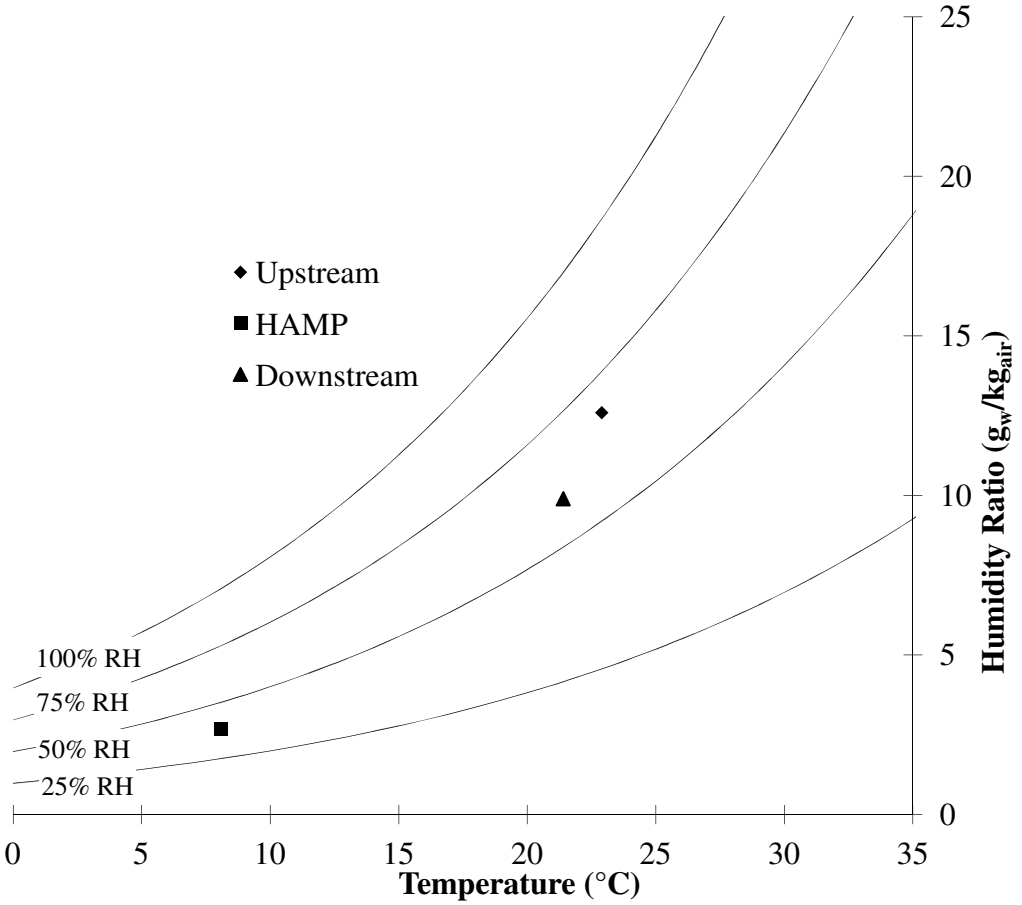

FIGURE 3.1. Psychrometric chart showing the conditions of the air and liquid desiccant inside the HAMP for the test case presented in this chapter.

3.1 TRANSIENT DATA

Before beginning each test, the temperature and relative humidity of the air and the temperature of the liquid desiccant were at approximately the same conditions as the air in the laboratory. When the system was turned on, the values gradually changed, until they reached the set point values for the given test. The downstream air temperature and relative humidity also changed, based on the change in the upstream air and liquid desiccant conditions, as well as the amount of heat and moisture transfer that occurred between the prototype HAMP and the air.

The transient response of each measurement was due in part to the changing conditions, from the initial start-up of the test facility, but also to the response time of the sensors used to take each measurement as well as some other factors, such as heat and moisture storage in the membrane and heat storage in the walls of the duct. In order to determine the steady state performance of the prototype HAMP, it is important to know when steady state was achieved in the test facility. The time the system took to reach steady state was different for each test case, due to the different operating conditions used for each test. This section will show the transient pre-test data for one test case to show when steady state was achieved for that test.

The transient responses of the temperature of the upstream air, downstream air and liquid desiccant, are shown in Figure 3.2. Initially, the three temperatures were close to the temperature of the lab, which was approximately 22.5°C. The time it took for each temperature measurement to reach steady state is defined as the time it took for the measurement to reach ±0.1°C of the average temperature value during the test. The steady-state upstream air temperature was 22.9°C. It took ~16 min for the upstream air to reach this value. The temperature of the liquid desiccant that is presented is the average of the temperature in the five channels inside the HAMP. The steady-state temperature of the liquid desiccant was 8.1°C, and it took ~53 min for the sensor to reach this value. The downstream air temperature was dependent on the upstream and liquid desiccant values as well as the amount of heat and mass transfer that occurred between the air and the HAMP, so the downstream temperature measurement took the longest to reach steady state. The steady-state value reached in this test was 21.4°C and it took ~57 min for the sensor to achieve this value.

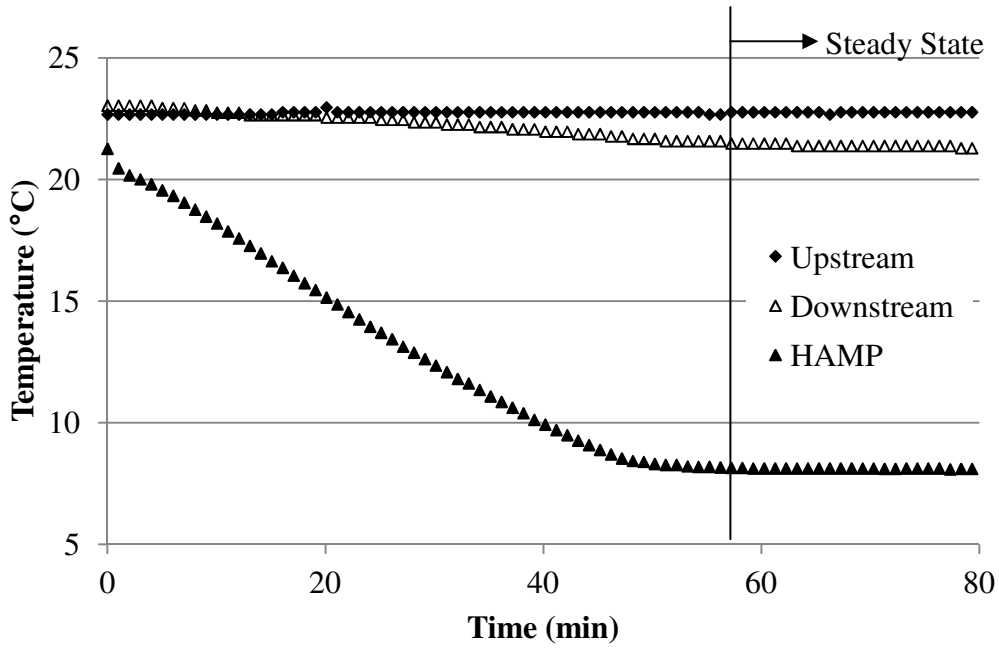

FIGURE 3.2. Transient temperature of the air upstream and downstream of the test section and the average temperature inside the prototype HAMP.

The transient responses of the upstream and downstream air relative humidity sensors are shown in Figure 3.3. The time it took for the relative humidity measurements to reach steady state is defined as the time it took for the value to reach ±0.2% RH of the average relative humidity measurement for the test. The steady-state upstream air relative humidity was 68.1% RH for this test. It took ~130 min for the upstream air relative humidity to reach within ±0.2% RH of this value. The downstream air relative humidity was dependent on the relative humidity of the upstream air, the surface relative humidity of the liquid desiccant inside the HAMP and the amount of heat and mass transfer that occurred between the air and the HAMP. Initially the downstream relative humidity decreases slightly, due to the moisture transfer into the HAMP. As the upstream relative humidity begins to increase, the downstream relative humidity also

increases. It took approximately 135 min for the downstream relative humidity to reach the steady-state value of 58.8% RH.

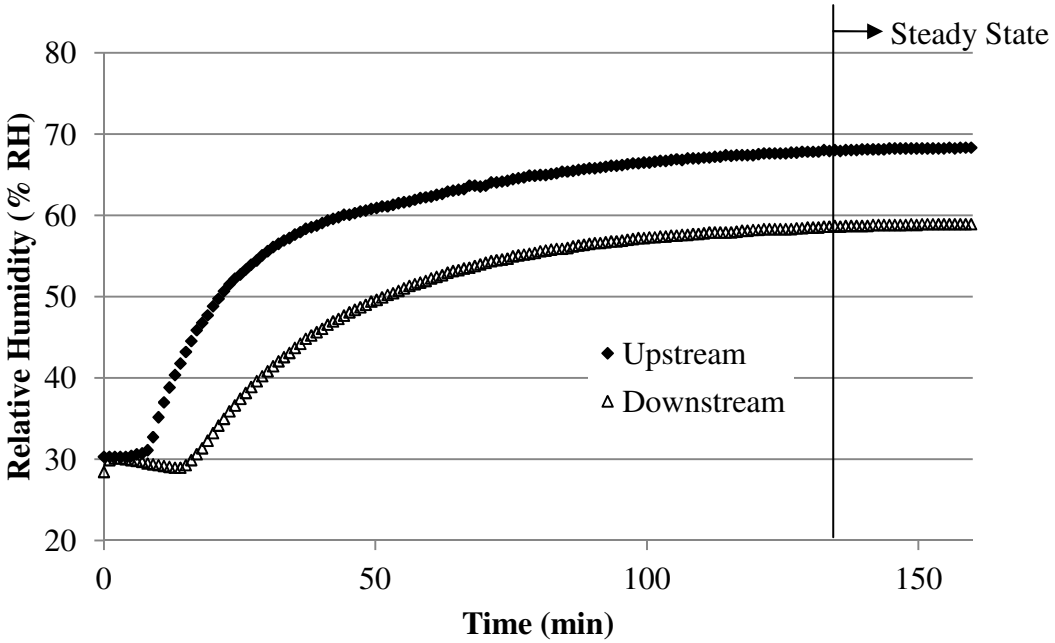

FIGURE 3.3. Transient relative humidity of the air upstream and downstream of the test section.

The relative humidity measurements took considerably longer to reach steady state than the temperature measurements. This was mostly due to the response time of the relative humidity sensors, which react slower to changing conditions. For this sample test, it took 135 min for the whole system to reach steady-state. During testing, this analysis was performed for each test to ensure that steady state was achieved before data was collected. After steady state was achieved, each test was run for one hour, with data recorded every 30 s. The results that will be presented in this thesis are the time average steady-state values for each measurement.

3.2 STEADY STATE RESULTS

This section presents the measurements taken during one test, after steady state was achieved. The results presented here are for the same sample case of cooling and dehumidification discussed in Section 3.1. Figure 3.4 shows the steady-state volume flow rate of the dry airflow, humid airflow and total airflow. To obtain an airflow with a high humidity ratio upstream of the test section, the volume flow rate of the dry airflow was set to 0.5 L/min and the volume flow rate of the humid airflow was set to 10.6 L/min. This resulted in a total volume flow rate of 11.1 L/min which corresponds to a velocity of 0.005 m/s through the test section, with a Reynolds number of 65. The standard deviation in the volume flow rate measurements was ±0.01 L/min. The uncertainty of each measurement will be discussed in Section 3.3.

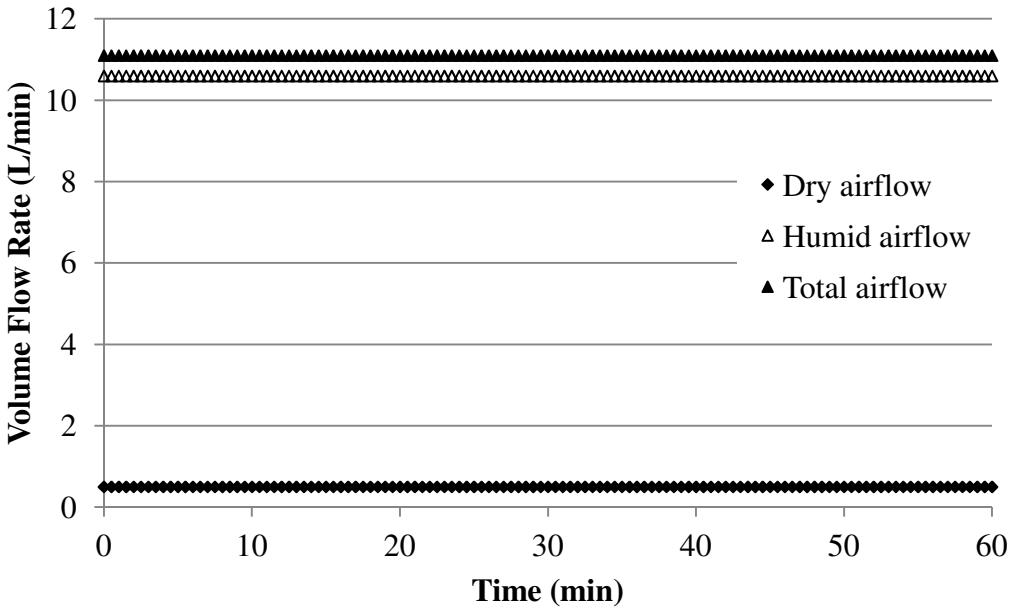

FIGURE 3.4. Steady-state volume flow rate of the dry, humid and total airflows.

As discussed in Chapter 2, the temperature of the liquid desiccant was measured in five locations inside the prototype HAMP. Figure 3.5 shows the steady-state temperature of the liquid

desiccant at each of the five locations. The average values over the one hour time frame were 8.2°C, 8.0°C, 8.2°C, 8.0°C and 8.2°C. The standard deviations that correspond to these measurements were ±0.01°C, ±0.02°C, ±0.01°C, ±0.05°C and ±0.04°C, respectively. Since the temperature of the liquid desiccant inside the prototype HAMP did not change significantly from the inlet to the outlet and the difference was less than the uncertainty of the measurements, the temperature was assumed to be constant across the entire surface of the prototype HAMP and only the average temperature value will be reported in future cases.

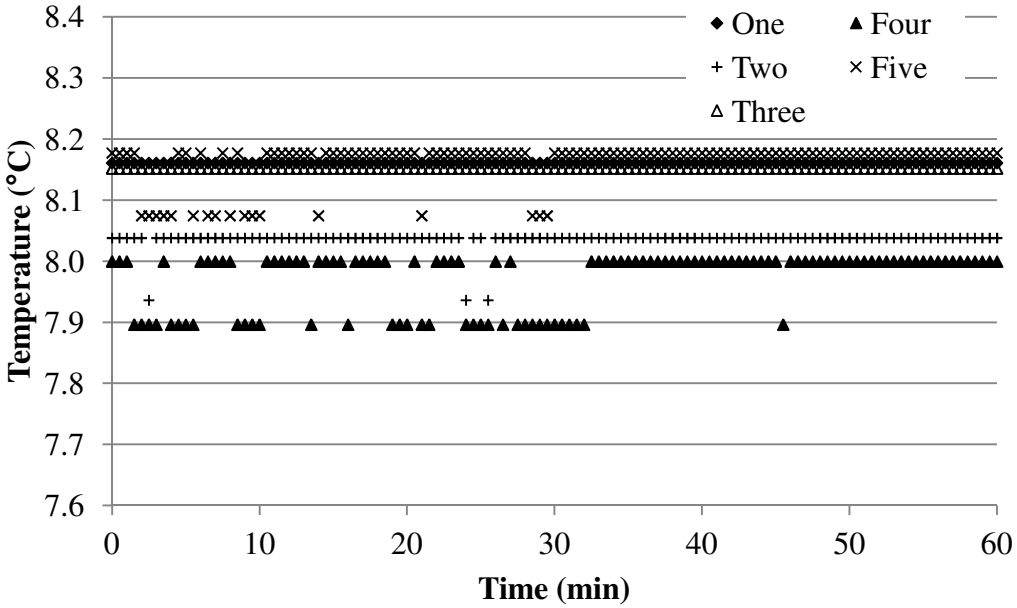

FIGURE 3.5. Steady-state temperature of the liquid desiccant in each of the five channels inside the prototype HAMP.

During this test, the air entered the test facility at an upstream temperature of 22.9°C, with a standard deviation of ±0.06°C. The temperature of the liquid desiccant inside the prototype HAMP was set at 8.1°C with a standard deviation of ±0.01°C. Since the prototype HAMP was being used to cool the airflow, the downstream air temperature was expected to be lower than the

upstream air temperature. This was the case, as seen in Figure 3.6, the temperature of the air exiting the test section was 21.4°C with a standard deviation of ±0.04°C. The air was cooled by 1.5°C during this test.

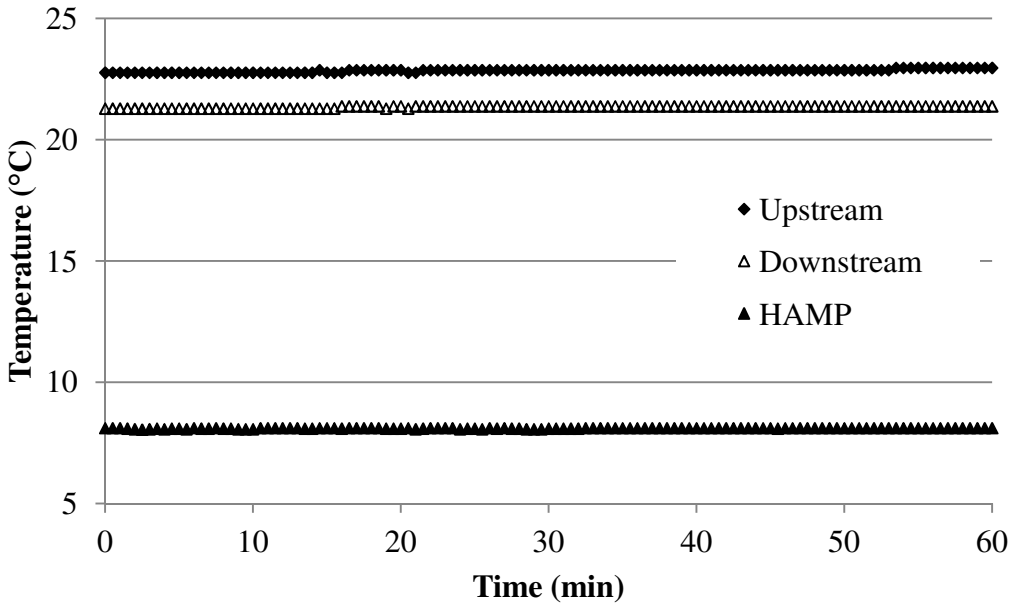

FIGURE 3.6. Steady state temperature of the upstream air, downstream air and liquid desiccant inside the prototype HAMP.

ASHRAE Standard 84 (2008) presents requirements for fluctuations of properties for testing performance of air-to-air heat and energy exchangers. For temperature measurements, the fluctuations in the measurements (δT) must meet the following inequality

$$\frac{|\delta T|}{|T_{in,1}-T_{in,2}|} < 0.02 \tag{3.1}$$

where $T_{in,1}$ and $T_{in,2}$ are the temperature of the air streams at the two inlets of an energy exchanger. To apply this to the tests done in this study, the upstream air temperature was used for $T_{in,1}$ and the temperature of the liquid desiccant was used for $T_{in,2}$. For the sample test case,

the left hand side of the inequality was equal to 0.007 for both the upstream air and liquid desiccant temperatures, which satisfied the requirements of the standard.

During this test, the density of the liquid desiccant inside the prototype HAMP was measured every 10 min. Figure 3.7 shows the steady-state density measurements at each point in time. The average density of the liquid desiccant was 1197.2 kg_{sol}/m^3 with a standard deviation of ±0.12 kg_{sol}/m^3. This corresponded to a salt solution concentration of 32.0%. The density of the liquid desiccant did not change significantly during one test, so for future tests the density was measured only at the beginning and end of each test, rather than throughout the test.

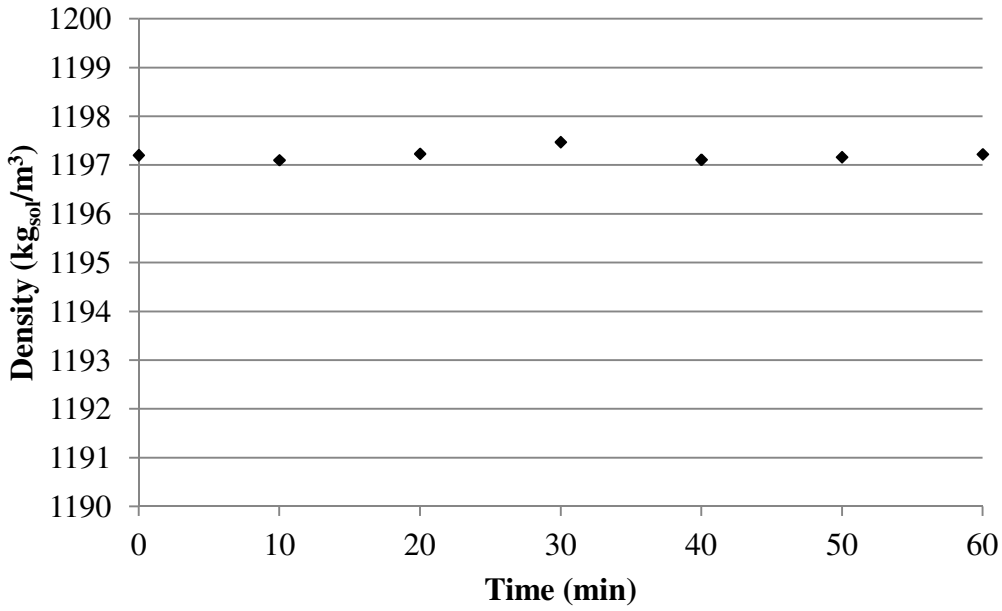

FIGURE 3.7. Steady-state density of the liquid desiccant inside the prototype HAMP.

In this test, the upstream airflow was humidified to a relative humidity of 68.1% RH, with a standard deviation of ±0.1% RH. The steady-state relative humidity of the upstream air is shown in Figure 3.8, along with the downstream air relative humidity and the calculated relative humidity inside the prototype HAMP. The relative humidity inside the prototype HAMP was

calculated using the correlations presented in Appendix B, based on the density and temperature of the liquid desiccant. The relative humidity inside the prototype HAMP was calculated to be 37.8% RH. The downstream relative humidity was 58.8% RH with a standard deviation of ±0.1% RH. In this test, the airflow was dehumidified by 9.3% RH.

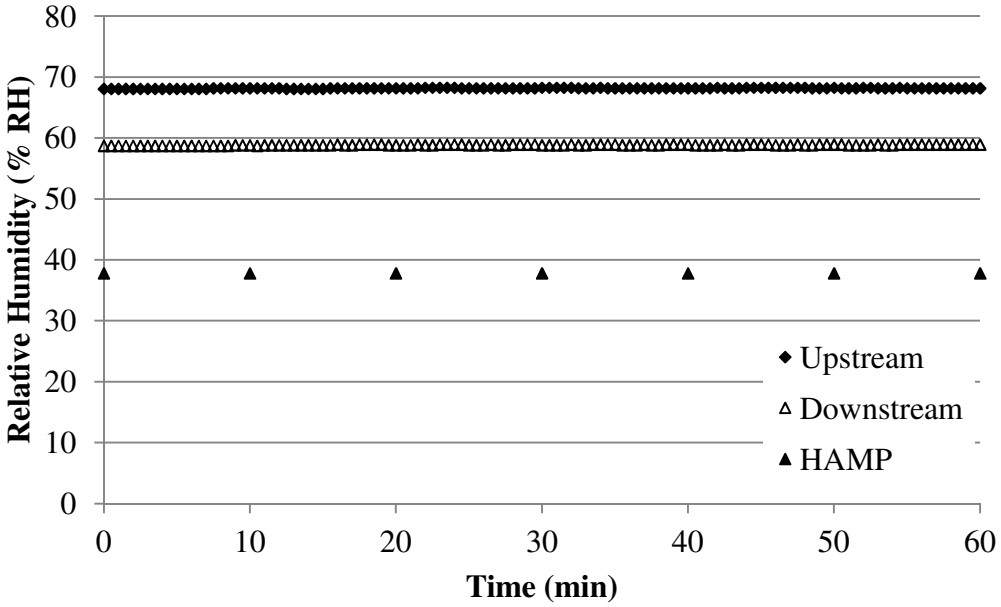

FIGURE 3.8. Steady-state relative humidity of the upstream air, downstream air and liquid desiccant inside the prototype HAMP.

The latent effectiveness of the prototype HAMP, which is one of the parameters used to quantify the performance of the HAMP, was calculated from the humidity ratio of the air upstream and downstream of the test section, and inside the HAMP. Figure 3.9 shows the humidity ratio of the upstream air, downstream air and the liquid desiccant inside the prototype HAMP for this test. The upstream air had a steady-state humidity ratio of 12.6 g_w/kg_{air} with a standard deviation of ±0.05 g_w/kg_{air}. The humidity ratio of the liquid desiccant was 2.7 g_w/kg_{air}, calculated from the correlations in Appendix B. The air downstream of the test section had a steady-state humidity

ratio of 9.9 g_w/kg_{air} with a standard deviation of ±0.04 $g_w/kg_{air.}$ In this test, the amount of moisture removed from the airflow was 2.7 g_w/kg_{air}.

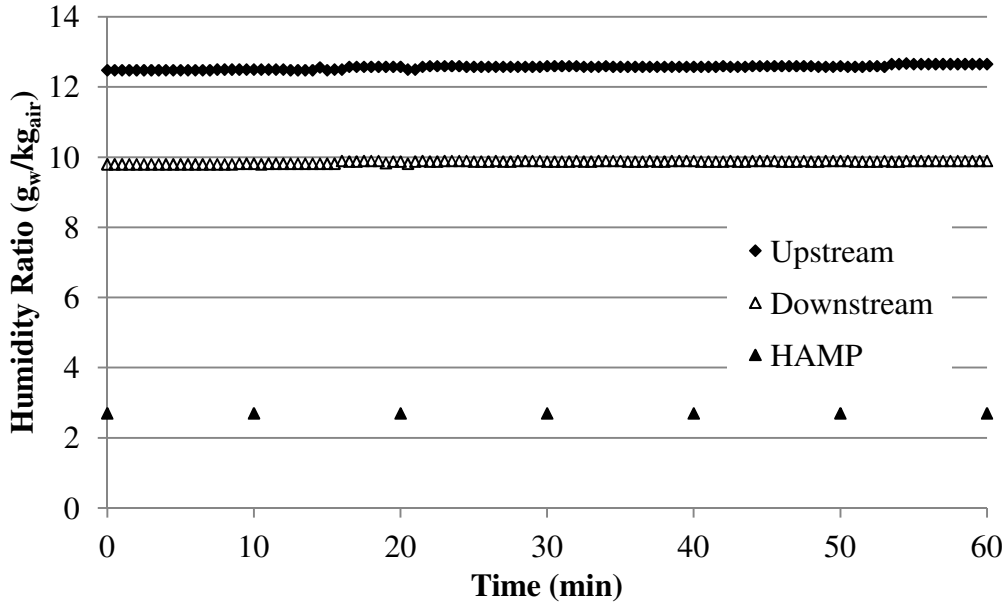

FIGURE 3.9. Calculated humidity ratio for the steady-state upstream air, downstream air and liquid desiccant inside the prototype HAMP.

As with the temperature measurements, ASHRAE Standard 84 (2008) presents requirements for the acceptable fluctuations in the humidity ratio measurements of air-to-air energy exchangers. The fluctuations in the humidity ratio (δW) must satisfy the following inequality

$$\frac{|\delta W|}{|W_{in,1}-W_{in,2}|} < 0.05 \tag{3.2}$$

for dehumidification or

$$\frac{|\delta W|}{|W_{in,1}-W_{in,2}|} < 0.1 \tag{3.3}$$

for humidification, where $W_{in,1}$ and $W_{in,2}$ are equivalent to the humidity ratios of the upstream air and the liquid desiccant inside the HAMP. For this test case, the left hand side of the inequality was equal to 0.005, which satisfied the requirements of the standard.

The results presented in this section show that steady state was achieved and the values of each measurement were kept within a reasonable standard deviation of the steady-state value. For the remainder of tests shown in this thesis, only the time average result will be shown for each measurement and calculated result.

3.3 UNCERTAINTY ANALYSIS

The measurements discussed in Chapter 2 and presented in Sections 3.1 and 3.2 are used to calculate the sensible and latent effectivenesses of the prototype HAMP. In order to have confidence in these calculated results, the uncertainty of each measurement and each calculated result must be determined. ASME PTC 19.1 Test Uncertainty (2005) defines the total uncertainty in a measurement as

$$U_x = 2\sqrt{b_x^2 + s_x^2} \tag{3.4}$$

where b_x is the bias uncertainty and s_x is the precision uncertainty in the measurement at 68% confidence level (one standard deviation). The total uncertainty has a confidence level of 95% (two standard deviations). The bias, precision and total uncertainties have the same units as the measurements for which the uncertainty is being calculated. A summary of the uncertainty analysis is presented here, and a more detailed analysis is given in Appendix C.

3.3.1 Uncertainty of Measured Values

The bias uncertainty of a measurement is due to elements such as instrument error, calibration and environmental effects. This uncertainty causes the measured value to deviate from the true value by a constant amount. The bias uncertainty for each element is

$$b_x = \frac{B_x}{2} \tag{3.5}$$

where B_x is the bias uncertainty of that element with 95% confidence. The bias uncertainty for a measurement is a combination of the bias uncertainty of each element associated with that measurement

$$b_x = \left[\sum_{j=1}^{J} \left(b_{x_j}\right)^2\right]^{1/2} \tag{3.6}$$

where b_{x_j} is the bias uncertainty of each element with 68% confidence, for J elements.

In this study, each of the instruments used to take measurements was calibrated with a transfer standard, as described in Chapter 2. The purpose of calibration is to reduce the bias uncertainty of each measurement, by comparing the measurements to a transfer standard which has a lower bias uncertainty than the sensor, and then correcting the measurement based on this data. Calibration of each instrument was performed before the initial experiments (pre-test) and after the final experiments (post-test). The bias uncertainty in each measured value will include the bias uncertainty of the pre-test calibration, the post-test calibration and the transfer standard used for calibration. These bias uncertainties are combined using equation (3.6) to find the total bias uncertainty of each measurement. The pre-test, post-test, transfer standard and total bias uncertainty of each measurement, at 95% confidence levels, are presented in Table 3.1. The uncertainty in the transfer standard is taken from the manufacturer's data for the machine used to calibrate the sensors.

TABLE 3.1. Bias uncertainties of measured values at 95% confidence.

Measurement	Value	Pre-test	Post-test	Transfer Standard	Total
$T_{UPSTREAM}$ [°C]	22.9	±0.2	±0.1	±0.2	±0.3
$RH_{UPSTREAM}$ [% RH]	68.1	±0.9	±0.4	±0.5	±1.1
$T_{DOWNSTREAM}$ [°C]	21.4	±0.2	±0.2	±0.2	±0.3
$RH_{DOWNSTREAM}$ [% RH]	58.8	±0.3	±0.5	±0.5	±0.8
TC_1 [°C]	8.2	±0.1	±0.1	±0.2	±0.2
TC_2 [°C]	8.0	±0.1	±0.1	±0.2	±0.3
TC_3 [°C]	8.2	±0.1	±0.1	±0.2	±0.2
TC_4 [°C]	8.0	±0.1	±0.2	±0.2	±0.3
TC_5 [°C]	8.2	±0.1	±0.1	±0.2	±0.2
ρ_{HAMP} [kg_{sol}/m^3]	1197.2	±0.35	±0.35	±11.7	±11.7

The precision uncertainty of a measurement is due to statistical fluctuations in the measured data. The precision uncertainty is calculated from

$$s_{\bar{X}} = \frac{s_x}{\sqrt{N}} \tag{3.7}$$

where s_x is the standard deviation of the sample of measurements and N is the number of data points in the sample. The standard deviation of a sample of measurements is

$$s_x = \sqrt{\sum_{j=1}^{N} \frac{(X_j - \bar{X})^2}{N-1}} \tag{3.8}$$

where X_j is the value of the J^{th} measurement and $\bar{X}$ is the average value of the sample of measurements. When more than one element contributes to the precision uncertainty of the measurement, the total precision uncertainty is calculated using equation (3.6) with the precision uncertainty of each element instead of the bias uncertainty.

In this study, the precision uncertainty of each measurement included the precision uncertainties of the pre-test calibration and the post-test calibration, as well as the precision uncertainty of the data collected during each test. The precision uncertainty from the pre-test data, post-test data and fluctuation in the data of one test are presented in Table 3.2, for each measurement, at 95% confidence level. The precision uncertainty calculated from the fluctuations in the data varied slightly for each test, so the total precision uncertainty of each measurement was different for each test. The values presented here are for the sample case used in Sections 3.1 and 3.2.

TABLE 3.2. Precision uncertainties of measured values at 95% confidence.

Measurement	**Value**	**Pre-test**	**Post-test**	**Data**	**Total**
$T_{UPSTREAM}$ [°C]	22.9	±0.01	±0.01	±0.01	±0.02
$RH_{UPSTREAM}$ [% RH]	68.1	±0.02	±0.02	±0.03	±0.04
$T_{DOWNSTREAM}$ [°C]	21.4	±0.01	±0.01	±0.01	±0.02
$RH_{DOWNSTREAM}$ [% RH]	58.8	±0.02	±0.02	±0.03	±0.04
TC_1 [°C]	8.2	±0.004	±0.006	±0.016	±0.02
TC_2 [°C]	8.0	±0.002	±0.010	±0.013	±0.02
TC_3 [°C]	8.2	±0.004	±0.006	±0.016	±0.02
TC_4 [°C]	8.0	±0.002	±0.016	±0.003	±0.02
TC_5 [°C]	8.2	±0.004	±0.014	±0.003	±0.02
ρ_{HAMP} [kg_{sol}/m^3]	1197.2	±0.38	±0.38	±0.04	±0.54

The bias and precision uncertainties of each measurement were combined using equation (3.4) to find the total uncertainty at 95% confidence levels of each measurement. The results are presented in Table 3.3.

TABLE 3.3. Total uncertainty of measured values at 95% confidence.

Measurement	Value	U_x
$T_{UPSTREAM}$ [°C]	22.9	±0.3
$RH_{UPSTREAM}$ [% RH]	68.1	±1.1
$T_{DOWNSTREAM}$ [°C]	21.4	±0.3
$RH_{DOWNSTREAM}$ [% RH]	58.8	±0.8
TC_1 [°C]	8.2	±0.2
TC_2 [°C]	8.0	±0.3
TC_3 [°C]	8.2	±0.2
TC_4 [°C]	8.0	±0.3
TC_5 [°C]	8.2	±0.2
ρ_{HAMP} [kg_{sol}/m^3]	1197.2	±11.7

3.3.2 Uncertainty of Calculated Values

Values that are calculated from measurements also have uncertainty, due to the uncertainty of the measured values. The bias uncertainty of a calculated result (R) is

$$b_R = \left[\sum_{j=1}^{J} \left(\frac{\partial R}{\partial x_j} b_{x_j} \right)^2 \right]^{1/2} \tag{3.9}$$

where $\frac{\partial R}{\partial x_j}$ is the derivative of the result with respect to variable x and b_x is the bias uncertainty in variable x. The precision uncertainty of a calculated result, s_R, is also calculated using equation (3.9), using the precision uncertainty in variable x, instead of the bias uncertainty. The total uncertainty in a calculated result was calculated using equation (3.4).

The sensible, latent and total effectivenesses of the HAMP were calculated from the temperature, humidity ratio and enthalpy of the air upstream and downstream of the test section, as well as

inside the prototype HAMP. The bias, precision and total uncertainties for the calculated values needed to determine the effectivenesses are given in Table 3.4 for the test case presented in Sections 3.1 and 3.2. Since the uncertainty in calculated results depended on the values used to calculate each result, the uncertainty in the effectivenesses varied for each test case.

TABLE 3.4. Bias, precision and total uncertainties of calculated results for the test case.

Calculated Result	**Value**	**Bias (68%)**	**Precision (68%)**	**Total (95%)**
T_{HAMP} [°C]	8.1	±0.06	±0.004	±0.1
C_{salt} [%]	32.0	±0.9	±0.04	±1.8
RH_{HAMP} [% RH]	37.8	±0.3	±0.01	±0.5
W_{HAMP} [g_w/kg_{air}]	2.7	±0.02	±0.01	±0.04
$W_{UPSTREAM}$ [g_w/kg_{air}]	12.6	±0.2	±0.01	±0.4
$W_{DOWNSTREAM}$ [g_w/kg_{air}]	9.9	±0.1	±0.01	±0.3
$h_{UPSTREAM}$ [kJ/kg_{air}]	55.0	±0.5	±0.03	±1.1
$h_{DOWNSTREAM}$ [kJ/kg_{air}]	46.6	±0.4	±0.03	±0.8
h_{HAMP} [kJ/kg_{air}]	14.9	±0.1	±0.01	±0.2
ε_{latent} [%]	27.3	±2.0	±0.1	±4.0
$\varepsilon_{sensible}$ [%]	10.1	±1.8	±0.1	±3.6
ε_{total} [%]	20.9	±1.4	±0.1	±2.8

According to ASHRAE Standard 84 (2008), the uncertainty in the sensible and latent effectivenesses must be less than ±5% and ±7%, respectively. The uncertainty in the total effectiveness must fall within the limits of

$$U_{\varepsilon_{total}} < \pm \frac{|\varepsilon_{total}-\varepsilon_{latent}|*5+|\varepsilon_{total}-\varepsilon_{sensible}|*7}{|\varepsilon_{latent}-\varepsilon_{sensible}|}. \quad (3.10)$$

In this sample case, the uncertainty in the total effectiveness must be less than ±6.3% in order to satisfy the standard. Comparing the data in Table 3.4 with the constraints given by the standard, the uncertainty results of this test case were acceptable. The constraints given by the standard were applied to all test cases, to ensure that all reported data was within acceptable uncertainty limits.

3.4 ENERGY AND MASS BALANCES

The final analyses performed to ensure that the test facility was functioning properly and the measurements taken were accurate were energy and mass balances on the system. The purpose of these balances are to verify that mass and energy were conserved within the system. It is important to ensure there are no systematic heat or moisture exchanges between the system and the environment and that there are no unaccounted for systematic errors in the measurements. To be acceptable, the energy and mass balances must agree within experimental uncertainty.

A schematic of the control volume used for the energy and mass balances in the test section, is shown in Figure 3.10. The schematic shows the HAMP on the top of the test section, with airflow from left to right, through the test section. The test case discussed in this chapter was a case of cooling and dehumidification, so the heat and mass transfer were both from the air, into the HAMP, as indicated by the arrows on the schematic. The direction of the heat and mass transfer was different for each test case, depending on the operating conditions.

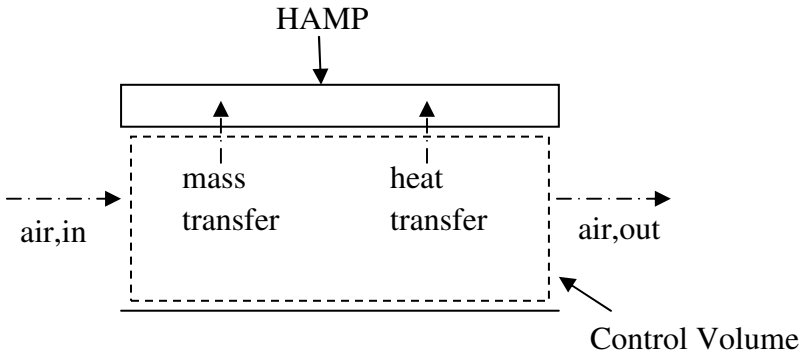

FIGURE 3.10. Schematic of the control volume used for energy and mass balances.

3.4.1 Energy Balance

The conservation of energy equation can be written as

$$\dot{E}_{in}-\dot{E}_{out}=\dot{E}_{storage} \tag{3.11}$$

where $\dot{E}_{in}$ is the rate at which energy enters the control volume [W], $\dot{E}_{out}$ is the rate at which energy leaves the control volume [W] and $\dot{E}_{storage}$ is the rate at which energy is stored in the control volume [W]. Since the tests are at steady state, it was assumed that the amount of energy stored in the control volume did not change with time, so the rate of energy into the control volume minus the rate of energy leaving the control volume was equal to zero.

For the given control volume, and with the heat and mass transfer in the directions indicated in the schematic, the conservation of energy becomes

$$(\dot{m}_{air}h_{air})_{UPSTREAM}-(\dot{m}_{air}h_{air})_{DOWNSTREAM}-(\dot{m}_{w}h_{w})-h_{conv}A_{surface}\Delta T_{lm}=0 \tag{3.12}$$

where $\dot{m}$ is the mass flow rate of air [kg_{air}/s] or water vapour [kg_{w}/s], h_{air} and h_{w} are the enthalpy of air [kJ/kg_{air}] or water vapour [kJ/kg_{w}], h_{conv} is the convection heat transfer coefficient in the duct [W/(m^2·K)], $A_{surface}$ is the surface area of the HAMP [m^2] and ΔT_{lm} is the log mean temperature difference between the airflow and the HAMP [°C or K].

The log mean temperature difference is defined as

$$\Delta T_{lm} = \frac{\Delta T_{in} - \Delta T_{out}}{\ln\left(\Delta T_{in} / \Delta T_{out}\right)} \tag{3.13}$$

where ΔT_{in} is the temperature difference between the HAMP and the air at the entrance of the test section and ΔT_{out} is the temperature difference between the HAMP and the air at the outlet of the test section [°C or K].

The mass flow rate of the air was measured during the test and the enthalpy of the air was calculated from the measured temperature and humidity ratio. The mass flow rate of the water vapour was calculated from a mass balance on the control volume. The enthalpy of the water vapour was calculated based on the temperature of the water vapour, which depended on the direction of the mass transfer in the control volume. If the mass transfer was from the air into the HAMP, then the water vapour would be at the temperature of the air in the duct. If the mass transfer was from the HAMP into the air, then the water vapour would be at the temperature of the liquid desiccant inside the HAMP. The heat transfer coefficient was calculated from a correlation for heat transfer in a rectangular duct, with laminar airflow and heat transfer from one wall. Table 3.5 lists the values of each variable used in equation (3.12) for the sample case. The equations used to calculate these values can be found in Appendix A.

TABLE 3.5. Values of variables used for conservation of energy equation.

Variable	Value
$\dot{m}_{air}$ [kg_{air}/s]	0.0002
$h_{UPSTREAM}$ [kJ/kg_{air}]	55.0
$h_{DOWNSTREAM}$ [kJ/kg_{air}]	46.6
$\dot{m}_w$ [kg_w/s]	$5.4x10^{-7}$
T_w [°C]	17.5
h_w [kJ/kg_w]	2533.9
h [$W/(m^2 \cdot K)$]	0.65
$A_{surface}$ [m^2]	0.043
ΔT_{lm} [°C]	14.0

There were two checks performed to ensure that the energy balance was acceptable. The first was that the unaccounted for energy from equation (3.12) was less than the uncertainty in equation (3.12). For the sample case, there was 0.07 W of energy that was unaccounted for in the system. The uncertainty of this calculation was ±0.40 W. This meant that the energy balance performed was within acceptable uncertainty limits, as the unaccounted for energy was less than the uncertainty in the calculation, and the uncertainty value was also acceptable.

The second check was that the energy that was unaccounted for was small compared to the total amount of heat transfer through the air (from upstream to downstream). In this case, the total amount of energy transfer through the air was 1.73 W. The energy that was unaccounted for in the system was less than 5% of the total energy transfer through the air. These checks was performed for each test case used in this thesis, ensuring that the energy balance was within the acceptable uncertainty limits and that the unaccounted for energy was less than 5% of the energy

transfer through the air in each case. Any tests that did not meet these requirements was not considered in the analysis.

3.4.2 Mass Balance

Using the control volume shown in Figure 3.10, the conservation of mass equation can be written as

$$\dot{m}_{w,in}-\dot{m}_{w,out}=\dot{m}_{w,storage} \tag{3.14}$$

where $\dot{m}_{w,in}$ is the rate at which the mass of water vapour enters the control volume [kg_w/s], $\dot{m}_{w,out}$is the rate at which the mass of water vapour leaves the control volume [kg_w/s] and $\dot{m}_{w,storage}$ is the rate at which the mass of water vapour is stored in the control volume [kg_w/s]. Since the system was at steady state, it was assumed that the amount of water vapour stored in the system did not change over the length of the test.

The mass flow rate of water vapour in the air entering and exiting the test section was equal to the mass flow rate of the air multiplied by the humidity ratio of the air upstream of the test section and downstream of the test section, respectively. The mass flow rate of water vapour from the air into the HAMP was determined by measuring the change in mass of the liquid desiccant over the length of the test.

The conservation of mass equation becomes

$$(\dot{m}_{air}W_{air})_{UPSTREAM}-(\dot{m}_{air}W_{air})_{DOWNSTREAM}-\frac{\Delta mass}{t}=0 \tag{3.15}$$

where $\dot{m}_{air}$ is the mass flow rate of air [kg_{air}/s], W_{air} is the humidity ratio of the air [kg_w/kg_{air}], Δmass is the change in mass of the liquid desiccant inside the reservoir tank [kg_w] and t is the length of time of the steady state test [s].

The values required for the mass balance are presented in Table 3.6, for the sample case. The change in mass of the liquid desiccant in the reservoir tank was 0.0019 kg_w, over the one hour (3600 s) test. For this case, the result of the mass balance was 2.7×10^{-8} kg_w/s, which is the mass flow rate of water vapour that was unaccounted for in the system. The uncertainty in this calculation was $\pm 6.7 \times 10^{-8}$ kg_w/s. When compared to the total mass transfer through the duct, the portion unaccounted for was less than 5%, which is acceptable.

TABLE 3.6. Values of variable used in the conservation of mass equation.

Variable	**Value**
$\dot{m}_{air}$ [kg_{air}/s]	0.0002
$W_{UPSTREAM}$ [kg_w/kg_{air}]	0.0126
$W_{DOWNSTREAM}$ [kg_w/kg_{air}]	0.0099
Δmass [kg_w]	0.0019
t [s]	3600

3.5 SUMMARY

The analysis presented in this chapter showed that the test facility and instrumentation discussed in Chapter 2 provide reliable experimental results. The uncertainties in each measurement as well as important calculated values were presented. The uncertainties in the sensible, latent and total effectivenesses meet the requirements set out by ASHRAE Standard 84 (2008) for testing

air-to-air energy exchangers. The energy and mass balances agreed within experimental uncertainty limits. The energy and mass balances showed that the systematic heat and moisture exchange between the test facility and the environment were small compared to the amount of heat and moisture transfer through the airflow (<5%). These results showed that the experimental results recorded in this study can be used to determine the performance of the prototype HAMP with a high level of confidence.

CHAPTER 4 – OPERATING CONDITIONS AND DESIGN PARAMETERS

One of the objectives of this thesis is to determine the performance of the prototype HAMP under different operating conditions. It will be shown in Chapters 5 and 6 that the performance of the HAMP is dependent on the operating conditions, as well as several other design parameters. Before the performance can be presented however, these conditions and parameters need to be defined and the range of each parameter covered in the experiments presented. In this chapter, the range of test conditions, including the temperature and humidity ratio of the upstream air, the temperature and density of the liquid desiccant inside the HAMP and the mass flow rates of the air and liquid desiccant will be presented.

The key design parameters used in the analysis presented in this thesis include the number of heat transfer units (NTU), number of mass transfer units (NTU_m) and heat capacity ratio (Cr) of the HAMP, as well as the operating condition factor (H^*) which quantifies the inlet conditions of each test. In addition to these values, it is important to understand the airflow patterns in the duct, and whether forced convection or natural convection is dominant in the test section during each test. The Reynolds number (Re), heat transfer Rayleigh number (Ra_h), mass transfer Rayleigh number (Ra_m), effective Rayleigh number (Ra^+) and Richardson number (Ri) are defined and the ranges covered in the experiments are discussed.

4.1 RANGE OF TEST CONDITIONS

A total of 83 tests were performed which met the requirements presented in Chapter 3 for acceptable test conditions, based on the energy and mass balances and the uncertainty in the sensible and latent effectivenesses. Of these tests, 13 were performed with the HAMP in the floor panel configuration and 70 were performed with the HAMP in the ceiling panel configuration. In 12 of the tests, water was used in the HAMP and in the remaining 71 tests, a lithium chloride solution was used. The upstream air and HAMP conditions for all tests are summarized in Figure 4.1, on a psychrometric chart. The complete data set for all 83 tests is presented in Appendix D.

Figure 4.1 shows the range of upstream air temperature and relative humidity values used in the experiments. The upstream air was kept close to the room temperature of the laboratory, covering a range of approximately 20°C to 25°C. The relative humidity of the upstream air was varied to create conditions where humidification was needed and conditions where dehumidification was needed. The upstream relative humidity ranged from 3% RH to 87% RH.

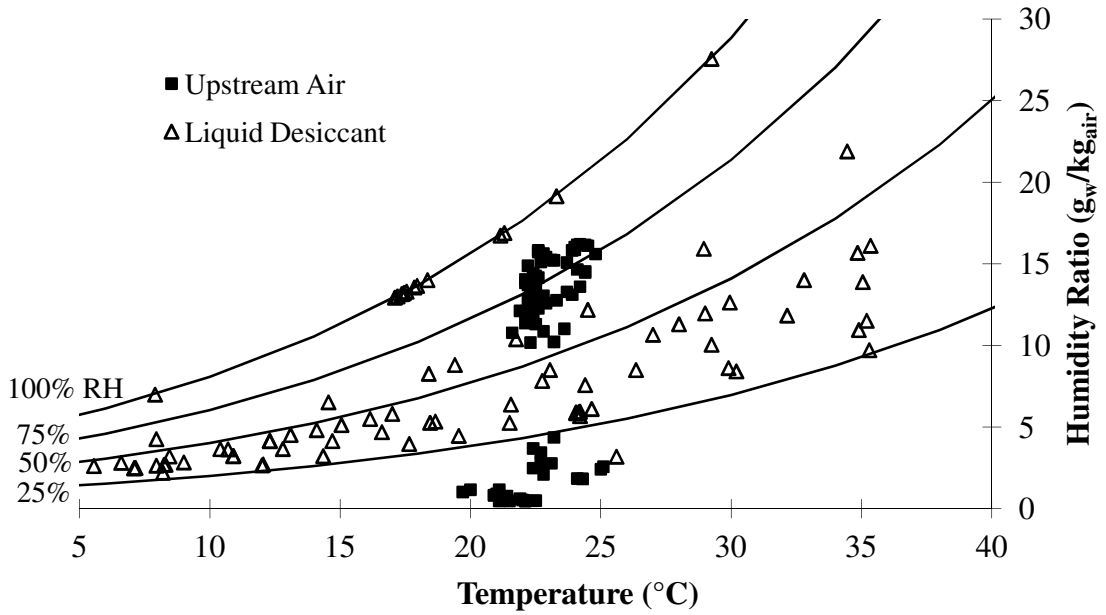

FIGURE 4.1. Upstream air and HAMP test conditions for all tests in this thesis.

The conditions inside the prototype HAMP were varied to create cooling, heating, humidifying and dehumidifying cases. The temperature of the liquid inside the HAMP ranged from 6°C to 35°C. The density of the liquid desiccant was varied from 1141 kg/m^3 to 1398 kg/m^3 with the lithium chloride solution and was approximately 998 kg/m^3 with water. The concentration of the salt solution varied from 24% to 60% and the relative humidity ranged from 15% RH to 60% RH. The cases shown in Figure 4.1 that are on the 100% RH line are the tests where water was used in the HAMP.

The ranges of the upstream air conditions and the HAMP conditions used in the experiments are summarized in Table 4.1 for all tests. In addition to the parameters discussed, the range of humidity ratios of the upstream air and the equivalent surface humidity ratio of the liquid desiccant are also presented. When discussing the driving potential for moisture, it is more appropriate to use humidity ratio, as it is independent of temperature, unlike relative humidity,

which varies with temperature. The latent effectiveness of the prototype HAMP is calculated from the measured humidity ratios.

The mass flow rate of the liquid desiccant was kept constant, for all tests, at 0.013 kg_{sol}/s. The velocity of the liquid desiccant was dependent on the density of the solution, so it varied from one test to another. The range of velocities of the liquid desiccant was 0.010 m/s to 0.014 m/s. This translates into a Reynolds number of ~120 for the tests with a lithium chloride solution and ~450 for the tests with water. During 63 of the test cases, the mass flow rate of the air was 0.0002 kg_{air}/s, which equates to an average velocity of 0.005 m/s and a Reynolds number of ~65. For ten of the test cases, the mass flow rate of the air stream was 0.0004 kg_{air}/s, which equates to a velocity of 0.01 m/s and a Reynolds number of ~115. Table 4.1 presents a summary of the flow conditions for the liquid desiccant and the air streams.

TABLE 4.1. Summary of upstream air and HAMP conditions in experiments.

Parameter	**Range**	**Parameter**	**Range**
$T_{UPSTREAM}$ [°C]	20 – 25	W_{HAMP} [g_w/kg_{air}]	2 – 28
$RH_{UPSTREAM}$ [% RH]	3 – 87	$\dot{m}_{air}$ [kg_{air}/s]	0.0002 or 0.0004
$W_{UPSTREAM}$ [g_w/kg_{air}]	0.5 – 16	V_{air} [m/s]	0.005 or 0.01
T_{HAMP} [°C]	6 – 35	Re_{air} [-]	65 or 115
ρ_{HAMP} [kg/m^3]	995 (water) or 1141 – 1398 (LiCl)	$\dot{m}_{sol}$ [kg_{sol}/s]	0.013
		V_{sol} [m/s]	0.010 – 0.014
C_{salt} [%]	24 – 60	Re_{sol} [-]	450 (water) or 120 (LiCl)
RH_{HAMP} [% RH]	100 (water) or 15 – 61 (LiCl)		

The test conditions presented in this section are used to calculate the design parameters of the prototype HAMP for each test case. The following sections will present the equations and methods used.

4.2 HEAT EXCHANGER PARAMETERS

The sensible effectiveness of a heat exchanger is defined as the ratio of the actual heat transfer rate between the two fluid streams (q), to the maximum possible heat transfer rate (q_{max}), as

$$\varepsilon_{sensible} \equiv \frac{q}{q_{max}}. \tag{4.1}$$

The maximum possible heat transfer rate can be calculated from the difference in temperatures between the two fluid streams

$$q_{max}=\left(\dot{m}c_p\right)_{min}\left(T_H-T_C\right) \tag{4.2}$$

where $\dot{m}$ is the mass flow rate [kg/s], c_p is the specific heat [J/(kg·K)] and T is the temperature [°C or K]. The subscript 'H' refers to the hot fluid stream and the subscript 'C' refers to the cool fluid stream. The subscript 'min' refers to the minimum product of $\dot{m}c_p$ for the two streams.

In order to calculate the actual heat transfer rate, the temperature at the outlets of the fluid streams must be known, in addition to the temperatures at the inlets of the streams, and is calculated from

$$q=\left(\dot{m}c_p\right)_C\left(T_{C,out}-T_{C,in}\right)=\left(\dot{m}c_p\right)_H\left(T_{H,out}-T_{H,in}\right) \tag{4.3}$$

where the subscripts 'out' and 'in' refer to the outlets and inlets of the streams, respectively.

In the experiments, the downstream temperature of the air was measured, as well as the temperature at the outlet of the HAMP, allowing the actual heat transfer rate to be calculated for each test. In the design of a heat exchanger, however, the outlet conditions are not usually known. Another method for determining the sensible effectiveness of a heat exchanger when the outlet conditions are not known is the effectiveness-NTU method, which states that

$$\varepsilon_{\text{sensible}} = f(\text{NTU}, \text{Cr}) \tag{4.4}$$

where NTU is the number of heat transfer units and Cr is the heat capacity ratio of the heat exchanger, defined below. Specific correlations for the sensible effectiveness can be found from ASHRAE (2009) based on the flow configuration of the heat exchanger.

4.2.1 Heat Capacity Ratio, Cr

The heat capacity ratio of a heat exchanger is defined as

$$\text{Cr} = \frac{(\dot{m}c_p)_{\text{min}}}{(\dot{m}c_p)_{\text{max}}} \tag{4.5}$$

where $\dot{m}$ is the mass flow rate [kg/s] and c_p is the specific heat [J/(kg·K)] of a fluid. For the tests performed in this thesis (and for most HAMP applications), the minimum value of the product $\dot{m}c_p$ is the airflow and the maximum value is the liquid desiccant.

The mass flow rates of the air and liquid desiccant streams were discussed in Section 4.1. The specific heat of moist air is dependent on the temperature and humidity ratio of the air and is calculated from

$$c_{p,\text{air}} = c_{p,\text{dry air}} + \text{W}c_{p,\text{w}} \tag{4.6}$$

where $c_{p,\text{dry air}}$ is the specific heat of dry air [J/(kg·K)], W is the humidity ratio of the air [$\text{kg}_\text{w}/\text{kg}_\text{air}$] and $c_{p,\text{w}}$ is the specific heat of water vapour [J/(kg·K)]. The values of $c_{p,\text{dry air}}$ and

$c_{p,w}$ were taken from Incropera and DeWitt (2002) at the temperature of the moist air. For the tests performed, $c_{p,air}$ ranged from 1008 J/(kg·K) to 1036 J/(kg·K).

The specific heat of the liquid desiccant was calculated from the temperature and concentration of the salt solution, based on the correlations presented in Appendix B. For the tests performed, $c_{p,sol}$ ranged from 2657 J/(kg·K) to 3115 J/(kg·K) for LiCl and 4139 J/(kg·K) to 4156 J/(kg·K) for water.

For the range of test conditions in this thesis, the heat capacity ratio for the prototype HAMP ranged from 0.0004 to 0.011. These values were very small, so the heat capacity ratio of the prototype HAMP was considered equal to zero for all tests.

4.2.2 Number of Heat Transfer Units, NTU

The number of heat transfer units of a heat exchanger is defined by

$$NTU = \frac{UA_{surface}}{(\dot{m}c_p)_{min}} \tag{4.7}$$

where U is the overall heat transfer coefficient of the exchanger [W/(m^2·K)] and $A_{surface}$ is the heat transfer surface area of the exchanger [m^2]. The heat transfer surface area of the prototype HAMP was 0.043 m^2. The minimum value of the product of $\dot{m}$ and c_p for the HAMP will be for the airflow for all of the tests.

The overall heat transfer coefficient of a heat exchanger can be determined in two ways. The most common method used when designing a heat exchanger, is to use correlations from the literature to predict the heat transfer coefficients in the two streams, based on known inlet

conditions. For complex heat exchangers, the overall heat transfer coefficient can also be measured from experimental data. In this thesis, both methods are used. The theoretical values, based on correlations found in the literature are given the subscript 'theo' and are presented in this chapter and in Chapter 5. The experimental values, calculated from measured data are given the subscript 'exp' and will be discussed in Chapter 6.

4.2.3 Overall Heat Transfer Coefficient, U_{theo}

The total heat transfer rate of a heat exchanger (q) is given by

$$q = UA_{surface}\Delta T_{lm} \tag{4.8}$$

where U is the overall heat transfer coefficient between the two streams [$W/(m^2 \cdot K)$], $A_{surface}$ is the total surface area for heat transfer [m^2] and ΔT_{lm} is the log mean temperature difference, calculated using equation (3.13) [°C or K]. Using equation (3.13) to calculate the log mean temperature difference is applicable for counter flow heat exchangers. For more complicated flow conditions, a correction factor needs to be applied to the log mean temperature difference (Incropera and DeWitt (2002)).

The overall heat transfer coefficient is related to the total resistance to heat transfer from one stream to the other, inside the heat exchanger. Figure 4.2 shows a schematic of the equivalent thermal circuit for the prototype HAMP. Heat is transferred between the liquid desiccant and the air, through the membrane.

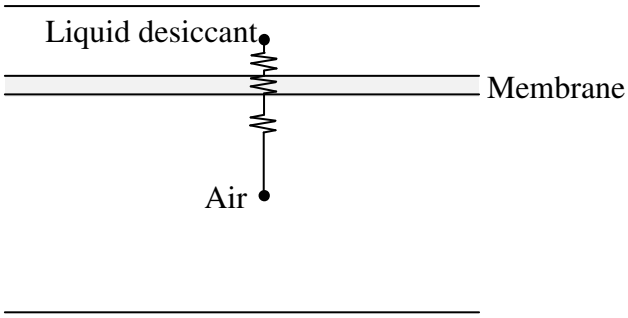

FIGURE 4.2. Equivalent thermal circuit for the prototype HAMP.

Using the thermal circuit in Figure 4.2, the overall heat transfer coefficient can be expressed as

$$U_{theo}=\left[\frac{1}{h_{eff,air}}+\frac{\delta_{membrane}}{k_{membrane}}+\frac{1}{h_{sol}}\right]^{-1} \tag{4.9}$$

where $h_{eff,air}$ is the effective heat transfer coefficient in the air [W/(m^2·K)], h_{sol} is the convection heat transfer coefficient in the liquid desiccant [W/(m^2·K)], and $\delta_{membrane}$ and $k_{membrane}$ are the thickness [m] and thermal conductivity [W/(m·K)] of the semi-permeable membrane. The thickness and thermal conductivity of the semi-permeable membrane used in the prototype HAMP are taken from Larson (2006).

In the air, an effective heat transfer coefficient is used, as there will be heat transfer by both convection and radiation. The effective heat transfer coefficient of the air is found from

$$h_{eff,air}=h_r+h_{conv} \tag{4.10}$$

where h_r [W/(m^2·K)] is the radiation heat transfer coefficient and h_{conv} is the convection heat transfer coefficient [W/(m^2·K)] in the air.

An analysis of the heat transfer inside the liquid desiccant showed that the temperature difference between the middle of the stream (where T_{HAMP} is measured) and the surface of the membrane, on the liquid side, was negligible. This meant that the resistance to heat transfer inside the liquid desiccant was very small, and could therefore be neglected from the overall heat transfer coefficient. The analysis showing the calculation of the temperature difference across the height of the liquid desiccant channel can be found in Appendix E.

The radiation heat transfer between the HAMP surface and the other surfaces in the duct can be approximated from an equation for radiation heat transfer in a two-surface enclosure (Incropera and DeWitt (2002))

$$q_r = \frac{\sigma\left(T_1^4 - T_2^4\right)}{\frac{1-\varepsilon_1}{\varepsilon_1 A_1} + \frac{1}{A_1 F_{12}} + \frac{1-\varepsilon_2}{\varepsilon_2 A_2}} \tag{4.11}$$

where σ is the Stefan-Boltzmann constant, equal to 5.67×10^{-8} W/(m^2·K^4), ε is the emissivity of the surface [-], A is the area of the surface [m^2] and F_{12} is the view factor from surface one to surface two [-]. The prototype HAMP is taken as surface '1' and the remaining three walls as surface '2'. This is a simplified analysis which assumes that all of the radiation heat transfer occurs in the test section. It was assumed that the surface temperature of the three remaining walls would be the same, and approximately equal to the air temperature in the duct. This assumption was based on the fact that the temperature of the air in the laboratory was not drastically different from the air inside the test section, so there was no additional heat added to/lost from the test section walls.

In order to determine the radiation heat transfer coefficient, equation (4.11) is rearranged in a form similar to Newton's law of cooling for convection heat transfer,

$$q_r = h_r A_{surface}\left(T_1 - T_2\right) \tag{4.12}$$

where the radiation heat transfer coefficient [W/(m^2·K)] is

$$h_r = \frac{\sigma}{\frac{1-\varepsilon_1}{\varepsilon_1 A_1} + \frac{1}{A_1 F_{12}} + \frac{1-\varepsilon_2}{\varepsilon_2 A_2}} \frac{(T_1+T_2)\left(T_1^2+T_2^2\right)}{A_{surface}}. \tag{4.13}$$

The emissivity of all of the surfaces was assumed to be 0.9, which, according to ASHRAE (2012) is a good approximation for nonmetallic surfaces. F_{12} was assumed to be one, meaning that all of the heat transfer is absorbed by the two side walls and the bottom of the duct. Based on the experiments performed, the radiation coefficient in the HAMP ranged from approximately 5.4 W/(m^2·K) to 6.4 W/(m^2·K) for all tests. According to ASHRAE (2012), these values are similar to typical values found for radiant ceiling panels.

The convection heat transfer coefficient in the air is more difficult to predict than the radiation heat transfer coefficient. Where the radiation coefficient is mainly dependent on the temperatures of the panel and the air, the convection coefficient is dependent on several other parameters, including the flow regime in the test section and the geometry of the duct. A summary of the current literature on convection heat transfer in rectangular ducts was presented in Chapter 1. In the experiments performed, both forced convection and natural convection may be present in the duct. The following sections will discuss the dimensionless parameters and correlations used to determine the convection heat transfer coefficient in the air for each test.

4.2.4 Reynolds Number, Re

When forced convection is dominant in the duct, the convection heat transfer coefficient is dependent on the Reynolds number of the flow. For a rectangular duct, Reynolds number is given by

$$Re = \frac{V_{air} D_h}{\upsilon_{air}} \tag{4.14}$$

where V_{air} is the velocity of the air [m/s], D_h is the hydraulic diameter of the duct [m] and ν_{air} is the kinematic viscosity of the air [m^2/s]. As discussed in Section 4.1, Reynolds number was equal to 65 for the majority of the tests performed.

For forced convection, the correlation from Krishnamurty and Sambasiva Rao (1967) for hydrodynamically fully developed, thermally developing laminar flow through a rectangular duct, with a constant temperature on the bottom wall is used to predict the average Nusselt number in the duct. The correlation is

$$Nu = 0.93 Re^{1/3} Pr^{1/3} \left(\frac{\mu_{avg}}{\mu_{bulk}}\right)^{0.14} \left(\frac{Z}{D_h}\right)^{-1/3} \int_0^1 \phi_x^{1/3} dr \tag{4.15}$$

where Pr is the Prandtl number [-], μ_{avg} is the dynamic viscosity at the average air temperature [Pa·s], μ_{bulk} is the dynamic viscosity at the bulk air temperature [Pa·s], Z is the length of the heat transfer surface [m], D_h is the hydraulic diameter of the duct [m] and $\phi_x^{1/3}$ is a constant dependent on the aspect ratio of the duct.

The convection heat transfer coefficient was calculated from the Nusselt number, based on the hydraulic diameter of the duct, as

$$h_{conv} = \frac{Nuk_{air}}{D_h} \tag{4.16}$$

where k_{air} is the thermal conductivity of the air [W/(m·K)].

4.2.5 Rayleigh Number, Ra

In addition to the air movement caused by forced convection, air movement in the duct may be caused by buoyancy forces, due to the presence of a density gradient in the duct. When the density of the air at the top of the duct was higher than the density of the air at the bottom of the duct, buoyancy forces were present in the duct. When these buoyancy forces become large enough, natural convection will occur in the duct, causing the air in the duct to become unstable. A density gradient can be caused by:

- a temperature gradient, where the temperature of the air is different at the top and the bottom of the test section,
- a concentration gradient, where the concentration of water vapour is different at the top and the bottom of the test section, or
- a combination of temperature and concentration gradients, where both the temperature and concentration of water vapour are different at the top and the bottom of the test section.

Each density gradient has both a direction and a magnitude. Cooling and dehumidifying the air from the top of the test section both create positive density gradients (higher density at the top of the duct), resulting in unstable airflow in the test section. Heating and humidifying the air both create negative density gradients (higher density at the bottom of the duct), so the airflow will remain stable during these cases. Note that the directions of the density gradients listed here are for a HAMP in the ceiling of a space, or the top of the test section. The directions would be opposite if the panel were in the floor of a space, or the bottom of the test section. The magnitude of the buoyancy forces can be quantified using the Rayleigh number.

The Grashof number for heat transfer is the ratio of the buoyancy forces in the duct (caused by a temperature gradient) to the viscous forces in the duct. In this thesis, the Rayleigh number will be used, which is the Grashof number multiplied by the Prandtl number (Pr) and is calculated from (Incropera and DeWitt (2002))

$$Ra_h = \frac{g\beta(T_{air}-T_{surface})L^3 Pr}{\nu^2} \tag{4.17}$$

where g is acceleration due to gravity [m/s^2], β is the volumetric thermal expansion coefficient [1/K], $T_{surface}$ is the temperature of the heat transfer surface [K], T_{air} is the average temperature of the air [K], L is the characteristic length [m] and ν is the kinematic viscosity of the air [m^2/s]. Equation (4.17) can be used to calculate the Rayleigh number for the air in the test section when the heat transfer surface is in the ceiling. For a heat transfer surface in the floor, the temperature of the air and the temperature of the surface must be switched to yield the correct direction of the density gradient.

The Grashof number for mass transfer relates the ratio of buoyancy forces caused by a concentration gradient to the viscous forces in the fluid. The Rayleigh number for mass transfer is the mass transfer Grashof number multiplied by the Schmidt number (Sc). The mass transfer Rayleigh number is calculated from (Lin et al. (1992a))

$$Ra_m = \frac{g\left(\frac{M_{air}}{M_w}-1\right)(C_{air}-C_{surface})L^3 Sc}{\nu^2} \tag{4.18}$$

where M_{air} is the molecular weight of air [kg_{air}/mol], M_w is the molecular weight of water vapour [kg_w/mol], C_{air} is the average concentration (mass fraction) of water vapour in the air [kg_w/kg_{air}] and $C_{surface}$ is the concentration (mass fraction) of water vapour at the surface of mass

transfer [kg_w/kg_{air}]. As with the heat transfer Rayleigh number, equation (4.18) assumes the mass transfer surface is in the ceiling.

When both temperature and concentration gradients are present and both are positive or both are negative, the two gradients will add together to create a larger positive or negative density gradient. If both temperature and concentration gradients are present, but are acting in opposite directions (one positive and one negative) the smaller gradient will be subtracted from the larger gradient, creating a smaller overall density gradient. The overall density gradient is quantified by Lin et al. (1992b) using an effective Rayleigh number (Ra^+), which takes into account both the magnitude and direction of the temperature and concentration gradients. The effective Rayleigh number, is

$$Ra^+ = Ra_h + Ra_m. \tag{4.19}$$

For natural convection in a horizontal, rectangular duct, with heat transfer from the bottom wall, the correlation of Raithby and Hollands (1985) can be used to predict the heat transfer coefficient in the air, as a function of the Rayleigh number. The correlation is

$$Nu = 1 + \left[1 - \frac{Ra_{cr}}{Ra}\right]^{\blacksquare} \left[k_1 + 2\left(\frac{Ra^{1/3}}{k_2}\right)^{1-\ln\left(Ra^{1/3}/k_2\right)}\right] + \left[\left(\frac{Ra}{5380}\right)^{1/3} - 1\right]^{\blacksquare} \left(1 - \exp\left\{-0.95\left[\left(\frac{Ra}{Ra_{cr}}\right)^{1/3} - 1\right]^{\blacksquare}\right\}\right) \tag{4.20}$$

where Ra_{cr} is the critical Rayleigh number for the duct [-] and k_1 and k_2 are constants equal to 1.40 and 446, respectively, for air [-]. The symbol $[\ ]^{\blacksquare}$ indicates that only positive values of that expression are to be taken.

The critical Rayleigh number, for the onset of buoyancy in this test facility is approximately 3000 based on values taken from Raithby and Hollands (1985). For the tests where natural convection is dominant in the test section, the convection heat transfer coefficient is calculated from the Nusselt number, based on the height of the duct (H), as

$$h_{conv}=\frac{Nuk_{air}}{H}. \tag{4.21}$$

4.2.6 Richardson Number, Ri

To determine which type of convection is dominant in the duct during each test, the Richardson number is calculated. The Richardson number represents the importance of natural convection relative to forced convection. From Incropera and DeWitt (2002)

$$Ri=\frac{Ra/Pr}{Re^2} \tag{4.22}$$

where Ra is the Rayleigh number, Pr is the Prandtl number and Re is the Reynolds number. Forced convection is dominant when $Ri << 1$, natural convection is dominant when $Ri >> 1$ and both forced and natural convection are important when $Ri \approx 1$.

Based on the Richardson number determined for each case, the appropriate convection correlation was used to determine the convection heat transfer coefficients. For cases where $Ri \approx 1$, a mixed convection heat transfer coefficient was determined from

$$Nu^n_{mixed}=Nu^n_{forced}+Nu^n_{natural} \tag{4.23}$$

where the exponent n depends on the geometry of the channel and is taken as 7/2 (Incropera and DeWitt (2002)).

4.2.7 Summary of NTU_{theo} Values

Using the correlations for heat transfer coefficients discussed, the theoretical convection heat transfer coefficient was determined for each test. Table 4.2 summarizes the range of radiation heat transfer coefficients, as well as the convection heat transfer coefficients for the cases with Re = 65. The radiation heat transfer coefficient and convection heat transfer coefficients were combined to determine the effective heat transfer coefficient in the air, based on equation (4.10). The theoretical overall heat transfer coefficient was then determined based on equation (4.9). The overall heat transfer coefficient was approximately the same as the effective heat transfer coefficient, which indicates that the resistance to heat transfer of the membrane was negligible compared to the resistance in the air. NTU_{theo}, calculated from U_{theo}, ranges from 1.4 to 1.6.

TABLE 4.2. Summary of theoretical values used to find NTU_{theo}.

Parameter	Range	Parameter	Range
Re [-]	~65	h_r [W/m^2·K]	5.4 – 6.4
Ra^+ [-]	-42x10^5 – 65x10^5	$h_{eff,air}$ [W/m^2·K]	6.7 – 7.6
Nu [-]	5.4 – 12.6	U_{theo} [W/m^2·K]	6.7 – 7.6
h_{conv} [W/m^2·K]	0.8 – 2.2	NTU_{theo} [-]	1.4 – 1.6

Typically, for radiant ceiling panels, the convection heat transfer coefficient makes up approximately 40% of the effective heat transfer coefficient (ASHRAE (2012)). Based on the theoretical values discussed, the convection heat transfer coefficient accounted for ~20% of the effective heat transfer coefficient for the prototype HAMP in the test facility. The radiation heat transfer coefficients were approximately the same for the HAMP as for a radiant ceiling panel, however, the convection heat transfer coefficients were approximately 2 to 8 times smaller for

the HAMP, than for a radiant ceiling panel. The smaller convection heat transfer coefficients are due to the low velocity of the air used in the tests, compared to the flow rates that would be found in a space with a radiant ceiling panel.

Flow visualization photographs of the airflow through the test section will be shown in Chapter 5 to demonstrate the stable and unstable nature of the airflow during different tests. During some of the tests, it appears that the airflow may be limited to the top half or top quarter of the duct. The analysis provided to determine the convection heat transfer coefficients for forced convection is based on airflow through a rectangular duct. It may be more appropriate however, to consider the airflow as flow over a flat plate instead.

If the height of the duct was altered, this would change the cross-sectional area of the airflow, as well as the hydraulic diameter of the airflow. Table 4.3 presents these values, as well as the resulting Reynolds numbers for an airflow with a height equal to the height of the duct, a height equal to half the height of the duct and a height equal to one quarter the height of the duct. A correlation from Incropera and DeWitt (2002) for the average Nusselt number for laminar airflow over a flat plate, based on Reynolds number and Prandtl number is used to determine the convection heat transfer coefficient of the air. The correlation is given in Appendix A. Although the Nusselt number varies slightly from the value obtained for forced convection through a rectangular duct, the convection heat transfer coefficient in the air does not vary significantly. The resulting NTU_{theo} values are the same whether the convection heat transfer coefficient of the air is calculated from flat plate theory or correlations for rectangular ducts.

TABLE 4.3. NTU_{theo} based on flat plate theory.

	Height (m)		
Parameter	**0.15**	**0.08**	**0.04**
A_c [m^2]	0.035	0.017	0.009
D_h [m]	0.183	0.114	0.065
Re [-]	65	80	95
Nu_{forced} [-]	4.8	5.4	5.8
$h_{air,forced}$ [$W/m^2 \cdot K$]	0.7	0.8	0.8
NTU [-]	1.4	1.4	1.4

This section has defined some key parameters that are used in the design of a heat exchanger. These parameters are presented to give an understanding of the size and characteristics of the prototype HAMP. A HAMP however, has the ability to transfer both heat and moisture with an airflow. The following section will present some parameters that are used, in addition to NTU_{theo} and Cr to characterize the performance of a heat and moisture exchanger.

4.3 ENERGY EXCHANGER PARAMETERS

As a HAMP is designed to exchange both heat and moisture with the air in a space, a HAMP is characterized by a latent effectiveness as well as a sensible effectiveness. The latent effectiveness of an energy exchanger is defined as the actual amount of moisture transfer to the maximum possible amount of moisture transfer, and like the sensible effectiveness, can be related to two parameters,

$$\varepsilon_{latent} = f(NTU_m, Cr) \tag{4.24}$$

where NTU_m is the number of mass transfer units of the energy exchanger. In addition to NTU, NTU_m and Cr, the performance of an energy exchanger is also dependent on the temperature and

humidity ratio of the inlet streams (Simonson and Besant (1999a)). Simonson and Besant used an operating condition factor, H^* to quantify the inlet conditions. The following section will focus on the calculation of NTU_m and H^* for the prototype HAMP.

4.3.1 Number of Mass Transfer Units, NTU_m

The number of mass transfer units of an energy exchanger is defined as

$$NTU_m = \frac{U_m A_{surface}}{\dot{m}_{air}} \tag{4.25}$$

where U_m is the overall mass transfer coefficient of the exchanger [$kg_{air}/(m^2 \cdot s)$]. The overall mass transfer coefficient of an energy exchanger is used to calculate the total mass transfer rate ($\dot{m}_w$) between streams, from the equation

$$\dot{m}_w = U_m^W A_{surface} \Delta W_{lm} \tag{4.26}$$

where ΔW_{lm} is the log mean humidity ratio difference [kg_w/kg_{air}] calculated from the difference in humidity ratios between the inlet streams and the difference in humidity ratios between the outlet streams, using equation (3.13).

The superscript W on the overall mass transfer coefficient indicates that it is used to calculate the total mass transfer rate based on the humidity ratio (W) and has units of $kg_{air}/(m^2 \cdot s)$. The total mass transfer rate can also be calculated based on the change in the concentration of water vapour (X) or the change in the density of the water vapour (ρ_v). Steeman (2009) studied the effects of calculating mass transfer coefficients based on these three variables (W, X and ρ_v) and found that using the humidity ratio was the most appropriate when studying coupled heat and moisture transfer.

The overall mass transfer coefficient can be determined from a moisture resistance circuit similar to the thermal circuit shown in Figure 4.2, as

$$U^{W}_{m,theo} = \left[\frac{1}{h^{W}_{m,air}} + \frac{R_{membrane}}{\rho_{air}} + \frac{1}{h^{W}_{m,sol}} \right]^{-1} \tag{4.27}$$

where h^{W}_{m} is the convection mass transfer coefficient in the air or the liquid desiccant [kg/(m^2·s)], $R_{membrane}$ is the resistance to vapour diffusion of the semi-permeable membrane [s/m] and ρ_{air} is the density of the air [kg_{air}/m^3]. The resistance to vapour diffusion of the membrane has been reported by Larson (2006). As with the temperature, the difference in the humidity ratio across the height of the liquid desiccant channel was found to be negligible, so the resistance to moisture transfer through the liquid desiccant was negligible and could be omitted from the overall mass transfer coefficient.

The convection mass transfer coefficient in the air can be determined from the Chilton-Colburn analogy for heat and mass transfer

$$\frac{h_{conv}}{c_{p,air} h^{W}_{m,air}} = Le^{2/3} \tag{4.28}$$

where h_{conv} is the convection heat transfer coefficient of the air [W/(m^2·K)], c_p is the specific heat of air [J/(kg·K)] and Le is the Lewis number of air [-]. The Lewis number is equal to the Schmidt number divided by the Prandtl number. Table 4.4 summarizes the values used to calculate $NTU_{m,theo}$ for the test cases.

TABLE 4.4. Summary of theoretical values used to find $NTU_{m,theo}$.

Parameter	Range
$h^{W}_{m,air}$ [$kg_{air}/(m^2 \cdot s)$]	0.0008 – 0.0025
$U^{W}_{m,air}$ [$kg_{air}/(m^2 \cdot s)$]	0.0008 – 0.0019
$NTU_{m,theo}$ [-]	0.2 – 0.4

4.3.2 Operating Condition Factor, H^*

As mentioned previously, the effectiveness of an energy exchanger (with both heat and moisture transfer) is dependent on the temperature and humidity ratio of the inlet air streams. The inlet conditions for an energy exchanger can be defined by an operating condition factor (Simonson and Besant (1999a)) as

$$H^* = 2500 \frac{\Delta W}{\Delta T} \tag{4.29}$$

where ΔW is the difference in the humidity ratio of the two inlet streams [kg_w/kg_{air}] and ΔT is the difference in the temperature of the two inlet streams [°C or K]. For the case of the prototype HAMP the difference in the humidity ratio is defined as

$$\Delta W = W_{UPSTREAM} - W_{HAMP,in} \tag{4.30}$$

and the difference in the temperature is defined as

$$\Delta T = T_{UPSTREAM} - T_{HAMP,in}. \tag{4.31}$$

The operating condition factor is the ratio of the latent energy to the sensible energy at the inlet of an energy exchanger. Figure 4.3 shows a schematic of the different possible combinations of operating conditions that will exist between the HAMP and the upstream air and the direction of the heat and mass transfer under each set of conditions. The top left schematic is a case of

cooling and humidification and the bottom right is a case of heating and dehumidification. In these two cases, the heat transfer is in the opposite direction as the mass transfer, resulting in a negative H^* value. The top right schematic is a case of heating and humidification and the bottom left is a case of cooling and dehumidification. In these two cases, the heat transfer is in the same direction as the mass transfer, resulting in a positive H^* value.

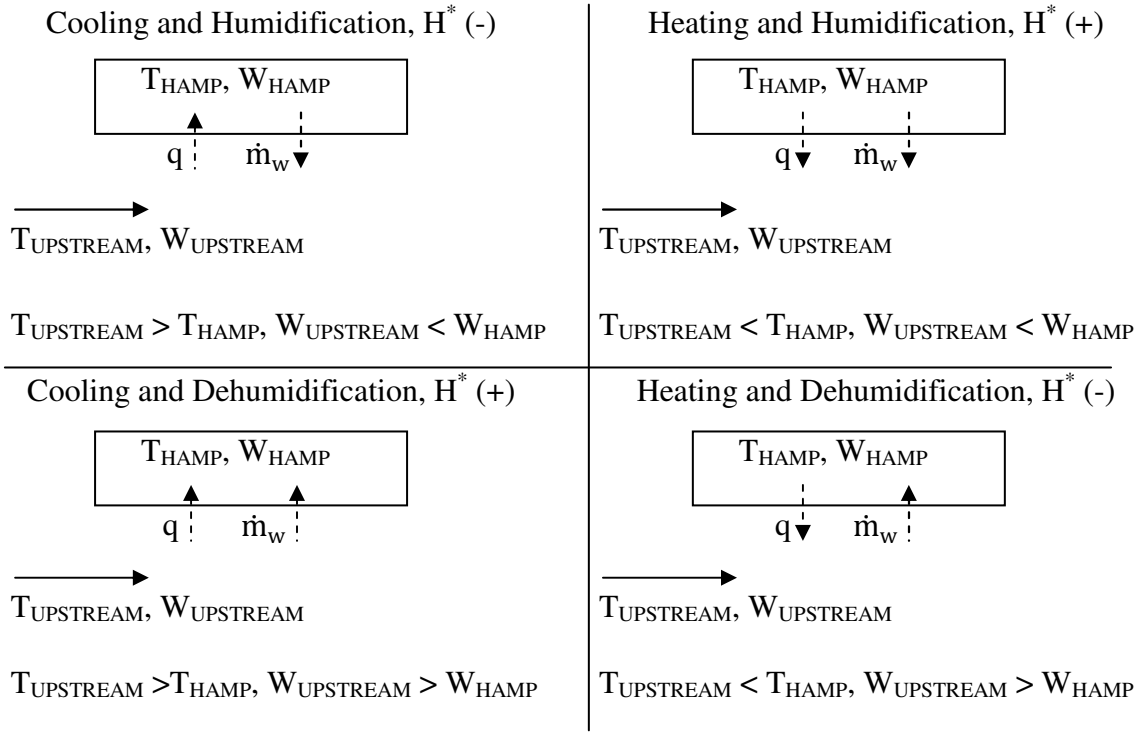

FIGURE 4.3. Schematic showing the operating conditions that create a (+) or (-) H^*.

The magnitude of H^* depends on the relative magnitude of each type of transfer. If the magnitude of the mass transfer is approximately the same as the magnitude of the heat transfer, H^* will be close to one. If the magnitude of the mass transfer is small compared to the heat transfer, H^* will be close to zero. On the other hand, if the magnitude of the mass transfer is large compared to the heat transfer, H^* will be very large. Theoretically, the value of H^* can vary

from negative infinity to positive infinity, but Simonson and Besant (1999a) suggest the typical range for an energy wheel used in HVAC applications is -6 to +6.

Figure 4.4 shows how the operating condition factor varies with the temperature and humidity ratio of the liquid desiccant, for an upstream air temperature of 24°C and a relative humidity of 50% RH (W = 9.3 g_w/kg_{air}). An H^* value of zero corresponds to the horizontal line of constant humidity ratio ($\Delta W = 0$). Moving clockwise from this line is the region of negative H^* values, approaching negative infinity along the vertical line of constant temperature ($\Delta T = 0$). Moving counter-clockwise from the horizontal line is the region of positive H^* values, approaching positive infinity along the vertical line of constant temperature. The line of $H^* = -1$ falls on the line of constant enthalpy, meaning that the enthalpy of the upstream air is the same as the enthalpy of the liquid desiccant for this condition.

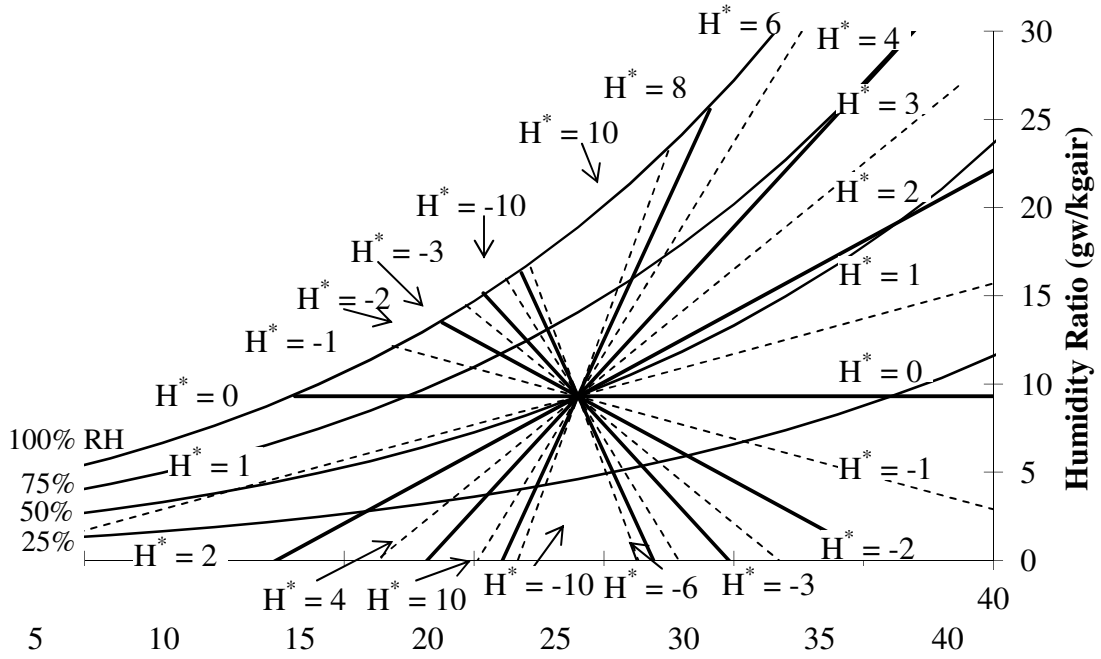

FIGURE 4.4. Operating condition factor (H^*) for upstream air conditions of 24°C and 50% RH and different liquid desiccant conditions.

The schematic shown in Figure 4.3 to illustrate the conditions which generate positive or negative H^* values is oriented in the same manner as Figure 4.4. The top left quadrant is the area where the HAMP would be used for cooling and humidification, the bottom right quadrant is the area where the HAMP would be used for heating and dehumidification, both resulting in negative H^* values. The top right quadrant is the area where the HAMP would be used for heating and humidification, the bottom left quadrant is the area where the HAMP would be used for cooling and dehumidification, both resulting in positive H^* values.

4.4 SUMMARY

In this chapter, the test conditions used to create different combinations of cooling, heating, dehumidification and humidification have been presented, along with important design

parameters of an energy exchanger. The ranges of each parameter are summarized in Table 4.5 for the 83 tests presented in this thesis. The design parameters, NTU and $NTU_{m,}$ have been calculated theoretically from heat transfer correlations and a heat and mass transfer analogy, as would typically be done when designing a new exchanger. These parameters, along with the operating condition factor, H^* are presented in Chapter 5 for each test case discussed and used in Chapter 6 in the discussion of how to predict the performance of a HAMP.

TABLE 4.5. Summary of test conditions and design parameters.

Parameter	**Range**	**Parameter**	**Range**
$T_{UPSTREAM}$ [°C]	20 – 25	Nu [-]	5.4 – 12.6
$W_{UPSTREAM}$ [g_w/kg_{air}]	0.5 – 16	h_r [$W/m^2 \cdot K$]	5.4 – 6.4
T_{HAMP} [°C]	6 – 35	h_{conv} [$W/m^2 \cdot K$]	0.8 – 2.2
W_{HAMP} [g_w/kg_{air}]	2 – 28	$h_{eff,air}$ [$W/m^2 \cdot K$]	6.7 – 7.6
$\dot{m}_{sol}$ [kg_{sol}/s]	0.013	NTU_{theo} [-]	1.4 – 1.6
$\dot{m}_{air}$ [kg_{air}/s]	0.0002	$h^W_{m,air}$ [$kg_{air}/(m^2 \cdot s)$]	0.0008 – 0.0025
Cr [-]	0.006	$NTU_{m,theo}$ [-]	0.2 – 0.4
Re_{air} [-]	65	H^* [-]	-100 - 80
Ra^+ [-]	$-42x10^5 – 65x10^5$		

CHAPTER 5 – PERFORMANCE OF THE PROTOTYPE HAMP

One of the main objectives of this thesis is to determine the performance of a prototype HAMP under different operating conditions. The performance of an energy exchanger is quantified by its sensible and latent effectivenesses. In this chapter, the sensible and latent effectivenesses of the prototype HAMP are presented for different operating conditions, including cases of: cooling and dehumidification, cooling and humidification, heating and humidification, heating and dehumidification, humidification, and dehumidification. In addition, the effects of buoyancy forces acting in the test section on the performance of the prototype HAMP are discussed. Cases of stable laminar airflow and unstable laminar airflow are highlighted using flow visualization. Finally, as another measure of performance, the total heat and mass fluxes between the HAMP and the air are presented for different panel temperatures and humidity ratios.

5.1 PERFORMANCE OF THE HAMP IN DIFFERENT MODES

In an actual building, a HAMP would be required to humidify or dehumidify a space, while simultaneously heating or cooling. There may also be times when only humidification or dehumidification are needed, with no heating or cooling. This section will discuss the results of six tests to show the performance of the HAMP in different modes under well controlled conditions and to demonstrate how the HAMP works during these different modes. The operating modes investigated are combinations of heating, cooling, dehumidification and humidification. In addition to these situations, a HAMP could also be used for heating or

cooling only, with no humidification or dehumidification, however, the focus of this study is on the ability of the prototype HAMP to transfer moisture, so these cases are not considered[§].

The operating conditions of the six tests are presented in Table 5.1. Each test is given a number (1 through 6), for easy reference to the full set of data presented in Appendix D. The upstream air is kept at approximately 24°C and the upstream air relative humidity varies between ~70% RH (~14 g_w/kg_{air}) for the dehumidification cases and ~10% RH (~2 g_w/kg_{air}) for the humidification tests. The temperature of the HAMP is set to approximately 14°C for cooling cases, 34°C for heating cases and 24°C for the humidification and dehumidification cases. The concentration of the salt solution was 35% for the dehumidification cases and 24% for the humidification cases, resulting in a relative humidity of ~30% RH and ~60% RH, respectively. The humidity ratio inside the HAMP varies for each test, based on the temperature and concentration of the salt solution.

[§] The results of these six tests and the flow visualization presented in Sections 5.3 and 5.4 were presented by M. Fauchoux at the 14th International Heat Transfer Conference in Washington, D.C., and published in the conference proceedings. The reference is Fauchoux, M.T., C.J. Simonson and D.A. Torvi, 2010. Flow visualization of airflow through a rectangular duct with combined heat and mass transfer, Proceedings of the ASME 14th International Heat Transfer Conference, Washington, D.C., USA, August 8-13.

TABLE 5.1. Upstream air and HAMP conditions for six samples tests to show the performance of the prototype HAMP under different conditions.

		UPSTREAM AIR			HAMP		
		T	**RH**	**W**	**T**	**RH**	**W**
TEST	**#**	**[°C]**	**[%]**	**[g_w/kg_{air}]**	**[°C]**	**[%]**	**[g_w/kg_{air}]**
Cooling, dehumidification	1	23.6	73.4	14.2	13.9	30.2	3.0
Cooling, humidification	2	24.2	10.1	2.0	14.3	60.1	6.1
Heating, dehumidification	3	24.3	68.1	13.7	33.8	29.7	9.8
Heating, humidification	4	24.3	10.1	2.0	33.9	59.7	20.0
Dehumidification	5	24.1	69.8	13.9	24.6	30.0	5.7
Humidification	6	24.0	10.4	2.0	24.3	59.9	11.4

The Rayleigh numbers for heat transfer and for mass transfer, along with the effective Rayleigh number for these six cases are presented in Table 5.2. The Rayleigh numbers show the magnitude and direction of the temperature (heat) and concentration (moisture) density gradients. As discussed in Chapter 4, cooling and dehumidification both result in positive density gradients, while heating and humidification both result in negative density gradients. The two cooling cases and the case of dehumidification only, have a positive effective Rayleigh number, so buoyancy forces will be present during these tests and natural convection will be dominant in the duct. During the two heating cases and the case of humidification only, the buoyancy forces will be negligible and forced convection will be dominant in the duct.

The energy exchanger parameters introduced in Chapter 4 are also shown in Table 5.2 for these six tests. NTU_{theo}, $NTU_{m,theo}$ and Cr are approximately the same for all six tests. The values of H^* are positive when the heat and mass transfer are in the same direction and negative when the

heat and mass transfer are in opposite directions. The cases of dehumidification only and humidification only, have very large H^* values, due to the small difference in the inlet temperatures.

TABLE 5.2. Dimensionless numbers and energy exchanger parameters for six samples tests to show the performance of the prototype HAMP under different conditions.

TEST	Ra_h [x10^5]	Ra_m [x10^5]	Ra^+ [x10^5]	Cr [-]	NTU_{theo} [-]	$NTU_{m,theo}$ [-]	H^* [-]
Cooling, dehumidification	33	4	37	0.006	1.6	0.36	3
Cooling, humidification	33	-2	31	0.005	1.6	0.36	-1
Heating, dehumidification	-29	2	-27	0.006	1.5	0.17	-1
Heating, humidification	-30	-8	-38	0.005	1.5	0.17	5
Dehumidification	-1	3	2	0.006	1.5	0.22	-100
Humidification	-1	-5	-6	0.005	1.4	0.17	80

The downstream air conditions are presented in Table 5.3, along with the sensible, latent and total effectivenesses of the prototype HAMP for each of these six tests. The uncertainty in each effectiveness is also presented. The sensible and latent effectivenesses are higher in the two cooling cases, than in the two heating cases. As well, the latent effectiveness is higher in the dehumidification case than in the humidification case. This is due to the presence of strong buoyancy forces in the test section during the two cooling cases and the dehumidification case. The buoyancy forces cause the airflow to become unstable, resulting in better mixing of the air and therefore higher effectivenesses. During the two heating cases and the humidification case, the airflow remains stable through the test section and the convection heat transfer coefficient is

lower, resulting in lower effectivenesses. This will be demonstrated in Sections 5.3 and 5.4 using flow visualization photographs.

TABLE 5.3. Downstream air and effectiveness results for six samples tests to show the performance of the prototype HAMP under different conditions.

	DOWNSTREAM AIR					
	T	RH	W	$\varepsilon_{sensible}$	ε_{latent}	ε_{total}
TEST	[°C]	[% RH]	[g_w/kg_{air}]	[%]	[%]	[%]
1. Cooling, dehumid	22.4	49.5	8.8	12 ± 5	48 ± 3	39 ± 3
2. Cooling, humid	22.6	21.5	3.9	16 ± 5	46 ± 5	--
3. Heating, dehumid	24.9	61.4	12.8	6 ± 5	23 ± 7	--
4. Heating, humid	24.7	33.4	6.8	4 ± 5	27 ± 2	23 ± 2
5. Dehumidification	24.7	55.4	11.4	--	30 ± 6	28 ± 6
6. Humidification	24.0	23.3	4.5	--	26 ± 3	25 ± 3

The sensible effectiveness of the HAMP is not shown for the dehumidification only and humidification only cases because the value is greater than 100% for the dehumidification case and extremely small for the humidification case. The dehumidification case can be explained by referring to the diagram in the lower right corner of Figure 4.3, which is reprinted in Figure 5.1 below. The upstream air temperature is 24.1°C and the average HAMP temperature is 24.6°C, which means there is a small amount of heat transfer from the HAMP to the airflow, as indicated in the schematic. The upstream air humidity ratio is 14 g_w/kg_{air} and the HAMP humidity ratio is 6 g_w/kg_{air}, which means the moisture transfer will be into the HAMP, as indicated in the schematic. As the water vapour enters the HAMP, it changes into liquid water. The process of the phase change from vapour to liquid gives off heat, causing the temperature of the HAMP to

increase. This creates a larger temperature difference between the HAMP and the upstream air than would be present if there was no moisture transfer. The temperature of the liquid desiccant increases from 24.4°C to 24.8°C, as shown in Figure 5.1. As a result, the downstream air temperature can be heated more when there is simultaneous heat and mass transfer, resulting in a sensible effectiveness value over 100%.

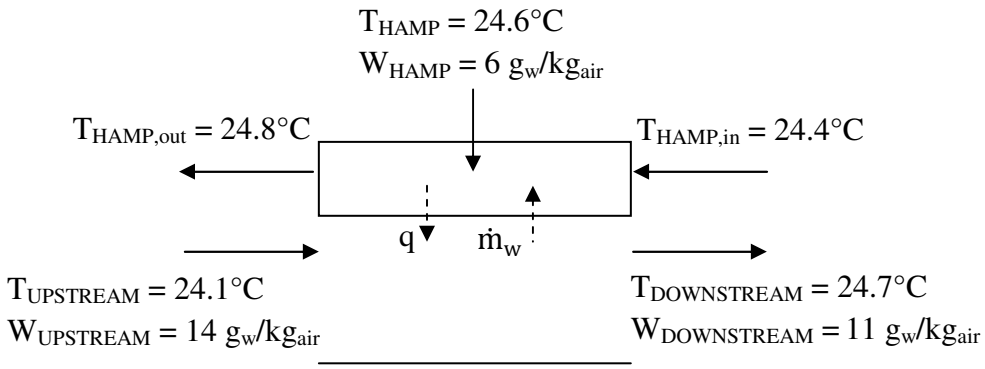

FIGURE 5.1. The direction of heat and mass transfer in a case of heating and dehumidification.

The negligible sensible effectiveness for the humidification only case can be explained in a similar manner as for the dehumidification only case. In the humidification case, the heat and mass transfer are in the same direction, from the HAMP into the airflow. In this case, the phase change is from liquid water to water vapour, inside the HAMP. This phase change requires heat input, leaving the temperature of the HAMP slightly cooler than if there was no moisture transfer present. In this case, the temperature of the HAMP decreases from 24.5°C at the inlet to 24.1°C at the outlet. The difference in temperature between the upstream air and the HAMP becomes smaller during the test, which results in a smaller increase in the downstream air temperature than if there was no moisture transfer present and subsequently a smaller sensible effectiveness. Since the difference in temperatures is small to begin with in this case, this effect causes the sensible effectiveness to be negligible.

The total effectiveness of the HAMP is also presented in Table 5.3 for all cases except for the case of cooling and humidification and the case of heating and dehumidification. In both of these cases the total effectiveness is greater than 100%. This can be explained by looking at H^*, which approaches -1 in both cases. Referring back to Figure 4.4 where different values of H^* were presented on a psychrometric chart, the value of H^* equal to -1 falls on a line of constant enthalpy, indicating that the enthalpy of the upstream air and the HAMP are essentially the same. The total effectiveness of an energy exchanger is calculated from the difference in enthalpy between the upstream air and downstream air divided by the difference in enthalpy between the upstream air and HAMP. If the difference in enthalpy between the upstream air and HAMP is close to zero, the total effectiveness will be a very large number, which is the result in the two cases described.

It can be seen from comparing the effectivenesses of the HAMP for these six cases that the HAMP performs the best under cooling and dehumidification tests. This is due to the presence of buoyancy forces and the resulting instability of the airflow which increases the convection heat transfer coefficient and therefore the effectivenesses of the HAMP. The next section will look at seven more experiments that were compared to a numerical model that did not include buoyancy forces to confirm the importance of buoyancy forces on the effectiveness of the HAMP.

5.2 IMPORTANCE OF BUOYANCY FORCES

A numerical simulation was performed by Mohit Bansal, an M.Sc. student at the Indian Institute of Technology Delhi,[**] to compare with the data collected during seven tests, again representing different operating modes of the HAMP. These seven tests are different than the six tests presented in Section 5.1. The model (presented in Appendix F) simulated heat and moisture transfer between the HAMP and air, but did not include buoyancy forces in the test section. The inputs to the program were the upstream air temperature and relative humidity, and the HAMP temperature and relative humidity from the experiments, as well as the air flow rate and properties of the membrane and the outputs of the program were the latent effectiveness and change in humidity ratio of the air.

The operating conditions for the seven tests are presented in Table 5.4, along with a description of the test conditions for each test. The tests run included two humidification tests, a dehumidification test, a cooling and dehumidification test and a heating and humidification test. In addition, there was a cooling and dehumidification test and a cooling and dehumidification test performed with the prototype HAMP in the bottom of the test section, acting as a floor panel. The floor panel tests are marked with an asterisk. Again each test is given a number, for easy reference to the full set of data in Appendix D. The ceiling panel tests are numbered 7 through 11 and the floor panel tests as 71 and 72.

[**] The results of these experiments and comparison to the numerical simulation were published under the reference: Fauchoux, M., M. Bansal, P. Talukdar, C.J. Simonson and D. Torvi, 2010. Testing and modeling of a novel ceiling panel for maintaining space relative humidity by moisture transfer, *International Journal of Heat and Mass Transfer*, **53**, 3961-3968.

TABLE 5.4. Operating conditions for a comparison between experimental data and numerical simulation without buoyancy forces.

		UPSTREAM AIR		HAMP	
		T	W	T	W
TEST	**#**	**[°C]**	**[g_w/kg_{air}]**	**[°C]**	**[g_w/kg_{air}]**
Humidification	7	23.1	2.6	21.3	16.9
Humidification	8	22.7	2.6	24.2	5.9
Dehumidification	9	22.6	11.6	24.2	5.9
Cooling, dehumidification	10	21.6	10.2	12.1	2.7
Heating, humidification	11	22.8	2.0	35.3	11.0
Cooling, dehumidification*	71	21.9	11.4	12.0	2.7
Heating, humidification*	72	23.2	4.1	35.2	10.9

* The last two cases were performed with the prototype HAMP in the floor of the test section.

Table 5.5 presents the effective Rayleigh numbers for the seven test cases. The overall density gradient is positive in cases 10 and 72, and negative in the remainder of the cases. This indicates that buoyancy forces are dominant during cases 10 and 72, whereas the remainder of the cases are forced convection cases. Although there is a positive concentration gradient in the dehumidification case there is also a slight temperature difference between the upstream air and the HAMP, which results in a negative temperature gradient and an overall negative density gradient. The change in humidity ratio through the air ($W_{DOWNSTREAM} - W_{UPSTREAM}$) and the latent effectiveness of the HAMP are presented for the experiments and for the numerical simulations. The results agree within experimental uncertainty for all cases, except cases 10 and 72.

TABLE 5.5. Results of the comparison between experimental data and numerical simulation without buoyancy forces.

			Experimental		Numerical	
		Ra^+	ΔW	ε_{latent}	ΔW	ε_{latent}
TEST	**#**	**[x10^5]**	**[g_w/kg_{air}]**	**[%]**	**[g_w/kg_{air}]**	**[%]**
Humidification	7	-2	2.6	19	2.2	16
Humidification	8	-6	0.5	15	0.5	15
Dehumidification	9	-1	-1.5	25	-1.4	23
Cooling, dehumidification	10	38	-2.0	27	-1.3	17
Heating, humidification	11	-42	1.5	15	1.4	14
Cooling, dehumidification*	71	-36	-2.4	28	-2.1	25
Heating, humidification*	72	38	2.4	28	1.4	16

* The last two cases were performed with the prototype HAMP in the floor of the test section.

Comparisons between the experimental results and the numerical results are presented in Figure 5.2 for the change in humidity ratio of the air and in Figure 5.3 for the latent effectiveness of the prototype HAMP. The uncertainty of the experimental values is also shown for each case. Again, it is clear that the numerical simulation and the experiments agree within experimental uncertainty for all cases, except cases 10 and 72. In cases 10 and 72, the model under-predicts the change in humidity ratio and the latent effectiveness, compared to the experimental results. The poor agreement between experimental and numerical results for cases 10 and 72 is due to the fact that the buoyancy forces are not accounted for in this model. The presence of buoyancy forces in the duct causes better mixing of the air in the test section and increases the amount of heat and moisture transferred between the HAMP and the air, therefore increasing the change in humidity ratio and the latent effectiveness.

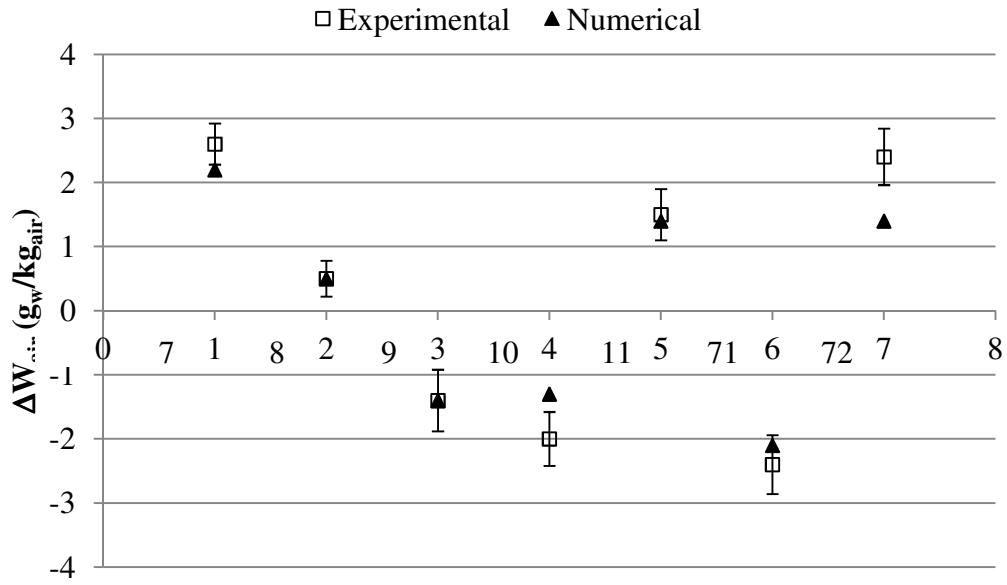

FIGURE 5.2. Comparison of change in humidity ratio across the airflow from experiments and numerical simulations without buoyancy effects.

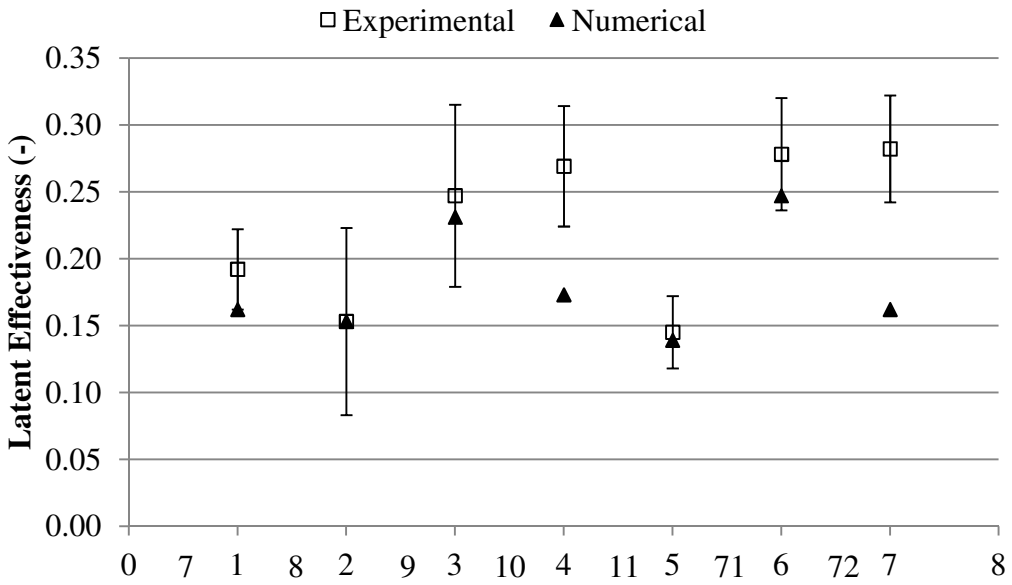

FIGURE 5.3. Comparison of latent effectiveness from experiments and numerical simulations without buoyancy effects.

The results shown in Figures 5.2 and 5.3 show that buoyancy forces can have a strong impact on the moisture transfer and on the latent effectiveness of the HAMP. In order to better understand

the effects of the buoyancy forces on the performance of the HAMP, flow visualization photographs were taken during different operating modes, to actually see when natural convection is dominant in the duct.

5.3 FLOW VISUALIZATION OF STABLE LAMINAR AIRFLOW

In a stable laminar airflow, the heat transfer between the HAMP and the air is dominated by forced convection. This occurs when the effective Rayleigh number is negative or when it falls below the critical Rayleigh number of the test section (~+3000, Raithby and Hollands (1985)). Table 5.6 presents the operating conditions and design parameters used for the heating and humidifying case (case 4) presented in Section 5.1, as representative of a stable airflow case.

TABLE 5.6. Operating conditions and design parameters for a stable laminar airflow case, Re = 65 (heating and humidifying, case 4).

Parameter	Value	Parameter	Value
$T_{UPSTREAM}$ [°C]	24.3	Ra_h [-]	-30×10^5
$RH_{UPSTREAM}$ [% RH]	10.1	Ra_m [-]	-8×10^5
$W_{UPSTREAM}$ [g_w/kg_{air}]	2.0	Ra^+ [-]	-38×10^5
T_{HAMP} [°C]	33.9	NTU_{theo} [-]	1.5
RH_{HAMP} [% RH]	59.7	$NTU_{m,theo}$ [-]	0.2
W_{HAMP} [g_w/kg_{air}]	20.0	Cr [-]	0.005
C_{salt} [%]	24.5	H^* [-]	5

The operating conditions and the resulting downstream air conditions for the heating and humidifying case are shown on a psychrometric chart in Figure 5.4. In this test, there is a large driving potential for both heat and moisture transfer. It can be seen however, that the

downstream air conditions (T = 24.7°C, W = 6.8 g_w/kg_{air}) are much closer to the upstream air conditions than the HAMP conditions, indicating that the sensible and latent effectivenesses are small for this test. The measured sensible effectiveness is 4% and the latent effectiveness is 27%.

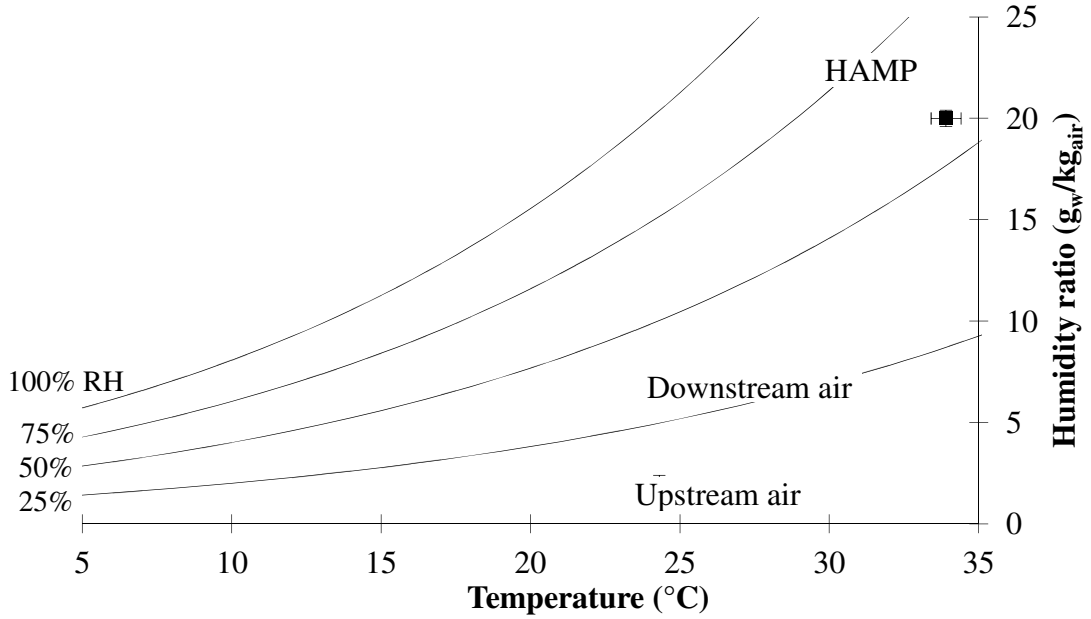

FIGURE 5.4. Upstream, downstream and HAMP test conditions for a stable laminar airflow case, Re = 65 (case 4).

In this test, the heat transfer Rayleigh number is $-30x10^5$ and the mass transfer Rayleigh number is $-8x10^5$ which results in an effective Rayleigh number of $-38x10^5$. Figure 5.5 includes flow visualization photographs of the airflow through the test section for this stable airflow case. The prototype HAMP is located at the top of the photograph, as indicated. The photographs shown in Figure 5.5 were taken at intervals of 8 s. In each photograph, the airflow enters on the left and continues as laminar boundary layer flow through the length of the test section. The flow does

not change from one picture to the next, indicating that the laminar flow is maintained throughout the length of the test.

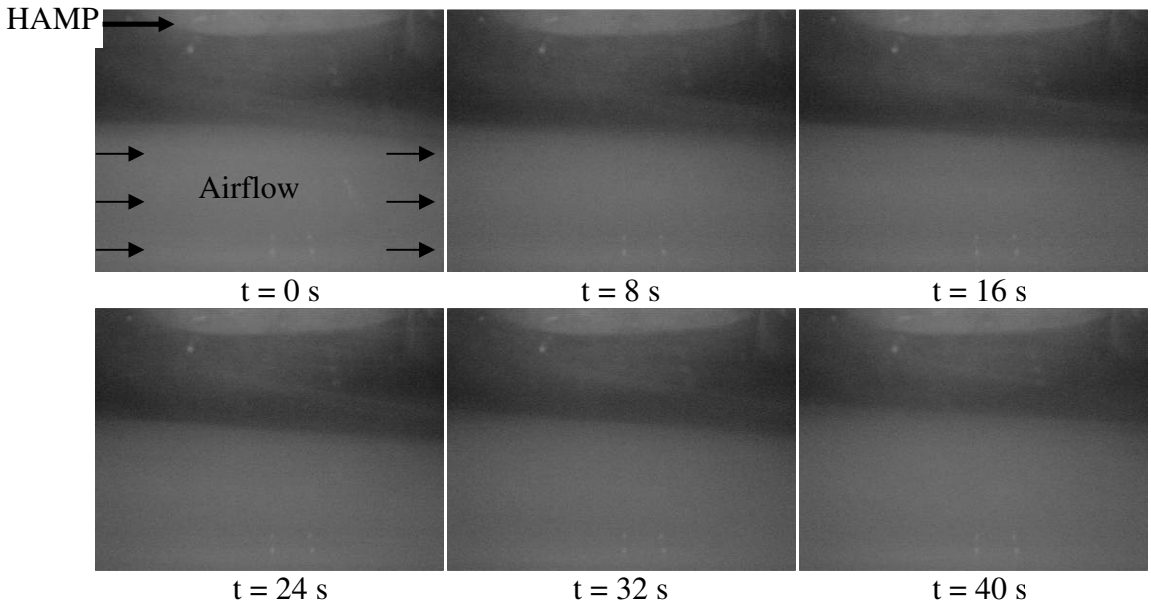

FIGURE 5.5. Visualization of stable laminar airflow through the test section ($Ra^{+} = -38x10^{5}$, $T_{UPSTREAM} = 24°C$, $RH_{UPSTREAM} = 10\%$ RH, $W_{UPSTREAM} = 2\ g_w/kg_{air}$, $T_{HAMP} = 34°C$, $RH_{HAMP} = 60\%$ RH, $W_{HAMP} = 20\ g_w/kg_{air}$, $NTU_{theo} = 1.5$, $NTU_{m,theo} = 0.2$, $H^{*} = 5$, $Cr \approx 0$, $Re = 65$, case 4).

A computational fluid dynamics (CFD) simulation of this experiment was done by Prabal Talukdar, of the Indian Institute of Technology Delhi, to compare to the flow visualization photographs taken during the experiments[††]. The CFD model, developed by Talukdar, is presented in more detail in Appendix F, includes the effects of buoyancy. The operating conditions from the experiments were input into the model. Figure 5.6 shows the results of the model for the stable airflow case. The area shown in Figure 5.6 is the same view as the flow

[††] A comparison of the numerical simulations and the flow visualization was presented by M. Fauchoux at the 8th Thermal Engineering Joint Conference in Honolulu, HI and was published in the conference proceedings. The reference is Fauchoux, M.T, C.J. Simonson, D.A. Torvi, P. Talukdar, 2011. CFD Modeling with buoyancy effects for a heat and moisture transfer ceiling panel, Proceedings of the ASME/JSME 8th Thermal Engineering Joint Conference, Honolulu, HI, USA, March 13-17.

visualization photographs shown in Figure 5.5. The arrows represent streamlines, showing how the air flows through the duct. The streamlines show that the airflow remains stable throughout the test section, as was seen in the flow visualization photographs.

The temperature at different places in the duct is also output from the CFD simulation. The shading of the background indicates the variation of temperature across the height of the test section. The top of the duct is warmest, because of the heat added by the HAMP. The bottom of the duct is coolest because the airflow is moving straight through the duct and not mixing with the warmer air at the top of the test section. The temperature in most of the test section remains cool, explaining the low sensible effectiveness values for stable airflow cases.

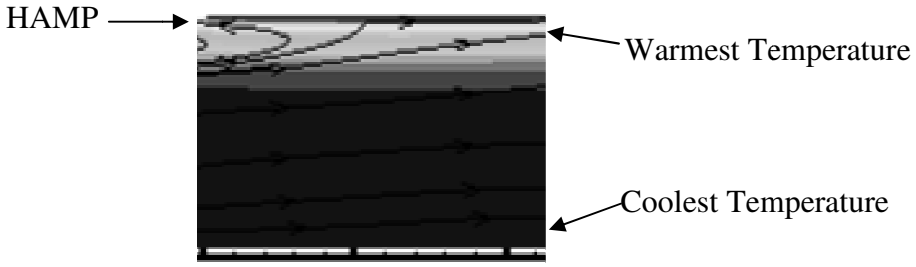

FIGURE 5.6. CFD simulation of streamlines and temperature gradient for stable laminar airflow through the test section at t = 40 s, where the light color background is the warmest temperature and the darker color background is the coolest temperature (Re = 65, $Ra^{+} = -38x10^{5}$).

The case described in this section is representative of all the stable airflow cases. The actual values of the sensible and latent effectivenesses will vary from one test to another (depending on NTU, NTU_m and H^*), but are lower in these cases than in the unstable airflow cases, which will be presented in Section 5.4. This indicates that using a HAMP in a ceiling panel configuration is not ideal for heating or humidifying the air below it. Future work on the HAMP could include

investigating ways of increasing the effectivenesses during heating and humidification situations by increasing the convection heat transfer between the panel and the air.

5.4 FLOW VISUALIZATION OF UNSTABLE LAMINAR AIRFLOW

When the buoyancy forces caused by a density gradient in the test section become large enough ($Ra^+ > \sim 3000$, Raithby and Hollands (1985)), natural convection dominates the airflow and the airflow becomes unstable. Table 5.7 presents the operating conditions and design parameters for an unstable laminar airflow case (the case of cooling and dehumidifying discussed in Section 5.1, case 1).

TABLE 5.7. Operating conditions and design parameters for an unstable laminar airflow case with Re = 65 (cooling and dehumidification, case 1).

Parameter	Value	Parameter	Value
$T_{UPSTREAM}$ [°C]	23.6	Ra_h [-]	$33x10^5$
$RH_{UPSTREAM}$ [% RH]	73.4	Ra_m [-]	$4x10^5$
$W_{UPSTREAM}$ [g_w/kg_{air}]	14.2	Ra^+ [-]	$37x10^5$
T_{HAMP} [°C]	13.9	NTU_{theo} [-]	1.6
RH_{HAMP} [% RH]	30.2	$NTU_{m,theo}$ [-]	0.4
W_{HAMP} [g_w/kg_{air}]	3.0	Cr [-]	0.006
C_{salt} [%]	35.3	H^* [-]	3

The operating conditions and resulting downstream air conditions for the case of cooling and dehumidifying are shown on a psychrometric chart in Figure 5.7. In this case, the difference between the downstream air conditions and the upstream air conditions is larger than in the stable airflow case presented in Section 5.3, indicating that the sensible and latent effectivenesses of the

HAMP are higher during this unstable case than the stable case. In this test, the sensible effectiveness is 12% and the latent effectiveness is 48%.

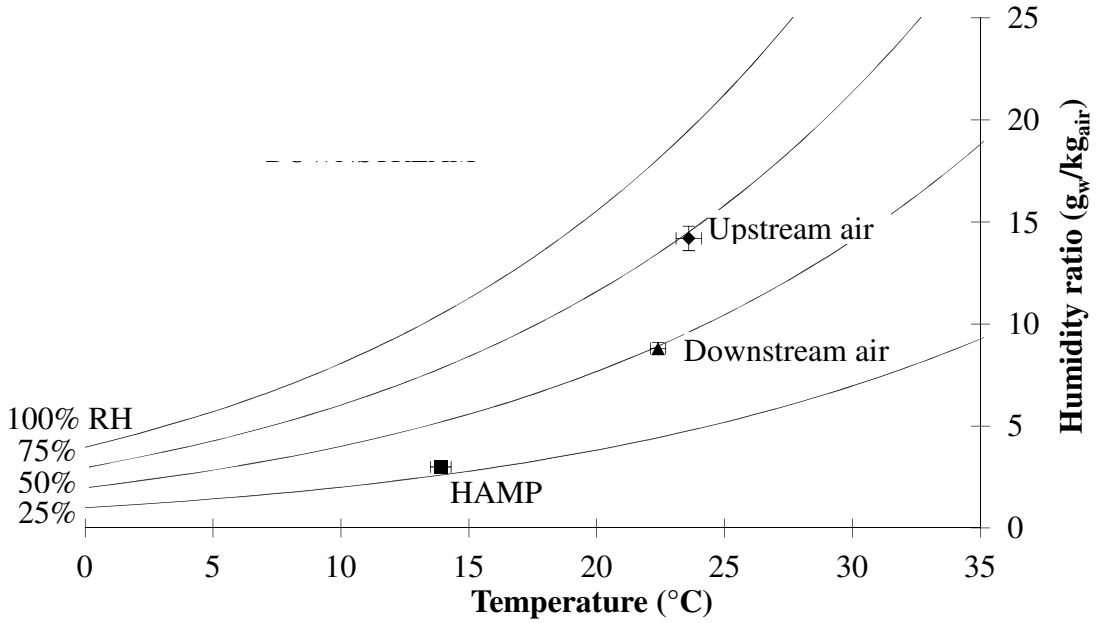

FIGURE 5.7. Upstream, downstream and HAMP test conditions for an unstable laminar airflow case, Re = 65 (case 1).

For this unstable airflow test, the heat transfer Rayleigh number is $33x10^5$ and the mass transfer Rayleigh number is $4x10^5$ resulting in an effective Rayleigh number of $37x10^5$. Figure 5.8 shows the flow visualization photographs for the unstable airflow test. The prototype HAMP is located at the top of the photograph, as indicated and the airflow in the test section is highlighted with arrows. The air enters on the left, at the top of the test section and passes along the surface of the HAMP. In the first couple of photographs the airflow begins to form a convection roll cell. At approximately t = 40 s the circulating airflow has filled the whole test section. During unstable airflow, there is enhanced mixing of the air in the test section, resulting in more heat and moisture transfer and therefore higher effectivenesses.

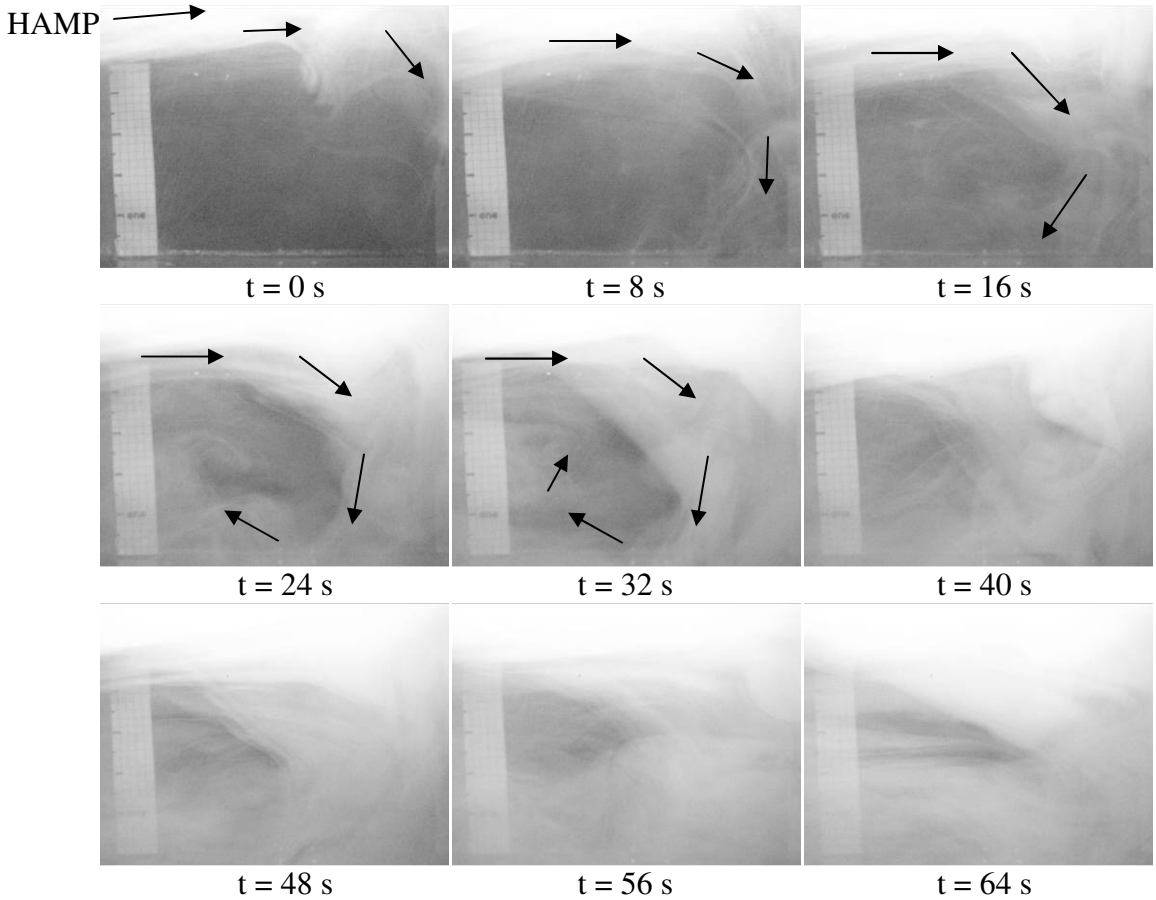

FIGURE 5.8. Visualization of unstable laminar airflow through the test section ($Ra^{+} = 37x10^{5}$, $T_{UPSTREAM} = 24°C$, $RH_{UPSTREAM} = 73\%$ RH, $W_{UPSTREAM} = 14\ g_w/kg_{air}$, $T_{HAMP} = 14°C$, $RH_{HAMP} = 30\%$ RH, $W_{HAMP} = 3\ g_w/kg_{air}$ $NTU_{theo} = 1.6$, $NTU_{m,theo} = 0.4$, $H^{*} = 3$, Cr ≈ 0, Re = 65, case 1).

The results of the CFD simulation of the airflow through the test section with unstable airflow is shown in Figure 5.9. This simulation was also performed by Talukdar (Fauchoux et al. (2011)). The arrows show the streamlines of the air and the different colors in the background show the temperature gradient through the test section. The air enters the test section in the upper left corner and passes along the surface of the HAMP. In this simulation, two convection roll cells

can be seen, one on the left and one on the right. The two rolls cells rotate in opposite directions. In this test, the HAMP is at the lowest temperature, indicated by the light color of the background. The area on the top left side, where the air enters the test section is at the warmest temperature.

FIGURE 5.9. CFD simulation of streamlines and temperature gradient for unstable laminar airflow through the test section at t = 40 s, where the light color background is the coolest temperature and the darker color is the warmest temperature (Re = 65, $Ra^{+} = 37x10^{5}$).

The unstable case presented is one of cooling and dehumidifying, where both the temperature and concentration gradients act in the same direction and therefore create a larger overall density gradient in the same direction. The airflow through the test section consists of convection roll cells, which cause enhanced mixing of the air and therefore increase the sensible and latent effectivenesses of the HAMP. These results show that the prototype HAMP performs better under unstable airflow conditions.

5.5 FLOW VISUALIZATION OF A STABLE COOLING CASE

The two cases presented in Sections 5.3 and 5.4 both involved temperature and concentration gradients acting in the same direction in the test section. A case of cooling and humidifying is a case where the temperature and concentration gradients are acting in opposite directions. For the majority of the tests run, the temperature gradient dominates the concentration gradient, so any

case of cooling is typically a case of unstable airflow. One test, however, was performed to see if a cooling case could be made stable by creating a large concentration gradient acting in the opposite direction as the temperature gradient. This test is case 12 in Appendix D.

For this test, water was used in the HAMP to create the largest possible negative concentration gradient. The temperature of the HAMP was set to 23.3°C to create a small positive temperature gradient. The heat transfer Rayleigh number for this case was $4.4x10^5$ while the mass transfer Rayleigh number was $-7.6x10^5$, resulting in an effective Rayleigh number of $-3.2x10^5$. The operating conditions and design parameters are presented in Table 5.8 for this test.

TABLE 5.8. Operating conditions and design parameters for a stable cooling case, Re = 65 (cooling and humidifying, case 12).

Parameter	**Value**	**Parameter**	**Value**
$T_{UPSTREAM}$ [°C]	25.0	Ra_h [-]	$4.4x10^5$
$RH_{UPSTREAM}$ [% RH]	11.7	Ra_m [-]	$-7.6x10^5$
$W_{UPSTREAM}$ [g_w/kg_{air}]	2.4	Ra^+ [-]	$-3.2x10^5$
T_{HAMP} [°C]	23.3	NTU_{theo} [-]	1.4
RH_{HAMP} [% RH]	100	$NTU_{m,theo}$ [-]	0.2
W_{HAMP} [g_w/kg_{air}]	19.1	Cr [-]	0.006
C_{salt} [%]	0	H^* [-]	-23

The operating conditions and resulting downstream conditions for the stable cooling case are shown on a psychrometric chart in Figure 5.10. The downstream air conditions are very close to the upstream air conditions, similar to the stable airflow case presented in Section 5.3. The sensible effectiveness in this case is 44% and the latent effectiveness is 21%.

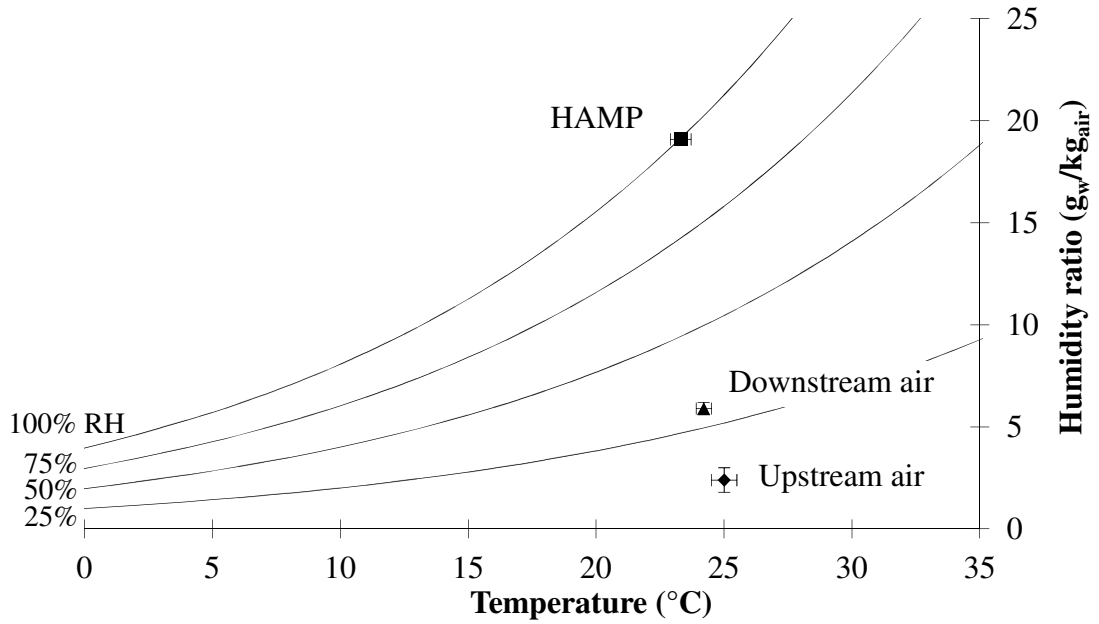

FIGURE 5.10. Upstream, downstream and HAMP test conditions for a stable cooling case Re = 65 (case 12).

The flow visualization photographs from this test are presented in Figure 5.11 at intervals of 8 s. As with the stable airflow case, the airflow is seen to enter on the left and maintains laminar boundary layer flow through the length of the test section. The photographs show that the airflow is not changing with time, but remains stable throughout the test.

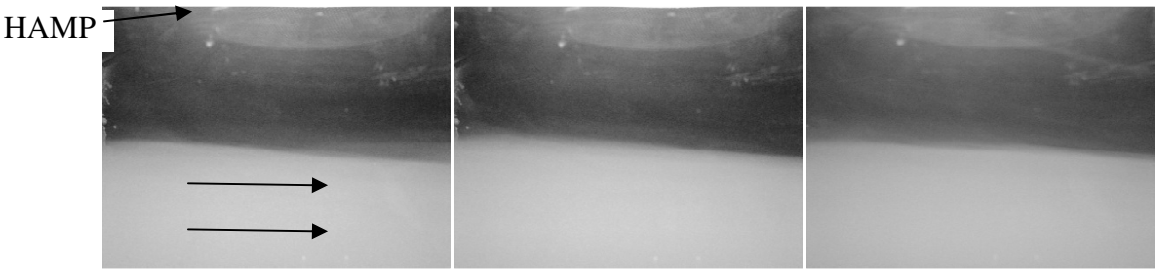

FIGURE 5.11. Visualization of stable laminar airflow during a cooling test (Ra^{+} = -3.2x10^{5}, $T_{UPSTREAM}$ = 25°C, $RH_{UPSTREAM}$ = 12% RH, $W_{UPSTREAM}$ = 2 g_w/kg_{air}, T_{HAMP} = 23°C, RH_{HAMP} = 100% RH, W_{HAMP} = 19 g_w/kg_{air}, NTU_{theo} = 1.4, $NTU_{m,theo}$ = 0.2, H^{*} = -23, Cr ≈ 0, Re = 65, case 12).

From a design point of view, it is not ideal to make an unstable airflow case into a stable airflow case, as the effectiveness of the HAMP is lower than it would be if the airflow was unstable. From a research point of view however, it is interesting to see that a large, negative concentration gradient can in fact negate a positive temperature gradient and cause the overall density gradient to become negative. Although several researchers have discussed the idea of the concentration and temperature gradients combining together (i.e.: Lin et al. (1992a), Yan (1994, 1996)), these photographs are the first to actually show this effect.

5.6 AN UNSTABLE HEATING CASE

In a similar manner, one test was performed in an attempt to make a heating case become unstable by creating a positive concentration gradient (by dehumidifying the air) to counter the negative temperature gradient. This test however was not successful. In this case, the heat transfer Rayleigh number was -3.5x10^{5} and the mass transfer Rayleigh number was 5.1x10^{5}, which resulted in an effective Rayleigh number of 1.6x10^{5}. This value of the effective Rayleigh number should have been enough to cause the buoyancy forces to become dominant in the duct and have unstable airflow, however, this was not seen in the flow visualization photographs. The

photographs showed the same airflow patterns as those presented for the stable airflow cases and the sensible and latent effectivenesses were also similar to the stable airflow case. More work is needed to determine the parameters that must be altered in the tests to create an unstable heating case. From a design point of view, an unstable heating case would be beneficial as the effectivenesses of the HAMP would increase compared to a typical heating case.

5.7 TOTAL HEAT AND MASS FLUXES

Up to this point, the performance of the HAMP has been quantified by the sensible and latent effectivenesses, which are important parameters for an energy exchanger. For radiant ceiling panels however, the performance of the panel is typically presented as the total heat flux between the panel and the space air at different air and panel temperatures. Since the HAMP transfers both heat and moisture with the space air, the total mass flux under different conditions is also of interest.

The total heat flux between the HAMP and the air in the test section will be a combination of both radiation and convection heat transfer. The total heat flux (q") is calculated from the experiments by

$$q'' = U\Delta T_{lm} \tag{5.1}$$

and has units of W/m^2. The total mass flux ($\dot{m}''$) is calculated by

$$\dot{m}'' = U_m^W \Delta W_{lm} \tag{5.2}$$

and has units of $g_w/(m^2 \cdot s)$.

The total heat flux between the HAMP and the air in the test section, with the HAMP in the ceiling panel configuration and Re = 65 is given in Figure 5.12 for both cooling and heating

cases. In the cooling tests, the panel temperature varied from 6°C to 18°C and in the heating tests, the panel temperature ranged from 24°C to 35°C. It can be seen that the total heat flux increases as the difference between the panel temperature and the upstream air temperature increases.

For a typical radiant ceiling panel, the total heat flux is considerably higher than the results presented for the HAMP in Figure 5.12. For a cooled ceiling panel with a temperature difference of approximately 3°C between the panel and the air temperature, the typical heat flux is about 25 W/m^2 (ASHRAE (2012)). From Figure 12, it can be seen that when HAMP is used for heating, a temperature difference of 3°C would yield a total heat flux of ~7 W/m^2, and when the HAMP is used for cooling a temperature difference of 3°C would yield a very small value. The low total heat flux values can be attributed to the low velocities used, which result in low convection heat transfer rates. An increase in the convection heat transfer would increase the overall heat flux of the HAMP.

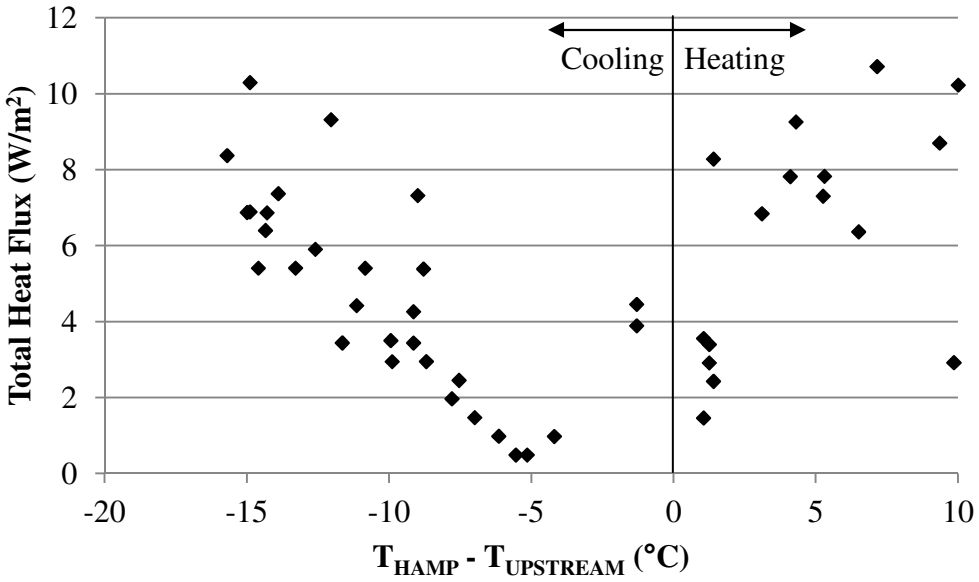

FIGURE 5.12. Total heat flux for the prototype HAMP in the ceiling panel configuration for both heating and cooling conditions.

The total mass flux between the HAMP and the air in the test section, with the HAMP in the ceiling panel configuration is presented in Figure 5.13 for both humidifying and dehumidifying conditions. As the difference between the panel humidity ratio and the upstream air humidity ratio gets larger, the total mass flux between the HAMP and the airflow gets larger. As the HAMP is a new concept design, there are no examples of mass flux rates for ceiling panels to compare these values to. According to ASHRAE (2009) a person generates 45 W of latent heat while seated, doing light work, as would be the case in a typical office building. This amount of latent heat generation equates to a production of 72 g_w/hr per person. Depending on the difference in the humidity ratios, a HAMP with a surface area of approximately 1 to 2 m^2 would be able to remove the latent heat produced by one person.

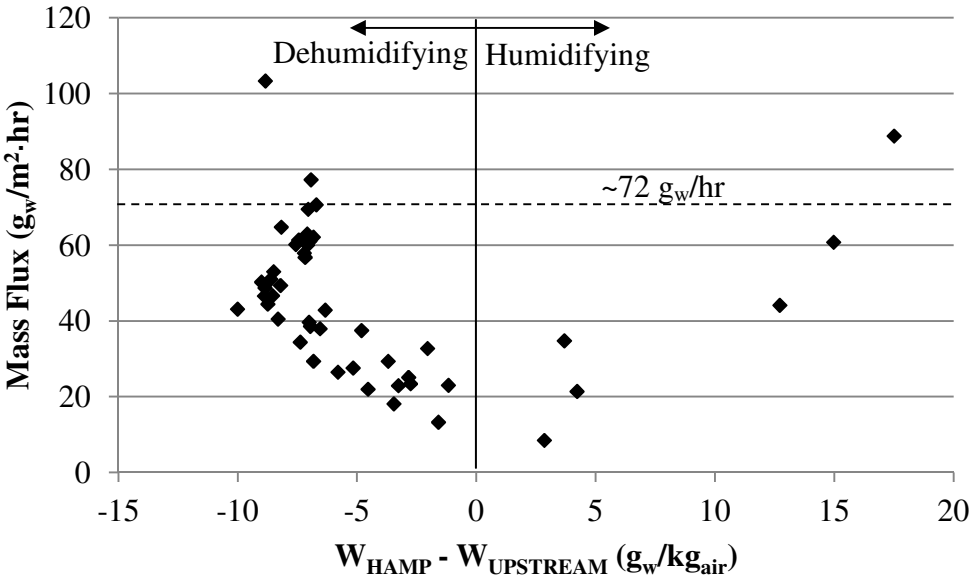

FIGURE 5.13. Total mass flux for the prototype HAMP in the ceiling panel configuration for both dehumidifying and humidifying conditions.

5.7 SUMMARY

In this chapter, the performance of the prototype HAMP was presented for different operating conditions. The performance was presented in terms of the sensible and latent effectivenesses of the HAMP and also in terms of the total heat and mass fluxes between the HAMP and the airflow. The sensible and latent effectivenesses of the prototype HAMP are highest under cooling and dehumidification conditions and lowest under heating and humidification conditions. When dehumidification alone is required, the latent effectiveness of the HAMP is higher than when humidification alone is required.

The experimental results of seven tests were compared against a numerical simulation performed by M. Bansal that did not include buoyancy forces in the test section. Good agreement was achieved for the cases where buoyancy forces were negligible, however the results did not agree as well for the case of cooling from the ceiling and the case of heating from the floor, where

buoyancy forces were dominant in the test section. This shows the importance of buoyancy forces on the performance of the HAMP. These results show that the effectivenesses of the HAMP are higher when buoyancy forces are large and natural convection is dominant in the test section, than when buoyancy forces are negligible.

Flow visualization was used to highlight the effects of buoyancy forces on the airflow patterns in the duct and to visualize the natural convection in the air. It was found that the effectivenesses of the HAMP were higher when the airflow was unstable than when the airflow was stable. By creating a large concentration gradient in the duct, a cooling case, which would normally be unstable, was made stable, as demonstrated with the flow visualization photographs. The sensible and latent effectivenesses during this case were also lower than typical cooling cases, due to the stable airflow.

Finally, the total heat and mass fluxes between the HAMP and the airflow were presented for different temperatures and humidity ratio differences. The total heat flux increases when the difference in temperature between the upstream air and the panel increases, and the total mass flux increases when the difference in the humidity ratio between the upstream air and the panel increases. The total heat flux values for the HAMP are lower than typical radiant ceiling panels, due to the low air velocities used, which results in a small convection heat transfer rate between the panel and the air. Depending on the difference in the humidity ratio between the upstream air and the HAMP, approximately 1 to 2 m^2 of panel area would be required to remove the latent heat produced by one person.

The performance of the HAMP presented in this chapter is for specific cases, with a limited range of inlet conditions (temperature and humidity ratio) for the air and the liquid desiccant. When designing an energy exchanger for a space, it is necessary to know how the exchanger will perform under a wide variety of conditions to ensure proper design for the space. These data may be collected by performing a very large number of experiments, but this would be labour intensive. A more beneficial method would be to determine a correlation that can be used to predict the performance of the energy exchanger. Although this thesis will not determine a specific correlation for a HAMP, some of the parameters that affect the performance of a HAMP will be discussed in Chapter 6 and may be used by future researchers to determine a specific correlation.

CHAPTER 6 – PREDICTING PERFORMANCE OF A HAMP

In practice, correlations for effectiveness are generally used to determine the performance of an energy exchanger. For heat exchangers these correlations are typically simple explicit equations, which can be solved to determine the sensible effectiveness of the exchanger. For energy exchangers with simultaneous heat and moisture transfer, these correlations have proven to be complex functions of the operating conditions and design parameters of the exchanger. Hemingson (2010) created correlations for sensible and latent effectiveness for a run-around membrane energy exchanger based on numerical data for H^* values greater than zero. The effectiveness correlations require the input of NTU, H^* and ΔH (difference in enthalpy between the two streams) and are complex equations. Akbari (2012) created a neural network to predict the effectivenesses of the same run-around membrane energy exchanger. The inputs used for the neural network were NTU, Cr^* (inverse of Cr), ΔT (between the two streams), and the humidity ratios of the two streams. Again, the relationship between the performance of the exchanger and these parameters was found to be very complex and the neural network required a very large number of nodes and connections to accurately predict the effectivenesses.

The models created by Hemingson (2010) and Akbari (2012) show that the relationship between performance and the operating conditions and design parameters of an energy exchanger with coupled heat and moisture transfer are very complex. Although the heat and moisture transfer in a run-around membrane energy exchanger will be similar to the heat and moisture transfer with a

HAMP, there are some important differences that add to the complexity of the performance correlations for a HAMP. The run-around membrane energy exchanger involves air and liquid flow through narrow channels, so the flow is completely dominated by forced convection, whereas with a HAMP, buoyancy forces have been shown to be very important. This means that Ra^+ must also be included in the correlation. In the run-around membrane energy exchanger, the ratio NTU/NTU_m is kept constant, which can be done numerically, but cannot be done in the experiments, due to the changing convection coefficients during each test. This ratio must also be considered in the investigation of an effectiveness correlation for a HAMP. This chapter will present some general relationships between the sensible and latent effectivenesses of a HAMP and the operating and design parameters – NTU, H^*, Ra^+, and NTU/NTU_m. The information presented in this chapter will be useful to future researchers as a starting point for developing correlations to predict the effectivenesses of a HAMP.

6.1 EXISTING CORRELATIONS FOR EXCHANGER PERFORMANCE

When designing an energy exchanger for a space, it is necessary to know the sensible and latent effectiveness of the exchanger in order to determine how it will perform in the given conditions. As mentioned in Section 4.2, the sensible effectiveness of an energy exchanger can be predicted using the effectiveness-NTU method which states that

$$\varepsilon_{\text{sensible}} = f(\text{NTU}, \text{Cr}) \tag{6.1}$$

and in a similar manner,

$$\varepsilon_{\text{latent}} = f(\text{NTU}_\text{m}, \text{Cr}). \tag{6.2}$$

ASHRAE (2009) presents correlations for the effectiveness-NTU method based on the flow configuration of the two streams in the exchanger. For any exchanger with Cr = 0, regardless of flow configuration, the correlations are

$$\varepsilon_{sensible}=1\text{-}\exp(\text{-NTU}) \text{ and} \tag{6.3}$$

$$\varepsilon_{latent}=1\text{-}\exp(\text{-NTU}_m). \tag{6.4}$$

These correlations for the sensible and latent effectivenesses of an energy exchanger are simple equations that can be calculated if NTU and NTU_m are known for a particular exchanger. If these correlations could be applied to a HAMP, predicting the sensible and latent effectivenesses would be very convenient. Using NTU_{theo} and $NTU_{m,theo}$ determined for each experiment, the sensible and latent effectivenesses of the HAMP are plotted for the experiments and compared to the correlations in Figure 6.1. Unfortunately, the theoretical values of NTU and NTU_m cannot be used to accurately predict the sensible and latent effectivenesses using the correlations. NTU_{theo} is nearly constant for all tests, but the sensible effectiveness of the HAMP is very different for the different tests, as was described in Chapter 5.

(a)

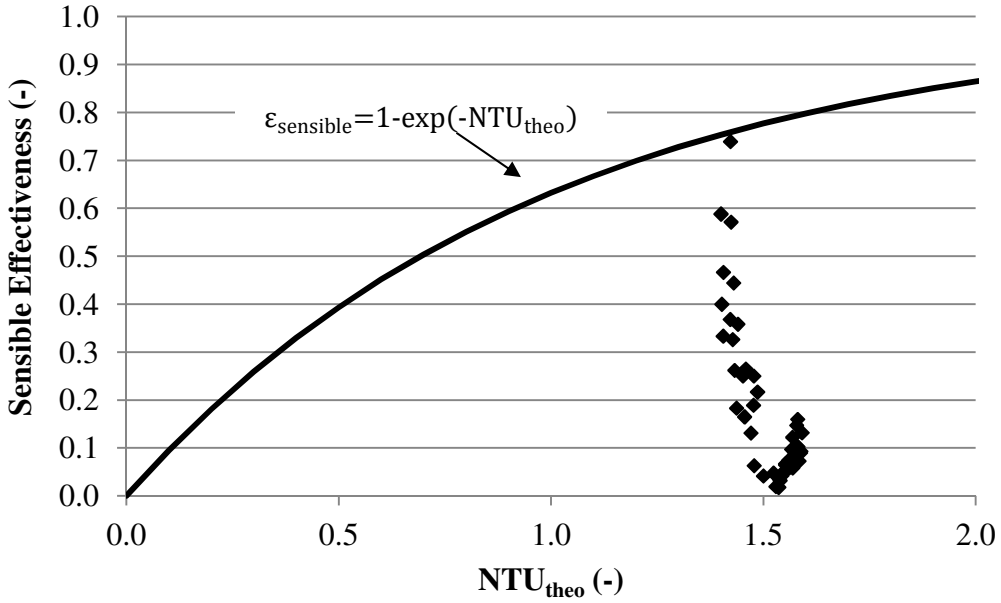

(b)

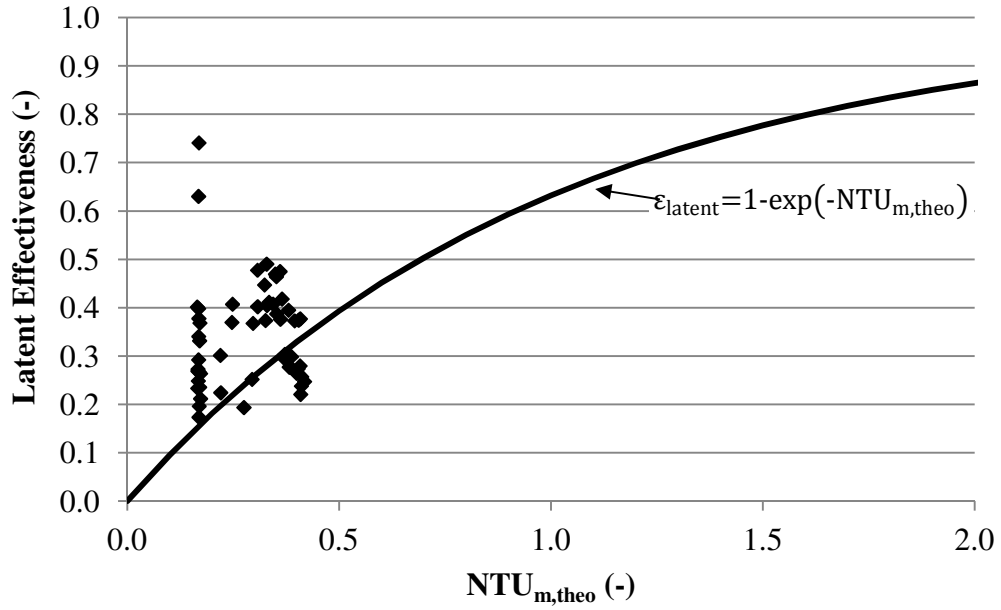

FIGURE 6.1. Comparison between (a) sensible effectiveness and (b) latent effectiveness calculated from correlations (solid line) and from measured data (points) against NTU_{theo} and $NTU_{m,theo}$.

The correlations presented in equations (6.3) and (6.4) are derived from equations for heat and moisture transfer in the duct. As defined in Section 4.2.2,

$$NTU = \frac{UA_{surface}}{(\dot{m}c_p)_{air}} \tag{6.5}$$

where U is the overall heat transfer coefficient of the exchanger [W/(m^2·K)], $A_{surface}$ is the heat transfer surface area of the exchanger [m^2], $\dot{m}$ is the mass flow rate of the air [kg_{air}/s] and c_p is the specific heat of the air [J/(kg_{air}·K)], and the number of mass transfer units is defined as

$$NTU_m = \frac{U_m A_{surface}}{\dot{m}_{air}} \tag{6.6}$$

where U_m is the overall mass transfer coefficient of the exchanger [kg_{air}/(m^2·s)].

In Chapter 4, the overall heat and mass transfer coefficients were determined from theoretical values, resulting in NTU_{theo} and $NTU_{m,theo}$. Using the equations for heat and moisture transfer in the duct however, the overall heat and moisture transfer coefficients can also be determined from the experimental data, resulting in NTU_{exp} and $NTU_{m,exp}$.

6.2 DEFINITION OF NTU_{exp} AND $NTU_{m,exp}$

The overall heat transfer coefficient can be calculated by setting the heat gain/loss by the air equal to the heat transfer across the semi-permeable membrane, as

$$\dot{m}_{air} c_{p,air} \left(T_{DOWNSTREAM} - T_{UPSTREAM}\right) = UA_{surface} \Delta T_{lm} \tag{6.7}$$

and therefore

$$U_{exp} = \frac{\dot{m}_{air} c_{p,air} \left(T_{DOWNSTREAM} - T_{UPSTREAM}\right)}{A_{surface} \Delta T_{lm}} \tag{6.8}$$

where ΔT_{lm} is the log mean temperature difference between the inlets and outlets of the two streams.

Similarly, the overall mass transfer coefficient can be calculated by setting the moisture gain/loss in the air equal to the moisture transfer across the semi-permeable membrane, as

$$\dot{m}_{air}\left(W_{DOWNSTREAM}-W_{UPSTREAM}\right)=U_m A_{surface}\Delta W_{lm} \tag{6.9}$$

and therefore

$$U_{m,exp}=\frac{\dot{m}_{air}\left(W_{DOWNSTREAM}-W_{UPSTREAM}\right)}{A_{surface}\Delta W_{lm}} \tag{6.10}$$

where ΔW_{lm} is the log mean humidity ratio difference between the inlets and outlets of the two streams. The ranges of NTU_{exp} and $NTU_{m,exp}$ for the experiments are presented in Table 6.1, along with the theoretical ranges presented first in Chapter 4.

TABLE 6.1. Ranges of theoretical and experimental NTU and NTU_m for test cases.

Parameter	**Range**
NTU_{theo} [-]	1.4 - 1.6
$NTU_{m,theo}$ [-]	0.2 – 0.4
U_{exp} [W/(m^2·K)]	0.1 – 6.7
NTU_{exp} [-]	0.02 – 1.4
$U_{m,exp}$ [kg_{air}/(m^2·s)]	0.001 – 0.006
$NTU_{m,exp}$ [-]	0.2 – 1.3

Since NTU_{exp} and $NTU_{m,exp}$ are calculated from the same equations used to derive the effectiveness-NTU correlations, the calculated sensible and latent effectiveness values should have better agreement with the correlations when plotted against NTU_{exp} and $NTU_{m,exp}$ than when plotted against NTU_{theo} and $NTU_{m,theo}$. A comparison between the correlations and the experimental sensible and latent effectivenesses are shown in Figure 6.2(a) and Figure 6.2(b), respectively. There is very good agreement between the experimental data and correlations,

which indicates that NTU_{exp} and $NTU_{m,exp}$ can be used with the correlations to predict the sensible and latent effectivenesses of a HAMP.

(a)

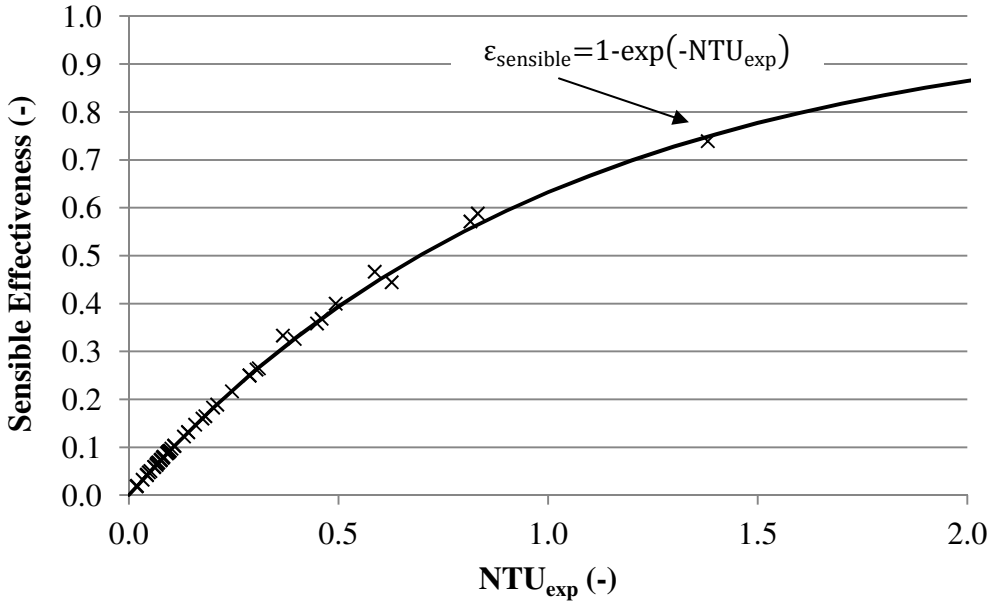

(b)

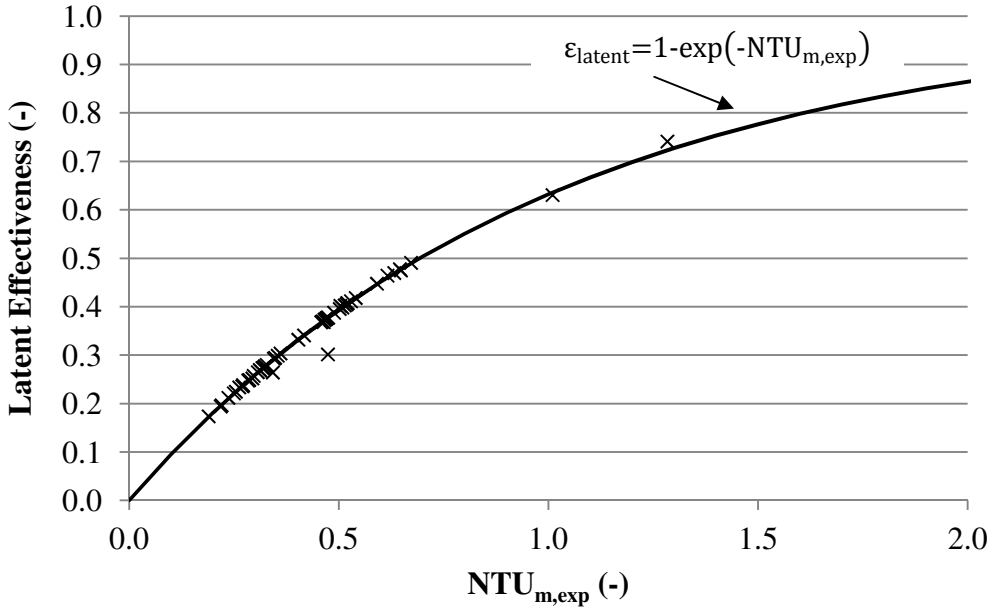

FIGURE 6.2. Comparison between (a) sensible effectiveness and (b) latent effectiveness calculated from correlations (solid line) and measured data against NTU_{exp} and $NTU_{m,exp}$.

Although the values of NTU_{exp} and $NTU_{m,exp}$ can be used to directly predict the sensible and latent effectivenesses of a HAMP, calculating the values of NTU_{exp} and $NTU_{m,exp}$ requires knowledge of the outlet conditions of the HAMP, which are known from the experiments, but would not be known in a typical design situation. Again, this brings up the need for new correlations to determine the relationships between NTU_{exp} and $NTU_{m,exp}$ and the various operating conditions and design parameters. Specific correlations for the sensible and latent effectivenesses could be determined so that only two correlations need to be used to determine performance, however, those correlations would be function of NTU_{exp} and $NTU_{m,exp}$, so determining correlations for NTU_{exp} and $NTU_{m,exp}$ and then using equations (6.3) and (6.4) to determine performance eliminates one variable from the analysis (the effectiveness). As mentioned previously, the relationships between these parameters are very complex and specific correlations will not be developed in this thesis, but the relationship between NTU_{exp} and $NTU_{m,exp}$ and each parameter will be investigated based on the experimental data collected.

6.3 EFFECT OF DESIGN PARAMETERS ON NTU_{exp} & $NTU_{m,exp}$

Ideally, the relationship between NTU_{exp} and $NTU_{m,exp}$ and each parameter should be studied by varying that parameter, while keeping all of the other parameters constant. This is very difficult to do during the experiments, however, as many of the parameters are dependent on the same variables. For example, H^* and Ra^+ are both related to the difference in moisture content between the inlet streams and the difference in temperature between the inlet streams, however H^* is the ratio of these values while Ra^+ sums them together. This makes it very complicated to vary H^* while maintaining the same Ra^+ value, or vice versa. As such, the results presented are not isolated for each parameters, but will include effects of other parameters as well.

6.3.1 Effect of Ra^+ on NTU_{exp} & $NTU_{m,exp}$

The relationship between NTU_{exp} and Ra^+ is shown in Figure 6.3(a) and the relationship between $NTU_{m,exp}$ and Ra^+ is shown in Figure 6.3(b). NTU_{exp} increases with increasing Ra^+ for the whole range of Ra^+ studied. There is some scatter in the curve, which is attributed to other design parameters changing for each test. For example, there are three points at $Ra^+ = \sim 30 \times 10^5$, which have been highlighted in Figure 6.3(a). The two points with $NTU_{exp} = \sim 0.05$ have an H^* value of 3, whereas the other point, at $NTU_{exp} = 0.18$ has an H^* value of -1. The effects of H^* will be shown in the next section.

$NTU_{m,exp}$ initially increases with increasing Ra^+, until a value of approximately $Ra^+ = 35 \times 10^5$. After this value, $NTU_{m,exp}$ is lower and approximately constant as Ra^+ increases further. In this region ($Ra^+ > 35 \times 10^5$), the mass transfer Rayleigh number is approximately the same for each case, whereas the heat transfer Rayleigh number increases, resulting in an increase in Ra^+. The heat transfer Rayleigh number is approximately ten times larger than the mass transfer Rayleigh number in this region, which indicates that the temperature gradient is much larger than the concentration gradient. It appears that when the temperature and concentration gradient have similar magnitudes the heat transfer assists the mass transfer (resulting in an increase in $NTU_{m,exp}$ as Ra^+ increases) but when the temperature gradient become significantly larger than the concentration gradient the heat transfer no longer assists the mass transfer (resulting in a constant $NTU_{m,exp}$ as Ra^+ increases, for a constant Ra_m). This effect needs to be studied further by running a series of tests with a constant Ra_m value, and different Ra_h values.

(a)

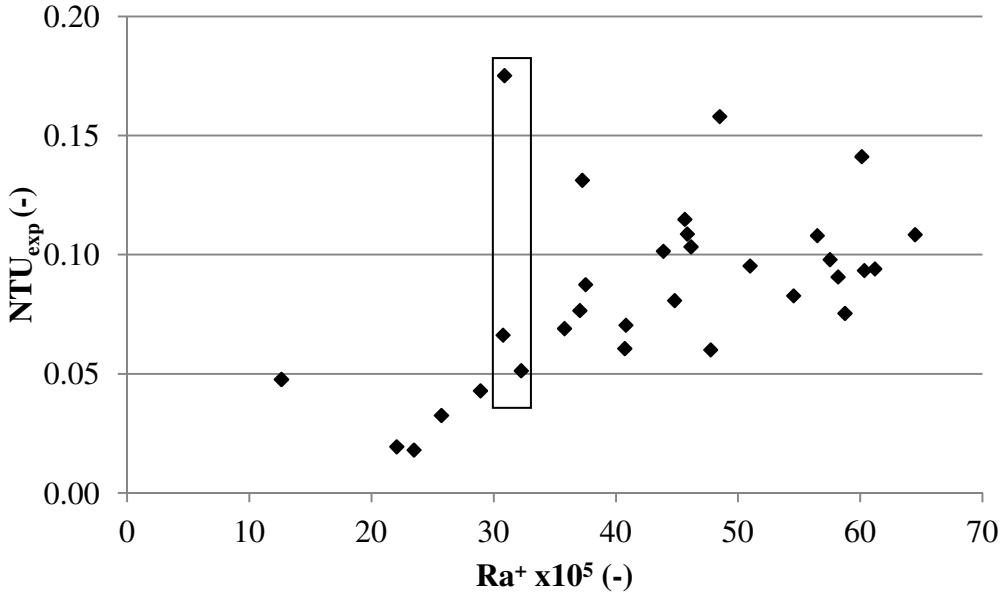

(b)

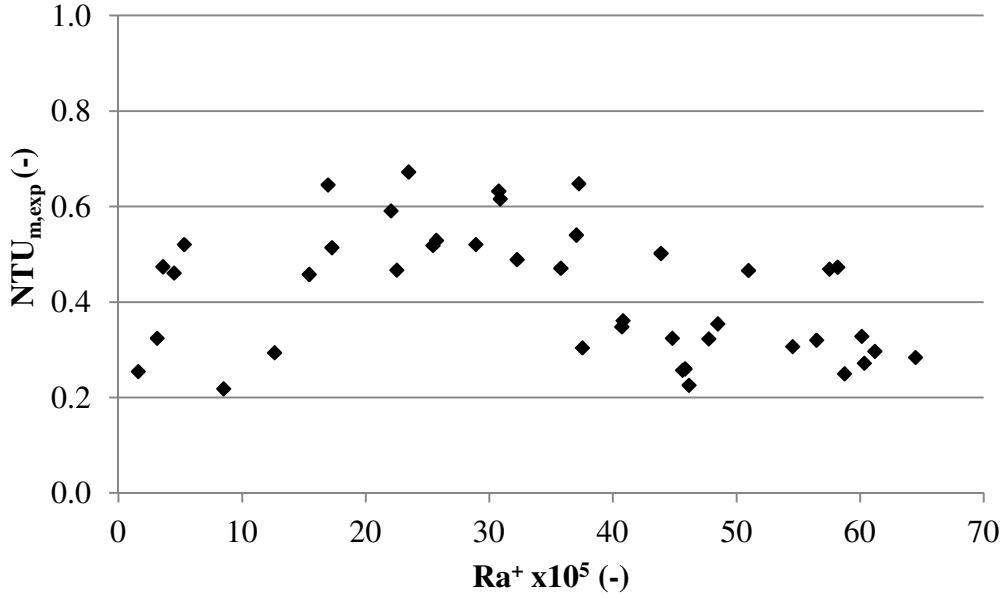

FIGURE 6.3. Effect of Ra^+ on (a) NTU_{exp} and (b) $NTU_{m,exp}$.

6.3.2 Effect of H^* on NTU_{exp} & $NTU_{m,exp}$

The relationship between NTU_{exp} and H^* is shown in Figure 6.4(a) and the relationship between $NTU_{m,exp}$ and H^* is shown in Figure 6.4(b). NTU_{exp} decreases, approximately linearly with increasing H^*. At large negative H^* values there is some discrepancy between the NTU_{exp} values. In these cases, the uncertainty of NTU_{exp} is quite large, as large negative H^* values are

created using a small temperature difference between the inlet streams. Again, there is some scatter in the data, due to the other parameters, such as Ra^+, that are different for each test. Referring back to the three data points that were highlighted in Figure 6.3(a), the relationship between NTU_{exp} and H^* explains why NTU_{exp} is higher for the case with $H^* = -1$, than for the two cases with $H^* = 3$, even though Ra^+ is approximately the same in all three cases.

$NTU_{m,exp}$ is approximately constant for large negative and large positive values of H^* but increases significantly when H^* approaches zero from the negative side and decreases significantly (into negative values) when H^* approaches zero from the positive side. An H^* value close to zero indicates that the difference in the humidity ratio between the two inlets of the exchanger is approximately zero. However, due to the coupling of the heat and moisture transfer, there will still be some moisture transfer in the exchanger, even if the driving potential for moisture transfer is very small. This is similar to the phenomenon discussed in Section 5.1 when the driving potential for heat transfer was small and the sensible effectiveness of the HAMP was greater than 100%. The positive and negative sign of $NTU_{m,exp}$ when H^* approaches zero is related to the direction of the moisture transfer in relation to the heat transfer.

(a)

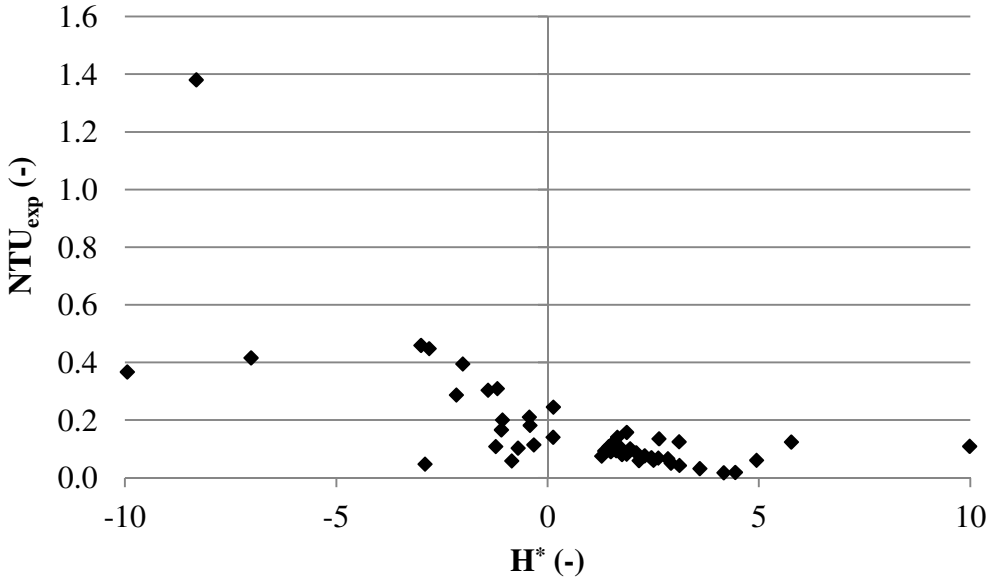

(b)

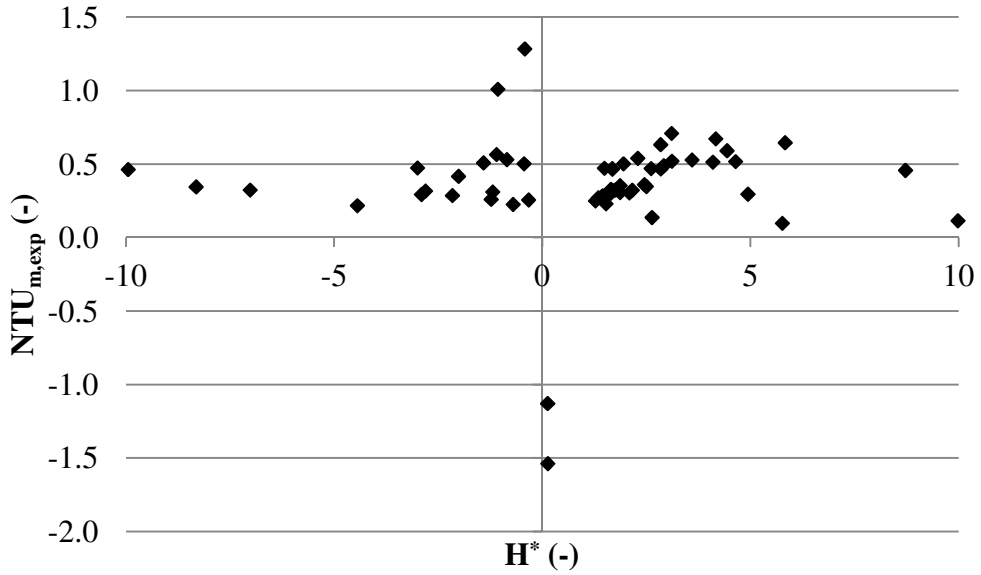

FIGURE 6.4. Effect of H^* on (a) NTU_{exp} and (b) $NTU_{m,exp}$.

Simonson and Besant (1999b) found similar results for the sensible and latent effectivenesses of an energy wheel for different H^* values. Their results, obtained using correlations are shown in Figure 6.5. The sensible effectiveness (related to NTU_{exp}) decreases with increasing H^* and the latent effectiveness (related to $NTU_{m,exp}$) is approximately constant except for when H^*

approaches 0. The results found by Simonson and Besant (1999b) are similar to the experimental results presented in this thesis, which gives confidence to the experimental results.

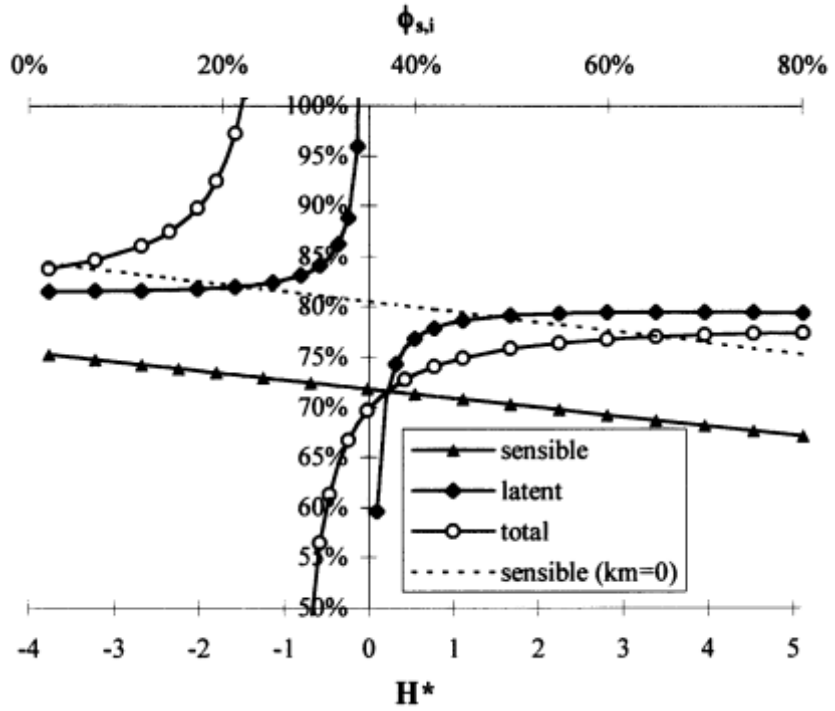

FIGURE 6.5. Predicted effectiveness of an energy wheel for different H* values (Simonson and Besant (1999b)).[‡‡]

6.3.3 Effect of $NTU_{exp}/NTU_{m,exp}$ ratio on NTU_{exp}

Since the heat and moisture transfer are coupled, $NTU_{m,exp}$ will have an effect on NTU_{exp} and vice versa. To determine this relationship, the values of NTU_{exp} and $NTU_{m,exp}$ are plotted against the ratio $NTU_{exp}/NTU_{m,exp}$ in Figure 6.6(a) and (b). NTU_{exp} increases as the ratio $NTU_{exp}/NTU_{m,exp}$ increases. The curved trend line shows that NTU_{exp} is dependent on $NTU_{m,exp}$, as the relationship would be linear if NTU_{exp} was independent of $NTU_{m,exp}$. $NTU_{m,exp}$ decreases as the ratio increases, which is expected as $NTU_{m,exp}$ is in the denominator of the ratio

[‡‡] Reprinted from International Journal of Heat and Mass Transfer, 42(12), C.J. Simonson and R.W. Besant, Energy wheel effectiveness: part II – correlations, 2171-2185, 1999, with permission from Elsevier.

$NTU_{exp}/NTU_{m,exp}$. The relationships between NTU_{exp} and $NTU_{m,exp}$ and the ratio $NTU_{exp}/NTU_{m,exp}$ confirms the complex nature of the correlations that define NTU_{exp} and $NTU_{m,exp}$, as these correlation would need to be solved iteratively.

(a)

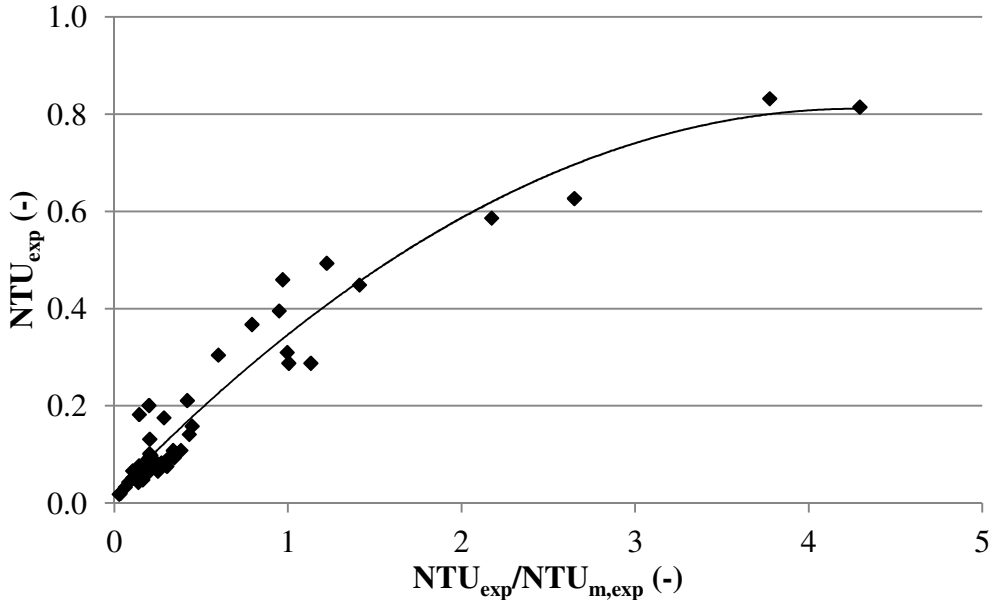

(b)

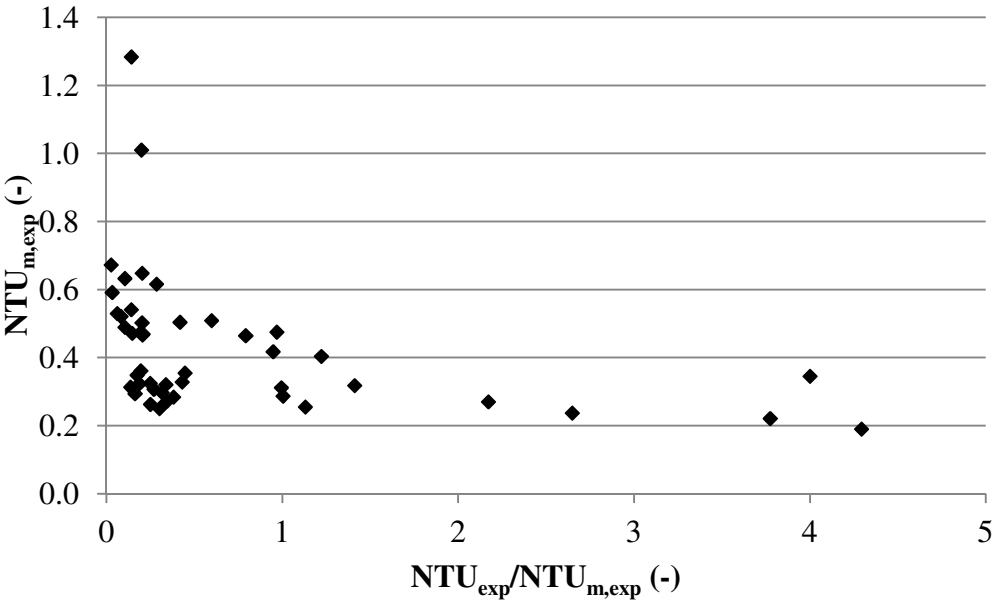

FIGURE 6.6. Effect of the ratio $NTU_{exp}/NTU_{m,exp}$ on (a) NTU_{exp} and (b) $NTU_{m,exp}$.

In addition to the parameters discussed above, the Reynolds number of the flow will also affect NTU_{exp} and $NTU_{m,exp}$. In this study, however, the Reynolds number was kept constant, so its effects on NTU_{exp} and $NTU_{m,exp}$ have not been determined. A future study of the performance of a HAMP should include the effects of Reynolds number as well.

6.4 SUMMARY

In this chapter, it was shown that NTU_{exp} and $NTU_{m,exp}$ can be used along with standard effectiveness-NTU correlations to accurately predict the performance of a HAMP. Determining NTU_{exp} and $NTU_{m,exp}$ however, is not an easy task if the outlet conditions of the exchanger are unknown, which is typical when designing an energy exchanger. In an effort to better understand the parameters that effect NTU_{exp} and $NTU_{m,exp}$, the relationships between these values and the parameters H^*, Ra^+ and the ratio $NTU_{exp}/NTU_{m,exp}$ have been presented. It was found that NTU_{exp} decreases with H^* and NTU_{exp} increases with Ra^+ and the ratio of $NTU_{exp}/NTU_{m,exp}$. The relationships for $NTU_{m,exp}$ are more complex. $NTU_{m,exp}$ is approximately constant for different H^* values, except when H^* approaches zero in which case $NTU_{m,exp}$ increases significantly. $NTU_{m,exp}$ increases with increasing Ra^+, up to a Ra^+ value of approximately $30x10^5$, at which point $NTU_{m,exp}$ remains approximately constant as Ra^+ increases further. $NTU_{m,exp}$ decreases as the ratio $NTU_{exp}/NTU_{m,exp}$ increases.

Although specific correlations for NTU_{exp} and $NTU_{m,exp}$ have not been determined, this thesis presents an analysis which is a good base for understanding the impact of different parameters on the performance of a HAMP and an extensive supply of experimental data which can be used to determine specific correlations to predict the performance of a HAMP.

CHAPTER 7 – SUMMARY AND CONCLUSIONS

The main objectives of this thesis are to design a prototype ceiling panel which can be used to simultaneously transfer heat and moisture and to determine the performance of this panel under different operating conditions. This Chapter will summarize the important results presented in this thesis, as well as suggest some topics for future work that may be done on a HAMP.

7.1 SUMMARY

7.1.1 Design of the Prototype HAMP and Test Facility

A HAMP is new type of panel, which can be installed into a room to add or remove heat and moisture, in an effort to simultaneously control the temperature and relative humidity of the room. In order to measure the performance of a HAMP, a prototype HAMP and a test facility were designed, as discussed in Chapter 2. The prototype HAMP is constructed from an acrylic tray, with a semi-permeable membrane attached to one side. A liquid desiccant, which has the ability to absorb or release moisture, is pumped through the tray. The semi-permeable membrane allows water vapour to pass through the membrane, but contains the liquid inside the HAMP.

The test facility used to measure the performance of the prototype HAMP consists of a horizontal, rectangular duct, with laminar airflow. For the majority of tests performed in this thesis, the prototype HAMP was located in the top of the duct, in the test section. The airflow in

the test section is hydrodynamically fully developed with developing temperature and concentration boundary layers. Measurements of the bulk air temperature and relative humidity were taken upstream and downstream of the test section. The density and temperature of the liquid desiccant were measured inside the HAMP.

7.1.2 Commissioning of the Test Facility

To ensure that the results presented from the experiments are reliable, a steady-state analysis of preliminary results, as well as an uncertainty analysis and energy and mass balances were presented. The steady-state analysis showed that the fluctuations in the steady-state temperature and humidity ratio are within acceptable limits ($\delta T < 0.02$ and $\delta W < 0.05$ for dehumidification or $\delta W < 0.1$ for humidification). The uncertainties in each measurement and calculated result were presented and determined to be acceptable. The uncertainties in the sensible and latent effectivenesses of the prototype HAMP are within acceptable limits for an energy exchanger ($U\varepsilon_{sensible} < 5\%$, $U\varepsilon_{latent} < 7\%$). Finally, the energy and mass balances ensure that the systematic heat and moisture exchanges between the test facility and the surroundings are small (<5%). This analysis shows that the experimental results recorded in this study can be used to determine the performance of the prototype HAMP with a high level of confidence.

7.1.3 Performance of the Prototype HAMP

The performance of an energy exchanger is quantified using sensible and latent effectivenesses. Chapter 5 presented the sensible and latent effectivenesses of the prototype HAMP under different operating conditions. Cases were considered for different combinations of cooling, heating, humidifying and dehumidifying of the airflow. First and foremost, the results show that

the HAMP works, as it is able to simultaneously transfer heat and moisture under all operating conditions.

The results of the experiments show that the sensible and latent effectivenesses are higher when the airflow in the test section becomes unstable ($\varepsilon_{sensible} \approx 15\%$, $\varepsilon_{latent} \approx 40\%$), due to the natural convection in the duct. These include cases of cooling and dehumidification. The sensible and latent effectivenesses are lower during stable airflow cases ($\varepsilon_{sensible} \approx 5\%$, $\varepsilon_{latent} \approx 25\%$), such as cases of heating and humidification. Comparison to a numerical model confirmed the importance of the buoyancy forces on the increase in latent effectiveness.

In order to illustrate the effects of the stability of the airflow on the performance of the HAMP, flow visualization photographs were presented for a stable airflow case and an unstable airflow case. In the stable airflow case, the airflow is characterized by laminar boundary layer flow through a duct. In the unstable airflow case, convection roll cells are seen to develop in the test section. The presence of roll cells in the test section indicates that the air is mixing and explains the increase in the sensible and latent effectivenesses of the HAMP.

The performance of the prototype HAMP was also quantified by the total heat and mass fluxes between the panel and the air in the test section. The total heat flux increases with an increase in the temperature difference between the panel and the air and the mass flux increases with an increase in the humidity ratio difference between the panel and the air. For a temperature difference of 10°C the HAMP can provide ~4 W/m^2 of cooling. Depending on the difference in the humidity ratio between the HAMP and the air, ~2 m^2 of panel area is required for the HAMP

to remove the moisture added by one occupant (~70 g_w/hr).. The total heat flux from the HAMP is lower than the total heat flux of a radiant ceiling panel, due to the low air velocities which are used in the test facility. An increase in the air velocity would increase the amount of heat transfer by convection and therefore the total heat flux from the panel.

7.1.4 Predicting Performance of a HAMP

In order to design a HAMP for a space, it is necessary to be able to predict the performance of the HAMP under different conditions. Typical methods of determining the number of heat and mass transfer units (NTU, NTU_m) of an energy exchanger from theoretical correlations and then using correlations for effectiveness as a function of NTU_{theo} and $NTU_{m,theo}$ cannot be used for a HAMP. However, the analysis showed that NTU and NTU_m, calculated from the experimental results (NTU_{exp} and $NTU_{m,exp}$) can be used with standard correlations to accurately predict the sensible and latent effectivenesses of a HAMP. The difficulty then becomes in predicting NTU_{exp} and $NTU_{m,exp}$ for a HAMP, as these values are dependent on several parameters and correlations for NTU_{exp} and $NTU_{m,exp}$ would be very complex and difficult to determine.

Using the extensive experimental data gathered in this thesis, general relationships between NTU_{exp} and $NTU_{m,exp}$ and several design parameters have been presented. NTU_{exp} is found to decrease with increasing H^* and increase with increasing Ra^+ and the ratio $NTU_{exp}/NTU_{m,exp}$. $NTU_{m,exp}$ is found to be approximately constant for most values of H^*, except when H^* approaches zero. $NTU_{m,exp}$ increases with Ra^+ when Ra^+ is less than ~$30x10^5$, and remains approximately constant above this value. $NTU_{m,exp}$ decreases as the ratio $NTU_{exp}/NTU_{m,exp}$ increases.

7.2 CONCLUSIONS

A prototype HAMP has been designed and its performance has been determined experimentally and presented for a variety of operating conditions. The sensible and latent effectivenesses of the HAMP are highest during tests where buoyancy forces are dominant in the test section, as the instability of the airflow increases the convection coefficients in the test section and therefore heat and moisture transfer between the HAMP and the air. As well, the total heat and mass flux between the HAMP and the air are presented for different panel temperatures and humidity ratios. Although the total heat and mass flux rates are small, the results show that a HAMP can be used to simultaneously transfer heat and moisture with the air in a space, and may be used as a ceiling panel in a space to control the temperature and relative humidity of the air.

The performance of a HAMP can be determined using two parameters: NTU_{exp} and $NTU_{m,exp}$. Determining these two parameters is very complicated and involves analysis of several design parameters, such as NTU_{theo}, $NTU_{m,theo}$, H^*, Ra^+ and the ratio $NTU_{exp}/NTU_{m,exp}$. The experimental data collected in this thesis was used to analyze the relationships between NTU_{exp} and $NTU_{m,exp}$ and these design parameters.

7.3 CONTRIBUTIONS

The specific contributions of this work were summarized in Chapter 1 and include the following:

- Design the first prototype of a device that has the ability to simultaneously transfer heat and moisture with air in a space (a HAMP), with transfer in any direction,
- Determine the performance of a HAMP under different combinations of cooling, heating, humidification and dehumidification,

- Present experimental data relating the performance of an energy exchanger with combined heat and mass transfer to specific design parameters (NTU_{exp}, $NTU_{m,exp}$, H^*, Ra^+ and $NTU_{exp}/NTU_{m,exp}$),
- Present flow visualization of forced convection and natural convection in an energy exchanger with combined heat and mass transfer for different temperature and concentration gradients,
- Provide an understanding of general heat and moisture transfer between a laminar airflow (with and without buoyancy) and a liquid desiccant separated by a semi-permeable membrane.

7.4 FUTURE WORK

One of the main objectives of this thesis was to determine the performance of a novel panel for heat and moisture transfer and included a discussion of the effects of different parameters on the performance. In order to determine the specific relationships between each parameter and the performance of the prototype HAMP, a study needs to be done where one parameter is varied and the others are held constant. This is difficult to do however, as the parameters are not independent of each other. In the experiments presented in this thesis, the mass flow rate was kept constant, to reduce the number of variables that were changing with each test, which means that the effects of Reynolds number on performance was not investigated. The performance of an energy exchanger will also vary with Cr, so this design parameter should also be investigated. These two variables should be investigated experimentally to determine the correct relationships between each of the parameters and the performance of a HAMP.

In order to create specific correlations for NTU_{exp} and $NTU_{m,exp}$, a numerical model could be created, to predict the performance of a HAMP under a wider variety of operating conditions. This model will need to include the effects of buoyancy, as these have been shown to have an important effect on the performance of a HAMP. In addition, the model should include different ratios of $NTU_{exp}/NTU_{m,exp}$, as the experiments show that this will have an effect of NTU_{exp}.

The idea behind a HAMP is that it will be able to add or remove heat and moisture from a space, simultaneously controlling the temperature and relative humidity of a space. Experimental and numerical work needs to be done on a HAMP in a real room situation to determine its performance and therefore its feasibility in a room. Eldeeb et al. (2012) performed simulations with a whole building commercial software package, comparing the indoor relative humidity conditions with a HAMP and with a typical all-air system. The simulations show that a HAMP has good potential to moderate the indoor relative humidity of a space. Further work needs to be done to determine the energy consumption of a HAMP system, compared to other systems.

During each test performed in this thesis, the temperature and density of the lithium chloride solution did not change much, as the total amount of heat and moisture transfer was small. However, in a real room situation, the amount of heat and moisture transfer will be larger and this will affect the temperature and density of the liquid desiccant. Future work needs to be done on regenerating the salt solution, so that the conditions inside the HAMP are at the appropriate temperature and density (concentration) required to control the indoor temperature and relative humidity. The regeneration of the liquid desiccant will add to the energy consumption of a

HAMP system, so it needs to be quantified before accurate comparisons can be made to other systems.

REFERENCES

Abou-Ellail, M.M.M. and S.M. Marcos, 1983. Buoyancy effects in the entrance region of horizontal rectangular channels, *Journal of Heat Transfer*, **105**, 924-928.

Afshin, M., 2010. Selection of the liquid desiccant in a run-around membrane energy exchanger, M.Sc. Thesis, Mechanical Engineering, University of Saskatchewan, Saskatoon, SK.

Akbari, S., 2012. Application of neural networks to predict the performance of a run-around membrane energy exchanger (RAMEE), M.Sc. Thesis, Mechanical Engineering, University of Saskatchewan, Saskatoon, SK.

Akbari, S., H.B. Hemingson, D. Beriault, C.J. Simonson, R.W. Besant, 2012. Application of neural networks to predict the steady state performance of a run-around membrane energy exchanger, *International Journal of Heat and Mass Transfer*, **55**, 1628-1641.

Almeida, F. and D. Naylor, 2011. Experimental study of free convection in a window with a heated between-panes blind, *Energy and Buildings*, **43**, 2647-2655.

ASHRAE, 2009. ASHRAE Handbook - Fundamentals, SI ed., American Society of Heating, Refrigerating and Air-Conditioning Engineers, Inc., Atlanta, GA.

ASHRAE, 2012. ASHRAE Handbook - HVAC systems and equipment, SI ed., American Society of Heating, Refrigerating and Air-Conditioning Engineers, Inc., Atlanta, GA, Chapter 6.

ASHRAE Standard 55 - 2010. Thermal environmental conditions for human occupancy, American Society of Heating, Refrigerating and Air-conditioning Engineers, Inc., Atlanta, GA.

ASHRAE Standard 84 – 2008. Method of testing air-to-air heat/energy exchangers, American Society of Heating, Refrigerating and Air-conditioning Engineers, Inc., Atlanta, GA.

ASME PTC 19.1 - 2005. Test Uncertainty, American Society of Mechanical Engineers, New York, NY.

ASTM Standard E104-2007. Standard practice for maintaining constant relative humidity by means of aqueous solutions, American Society for Testing and Materials International, West Conshohocken, PA.

Bergero, S. and A. Chiari, 2010. Performance analysis of a liquid desiccant and membrane contactor hybrid air conditioning system, *Energy and Buildings*, **42**, 1976-1986.

Bergero, S. and A. Chiari, 2011. Experimental and theoretical analysis of air humidification/dehumidification processes using hydrophobic capillary contactors, *Applied Thermal Engineering*, **21**, 1119-1135.

Bornehag, C.G., J. Sundell, S. Bonini, A. Custovic, P. Malmberg, S. Skerfving, T. Sigsgaard and A. Verhoeff, 2004. Dampness in buildings as a risk factor for health effects, EUROEXPO: a multidisciplinary review of literature (1998-2000) on dampness and mite exposure in buildings and health effects, *Indoor Air*, **14**, 243-257.

Catton, I., 1978. Natural convection in enclosures, Sixth International Heat Transfer Conference, Toronto, Canada, **6**, 13-31.

Chang, M.Y., C.H. Yu and T.F. Lin, 1997. Flow visualization and numerical simulations of transverse and mixed vortex roll formation in mixed convection of air in a horizontal flat duct, *International Journal of Heat and Mass Transfer*, **40**, 1907-1922.

Chen, H., S. Deng, H. Bruner Jr. and J. Garcia, 2004. Roots of mold problems and humidity control measures in institutional buildings with pre-existing mold condition, Proceedings of the Fourteenth Symposium on Improving Building Systems in Hot and Humid Climates, Richardson, Texas, May 17-20, paper ESL-HH-04-05-07.

Cheng, K.C, S.W. Hong and G.J. Hwang, 1972. Buoyancy effects on laminar heat transfer in the thermal entrance region of horizontal rectangular channels with uniform heat flux for large Prandtl Number fluid, *International Journal of Heat and Mass Transfer*, **15**, 1819-1836.

Chiranjivi, C. and S. Parabrahmachary, 1972. Experimental heat transfer studies in ducts of rectangular cross-section, *Indian Journal of Technology*, **10**, 296-298.

Chou, F.C., 1990. Laminar mixed convection in the thermal entrance region of horizontal rectangular channels with uniform heat input axially and uniform wall temperature circumferentially, *The Canadian Journal of Chemical Engineering*, **68**, 577-584.

Chou, F.C. and G.J. Hwang, 1984. Combined free and forced laminar convection in horizontal rectangular channels for high ReRa, *The Canadian Journal of Chemical Engineering*, **62**, 830-836.

Cisternas, L.A. and E.J. Lam, 1991. Analytic correlation for the vapour pressure of aqueous and non-aqueous solutions of single and mixed electrolytes: Part II - Application and extension, *Fluid Phase Equilibria*, **62**, 11-27.

Conde-Petit, M.R., 2009. Aqueous solutions of lithium and calcium chlorides: Property formulations for use in air conditioning equipment design, technical report published by M. Conde Engineering, Switzerland, 27 pages, available from http://www.mrc-eng.com/

Dieckmann, J., A. Cooperman and J. Brodrick, 2011. Cool and dry comfort, *ASHRAE Journal*, **53**(5), 90-94.

Djongyang, N., R. Tchinda and D. Njomo, 2009. A study of coupled heat and mass transfer across a semi-permeable building component in intertropical conditions, *Energy and Buildings*, **41**, 461-469.

Eldeeb, R., M. Fauchoux and C. Simonson, 2012. TRNSYS modeling of a novel ceiling panel designed to maintain space humidity in an office building, eSIM 2012 Building Simulation Conference, Halifax, N.S, May 1-4, 13 pages.

Fang, L., G. Clausen and P.O. Fanger, 1998a. Impact of temperature and humidity on the perception of indoor air quality, *Indoor Air*, **8**, 80-90.

Fang, L., G. Clausen and P.O. Fanger, 1998b. Impact of temperature and humidity on perception of indoor air quality during immediate and longer whole-body exposures, *Indoor Air*, **8**, 276-284.

Fauchoux, M.T., C.J. Simonson and D.A. Torvi, 2007. The effect of energy recovery on perceived air quality, energy consumption and the economics of an office building, *ASHRAE Transactions*, **113**(2), 436-448.

Fauchoux, M.T., C.J. Simonson and D.A. Torvi, 2009. Comfort, energy consumption and economics of a school with energy recovery, *ASHRAE Transactions*, **115**(2), 519-530.

Fauchoux, M.T., C.J. Simonson and D.A. Torvi, 2010. Flow visualization of airflow through a rectangular duct with combined heat and mass transfer, Proceedings of the ASME 14th International Heat Transfer Conference, Washington, D.C., USA, August 8-13.

Fauchoux, M., M. Bansal, P. Talukdar, C.J. Simonson and D. Torvi, 2010. Testing and modeling of a novel ceiling panel for maintaining space relative humidity by moisture transfer, *International Journal of Heat and Mass Transfer*, **53**, 3961-3968

Fauchoux, M.T., C. Simonson, D. Torvi and P. Talukdar, 2011. CFD modelling with buoyancy effects for a heat and moisture transfer ceiling panel, *Proceedings of the ASME/JSME 8th Thermal Engineering Joint Conference*, Honolulu, HI, USA, March 13-17.

Feustel, H.E. and C. Stetiu, 1995. Hydronic radiant cooling - preliminary assessment, *Energy and Buildings*, **22**, 193-205.

Fisk, W.J., Q. Lei-Gomez and M.J. Mendell, 2007. Meta-analysis of the associations of respiratory health effects with dampness and mold in homes, *Indoor Air*, **17**, 284-296.

Hemingson, H., 2010. The impacts of outdoor air conditions and non-uniform exchanger channels on a run-around membrane energy exchanger, M.Sc. Thesis, Mechanical Engineering, University of Saskatchewan, Saskatoon, SK.

Hemingson, H.B., C.J. Simonson, R.W. Besant, 2011. Steady-state performance of a run-around membrane energy exchanger (RAMEE) for a range of outdoor air conditions, *International Journal of Heat and Mass Transfer*, **54**, 1814-1824.

Huang, S.M., L.Z. Zhang, K. Tang and L.X. Pei, 2012. Fluid flow and heat mass transfer in membrane parallel-plates channels used for liquid desiccant air dehumidification, *International Journal of Heat and Mass Transfer*, **55**, 2571-2580.

Huisseune, H., 2012. Performance evaluation of louvered fin compact heat exchangers with vortex generators, Ph.D. Thesis, Ghent University, Ghent, Belgium.

Hutcheon, N.B., 1971. Buildings for the canadian climate, National Research Council of Canada Division of Building Research, Technical Report 336.

Idelchik I.E., 1986. Handbook of hydraulic resistance, 2nd ed., Hemisphere Publishing Corporations, New York, NY, Ch 1.

Incropera, F.P., A.L. Knox and J.R. Maughan, 1987. Mixed-convection flow and heat transfer in the entry region of horizontal rectangular duct, *Journal of Heat Transfer*, **109**, 434-439.

Incropera, F.P. and D.P. DeWitt, 2002. Fundamentals of heat and mass transfer, 5th ed., John Wiley and Sons, Inc., Toronto, ON.

Imanari, T., T. Omori and K. Bogaki, 1999. Thermal comfort and energy consumption of the radiant ceiling panel system - Comparison with the conventional all-air system, *Energy and Buildings*, **30**, 167-175.

Iskra, Conrad, 2007. Convective mass transfer between a hydrodynamically developed airflow and liquid water with and without a vapor permeable membrane, M.Sc. Thesis, Mechanical Engineering, University of Saskatchewan, Saskatoon, SK.

Kays, W.M. and H.C. Perkins, 1985. Forced convection - Internal flow in ducts. In W.M. Rohsenow, J.P. Hartnett and E.N. Ganic (Eds.), Handbook of heat transfer - Fundamentals, 2nd ed., McGraw-Hill Book Company, Toronto, ON, Chapter 7.

Kim, T., S. Kato, S. Murakami and J. Rho, 2005. Study on indoor thermal environment of office space controlled by cooling panel system using field measurement and the numerical simulation, *Building and Environment*, **40**, 301-310.

Kooijman, J.M, 1973. Laminar heat or mass transfer in rectangular channels and in cylindrical tubes for fully developed flow: Comparison of solutions obtained for various boundary conditions, *Chemical Engineering Science*, **28**, 1149-1160.

Kosonen, R. and F. Tan, 2004. Assessment of productivity loss in air-conditioned buildings using PMV index, *Energy and Buildings*, **36**, 987-993.

Kozubal, E., J. Wood, J. Burch, A. Boranian and T. Merrigan, 2011. Desiccant enhanced evaporative air-conditioning (DEVap): Evaluation of a new concept in ultra efficient air conditioning, *National Renewable Energy Laboratory Technical Report*, **TP-5500-49722**, 71 pages.

Krishnamurty, V.V.G and N.V. Sambasiva Rao, 1967. Heat transfer in non-circular conduits: Part IV - Laminar forced convection in rectangular channels, *Indian Journal of Technology*, **5**, 331-333.

Kurnitski, J., T. Kalamees, J. Palonen, L. Eskola and O. Seppanen, 2007. Potential effects of permeable and hygroscopic lightweight structures on thermal comfort and perceived IAQ in a cold climate, *Indoor Air*, **17**, 37-49.

Larson, Michael, 2006. The performance of membranes in a newly proposed run-around heat and moisture exchanger, M.Sc. Thesis, Mechanical Engineering, University of Saskatchewan, Saskatoon, SK.

Lin, J.N. and F.C. Chou, 1989. Laminar mixed convection in the thermal entrance region of horizontal isothermal rectangular channels, *The Canadian Journal of Chemical Engineering*, **67** (June), 361-367.

Lin, W.L. and T.F. Lin, 1996. Experimental study of unstable mixed convection of air in a bottom heated horizontal, rectangular duct, *International Journal of Heat and Mass Transfer*, **39**, 1649-1663.

Lin, J.N., F.C. Chou, W.M. Yan and P.Y. Tzeng, 1992a. Combined buoyancy effects of thermal and mass diffusion on laminar forced convection in the thermal entrance region of horizontal square channels, *The Canadian Journal of Chemical Engineering*, **70**, 681-689.

Lin, J.N., P.Y. Tzeng, F.C. Chou and W.M. Yan, 1992b. Convective instability of heat and mass transfer for laminar forced convection in the thermal entrance region of horizontal rectangular channels, *International Journal of Heat and Fluid Flow*, **13**(3), 250-258.

Lowenstein, A., 2008. Review of liquid desiccant technology for HVAC applications, *HVAC&R Research*, **14**, 819-839.

Lyczkowski, R.W., C.W. Solbrig and D. Gidaspow, 1981. Forced convection heat transfer in rectangular ducts - general case of wall resistances and peripheral conduction for ventilation cooling of nuclear waste repositories, *Nuclear Engineering and Design*, **67**, 357-378.

Mahmud, K., G.I. Mahmood, C.J. Simonson and R.W. Besant, 2010. Performance testing of a counter-cross-flow run-around membrane energy exchanger (RAMEE) system for HVAC applications, *Energy and Buildings*, **42**, 1139-1147.

McWhinney, M., A. Fanara, R. Clark, C. Hershberg, R. Schmeltz and J. Roberson, 2005. ENERGY STAR product specification development framework: using data and analysis to make program decisions, *Energy Policy*, **33**, 1613-1625.

Mehta, R.D. (1979). The aerodynamic design of blower tunnels with wide-angle diffusers, *Progress in Aerospace Sciences*, **18**, 59-120.

Miriel, J., L. Serres and A. Trombe, 2002. Radiant ceiling panel heating-cooling systems: experimental and simulated study of the performances, thermal comfort and energy consumptions, *Applied Thermal Engineering*, **22**, 1861-1873.

Moon, H.J. and Y.R. Yoon, 2010. Investigation of physical characteristics of houses and occupants' behavioural factors for mould infestation in residential buildings, *Indoor and Built Environment*, **19**, 57-64.

Morcos, S.M., M.M. Hilal, M.M. Kamel and M.S. Soliman, 1986. Experimental investigation of mixed laminar convection in the entrance region of inclined rectangular channels, *Journal of Heat Transfer*, **108**, 574-579.

Narusawa, U. 1993. Numerical analysis of mixed convection at the entrance region of a rectangular duct heated from below, *International Journal of Heat and Mass Transfer*, **36**, 2375-2384.

Nyce, T.A., J. Ouazzani, A. Durand-Daubin and F. Rosenberger, 1992. Mixed convection in a horizontal rectangular channel - experimental and numerical velocity distributions, *International Journal of Heat and Mass Transfer*, **35**, 1481-1494.

Olutimayin, S.O. and C.J. Simonson, 2005. Measuring and modeling vapour boundary layer growth during transient diffusion heat and moisture transfer in cellulose insulation, *International Journal of Heat and Mass Transfer*, **48**, 3319-3330.

Omega Engineering, 2011. Temperature products, Retrieved Jan 31, 2011, from Omega Engineering, Inc., Stamford CT: www.omega.com.

Ogasawara, T., T. Kurabuchi, Y.Asari and K. Kumagai, 2011. CFD simulation based on the relationship between absolute humidity and influenza survival rate, Proceedings of Roomvent 2011, 12th International Conference on Air Distribution in Rooms, Trondheim, Norway, June 19-22.

Ou J.W., K.C. Cheng and R.C. Lin, 1974. Natural convection effects on Graetz problem in horizontal rectangular channels with uniform wall temp for large Pr, *International Journal of Heat and Mass Transfer*, **17**, 835-843.

Ou J.W., K.C. Cheng and R.C. Lin, 1976. Combined free and forced laminar convection in inclined rectangular channels, *International Journal of Heat and Mass Transfer*, **19**, 277-283.

Qin, M. and R. Belarbi, 2005. Development of an analytical method for simultaneous heat and moisture transfer in building materials utilizing transfer function method, *Journal of Materials in Civil Engineering*, **17**, 492-497.

Qin, M., R. Belarbi, A. Aït-Mokhtar and A. Seigneurin, 2006. An analytical method to calculate the coupled heat and moisture transfer in building materials, *International Communications in Heat and Mass Transfer*, **33**, 39-48.

Raithby, G.D. and K.G.T. Hollands, 1985. Natural convection. In W.M. Rohsenow, J.P. Hartnett and E.N. Ganic (Eds.), Handbook of heat transfer – Fundamentals, 2nd ed., McGraw-Hill Book Company, Toronto, ON, Chapter 6.

Reinikainen, L.M., J.J.K. Jaakkola and O. Seppanen, 1992. The effect of air humidification on symptoms of perception of indoor air quality in office workers: a six-period cross-over trial, *Archives of Environmental Health*, **47**, 8-15.

Savino, J.M. and R. Siegel, 1964. Laminar forced convection in rectangular channels with unequal heat addition on adjacent sides, *International Journal of Heat and Mass Transfer*, **7**, 733-741.

Shah, R.K. and M.S. Bhatti, 1987. Laminar convective heat transfer in ducts. In S. Kakac, R.K. Shah and W. Aung (Eds.), Handbook of single-phase convective heat transfer, John Wiley and Sons, Inc., Toronto, ON, Chapter 3.

Shah, R.K. and A.L. London, 1974. Thermal boundary conditions and some solutions for laminar duct flow forced convection, *Journal of Heat Transfer*, **96**, 159-165.

Shah, R.K. and A.L. London, 1978. Laminar flow forced convection in ducts. In T.F. Irvine and J.P. Hartnett (Eds.), Advances in heat transfer, Supplement 1, Academic Press, New York, NY, Chapter 7.

Simmonds, P., 1997. Radiant systems offer users greater comfort control. (hydronic radiant conditioning systems), *Energy User News*, **March**, BNP Media, Troy, MI.

Simonson, C.J. and R.W. Besant, 1999a. Energy wheel effectiveness: part I – development of dimensionless groups, *International Journal of Heat and Mass Transfer*, **42**, 2161-2170.

Simonson, C.J. and R.W. Besant, 1999b. Energy wheel effectiveness: part II – correlations, *International Journal of Heat and Mass Transfer*, **42**, 2171-2185.

Simonson, C.J., M. Salonvaara and T. Ojanen, 2002. The effect of structures on indoor humidity - Possibility to improve comfort and perceived air quality, *Indoor Air*, **12**, 1-9.

Simonson, C.J., M. Salonvaara and T. Ojanen, 2004a. Heat and mass transfer between indoor air and a permeable and hygroscopic building envelope: Part I - Field measurements, *Journal of Thermal Envelope and Building Science*, **28**, 63-101.

Simonson, C.J., M. Salonvaara and T. Ojanen, 2004b. Heat and mass transfer between indoor air and a permeable and hygroscopic building envelope: Part II - Verification and numerical studies, *Journal of Thermal Envelope and Building Science*, **28**, 161-185.

Simonson, C.J., M. Salonvaara and T. Ojanen, 2004c. Moderating indoor conditions with hygroscopic building materials and outdoor ventilation, *ASHRAE Transactions*, **110**(2), 804-819.

Sodec, F., 1999. Economic viability of cooling ceiling systems, *Energy and Buildings*, **30**, 195-201.

Steeman, H.J., 2009. Modelling local hygrothermal interaction between airflow and porous materials for buildings applications, Ph.D. Thesis, Ghent University, Ghent, Belgium.

Talukdar, P., C.R. Iskra and C.J. Simonson, 2008. Combined heat and mass transfer for laminar flow of moist air in a 3D rectangular duct: CFD simulation and validation with experimental data, *International Journal of Heat and Mass Transfer*, **51**, 3091-3102.

Toftum, J., A.S. Jorgensen and P.O. Fanger, 1998a. Upper limits of air humidity for preventing warm respiratory discomfort, *Energy and Buildings*, **28**, 15-23.

Toftum, J., A.S. Jorgensen and P.O. Fanger, 1998b. Upper limits for indoor air humidity to avoid uncomfortably humid skin, *Energy and Buildings*, **28**, 1-13.

United States Department of Energy, 2010. Buildings energy data book. Retrieved Feb 28, 2012, from Energy Efficient and Renewable Energy, U.S. Department of Energy, Washington, D.C.: http://buildingsdatabook.eere.energy.gov.

Vali, A., C.J. Simonson, R.W. Besant and G. Mahmood, 2009. Numerical model and effectiveness correlations for a run-around heat recovery system with combined counter and cross flow exchangers, *International Journal of Heat and Mass Transfer*, **52**, 5827-5840.

Vangtook, P. and S. Chirarattananon, 2006. An experimental investigation of application of radiant cooling in hot humid climate, *Energy and Buildings*, **38**, 273-285.

Vangtook, P. and S. Chirarattananon, 2007. Application of radiant cooling as a passive cooling option in hot humid climate, *Building and Environment*, **42**, 543-556.

Witte, M.J. and R.H. Henninger, 2010. Evaluating the ability of unitary equipment to maintain adequate space humidity levels, *ASHRAE Transactions,* **116**(1), 365-381.

Wyon, D.P., L. Fang, L. Lagercrantz and P.O. Fanger, 2006. Experimental determination of the limiting criteria for human exposure to low winter humidity indoors, *HVAC&R Research*, **12**, 201-213.

Yan, W.M., 1994. Mixed convection heat and mass transfer in inclined rectangular ducts, *International Journal of Heat and Mass Transfer*, **37**, 1857-1866.

Yan, W.M., 1996. Combined buoyancy effects of thermal and mass diffusion on laminar forced convection in horizontal rectangular ducts, *International Journal of Heat and Mass Transfer*, **39**, 1479-1488.

Zaytsev, I.D. and G.G. Aseyev, 1992. Properties of aqueous solutions of electrolytes, CRC Press, Inc., Boca Raton, FL.

Zhang, L.Z., 2011. An analytical solution to heat and mass transfer in hollow fiber membrane contactors for liquid desiccant air dehumidification, *Journal of Heat Transfer*, **133**, 8 pages.

Zhang, L.Z and S.M. Huang, 2011. Coupled heat and mass transfer in a counter flow hollow fiber membrane module for air humidification, *International Journal of Heat and Mass Transfer*, **54**, 1055-1063.

Zhang, L.Z., S.M. Huang, J.H. Chi and L.X. Pei, 2012. Conjugate heat and mass transfer in a hollow fiber membrane module for liquid desiccant air dehumidification: a free surface model approach, *International Journal of Heat and Mass Transfer,* **55**, 3789-3799.

APPENDIX A – DETAILED LIST OF EQUATIONS

This appendix gives a detailed list of the important equations used in this thesis, to create an easy reference for the reader. Figure A.1 shows a schematic of the test section with the HAMP located in the top of the duct. The schematic shows the location of the three measurement points; upstream of the test section, downstream of the test section and inside the HAMP. These terms will be used in the equations in this Appendix.

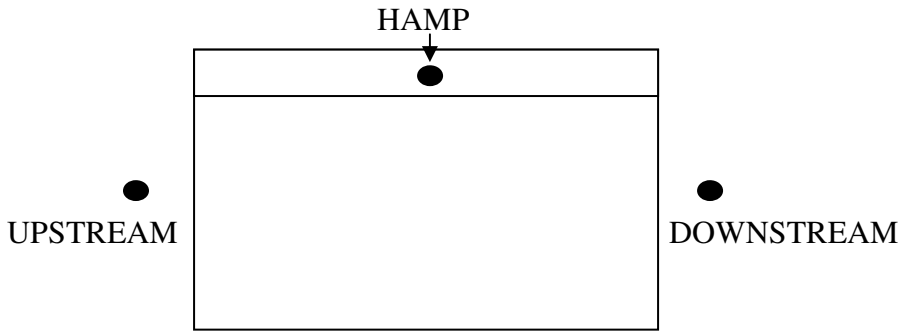

FIGURE A.1. Schematic of the test section, with measurement locations marked.

A.1 PERFORMANCE OF THE PROTOTYPE HAMP

Sensible effectiveness (Equation 1.1)

$$\varepsilon_{sensible}=\frac{T_{DOWNSTREAM}-T_{UPSTREAM}}{T_{HAMP}-T_{UPSTREAM}} \tag{A.1}$$

where T = temperature [°C or K]

Latent effectiveness (Equation 1.2)

$$\varepsilon_{latent}=\frac{W_{DOWNSTREAM}-W_{UPSTREAM}}{W_{HAMP}-W_{UPSTREAM}} \quad (A.2)$$

where W = humidity ratio [g_w/kg_{air}]

$$W=0.62198\frac{P_{ws}\phi}{P_{atm}-P_{ws}\phi} \quad (A.3)$$

where P_{ws} = saturated pressure of water vapour [Pa]
ϕ = relative humidity (as a fraction) [-]
P_{atm} = atmospheric pressure of the lab = 95,859 Pa

$$P_{ws}=\exp\left[\frac{C_8}{T}+C_9+C_{10}T+C_{11}T^2+C_{12}T^3+C_{13}(\ln T)\right] \quad (A.4)$$

where $C_8 = -5.8002206 \times 10^3$
$C_9 = 1.3914993$
$C_{10} = -4.8640239 \times 10^{-2}$
$C_{11} = 4.1764768 \times 10^{-5}$
$C_{12} = -1.4452093 \times 10^{-8}$
$C_{13} = 6.5459673$

Total effectiveness (Equation 1.3)

$$\varepsilon_{total}=\frac{h_{DOWNSTREAM}-h_{UPSTREAM}}{h_{HAMP}-h_{UPSTREAM}} \quad (A.5)$$

where h = enthalpy [kJ/kg_{air}]

$$h=1.006T+W(2501+1.86T) \quad (A.6)$$

where T = temperature [°C]
W = humidity ratio [kg_w/kg_{air}]

A.2 CONSERVATION OF ENERGY AND MASS

Conservation of energy (equation 3.12)

$$(\dot{m}_{air}h_{air})_{UPSTREAM}-(\dot{m}_{air}h_{air})_{DOWNSTREAM}-(\dot{m}_{w}h_{w})-h_{conv}A_{surface}\Delta T_{lm}=0 \quad (A.7)$$

where $\dot{m}_{air}$ = mass flow rate of air [kg_{air}/s]
h_{air} = enthalpy of air [kJ/kg_{air}] (equation A.5)
$\dot{m}_{w}$ = mass flow rate of water vapour [kg_{w}/s]
h_{w} = enthalpy of water vapour [kJ/kg_{w}]
h_{conv} = heat transfer coefficient of air [$W/(m^2 \cdot K)$]
$A_{surface}$ = surface area of the HAMP [m^2]
ΔT_{lm} = temperature difference between the air and the HAMP [°C]

$$\dot{m}_{w}=\dot{m}_{air}(W_{UPSTREAM}-W_{DOWNSTREAM}) \quad (A.8)$$

where W = humidity ratio [g_{w}/kg_{air}]

$$\dot{m}_{air}=\rho_{air}A_{c}V \quad (A.9)$$

where ρ_{air} = density of the airflow [kg_{air}/m^3]
A_c = cross-sectional area of the duct [m^2]
V = axial velocity of the airflow [m/s]

$$\rho_{air}=\frac{P_{atm}-P_{ws}\emptyset}{RT} \quad (A.10)$$

where P_{atm} = atmospheric pressure of the lab = 95,859 Pa
P_{ws} = saturated pressure of water vapour [Pa]
ϕ = relative humidity (as a fraction) [-]
R= ideal gas constant for air = 287 $kJ/(kg_{air} \cdot K)$
T = temperature of the air [K]

$$h_w=2501+1.86T_w \tag{A.11}$$

where T_w = temperature of the water vapour [°C or K]

$$Nu=0.93Re^{1/3}Pr^{1/3}\left(\frac{\mu_{avg}}{\mu_{bulk}}\right)^{0.14}\left(\frac{Z}{D_h}\right)^{-1/3}\int_0^1 \phi_x^{1/3}dr^* \tag{A.12}$$

where Re = Reynolds number [-]
Pr = Prandtl number [-]
μ_{avg} = dynamic viscosity at the average air temperature[Pa·s]
μ_{bulk} = dynamic viscosity at the bulk air temperature [Pa·s]
Z = length of the heat transfer surface [m]
D_h = hydraulic diameter of the duct [m]
$\phi_x^{1/3}$ = a constant dependent on the aspect ratio of the duct
* Krishnamurty and Sambasiva Rao (1967)

$$h=\frac{Nuk_{air}}{D_h} \tag{A.13}$$

where k_{air} = thermal conductivity of air [W/(m·K)]

Log mean temperature difference (equation 3.13)

$$\Delta T_{lm}=\frac{\Delta T_{in}-\Delta T_{out}}{\ln\left(\Delta T_{in}/\Delta T_{out}\right)} \tag{A.14}$$

where $\Delta T_{in} = T_{HAMP} - T_{UPSTREAM}$ [°C or K]
$\Delta T_{out} = T_{HAMP} - T_{DOWNSTREAM}$ [°C or K]

Conservation of mass (equation 3.15)

$$(\dot{m}_{air} W_{air})_{UPSTREAM} - (\dot{m}_{air} W_{air})_{DOWNSTREAM} - \frac{\Delta mass}{t} = 0 \quad \text{(A.15)}$$

where $\dot{m}_{air}$ = mass flow rate of air [kg_{air}/s]
W_{air} = humidity ratio of the air [g_w/kg_{air}]
$\Delta mass$ = mass of water added to or removed from reservoir tank [kg_w]
t = duration of test [s]

A.3 HEAT EXCHANGER PARAMETERS

Heat capacity rate (equation 4.5)

$$Cr = \frac{(\dot{m}c_p)_{air}}{(\dot{m}c_p)_{sol}} \quad \text{(A.16)}$$

where $\dot{m}$ = mass flow rate
c_p = specific heat [J/(kg·K)]

Number of heat transfer units (equation 4.7)

$$NTU = \frac{UA_{surface}}{\dot{m}_{air} c_{p,air}} \quad \text{(A.17)}$$

where U = overall heat transfer coefficient [$W/(m^2 \cdot K)$]
$A_{surface}$ = heat transfer surface area of the HAMP [m^2]
$\dot{m}_{air}$ = mass flow rate of air [kg_{air}/s] from equation (A.9)
$c_{p,air}$ = specific heat of air[J/(kg·K)]

Number of mass transfer units (equation 4.25)

$$NTU_m = \frac{U_m A_{surface}}{\dot{m}_{air}} \quad \text{(A.18)}$$

where U_m = overall mass transfer coefficient [$kg_{air}/(m^2 \cdot s)$]

Theoretical overall heat transfer coefficient (equation 4.9)

$$U_{theo}=\left[\left(h_{eff,air}\right)^{-1}+\left(\frac{k_{membrane}}{\delta_{membrane}}\right)^{-1}+\left(h_{sol}\right)^{-1}\right]^{-1} \tag{A.19}$$

where $h_{eff,air}$ = effective heat transfer coefficient in the air [W/(m^2·K)]
$k_{membrane}$ = thermal conductivity of the semi-permeable membrane [W/(m·K)]
$\delta_{membrane}$ = thickness of the semi-permeable membrane [m]
h_{sol} = convection heat transfer coefficient in the liquid desiccant [W/(m^2·K)]

$$h_{eff,air}=h_r+h_{conv} \tag{A.20}$$

where h_r = radiation heat transfer coefficient [W/(m^2·K)]
h_{conv} = convection heat transfer coefficient [W/(m^2·K)]

$$h_r=\frac{\sigma}{\frac{1-\varepsilon_1}{\varepsilon_1 A_1}+\frac{1}{A_1 F_{12}}+\frac{1-\varepsilon_2}{\varepsilon_2 A_2}}\frac{\left(T_1+T_2\right)\left(T_1^2+T_2^2\right)}{A_{surface}} \tag{A.21}$$

where T = temperature [°C or K]
σ = Stefan-Boltzmann constant, equal to 5.67x10^{-8} W/(m^2·K^4)
ε = emissivity of the surface [-]
A = surface area [m^2]
1 – refers to HAMP surface
2 – refers to other surfaces in the test section

Theoretical Overall mass transfer coefficient (equation 4.27)

$$U_{m,theo}=\left[\left(h^W_{m,air}\right)^{-1}+\left(\frac{\rho_{air}}{R_{membrane}}\right)^{-1}+\left(h^W_{m,sol}\right)^{-1}\right]^{-1} \tag{A.22}$$

where $h^W_{m,air}$ = convection mass transfer coefficient of the air [kg$_{air}$/(m^2·s)]
ρ_{air} = density of air [kg$_{air}$/m^3]
$R_{membrane}$ = resistance to vapour diffusion of the semi-permeable membrane [s/m]
$h^W_{m,sol}$ = convection mass transfer coefficient of the solution [kg$_{air}$/(m^2·s)]

A.4 FORCED CONVECTION PARAMETERS

Reynolds number (equation 4.14)

$$Re=\frac{V_{air}D_h}{\upsilon_{air}} \tag{A.23}$$

where V_{air} = velocity of the air [m/s]
D_h = hydraulic diameter [m]
ν_{air} = kinematic viscosity of the air [m^2/s]

Convection heat transfer coefficient (equation 4.16)

$$h_{air}=\frac{Nuk_{air}}{D_h} \tag{A.24}$$

where Nu = Nusselt number [-]
k_{air} = thermal conductivity of the air [W/(m·K)]
D_h = hydraulic diameter [m]

Forced convection correlation- Krishnamurty and S. Rao (1967) (equation 4.15)

$$Nu=0.93Re^{1/3}Pr^{1/3}\left(\frac{\mu_{avg}}{\mu_{bulk}}\right)^{0.14}\left(\frac{Z}{D_h}\right)^{-1/3}\int_0^1 \phi_x^{1/3}dr \tag{A.25}$$

where Re = Reynolds number [-]
Pr = Prandtl number [-]
μ_{avg} = dynamic viscosity at the average air temperature[Pa·s]
μ_{bulk} = dynamic viscosity at the bulk air temperature [Pa·s]
Z = length of the heat transfer surface [m]
D_h = hydraulic diameter of the duct [m]
$\phi_x^{1/3}$ = a constant dependent on the aspect ratio of the duct

A.5 NATURAL CONVECTION PARAMETERS

Heat transfer Rayleigh number (Equation 4.17)

$$Ra_h = \frac{g\beta(T_{avg}-T_{HAMP})H^3 Pr}{\nu^2} \quad (A.26)$$

where g = acceleration due to gravity [m/s^2]
β = volumetric expansion coefficient [1/K]
T = temperature [K]
H = height of the duct [m]
Pr = Prandtl number [-]
ν = kinematic viscosity of air [m^2/s]

$$\beta = \frac{1}{T_{bulk}} \quad (A.27)$$

where T_{bulk} = bulk temperature in the duct [°C or K]

$$T_{avg} = \frac{T_{UPSTREAM}+T_{DOWNSTREAM}}{2} \quad (A.28)$$

where T = temperature °[C]

Mass transfer Rayleigh number (Equation 4.18)

$$Ra_m = \frac{g\left(\frac{M_{air}}{M_w}-1\right)(C_{avg}-C_{HAMP})H^3 Sc}{\nu^2} \quad (A.29)$$

where M_{air} = molecular weight of air [kg_{air}/mol]
M_w = molecular weight of water vapour [kg_w/mol]
C = concentration of water vapour [-]
Sc = Schmidt number [-]

$$C=\frac{P_w M_w}{P_w M_w+(P_{atm}-P_w)M_{air}} \quad (A.30)$$

where P_w = partial pressure of water vapour [Pa]
P_{atm} = atmospheric pressure in the lab = 95,859 Pa

Effective Rayleigh number (Equation 4.19)

$$Ra^{+}=Ra_h+Ra_m \quad (A.31)$$

Convection heat transfer coefficient (equation 4.21)

$$h_{air}=\frac{Nuk_{air}}{H} \quad (A.32)$$

where Nu = Nusselt number [-]
k_{air} = thermal conductivity of the air [W/(m·K)]
H = height of the duct [m]

Natural convection correlation- Raithby and Hollands (1985) (equation 4.20)

$$Nu=1+\left[1-\frac{Ra_{cr}}{Ra}\right]^{\blacksquare}\left[k_1+2\left(\frac{Ra^{1/3}}{k_2}\right)^{1-\ln(Ra^{1/3}/k_2)}\right]+$$

$$\left[\left(\frac{Ra}{5380}\right)^{1/3}-1\right]^{\blacksquare}\left(1-\exp\left\{-0.95\left[\left(\frac{Ra}{Ra_{cr}}\right)^{1/3}-1\right]^{\blacksquare}\right\}\right) \quad (A.33)$$

where Ra_{cr} = critical Rayleigh number for the duct [-]
Ra = Rayleigh number [-]
k_1 = a constant, equal to 1.40 for air [-]
k_2 = a constant, equal to 446 for air [-]
$[\ ]^{\blacksquare}$ indicates that only positive values of the expression are to be taken

Richardson number (equation 4.22)

$$Ri = \frac{Ra/Pr}{Re^2} \tag{A.34}$$

where Ra = Rayleigh number [-]
Pr = Prandtl number [-]
Re = Reynolds number [-]

A.6 FLAT PLATE THEORY

Average Nusselt number (Incropera and DeWitt (2002))

$$Nu = 0.664 Re^{1/2} Pr^{1/3} \tag{A.35}$$

where Re = Reynolds number based on length of the plate [-]
Pr = Prandtl number [-]
valid for Pr > 0.6

A.7 CHILTON-COLBURN HEAT AND MASS TRANSFER ANALOGY

Convection mass transfer coefficient (equation 4.28)

$$\frac{h_{air}}{c_{p,air} h^{W}_{m,air}} = Le^{2/3} \tag{A.36}$$

where h_{air} = convection heat transfer coefficient [$W/(m^2 \cdot K)$]
$h_{m,air}$ = convection mass transfer coefficient [$kg_{air}/(m^2 \cdot s)$]
$c_{p,air}$ = specific heat of air [$J/(kg \cdot K)$]
Le = Lewis number [-]

$$Le = \frac{Sc}{Pr} \tag{A.37}$$

where Pr = Prandtl number [-]
Sc = Schmidt number [-]

A.8 OPERATING CONDITIONS

Operating condition factor (Equation 4.29)

$$H^{*}=2500\frac{\Delta W}{\Delta T} \tag{A.38}$$

where $\Delta W = W_{UPSTREAM} - W_{HAMP}$ [g_w/kg_{air}]
$\Delta T = T_{UPSTREAM} - T_{HAMP}$ [°C or K]

A.9 TOTAL HEAT AND MASS FLUXES

Total heat flux (equation 5.1)

$$q''=U\Delta T_{lm} \tag{A.39}$$

where U = overall heat transfer coefficient [$W/(m^2 \cdot K)$]
ΔT_{lm} = temperature difference between the air and the HAMP [°C]

Total mass flux (equation 5.2)

$$\dot{m}''=U_m^W \Delta W_{lm} \tag{A.40}$$

where U_m = overall mass transfer coefficient [$kg_{air}/(m^2 \cdot s)$]
ΔW_{lm} = humidity ratio difference between the air and the HAMP [g_w/kg_{air}]

A.10 DESIGN PARAMETERS

Effectiveness-NTU correlations (equations 6.3 and 6.4) for Cr = 0

$$\varepsilon_{sensible}=1-\exp(-NTU) \tag{A.41}$$

$$\varepsilon_{latent}=1-\exp(-NTU_m) \tag{A.42}$$

Experimental overall heat transfer coefficient (equation 6.8)

$$U_{exp} = \frac{\dot{m}_{air} c_{p,air} (T_{DOWNSTREAM} - T_{UPSTREAM})}{A_{surface} \Delta T_{lm}} \quad (A.43)$$

where $\dot{m}_{air}$ = mass flow rate of air [kg_{air}/s] from equation (A.9)
$c_{p,air}$ = specific heat of air[J/(kg·K)]
$A_{surface}$ = heat transfer surface area of the HAMP [m^2]
T = temperature [°C or K]
ΔT_{lm} = log mean temperature difference between the airflow and the HAMP from equation (A.14) [°C or K]

Experimental overall mass transfer coefficient (equation 6.10)

$$U_{m,exp} = \frac{\dot{m}_{air} (W_{DOWNSTREAM} - W_{UPSTREAM})}{A_{surface} \Delta W_{lm}} \quad (A.44)$$

where W = humidity ratio [g_w/kg_{air}]
ΔW_{lm} = log mean humidity ratio difference between the airflow and the HAMP from equation (A.14) [g_w/kg_{air}]

APPENDIX B – LIQUID DESICCANT CORRELATIONS

The temperature and density of the liquid desiccant inside the prototype HAMP are measured during each test. Although heat and moisture are being transferred between the HAMP and the airflow, there is little change in the temperature or density during each test. The temperature and density of the salt solution are therefore considered constant for each test. The temperature and density of the liquid desiccant are used to calculate the surface humidity ratio and relative humidity of the liquid desiccant for each test. This Appendix discusses the properties and correlations required for these calculations.

B.1 HUMIDITY RATIO AND RELATIVE HUMIDITY CORRELATIONS

The liquid desiccant used in this study is a mixture of lithium chloride and water. The concentration of lithium chloride in the salt solution is calculated from correlations given by Cisternas and Lam (1991), using the density of the liquid desiccant (ρ_{HAMP}) and the density of water at the temperature of the liquid desiccant (ρ_w). The concentration of the salt solution is given by

$$C_{salt}=\frac{\log(\rho_{HAMP})-\log(\rho_w)}{A_i}*100 \qquad (B.1)$$

where A_i is calculated from

$$A_i=0.2452+1.9x10^{-8}T_{HAMP}^2 \qquad (B.2)$$

for a lithium chloride solution, where T_{HAMP} is the temperature of the liquid desiccant inside the HAMP [K]. The concentration, C_{salt} is expressed as a percentage. It may also be expressed as a fraction, using the term γ_{salt}. The density of water is calculated as

$$\rho_w=1000-0.062T_{HAMP}-0.00355T_{HAMP}^2. \quad (B.3)$$

The surface humidity ratio of the liquid desiccant is calculated from ASHRAE (2009) as

$$W=621.98\left(\frac{P_w}{P_{atm}-P_w}\right) \quad (B.4)$$

where P_w is the partial pressure of water vapour [Pa], and P_{atm} is the atmospheric pressure in the lab, which is measured to be 95.9 kPa. The surface relative humidity is also defined by ASHRAE (2009) as

$$RH=\frac{P_w}{P_{ws}}*100 \quad (B.5)$$

where P_{ws} is the saturation pressure of water [Pa]. The relative humidity may be expressed as a percentage (as in Equation B.5) or as a fraction, using the symbol ϕ.

The partial pressure of water vapour for a salt solution is given by Cisternas and Lam (1991) as

$$LogP_w=KI\left[A-\frac{B}{T_{HAMP}-39.53}\right]+\left[C-\frac{D}{T_{HAMP}-39.53}\right] \quad (B.6)$$

where K = an electrolyte parameter (given as 0.72567 for LiCl),
I = ionic strength of the solution [mol/kg]
T_{HAMP} = temperature of the liquid desiccant inside the HAMP [K] and
A, B, C and D = parameters which depend on the type of salt solution used.

The ionic strength of the solution is

$$I=\frac{1}{2}z^2m \quad (B.7)$$

where z is the charge of the ionic species (equal to 2 for LiCl) [-] and m is the molality of the solution [$mol_{solute}/kg_{solvent}$]. The molality is calculated from

$$m=\frac{1000}{X_{sol}M_{salt}} \tag{B.8}$$

where X_{sol} is the ratio of the mass of water to the mass of pure salt in the solution [kg_w/kg_{salt}] and M_{salt} is the molecular weight of the salt (42.4 kg_{salt}/mol for LiCl). The ratio of the mass of water to the mass of pure salt in the solution is calculated from the concentration of the salt, expressed as a fraction,

$$X_{sol}=\frac{1}{\gamma_{salt}}-1. \tag{B.9}$$

The parameters A, B, C and D used in Equation (B.6) are calculated from the following set of equations, when water is the solvent:

$$A=-0.021+3.61x10^{-4}I+\frac{M_w}{2303} \tag{B.10}$$

$$B=-5.39+1.38I-0.031I^2 \tag{B.11}$$

$$C=7.19-3.99x10^{-3}I-1.12x10^{-4}I^2+M_wI\frac{(1-\chi)}{2303}, \text{ and} \tag{B.12}$$

$$D=1730-0.138I+0.028I^2-1.79x10^{-3}I^3. \tag{B.13}$$

In the above equations, M_w is the molecular weight of water, equal to 18 kg_w/mol. The value of the coefficients in each of these equations are specific to lithium chloride. The value of χ used in Equation (B.12) is calculated from

$$\chi=\frac{2\left(\upsilon_+ + \upsilon_-\right)}{\left(\upsilon_+ Z_+^2 + \upsilon_- Z_-^2\right)} \tag{B.14}$$

where ν_+ = number of moles of the cation in one mole of salt solution (1 for LiCl),
ν_- = number of moles of the anion in one mole of the salt solution (1 for LiCl),
Z_+ = valence number of the cation of the solute (1 for LiCl) and
Z_- = valence number of the anion of the solute (1 for LiCl).

The saturation pressure of water vapour, needed to calculate the surface relative humidity of the liquid desiccant is calculated from ASHRAE (2009)

$$P_{ws}=\exp\left[\frac{C_8}{T_{HAMP}}+C_9+C_{10}T_{HAMP}+C_{11}T_{HAMP}^2+C_{12}T_{HAMP}^3+C_{13}\ln(T_{HAMP})\right] \quad (B.15)$$

where $C_8 = -5.8002206\text{x}10^3$,
$C_9 = 1.3914993$,
$C_{10} = -4.8640239\text{x}10^{-2}$,
$C_{11} = 4.1764768\text{x}10^{-5}$,
$C_{12} = -1.4452093\text{x}10^{-8}$ and
$C_{13} = 6.5459673$.

Using the equations presented here, the surface relative humidity and humidity ratio are calculated for each test case. Many of the coefficients and values presented are specific to a mixture of lithium chloride and water. If these equations are to be used for other solutions, the values for that solution should be looked up in Cisternas and Lam (1991).

B.2 THERMODYNAMIC PROPERTIES OF AN AQUEOUS LiCl SOLUTION

The thermodynamic properties of a salt solution will vary with both temperature and concentration of the solution. These values are calculated from correlations for the specific salt used in the solution. This section outlines the equations used to calculate the thermal conductivity, dynamic viscosity, specific heat and diffusion coefficient of a mixture of lithium chloride and water. These correlations are taken from Zaytsev and Aseyev (1992) and Conde-Petit (2009).

Thermal Conductivity

The thermal conductivity of an aqueous lithium chloride solution (Zaytsev and Aseyev (1992)) is

$$k_{sol}=k_w\left[1-0.344\gamma_{salt}\right] \quad \text{(B.16)}$$

where γ_{salt} is the concentration of the salt solution [-] and k_w is the thermal conductivity of water, calculated from

$$k_w=0.5545+0.00246T_{HAMP}-0.00001184T_{HAMP}^2 \quad \text{(B.17)}$$

with T_{HAMP} as the temperature of the liquid desiccant [K].

The variation in thermal conductivity for an aqueous lithium chloride solution is shown in Figure B.1. Each line on the graph represents a line of constant concentration, from 2% at the top of the graph to 40% at the bottom. For a constant temperature, the thermal conductivity decreases with increasing concentration. For a constant concentration, the thermal conductivity increases with increasing temperature.

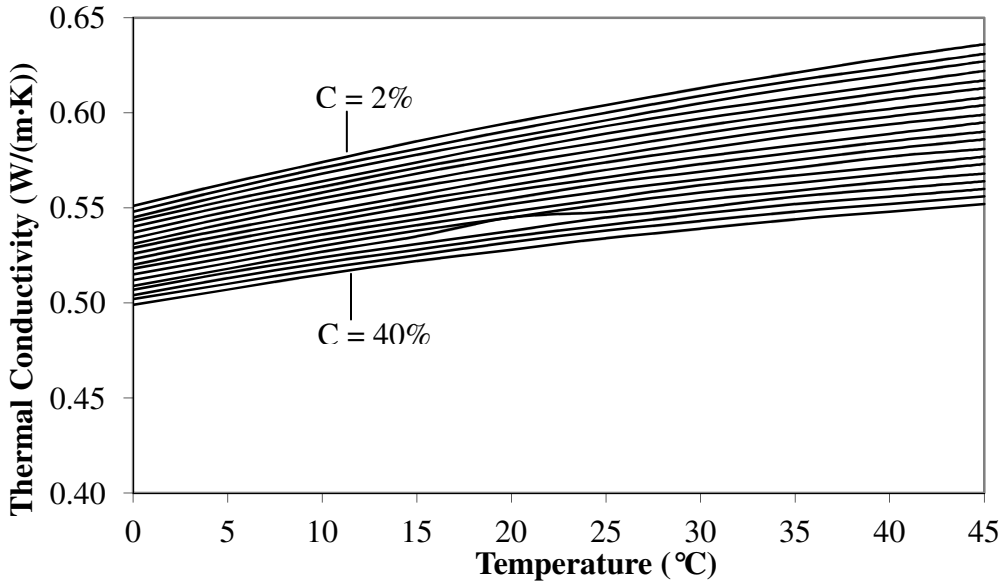

FIGURE B.1. Thermal conductivity of an aqueous lithium chloride solution as a function of temperature, for different salt concentrations (Zaytsev and Aseyev (1992)).

Dynamic Viscosity

The dynamic viscosity of an aqueous lithium chloride solution is calculated from (Zaytsev and Aseyev (1992))

$$\mu_{sol}=10\text{^}\left[\log \mu_w+D_i\gamma_{salt}\right] \tag{B.18}$$

where D_i is a constant based on the temperature of the solution, γ_{salt} is the concentration of the salt [-] and μ_w is the dynamic viscosity of water at the solution temperature [Pa·s]. The dynamic viscosity of water is calculated from

$$\mu_w=0.59849(43.252+T_{HAMP})^{-1.5423} \tag{B.19}$$

where T_{HAMP} is the temperature of the liquid desiccant [K]. The parameter D_i is calculated from

$$D_i=1.737+0.00028T_{HAMP}. \tag{B.20}$$

The coefficients used in Equation (B.20) are specific to a lithium chloride solution and will be different for other salt solutions.

The dynamic viscosity of an aqueous lithium chloride solution is shown in Figure B.2 for various concentrations, ranging from 2% to 30%. For a constant temperature solution, the dynamic viscosity increases with increasing concentration. For a constant concentration solution, the dynamic viscosity decreases with increasing temperature.

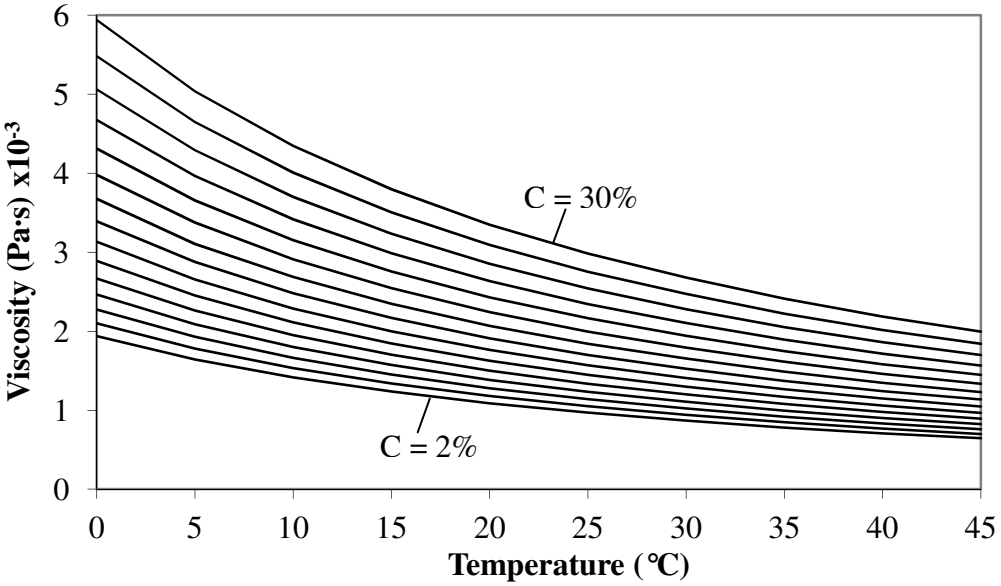

FIGURE B.2. Dynamic viscosity of an aqueous lithium chloride solution as a function of temperature, for different salt concentrations (Zaytsev and Aseyev (1992)).

Specific Heat

The specific heat of an aqueous lithium chloride solution is also a function of the temperature and concentration of the solution. The specific heat is calculated from Conde-Petit (2009) as

$$c_{p,sol}=c_{p,w}(1-f_1*f_2) \tag{B.21}$$

where $c_{p,w}$ is the specific heat of water at the liquid desiccant temperature [kJ/(kg_w·K)], f_1 is a function dependent on the concentration of the solution and f_2 is a function dependent on the temperature of the solution. The specific heat of water can be calculated from

$$c_{p,w}=88.79-120.2\Theta^{0.02}-16.93\Theta^{0.04}+52.47\Theta^{0.06}+0.1083\Theta^{1.8}+0.4699\Theta^{8} \tag{B.22}$$

where Θ is calculated from the liquid desiccant temperature [K] as

$$\Theta=\frac{T_{HAMP}}{228}-1. \tag{B.23}$$

If the concentration of the solution, γ_{salt} is lower than 0.31, the function f_1 is calculated from the equation

$$f_1=1.4390\gamma_{salt}-1.24317\gamma_{salt}^2-0.12070\gamma_{salt}^3 \quad \text{(B.24)}$$

otherwise, it is calculated from the equation

$$f_1=0.12825+0.62934\gamma_{salt}. \quad \text{(B.25)}$$

The function f_2 is calculated from the parameter Θ as defined in Equation (B.23), using the equation

$$f_2=58.5225\Theta^{0.02}-105.6343\Theta^{0.04}+47.7948\Theta^{0.06}. \quad \text{(B.26)}$$

The specific heat of an aqueous lithium chloride solution is shown in Figure B.3 for concentrations ranging from 2% to 40%. The specific heat of the solution does not vary significantly with temperature. For a constant temperature however, the heat capacity decreases with increasing concentration.

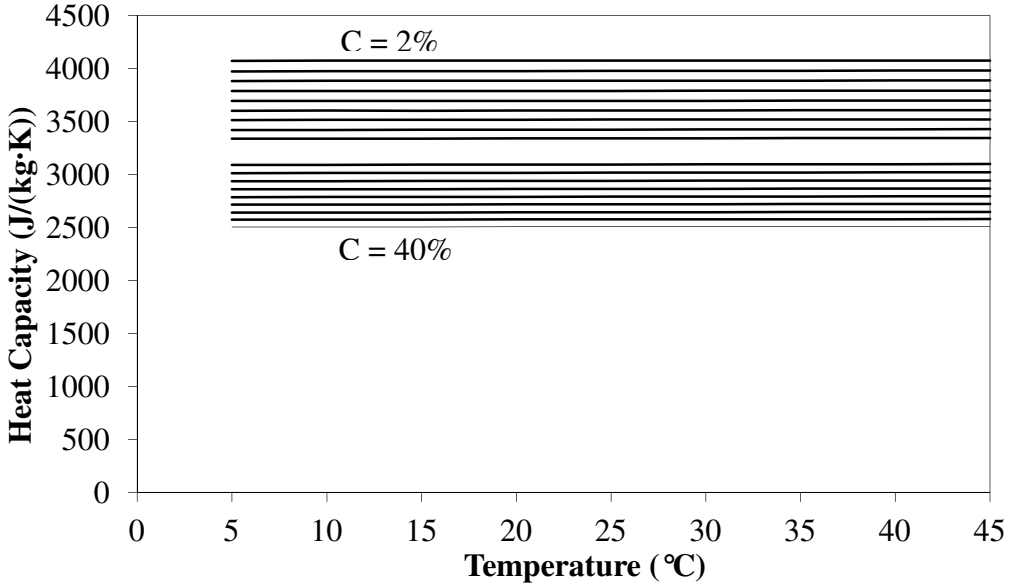

FIGURE B.3. Specific heat of an aqueous lithium chloride solution as a function of temperature, for different salt concentrations (Conde-Petit (2009)).

Diffusion Coefficient

The diffusion coefficient relates how fast one substance will diffuse into another substance. In this case, water vapour is the substance diffusing into the salt solution. The diffusion coefficient of water vapour into a salt solution can be calculated from Conde-Petit (2009) as

$$D_{sol}=D_w\left\{1-\left[1+\left(\frac{\sqrt{\gamma_{salt}}}{0.52}\right)^{-4.92}\right]^{-0.56}\right\} \tag{B.27}$$

where D_w is the self diffusion coefficient of water (the diffusion of water vapour into liquid water) which has a value of $2.2\text{x}10^{-9}$ m^2/s. Unlike the other properties, the diffusion coefficient varies only with concentration, not with temperature.

The diffusion coefficient of water vapour into an aqueous lithium chloride solution is shown in Figure B.4. As the concentration of the salt solution increases, the diffusion coefficient decreases.

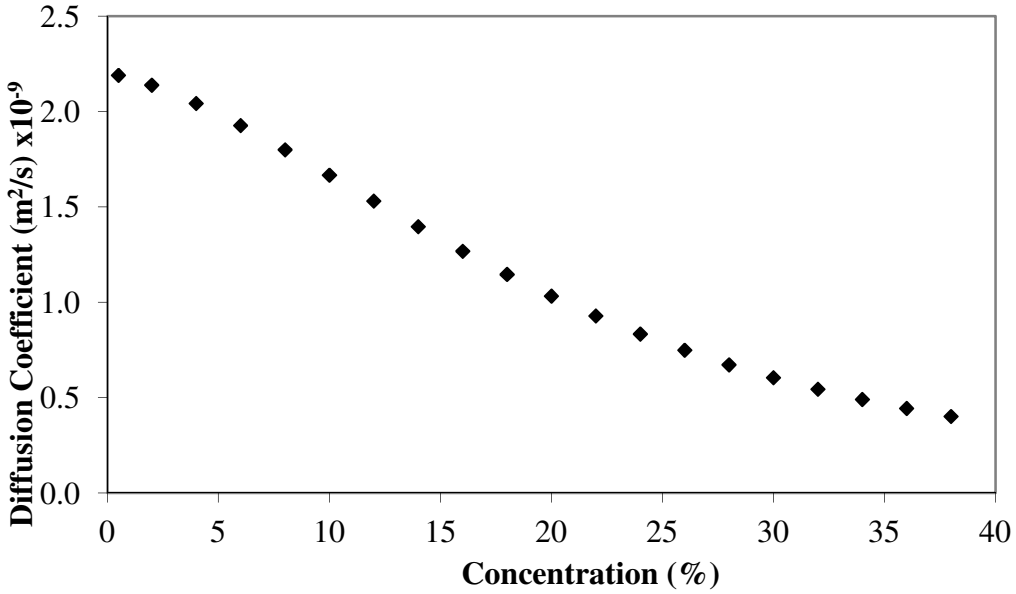

FIGURE B.4. Diffusion coefficient of an aqueous lithium chloride solution as a function of salt concentration (Conde-Petit (2009)).

Using the equations presented in this Appendix, along with the measured density and temperature of the salt solution, the thermodynamic properties required for analysis are calculated.

APPENDIX C – UNCERTAINTY ANALYSIS

As discussed in Chapter 3, it is important to know the uncertainty in each measured and calculated value determined from an experiment, so that the results may be presented with some confidence. The uncertainty in each measured value was presented in Chapter 3, along with the uncertainty in the calculated results of one test run. This appendix expands on that analysis by detailing the equations used to obtain each of those uncertainties. As well, the uncertainty of other parameters that are used throughout the thesis are added here for the same test.

The bias uncertainty of a measurement is independent of the actual measured value, so it will be the same for all tests throughout the thesis. The precision uncertainty may be different for each test, as the fluctuations in the measurements during the test are included in this uncertainty. However, these fluctuations tend to be small and are similar for each test, so the values do not change significantly from one test to the next. Table C.1 lists the value of each measurement during the test run used in Chapter 3, along with the bias (b_x), precision (s_x) and total (U_x) uncertainties for each measurement, at 95% confidence levels.

TABLE C.1. Bias, precision and total uncertainty of measurements for a sample test, at 95% confidence levels.

Measurement	Value	b_x	s_x	U_x
$T_{UPSTREAM}$ [°C]	22.9	±0.3	±0.02	±0.3
$RH_{UPSTREAM}$ [% RH]	68.1	±1.1	±0.04	±1.1
$T_{DOWNSTREAM}$ [°C]	21.4	±0.3	±0.02	±0.3
$RH_{DOWNSTREAM}$ [% RH]	58.8	±0.8	±0.04	±0.8
TC_1 [°C]	8.2	±0.2	±0.02	±0.2
TC_2 [°C]	8.0	±0.3	±0.02	±0.3
TC_3 [°C]	8.2	±0.2	±0.02	±0.2
TC_4 [°C]	8.0	±0.3	±0.02	±0.3
TC_5 [°C]	8.2	±0.2	±0.02	±0.2
ρ_{HAMP} [kg_{sol}/m^3]	1197.2	±11.7	±0.54	±11.7
Q_{dry} [L/min]	0.5	±0.3	±0.01	±0.5
Q_{humid} [L/min]	11.1	±0.1	±0.01	±0.2

The uncertainty of a calculated result is dependent on the measurements or results used to calculate that particular result. The uncertainty of the calculated results will be different for each test. The bias uncertainty of a calculated result (R) is

$$b_R = \left[\sum_{j=1}^{J} \left(\frac{\partial R}{\partial x_j} b_{x_j} \right)^2 \right]^{1/2} \quad \text{(C.1)}$$

and the precision uncertainty is

$$s_R = \left[\sum_{j=1}^{J} \left(\frac{\partial R}{\partial x_j} s_{x_j} \right)^2 \right]^{1/2} \quad \text{(C.2)}$$

where $\frac{\partial R}{\partial x_j}$ is the derivative of R with respect to variable x and b_x and s_x are the bias and precision uncertainties of variable x. The total uncertainty of a calculated result is the same as for a measured value

$$U_R = 2\sqrt{b_R^2 + s_R^2}. \tag{C.3}$$

The order of the uncertainty calculations in this appendix will follow the same order as Appendices A and B, which list the important equations used in the analysis for this thesis.

C.1 PERFORMANCE OF THE PROTOTYPE HAMP

Sensible Effectiveness (equation 1.1)

$$b\varepsilon_{sensible} = \left[\left(\frac{\partial \varepsilon_{sensible}}{\partial T_{DOWN}} bT_{DOWN}\right)^2 + \left(\frac{\partial \varepsilon_{sensible}}{\partial T_{UP}} bT_{UP}\right)^2 + \left(\frac{\partial \varepsilon_{sensible}}{\partial T_{HAMP}} bT_{HAMP}\right)^2\right]^{1/2} \tag{C.4}$$

$$s\varepsilon_{sensible} = \left[\left(\frac{\partial \varepsilon_{sensible}}{\partial T_{DOWN}} sT_{DOWN}\right)^2 + \left(\frac{\partial \varepsilon_{sensible}}{\partial T_{UP}} sT_{UP}\right)^2 + \left(\frac{\partial \varepsilon_{sensible}}{\partial T_{HAMP}} sT_{HAMP}\right)^2\right]^{1/2} \tag{C.5}$$

where

$$\frac{\partial \varepsilon_{sensible}}{\partial T_{DOWN}} = \frac{1}{T_{HAMP} - T_{UPSTREAM}} \tag{C.6}$$

$$\frac{\partial \varepsilon_{sensible}}{\partial T_{UP}} = \frac{T_{DOWNSTREAM} - T_{HAMP}}{(T_{HAMP} - T_{UPSTREAM})^2} \tag{C.7}$$

$$\frac{\partial \varepsilon_{sensible}}{\partial T_{HAMP}} = \frac{T_{DOWNSTREAM} - T_{UPSTREAM}}{(T_{HAMP} - T_{UPSTREAM})^2} \tag{C.8}$$

$$bT_{HAMP} = \left[\left(\frac{\partial T_{HAMP}}{\partial T_1} bT_1\right)^2 + \left(\frac{\partial T_{HAMP}}{\partial T_2} bT_2\right)^2 + \left(\frac{\partial T_{HAMP}}{\partial T_3} bT_3\right)^2 + \left(\frac{\partial T_{HAMP}}{\partial T_4} bT_4\right)^2 + \left(\frac{\partial T_{HAMP}}{\partial T_5} bT_5\right)^2\right]^{1/2} \tag{C.9}$$

$$sT_{HAMP} = \left[\left(\frac{\partial T_{HAMP}}{\partial T_1} sT_1\right)^2 + \left(\frac{\partial T_{HAMP}}{\partial T_2} sT_2\right)^2 + \left(\frac{\partial T_{HAMP}}{\partial T_3} sT_3\right)^2 + \left(\frac{\partial T_{HAMP}}{\partial T_4} sT_4\right)^2 + \left(\frac{\partial T_{HAMP}}{\partial T_5} sT_5\right)^2\right]^{1/2} \tag{C.10}$$

where

$$\frac{\partial T_{HAMP}}{\partial T_1}=\frac{\partial T_{HAMP}}{\partial T_2}=\frac{\partial T_{HAMP}}{\partial T_3}=\frac{\partial T_{HAMP}}{\partial T_4}=\frac{\partial T_{HAMP}}{\partial T_5}=\frac{1}{5} \tag{C.11}$$

Latent Effectiveness (equation 1.2)

$$b\varepsilon_{latent}=\left[\left(\frac{\partial \varepsilon_{latent}}{\partial W_{DOWN}}bW_{DOWN}\right)^2+\left(\frac{\partial \varepsilon_{latent}}{\partial W_{UP}}bW_{UP}\right)^2+\left(\frac{\partial \varepsilon_{latent}}{\partial W_{HAMP}}bW_{HAMP}\right)^2\right]^{1/2} \tag{C.12}$$

$$s\varepsilon_{latent}=\left[\left(\frac{\partial \varepsilon_{latent}}{\partial W_{DOWN}}sW_{DOWN}\right)^2+\left(\frac{\partial \varepsilon_{latent}}{\partial W_{UP}}sW_{UP}\right)^2+\left(\frac{\partial \varepsilon_{latent}}{\partial W_{HAMP}}sW_{HAMP}\right)^2\right]^{1/2} \tag{C.13}$$

where

$$\frac{\partial \varepsilon_{latent}}{\partial W_{DOWNSTREAM}}=\frac{1}{W_{HAMP}-W_{UPSTREAM}} \tag{C.14}$$

$$\frac{\partial \varepsilon_{latent}}{\partial W_{UPSTREAM}}=\frac{W_{DOWNSTREAM}-W_{HAMP}}{\left(W_{HAMP}-W_{UPSTREAM}\right)^2} \tag{C.15}$$

$$\frac{\partial \varepsilon_{latent}}{\partial W_{UPSTREAM}}=\frac{W_{DOWNSTREAM}-W_{HAMP}}{\left(W_{HAMP}-W_{UPSTREAM}\right)^2} \tag{C.16}$$

$$bW=\left[\left(\frac{\partial W}{\partial P_{ws}}bP_{ws}\right)^2+\left(\frac{\partial W}{\partial \phi}b\phi\right)^2\right]^{1/2} \tag{C.17}$$

$$sW=\left[\left(\frac{\partial W}{\partial P_{ws}}sP_{ws}\right)^2+\left(\frac{\partial W}{\partial \phi}s\phi\right)^2\right]^{1/2} \tag{C.18}$$

where

$$\frac{\partial W}{\partial P_{ws}}=\frac{621.98P_{atm}\phi}{\left(P_{atm}-P_{ws}\phi\right)^2} \tag{C.19}$$

$$\frac{\partial W}{\partial \phi}=\frac{621.98P_{atm}P_{ws}}{\left(P_{atm}-P_{ws}\phi\right)^2} \tag{C.20}$$

$$bP_{ws}=\left[\left(\frac{\partial P_{ws}}{\partial T}bT\right)^2\right]^{1/2} \tag{C.21}$$

$$sP_{ws}=\left[\left(\frac{\partial P_{ws}}{\partial T}sT\right)^2\right]^{1/2} \tag{C.22}$$

where

$$\frac{\partial P_{ws}}{\partial T}=\exp\left[\frac{C_8}{T}+C_9+C_{10}T+C_{11}T^2+C_{12}T^3+C_{13}(\ln T)\right]*\left[\frac{-C_8}{T}+C_{10}+2C_{11}T+3C_{12}T^2+\frac{C_{13}}{T}\right] \quad (C.23)$$

Total Effectiveness (equation 1.3)

$$b\varepsilon_{total}=\left[\left(\frac{\partial\varepsilon_{total}}{\partial h_{DOWN}}bh_{DOWN}\right)^2+\left(\frac{\partial\varepsilon_{total}}{\partial h_{UP}}bh_{UP}\right)^2+\left(\frac{\partial\varepsilon_{total}}{\partial h_{HAMP}}bh_{HAMP}\right)^2\right]^{1/2} \quad (C.24)$$

$$s\varepsilon_{total}=\left[\left(\frac{\partial\varepsilon_{total}}{\partial h_{DOWN}}sh_{DOWN}\right)^2+\left(\frac{\partial\varepsilon_{total}}{\partial h_{UP}}sh_{UP}\right)^2+\left(\frac{\partial\varepsilon_{total}}{\partial h_{HAMP}}sh_{HAMP}\right)^2\right]^{1/2} \quad (C.25)$$

where

$$\frac{\partial\varepsilon_{total}}{\partial h_{DOWNSTREAM}}=\frac{1}{h_{HAMP}-h_{UPSTREAM}} \quad (C.26)$$

$$\frac{\partial\varepsilon_{total}}{\partial h_{UPSTREAM}}=\frac{h_{DOWNSTREAM}-h_{HAMP}}{(h_{HAMP}-h_{UPSTREAM})^2} \quad (C.27)$$

$$\frac{\partial\varepsilon_{total}}{\partial h_{HAMP}}=\frac{h_{DOWNSTREAM}-h_{UPSTREAM}}{(h_{HAMP}-h_{UPSTREAM})^2} \quad (C.28)$$

$$bh=\left[\left(\frac{\partial h}{\partial T}bT\right)^2+\left(\frac{\partial h}{\partial W}bW\right)^2\right]^{1/2} \quad (C.29)$$

$$sh=\left[\left(\frac{\partial h}{\partial T}sT\right)^2+\left(\frac{\partial h}{\partial W}sW\right)^2\right]^{1/2} \quad (C.30)$$

where

$$\frac{\partial h}{\partial T}=1+\frac{1.86W}{1000} \quad (C.31)$$

$$\frac{\partial h}{\partial W}=\frac{2501.3+1.86T}{1000} \quad (C.32)$$

TABLE C.2. Bias, precision and total uncertainties related to the performance of the prototype HAMP.

Calculated Result	Value	b_x (68%)	s_x (68%)	U_x (95%)
$\varepsilon_{sensible}$ [%]	10.1	±1.8	±0.1	±3.6
ε_{latent} [%]	27.3	±2.0	±0.1	±4.0
ε_{total} [%]	20.9	±1.4	±0.1	±2.8
T_{HAMP} [°C]	8.1	±0.06	±0.004	±0.1
$W_{UPSTREAM}$ [g_w/kg_{air}]	12.6	±0.2	±0.01	±0.4
$W_{DOWNSTREAM}$ [g_w/kg_{air}]	9.9	±0.1	±0.01	±0.3
W_{HAMP} [g_w/kg_{air}]	2.7	±0.02	±0.01	±0.04
$h_{UPSTREAM}$ [kJ/kg_{air}]	55.0	±0.5	±0.03	±1.1
$h_{DOWNSTREAM}$ [kJ/kg_{air}]	46.6	±0.4	±0.03	±0.8
h_{HAMP} [kJ/kg_{air}]	14.9	±0.1	±0.01	±0.2

C.2 CONSERVATION OF ENERGY AND MASS

Conservation of Energy (equation 3.12)

$$bE=\left[\left(\frac{\partial E}{\partial \dot{m}_{air}}b\dot{m}_{air}\right)^2+\left(\frac{\partial E}{\partial h_{UP}}bh_{UP}\right)^2+\left(\frac{\partial E}{\partial h_{DOWN}}bh_{DOWN}\right)^2+\left(\frac{\partial E}{\partial \dot{m}_{w}}b\dot{m}_{w}\right)^2+\left(\frac{\partial E}{\partial h_{w}}bh_{w}\right)^2+\left(\frac{\partial E}{\partial h_{conv}}bh_{conv}\right)^2+\left(\frac{\partial E}{\partial A_s}bA_s\right)^2+\left(\frac{\partial E}{\partial \Delta T_{lm}}b\Delta T_{lm}\right)^2\right]^{1/2} \quad (C.33)$$

$$sE=\left[\left(\frac{\partial E}{\partial \dot{m}_{air}}s\dot{m}_{air}\right)^2+\left(\frac{\partial E}{\partial h_{UP}}sh_{UP}\right)^2+\left(\frac{\partial E}{\partial h_{DOWN}}sh_{DOWN}\right)^2+\left(\frac{\partial E}{\partial \dot{m}_{w}}s\dot{m}_{w}\right)^2+\left(\frac{\partial E}{\partial h_{w}}sh_{w}\right)^2+\left(\frac{\partial E}{\partial h_{conv}}sh_{conv}\right)^2+\left(\frac{\partial E}{\partial A_s}sA_s\right)^2+\left(\frac{\partial E}{\partial \Delta T_{lm}}s\Delta T_{lm}\right)^2\right]^{1/2} \quad (C.34)$$

where

$$\frac{\partial E}{\partial \dot{m}_{air}} = (h_{UP} - h_{DOWN}) \tag{C.35}$$

$$\frac{\partial E}{\partial h_{UP}} = \dot{m}_{air} \tag{C.36}$$

$$\frac{\partial E}{\partial h_{DOWN}} = -\dot{m}_{air} \tag{C.37}$$

$$\frac{\partial E}{\partial \dot{m}_{w}} = -h_{w} \tag{C.38}$$

$$\frac{\partial E}{\partial h_{w}} = -\dot{m}_{w} \tag{C.39}$$

$$\frac{\partial E}{\partial h_{conv}} = -A_c \Delta T_{lm} \tag{C.40}$$

$$\frac{\partial E}{\partial A_c} = -h_{conv} \Delta T_{lm} \tag{C.41}$$

$$\frac{\partial E}{\partial \Delta T_{lm}} = -h_{conv} A_c \tag{C.42}$$

$$b\dot{m}_{w} = \left[\left(\frac{\partial \dot{m}_{w}}{\partial \dot{m}_{air}} b\dot{m}_{air} \right)^2 + \left(\frac{\partial \dot{m}_{w}}{\partial W_{UP}} bW_{UP} \right)^2 + \left(\frac{\partial \dot{m}_{w}}{\partial W_{DOWN}} bW_{DOWN} \right)^2 \right]^{1/2} \tag{C.43}$$

$$s\dot{m}_{w} = \left[\left(\frac{\partial \dot{m}_{w}}{\partial \dot{m}_{air}} s\dot{m}_{air} \right)^2 + \left(\frac{\partial \dot{m}_{w}}{\partial W_{UP}} sW_{UP} \right)^2 + \left(\frac{\partial \dot{m}_{w}}{\partial W_{DOWN}} sW_{DOWN} \right)^2 \right]^{1/2} \tag{C.44}$$

where

$$\frac{\partial \dot{m}_{w}}{\partial \dot{m}_{air}} = W_{UP} - W_{DOWN} \tag{C.45}$$

$$\frac{\partial \dot{m}_{w}}{\partial W_{UP}} = \dot{m}_{air} \tag{C.46}$$

$$\frac{\partial \dot{m}_{w}}{\partial W_{DOWN}} = -\dot{m}_{air} \tag{C.47}$$

$$b\dot{m}_{air} = \left[\left(\frac{\partial \dot{m}_{air}}{\partial \rho_{air}} b\rho_{air} \right)^2 + \left(\frac{\partial \dot{m}_{air}}{\partial A_c} bA_c \right)^2 + \left(\frac{\partial \dot{m}_{air}}{\partial V} bV \right)^2 \right]^{1/2} \tag{C.48}$$

$$s\dot{m}_{air} = \left[\left(\frac{\partial \dot{m}_{air}}{\partial \rho_{air}} s\rho_{air} \right)^2 + \left(\frac{\partial \dot{m}_{air}}{\partial A_c} sA_c \right)^2 + \left(\frac{\partial \dot{m}_{air}}{\partial V} sV \right)^2 \right]^{1/2} \tag{C.49}$$

where

$$\frac{\partial \dot{m}_{air}}{\partial \rho_{air}} = A_c V \tag{C.50}$$

$$\frac{\partial \dot{m}_{air}}{\partial A_c} = \rho_{air} V \tag{C.51}$$

$$\frac{\partial \dot{m}_{air}}{\partial V} = \rho_{air} A_c \tag{C.52}$$

$$b\rho_{air} = \left[\left(\frac{\partial \rho_{air}}{\partial P_{ws}} bP_{ws} \right)^2 + \left(\frac{\partial \rho_{air}}{\partial \phi} b\phi \right)^2 + \left(\frac{\partial \rho_{air}}{\partial T} bT \right)^2 \right]^{1/2} \tag{C.53}$$

$$s\rho_{air} = \left[\left(\frac{\partial \rho_{air}}{\partial P_{ws}} sP_{ws} \right)^2 + \left(\frac{\partial \rho_{air}}{\partial \phi} s\phi \right)^2 + \left(\frac{\partial \rho_{air}}{\partial T} sT \right)^2 \right]^{1/2} \tag{C.54}$$

where

$$\frac{\partial \rho_{air}}{\partial P_{ws}} = \frac{-\phi}{RT} \tag{C.55}$$

$$\frac{\partial \rho_{air}}{\partial \phi} = \frac{-P_{ws}}{RT} \tag{C.56}$$

$$\frac{\partial \rho_{air}}{\partial T} = \frac{-(P_{atm} - P_{ws}\phi)}{RT^2} \tag{C.57}$$

$$bh_w = \left[\left(\frac{\partial h_w}{\partial T} bT \right)^2 \right]^{1/2} \tag{C.58}$$

$$sh_w = \left[\left(\frac{\partial h_w}{\partial T} sT \right)^2 \right]^{1/2} \tag{C.59}$$

where

$$\frac{\partial h_w}{\partial T} = 1.86 \tag{C.60}$$

$$b\Delta T_{lm} = \left[\left(\frac{\partial \Delta T_{lm}}{\partial \Delta T_{in}} b\Delta T_{in} \right)^2 + \left(\frac{\partial \Delta T_{lm}}{\partial \Delta T_{out}} b\Delta T_{out} \right)^2 \right]^{1/2} \tag{C.61}$$

$$s\Delta T_{lm} = \left[\left(\frac{\partial \Delta T_{lm}}{\partial \Delta T_{in}} s\Delta T_{in} \right)^2 + \left(\frac{\partial \Delta T_{lm}}{\partial \Delta T_{uto}} s\Delta T_{out} \right)^2 \right]^{1/2} \tag{C.62}$$

where

$$\frac{\partial \Delta T_{lm}}{\partial \Delta T_{in}} = \frac{\ln\left({}^{\Delta T_{in}}/_{\Delta T_{out}}\right) - 1 + {}^{\Delta T_{out}}/_{\Delta T_{in}}}{\left[\ln\left({}^{\Delta T_{in}}/_{\Delta T_{out}}\right)\right]^2} \tag{C.63}$$

$$\frac{\partial \Delta T_{lm}}{\partial \Delta T_{out}} = \frac{-\ln\left({}^{\Delta T_{in}}/_{\Delta T_{out}}\right) - 1 + {}^{\Delta T_{in}}/_{\Delta T_{out}}}{\left[\ln\left({}^{\Delta T_{in}}/_{\Delta T_{out}}\right)\right]^2} \tag{C.64}$$

$$b\Delta T_{in} = \left[\left(\frac{\partial \Delta T_{in}}{\partial T_{UP}} bT_{UP}\right)^2 + \left(\frac{\partial \Delta T_{in}}{\partial T_{HAMP}} bT_{HAMP}\right)^2\right]^{1/2} \tag{C.65}$$

$$s\Delta T_{in} = \left[\left(\frac{\partial \Delta T_{in}}{\partial T_{UP}} sT_{UP}\right)^2 + \left(\frac{\partial \Delta T_{in}}{\partial T_{HAMP}} sT_{HAMP}\right)^2\right]^{1/2} \tag{C.66}$$

where

$$\frac{\partial \Delta T_{in}}{\partial T_{UP}} = -1 \tag{C.67}$$

$$\frac{\partial \Delta T_{in}}{\partial T_{HAMP}} = 1 \tag{C.68}$$

$$b\Delta T_{out} = \left[\left(\frac{\partial \Delta T_{out}}{\partial T_{HAMP}} bT_{HAMP}\right)^2 + \left(\frac{\partial \Delta T_{out}}{\partial T_{DOWN}} bT_{DOWN}\right)^2\right]^{1/2} \tag{C.69}$$

$$s\Delta T_{out} = \left[\left(\frac{\partial \Delta T_{out}}{\partial T_{HAMP}} sT_{HAMP}\right)^2 + \left(\frac{\partial \Delta T_{out}}{\partial T_{DOWN}} sT_{DOWN}\right)^2\right]^{1/2} \tag{C.70}$$

where

$$\frac{\partial \Delta T_{out}}{\partial T_{DOWN}} = -1 \tag{C.71}$$

$$\frac{\partial \Delta T_{out}}{\partial T_{HAMP}} = 1 \tag{C.72}$$

Conservation of Mass (equation 3.15)

$$bM=\left[\left(\frac{\partial M}{\partial \dot{m}_{air}}b\dot{m}_{air}\right)^2+\left(\frac{\partial M}{\partial W_{UP}}bW_{UP}\right)^2+\left(\frac{\partial M}{\partial W_{DOWN}}bW_{DOWN}\right)^2+\left(\frac{\partial M}{\partial \Delta mass}b\Delta mass\right)^2+\left(\frac{\partial M}{\partial t}bt\right)^2\right]^{1/2} \quad (C.73)$$

$$sM=\left[\left(\frac{\partial M}{\partial \dot{m}_{air}}s\dot{m}_{air}\right)^2+\left(\frac{\partial M}{\partial W_{UP}}sW_{UP}\right)^2+\left(\frac{\partial M}{\partial W_{DOWN}}sW_{DOWN}\right)^2+\left(\frac{\partial M}{\partial \Delta mass}s\Delta mass\right)^2+\left(\frac{\partial M}{\partial t}st\right)^2\right]^{1/2} \quad (C.74)$$

where

$$\frac{\partial M}{\partial \dot{m}_{air}}=W_{UP}-W_{DOWN} \quad (C.75)$$

$$\frac{\partial M}{\partial W_{UP}}=\dot{m}_{air} \quad (C.76)$$

$$\frac{\partial M}{\partial W_{UP}}=-\dot{m}_{air} \quad (C.77)$$

$$\frac{\partial M}{\partial \Delta mass}=\frac{1}{t} \quad (C.78)$$

$$\frac{\partial M}{\partial t}=\frac{-\Delta mass}{(t)^2} \quad (C.79)$$

TABLE C.3. Bias, precision and total uncertainties related energy and mass balances.

Calculated Result	Value	b_x (68%)	s_x (68%)	U_x (95%)
E [W]	0.07	±0.2	±0.04	±0.4
M [kg_w/s]	$2.7x10^{-8}$	$±3.3x10^{-8}$	$±3.5x10^{-9}$	$±6.7x10^{-8}$
$\dot{m}_{air}$ [kg_{air}/s]	$2.1x10^{-4}$	$±6.2x10^{-6}$	$±2.6x10^{-7}$	$±1.2x10^{-5}$
$h_{UPSTREAM}$ [kJ/kg_{air}]	55.0	±0.5	±0.03	±1.0
$h_{DOWNSTREAM}$ [kJ/kg_{air}]	46.6	±0.4	±0.03	±0.8
$\dot{m}_w$ [kg_w/s]	$5.4x10^{-7}$	$±5.1x10^{-8}$	$±3.0x10^{-9}$	$±1.0x10^{-7}$
h_w [kJ/kg_w]	2533.8	±0.2	±0.009	±0.4
h_{conv} [$W/(m^2 \cdot K)$]	0.81	±0.06	±0.06	±0.16
$A_{surface}$ [m^2]	0.043	±0.0005	±0	±0.001
ΔT_{lm} [°C]	14.0	±0.2	±0.01	±0.3
$W_{UPSTREAM}$ [g_w/kg_{air}]	12.6	±0.2	±0.01	±0.4
$W_{DOWNSTREAM}$ [g_w/kg_{air}]	9.9	±0.1	±0.01	±0.03
Δmass [g_w]	1.9	±0.01	±0.01	±0.03
t [s]	3600	±0.1	±0	±0.2

C.3 OPERATING CONDITIONS

Operating condition factor (equation 4.29)

$$bH^* = \left[\left(\frac{\partial H^*}{\partial \Delta W} b\Delta W \right)^2 + \left(\frac{\partial H^*}{\partial \Delta T} b\Delta T \right)^2 \right]^{1/2} \tag{C.80}$$

$$sH^* = \left[\left(\frac{\partial H^*}{\partial \Delta W} s\Delta W \right)^2 + \left(\frac{\partial H^*}{\partial \Delta T} s\Delta T \right)^2 \right]^{1/2} \tag{C.81}$$

where

$$\frac{\partial H^*}{\partial \Delta W} = \frac{2500}{\Delta T} \tag{C.82}$$

$$\frac{\partial H^*}{\partial \Delta T} = \frac{-2500 \Delta W}{(\Delta T)^2} \tag{C.83}$$

$$b\Delta W=\left[\left(\frac{\partial \Delta W}{\partial W_{UP}} bW_{UP}\right)^2+\left(\frac{\partial \Delta W}{\partial W_{HAMP}} bW_{HAMP}\right)^2\right]^{1/2} \quad \text{(C.84)}$$

$$s\Delta W=\left[\left(\frac{\partial \Delta W}{\partial W_{UP}} sW_{UP}\right)^2+\left(\frac{\partial \Delta W}{\partial W_{HAMP}} sW_{HAMP}\right)^2\right]^{1/2} \quad \text{(C.85)}$$

where

$$\frac{\partial \Delta W}{\partial W_{UP}}=1 \quad \text{(C.86)}$$

$$\frac{\partial \Delta W}{\partial W_{HAMP}}=-1 \quad \text{(C.87)}$$

$$b\Delta T=\left[\left(\frac{\partial \Delta T}{\partial T_{UP}} bT_{UP}\right)^2+\left(\frac{\partial \Delta T}{\partial T_{HAMP}} bT_{HAMP}\right)^2\right]^{1/2} \quad \text{(C.88)}$$

$$s\Delta T=\left[\left(\frac{\partial \Delta T}{\partial T_{UP}} sT_{UP}\right)^2+\left(\frac{\partial \Delta T}{\partial T_{HAMP}} sT_{HAMP}\right)^2\right]^{1/2} \quad \text{(C.89)}$$

where

$$\frac{\partial \Delta T}{\partial T_{UP}}=1 \quad \text{(C.90)}$$

$$\frac{\partial \Delta T}{\partial T_{HAMP}}=-1 \quad \text{(C.91)}$$

C.4 TOTAL HEAT AND MASS FLUXES

Total Heat Flux (equation 5.1)

$$bq''=\left[\left(\frac{\partial q''}{\partial U} bU\right)^2+\left(\frac{\partial q''}{\partial \Delta T_{lm}} b\Delta T_{lm}\right)^2\right]^{1/2} \quad \text{(C.92)}$$

$$sq''=\left[\left(\frac{\partial q''}{\partial U} sU\right)^2+\left(\frac{\partial q''}{\partial \Delta T_{lm}} s\Delta T_{lm}\right)^2\right]^{1/2} \quad \text{(C.93)}$$

where

$$\frac{\partial q''}{\partial U}=\Delta T_{lm} \quad \text{(C.94)}$$

$$\frac{\partial q''}{\partial \Delta T_{lm}}=U \quad \text{(C.95)}$$

Total Mass Flux (equation 5.2)

$$b\dot{m}'' = \left[\left(\frac{\partial \dot{m}''}{\partial U_m^W} b U_m^W \right)^2 + \left(\frac{\partial \dot{m}''}{\partial \Delta W_{lm}} b \Delta W_{lm} \right)^2 \right]^{1/2} \tag{C.96}$$

$$s\dot{m}'' = \left[\left(\frac{\partial \dot{m}''}{\partial U_m^W} s U_m^W \right)^2 + \left(\frac{\partial \dot{m}''}{\partial \Delta W_{lm}} s \Delta W_{lm} \right)^2 \right]^{1/2} \tag{C.97}$$

where

$$\frac{\partial \dot{m}''}{\partial U_m^W} = \Delta W_{lm} \tag{C.98}$$

$$\frac{\partial \dot{m}''}{\partial \Delta W_{lm}} = U_m^W \tag{C.99}$$

C.5 EXPERIMENTAL TRANSFER COEFFICIENTS

Overall heat transfer coefficient (equation 6.8)

$$bU_{exp} = \left[\begin{array}{c} \left(\frac{\partial U_{exp}}{\partial \dot{m}_{air}} b\dot{m}_{air} \right)^2 + \left(\frac{\partial U_{exp}}{\partial c_{p,air}} b c_{p,air} \right)^2 + \left(\frac{\partial U_{exp}}{\partial T_{UP}} b T_{UP} \right)^2 + \left(\frac{\partial U_{exp}}{\partial T_{DOWN}} b T_{DOWN} \right)^2 \\ + \left(\frac{\partial U_{exp}}{\partial A_S} b A_S \right)^2 + \left(\frac{\partial U_{exp}}{\partial \Delta T_{lm}} b \Delta T_{lm} \right)^2 \end{array} \right]^{1/2} \tag{C.100}$$

$$sU_{exp} = \left[\begin{array}{c} \left(\frac{\partial U_{exp}}{\partial \dot{m}_{air}} s\dot{m}_{air} \right)^2 + \left(\frac{\partial U_{exp}}{\partial c_{p,air}} s c_{p,air} \right)^2 + \left(\frac{\partial U_{exp}}{\partial T_{UP}} s T_{UP} \right)^2 + \left(\frac{\partial U_{exp}}{\partial T_{DOWN}} s T_{DOWN} \right)^2 \\ + \left(\frac{\partial U_{exp}}{\partial A_S} s A_S \right)^2 + \left(\frac{\partial U_{exp}}{\partial \Delta T_{lm}} s \Delta T_{lm} \right)^2 \end{array} \right]^{1/2} \tag{C.101}$$

where

$$\frac{\partial U_{exp}}{\partial \dot{m}_{air}} = \frac{c_{p,air}(T_{DOWN} - T_{UP})}{A_S \Delta T_{lm}} \tag{C.102}$$

$$\frac{\partial U_{exp}}{\partial c_{p,air}} = \frac{\dot{m}_{air}(T_{DOWN} - T_{UP})}{A_S \Delta T_{lm}} \tag{C.103}$$

$$\frac{\partial U_{exp}}{\partial T_{DOWN}} = \frac{\dot{m}_{air} c_{p,air}}{A_S \Delta T_{lm}} \tag{C.104}$$

$$\frac{\partial U_{exp}}{\partial T_{UP}} = \frac{\dot{m}_{air} c_{p,air}}{A_S \Delta T_{lm}} \tag{C.105}$$

$$\frac{\partial U_{exp}}{\partial A_S} = \frac{-\dot{m}_{air} c_{p,air} (T_{DOWN} - T_{UP})}{(A_S)^2 \Delta T_{lm}} \quad \text{(C.106)}$$

$$\frac{\partial U_{exp}}{\partial A_S} = \frac{-\dot{m}_{air} c_{p,air} (T_{DOWN} - T_{UP})}{A_S (\Delta T_{lm})^2} \quad \text{(C.107)}$$

Overall mass transfer coefficient (6.10)

$$bU_{m,exp} = \left[\left(\frac{\partial U_{m,exp}}{\partial \dot{m}_{air}} b\dot{m}_{air} \right)^2 + \left(\frac{\partial U_{m,exp}}{\partial W_{UP}} bW_{UP} \right)^2 + \left(\frac{\partial U_{m,exp}}{\partial W_{DOWN}} bW_{DOWN} \right)^2 + \left(\frac{\partial U_{m,exp}}{\partial A_S} bA_S \right)^2 + \left(\frac{\partial U_{m,exp}}{\partial \Delta W_{lm}} b\Delta W_{lm} \right)^2 \right]^{1/2} \quad \text{(C.108)}$$

$$sU_{m,exp} = \left[\left(\frac{\partial U_{m,exp}}{\partial \dot{m}_{air}} s\dot{m}_{air} \right)^2 + \left(\frac{\partial U_{m,exp}}{\partial W_{UP}} sW_{UP} \right)^2 + \left(\frac{\partial U_{m,exp}}{\partial W_{DOWN}} sW_{DOWN} \right)^2 + \left(\frac{\partial U_{m,exp}}{\partial A_S} sA_S \right)^2 + \left(\frac{\partial U_{m,exp}}{\partial \Delta W_{lm}} s\Delta W_{lm} \right)^2 \right]^{1/2} \quad \text{(C.109)}$$

where

$$\frac{\partial U_{m,exp}}{\partial \dot{m}_{air}} = \frac{(W_{DOWN} - W_{UP})}{A_S \Delta W_{lm}} \quad \text{(C.110)}$$

$$\frac{\partial U_{m,exp}}{\partial W_{DOWN}} = \frac{\dot{m}_{air}}{A_S \Delta W_{lm}} \quad \text{(C.111)}$$

$$\frac{\partial U_{m,exp}}{\partial W_{UP}} = \frac{-\dot{m}_{air}}{A_S \Delta W_{lm}} \quad \text{(C.112)}$$

$$\frac{\partial U_{m,exp}}{\partial A_S} = \frac{-\dot{m}_{air} (W_{DOWN} - W_{UP})}{(A_S)^2 \Delta W_{lm}} \quad \text{(C.113)}$$

$$\frac{\partial U_{m,exp}}{\partial \Delta W_{lm}} = \frac{-\dot{m}_{air} (W_{DOWN} - W_{UP})}{A_S (\Delta W_{lm})^2} \quad \text{(C.114)}$$

C.6 LIQUID DESICCANT CORRELATIONS

Concentration (equation B.1)

$$bC_{salt} = \left[\left(\frac{\partial C_{salt}}{\partial \rho_{HAMP}} b\rho_{HAMP} \right)^2 + \left(\frac{\partial C_{salt}}{\partial \rho_w} b\rho_w \right)^2 + \left(\frac{\partial C_{salt}}{\partial A_i} bA_i \right)^2 \right]^{1/2} \quad \text{(C.115)}$$

$$sC_{salt} = \left[\left(\frac{\partial C_{salt}}{\partial \rho_{HAMP}} s\rho_{HAMP} \right)^2 + \left(\frac{\partial C_{salt}}{\partial \rho_w} s\rho_w \right)^2 + \left(\frac{\partial C_{salt}}{\partial A_i} sA_i \right)^2 \right]^{1/2} \quad \text{(C.116)}$$

where

$$\frac{\partial C_{salt}}{\partial \rho_{HAMP}} = \frac{100}{A_i \rho_{HAMP}} \log(e) \tag{C.117}$$

$$\frac{\partial C_{salt}}{\partial \rho_{w}} = \frac{-100}{A_i \rho_{w}} \log(e) \tag{C.118}$$

$$\frac{\partial C_{salt}}{\partial \rho_{w}} = \frac{-\left(\log(\rho_{HAMP}) - \log(\rho_{w})\right)}{A_i^{\,2}} \tag{C.119}$$

Partial Pressure of Water Vapour (equation B.6)

$$bP_w = \left[\begin{array}{c} \left(\frac{\partial P_w}{\partial I} bI\right)^2 + \left(\frac{\partial P_w}{\partial A} bA\right)^2 + \left(\frac{\partial P_w}{\partial B} bB\right)^2 + \left(\frac{\partial P_w}{\partial C} bC\right)^2 + \\ \left(\frac{\partial P_w}{\partial D} bD\right)^2 + \left(\frac{\partial P_w}{\partial T_{HAMP}} bT_{HAMP}\right)^2 \end{array} \right]^{1/2} \tag{C.120}$$

$$sP_w = \left[\begin{array}{c} \left(\frac{\partial P_w}{\partial I} sI\right)^2 + \left(\frac{\partial P_w}{\partial A} sA\right)^2 + \left(\frac{\partial P_w}{\partial B} sB\right)^2 + \left(\frac{\partial P_w}{\partial C} sC\right)^2 + \\ \left(\frac{\partial P_w}{\partial D} sD\right)^2 + \left(\frac{\partial P_w}{\partial T_{HAMP}} sT_{HAMP}\right)^2 \end{array} \right]^{1/2} \tag{C.121}$$

where

$$\frac{\partial P_w}{\partial I} = 10^{\left\{KI\left[A - \frac{B}{T_{HAMP}-E}\right] + \left[C - \frac{D}{T_{HAMP}-E}\right]\right\}} * \ln(10) * K\left[A - \frac{B}{T_{HAMP}-E}\right] \tag{C.122}$$

$$\frac{\partial P_w}{\partial A} = 10^{\left\{KI\left[A - \frac{B}{T_{HAMP}-E}\right] + \left[C - \frac{D}{T_{HAMP}-E}\right]\right\}} * \ln(10) * KI \tag{C.123}$$

$$\frac{\partial P_w}{\partial B} = 10^{\left\{KI\left[A - \frac{B}{T_{HAMP}-E}\right] + \left[C - \frac{D}{T_{HAMP}-E}\right]\right\}} * \ln(10) * KI\left[\frac{-1}{T_{HAMP}-E}\right] \tag{C.124}$$

$$\frac{\partial P_w}{\partial C} = 10^{\left\{KI\left[A - \frac{B}{T_{HAMP}-E}\right] + \left[C - \frac{D}{T_{HAMP}-E}\right]\right\}} * \ln(10) \tag{C.125}$$

$$\frac{\partial P_w}{\partial D} = 10^{\left\{KI\left[A - \frac{B}{T_{HAMP}-E}\right] + \left[C - \frac{D}{T_{HAMP}-E}\right]\right\}} * \ln(10) * \left[\frac{-1}{T_{HAMP}-E}\right] \tag{C.126}$$

$$\frac{\partial P_w}{\partial T_{HAMP}} = 10^{\left\{KI\left[A - \frac{B}{T_{HAMP}-E}\right] + \left[C - \frac{D}{T_{HAMP}-E}\right]\right\}} * \ln(10) * \left\{KI\left[\frac{-B}{(T_{HAMP}-E)^2}\right] + \left[\frac{-D}{(T_{HAMP}-E)^2}\right]\right\} \tag{C.127}$$

Relative Humidity (equation B.5)

$$b\phi_{HAMP} = \left[\left(\frac{\partial \phi_{HAMP}}{\partial P_w} bP_w \right)^2 + \left(\frac{\partial \phi_{HAMP}}{\partial P_{ws}} bP_{ws} \right)^2 \right]^{1/2} \quad \text{(C.128)}$$

$$s\phi_{HAMP} = \left[\left(\frac{\partial \phi_{HAMP}}{\partial P_w} sP_w \right)^2 + \left(\frac{\partial \phi_{HAMP}}{\partial P_{ws}} sP_{ws} \right)^2 \right]^{1/2} \quad \text{(C.129)}$$

where

$$\frac{\partial \phi_{HAMP}}{\partial P_w} = \frac{1}{P_{ws}} \quad \text{(C.130)}$$

$$\frac{\partial \phi_{HAMP}}{\partial P_{ws}} = \frac{-P_w}{P_{ws}^2} \quad \text{(C.131)}$$

TABLE C.4. Bias, precision and total uncertainties of the liquid desiccant.

Calculated Value	**Value**	**b_x (68%)**	**s_x (68%)**	**U_x (95%)**
C_{salt} [%]	32.0	±0.9	±0.04	±1.8
P_w [Pa]	408.4	±1.7	±0.1	±3.4
P_{ws} [Pa]	1080.2	±4.4	±0.3	±8.8
W_{HAMP} [g_w/kg_{air}]	2.7	±0.01	±0.001	±0.02
RH_{HAMP} [% RH]	37.8	±0.2	±0.01	±0.3

APPENDIX D – COMPLETE DATA SET

This appendix presents the complete data set for all 83 tests. The data is separated by Reynolds number and the orientation of the HAMP in the test facility. Tables D.1 to D.3 present the data for the cases with the HAMP in the ceiling of the test section and Re = 65. Tables D.4 to D.6 present the data for the remainder of the cases with the HAMP in the ceiling of the test section. Table D.7 to D.9 present the data for the tests with the HAMP in the floor of the test section.

TABLE D.1. Operating conditions for ceiling panel tests with Re = 65.

Test	T_{up} [°C]	RH_{up} [% RH]	W_{up} [g_w/kg_{air}]	$T_{HAMP,1}$ [°C]	$T_{HAMP,2}$ [°C]	ρ_{HAMP} [kg/m^3]	RH_{HAMP} [% RH]	$W_{HAMP,1}$ [g_w/kg_{air}]	$W_{HAMP,2}$ [g_w/kg_{air}]
1	23.7	77.4	15.1	14.1	14.6	1218.7	30.1	3.2	3.3
2	24.3	9.3	1.8	14.1	15.0	1144.0	60.0	6.3	6.7
3	24.4	71.6	14.5	34.9	34.9	1218.7	29.6	10.9	10.9
4	24.3	9.2	1.8	34.5	34.4	1141.0	59.7	22.0	21.8
5	24.1	73.5	14.7	24.6	24.7	1218.7	30.1	6.1	6.1
6	24.1	9.5	1.9	24.5	24.5	1143.0	59.9	12.2	12.2
7	23.1	15.1	2.8	21.4	21.2	997.0	100.0	17.0	16.8
8	22.7	15.5	2.8	24.1	24.2	1214.1	31.6	5.9	5.9
9	22.6	67.6	12.3	24.1	24.3	1217.6	30.4	5.7	5.7
10	21.6	63.3	10.8	11.9	12.2	1215.6	31.2	2.7	2.7
11	22.8	11.6	2.1	35.2	35.4	1226.3	27.2	9.7	9.8
12	25.0	11.7	2.4	23.2	23.4	996.6	100.0	19.0	19.3
13	24.4	71.3	14.5	25.6	25.6	1397.9	14.7	3.2	3.2
14	22.4	20.9	3.7	19.5	19.3	1145.0	59.4	8.9	8.7
15	22.7	19.1	3.4	18.5	18.3	1145.0	59.4	8.3	8.2
16	23.6	57.3	11.0	19.6	19.5	1219.0	30.0	4.5	4.5
17	23.2	54.5	10.2	17.7	17.6	1219.0	30.1	4.0	4.0
18	24.2	67.9	13.6	30.2	30.2	1219.0	29.8	8.4	8.4
19	22.1	64.7	11.4	7.2	7.0	1197.2	37.8	2.5	2.5
20	22.2	65.9	11.7	9.1	8.9	1197.2	37.9	2.9	2.8
21	22.3	67.6	12.0	11.0	10.8	1197.2	37.9	3.2	3.2
22	22.3	69.0	12.3	12.9	12.7	1197.2	37.9	3.7	3.6
23	22.5	71.5	12.9	14.8	14.6	1197.2	37.9	4.2	4.1

TABLE D.1. Operating conditions for ceiling panel tests with Re = 65 continued.

Test	T_{up} [°C]	RH_{up} [% RH]	W_{up} [g_w/kg_{air}]	$T_{HAMP,1}$ [°C]	$T_{HAMP,2}$ [°C]	ρ_{HAMP} [kg/m^3]	RH_{HAMP} [% RH]	$W_{HAMP,1}$ [g_w/kg_{air}]	$W_{HAMP,2}$ [g_w/kg_{air}]
24	22.2	78.1	13.9	16.7	16.5	1197.2	37.9	4.7	4.7
25	22.2	77.2	13.7	18.6	18.3	1197.2	37.9	5.3	5.2
26	22.3	57.3	10.2	7.2	7.1	1197.2	37.8	2.5	2.5
27	22.5	62.8	11.3	11.0	10.8	1197.2	37.9	3.2	3.2
28	22.8	59.3	10.9	7.2	7.0	1197.2	37.8	2.5	2.5
29	23.3	67.4	12.8	8.3	8.3	1197.2	37.9	2.7	2.7
30	22.9	68.1	12.6	8.3	8.2	1197.2	37.9	2.7	2.7
31	24.0	79.9	15.9	35.1	35.0	1197.2	37.1	13.9	13.8
32	23.9	80.2	15.8	32.2	32.1	1197.2	37.3	11.9	11.8
33	24.0	80.7	16.0	29.3	29.2	1197.2	37.5	10.1	10.0
34	24.1	80.9	16.2	26.4	26.3	1197.2	37.6	8.5	8.5
35	24.2	80.6	16.2	24.5	24.3	1197.2	37.7	7.6	7.5
36	24.4	79.4	16.2	21.6	21.5	1197.2	37.8	6.4	6.4
37	24.5	78.7	16.1	18.7	18.6	1197.2	37.9	5.3	5.3
38	23.9	66.7	13.1	8.0	7.9	1197.2	37.9	2.6	2.6
39	23.7	68.4	13.3	10.8	10.6	1183.7	43.3	3.7	3.6
40	24.8	74.9	15.6	35.4	35.3	1183.7	42.2	16.2	16.1
41	22.7	82.4	15.1	34.9	34.8	1183.7	42.2	15.7	15.6
42	22.6	86.2	15.7	22.8	22.7	1183.7	43.0	7.8	7.8
43	22.6	86.7	15.8	32.9	32.7	1183.7	42.4	14.1	13.9
44	22.6	77.8	14.2	12.4	12.2	1181.1	44.4	4.2	4.1
45	22.5	78.8	14.3	12.4	12.2	1181.1	44.4	4.2	4.1
46	22.4	77.5	13.9	10.5	10.3	1181.1	44.4	3.7	3.6
47	22.3	75.3	13.4	8.6	8.3	1181.1	44.3	3.2	3.2
48	22.2	72.5	12.9	6.7	6.5	1181.1	44.3	2.8	2.8
49	22.1	68.8	12.1	5.7	5.4	1181.1	44.3	2.6	2.6
50	22.4	80.2	14.4	16.2	16.1	1177.5	45.8	5.5	5.5
51	22.2	78.2	13.9	15.2	14.9	1177.5	45.8	5.2	5.1
52	22.1	79.6	14.1	14.2	14.0	1177.5	45.8	4.9	4.8
53	22.1	78.4	13.8	13.2	13.0	1177.5	45.8	4.5	4.5
54	22.2	83.7	14.9	17.1	16.9	1177.5	45.7	5.8	5.8
55	22.8	84.7	15.6	29.9	30.0	1177.5	45.1	12.6	12.7
56	22.9	83.0	15.4	29.0	29.0	1177.5	45.1	12.0	12.0
57	23.1	81.1	15.2	28.0	28.0	1177.5	45.2	11.3	11.3
58	23.2	80.5	15.2	27.0	27.0	1177.5	45.3	10.7	10.7
59	22.4	65.7	11.8	23.9	24.2	1214.2	31.6	5.8	5.9
60	22.5	74.7	13.5	24.0	24.1	1214.2	31.6	5.9	5.9

TABLE D.2. HAMP design parameters for ceiling panel tests with Re = 65.

Test	Ra_h [x10^5]	Ra_m [x10^5]	Ra^+ [x10^5]	NTU_{theo} [-]	$NTU_{m,theo}$ [-]	Cr [-]	H* [-]
1	31.6	4.6	36.2	1.6	0.4	0.006	3
2	32.2	-1.9	30.2	1.6	0.4	0.005	-1
3	-32.4	1.4	-31.0	1.5	0.2	0.006	-1
4	-31.4	-8.7	-40.0	1.5	0.2	0.005	5
5	-2.0	3.4	1.4	1.5	0.2	0.006	-43
6	-0.2	-4.5	-4.7	1.4	0.2	0.005	65
7	4.5	-6.5	-2.0	1.4	0.2	0.004	-21
8	-3.6	-1.6	-5.2	1.4	0.2	0.005	6
9	-4.3	2.8	-1.5	1.4	0.2	0.006	-11
10	33.9	3.6	37.5	1.4	0.2	0.006	2
11	-37.9	-3.7	-41.6	1.4	0.2	0.008	2
12	4.4	-7.6	-3.2	1.4	0.2	0.004	-23
13	-3.5	5.1	1.6	1.5	0.2	0.006	-24
14	10.9	-2.4	8.5	1.5	0.3	0.005	-4
15	14.8	-2.2	12.6	1.5	0.3	0.005	-3
16	14.6	2.7	17.3	1.5	0.3	0.006	4
17	19.9	2.6	22.5	1.6	0.3	0.006	3
18	-17.1	2.3	-14.8	1.5	0.2	0.006	-2
19	54.3	3.9	58.2	1.6	0.4	0.006	1
20	47.1	3.8	51.0	1.6	0.4	0.006	2
21	40.1	3.7	43.9	1.6	0.4	0.006	2
22	33.4	3.6	37.0	1.6	0.4	0.006	2
23	27.2	3.5	30.8	1.6	0.3	0.006	3
24	19.9	3.6	23.5	1.5	0.3	0.006	4
25	13.6	3.3	17.0	1.5	0.3	0.006	6
26	55.1	3.7	58.7	1.6	0.4	0.006	1
27	41.1	3.7	44.8	1.6	0.4	0.006	2
28	56.4	3.9	60.3	1.6	0.4	0.006	1
29	53.2	4.3	57.5	1.6	0.4	0.006	2
30	51.9	4.5	56.5	1.6	0.4	0.006	2
31	-31.6	0.8	-30.8	1.5	0.2	0.006	0
32	-23.0	1.7	-21.3	1.5	0.2	0.006	-1
33	-14.0	2.6	-11.4	1.4	0.2	0.006	-3
34	-4.6	3.3	-1.3	1.4	0.2	0.006	-8
35	1.8	3.5	5.3	1.5	0.2	0.006	-72
36	11.4	4.1	15.4	1.5	0.3	0.006	9
37	21.0	4.4	25.4	1.6	0.3	0.006	5
38	55.3	4.8	60.1	1.6	0.4	0.006	2
39	44.2	4.3	48.5	1.6	0.4	0.006	2
40	-29.4	-0.7	-30.1	1.5	0.2	0.005	0
41	-36.5	-0.6	-37.1	1.5	0.2	0.006	0
42	1.2	3.3	4.5	1.5	0.2	0.006	-99
43	-30.4	0.6	-29.8	1.5	0.2	0.006	0
44	36.4	4.5	40.8	1.6	0.4	0.006	2
45	36.2	4.5	40.7	1.6	0.4	0.006	2
46	43.1	4.7	47.8	1.6	0.4	0.006	2
47	49.8	4.7	54.5	1.6	0.4	0.006	2
48	56.5	4.7	61.2	1.6	0.4	0.006	2
49	60.0	4.5	64.5	1.6	0.4	0.006	1
50	22.0	3.7	25.7	1.5	0.3	0.006	4

TABLE D.2. HAMP design parameters for ceiling panel tests with Re = 65 cont.

Test	Ra_h [x10^5]	Ra_m [x10^5]	Ra^+ [x10^5]	NTU_{theo} [-]	$NTU_{m,theo}$ [-]	Cr [-]	H* [-]
51	25.3	3.7	28.9	1.5	0.3	0.006	3
52	28.3	3.9	32.2	1.5	0.4	0.006	3
53	31.8	4.0	35.8	1.6	0.4	0.006	3
54	18.4	3.7	22.1	1.5	0.3	0.006	4
55	-21.5	1.0	-20.4	1.4	0.2	0.006	-1
56	-17.5	1.4	-16.2	1.4	0.2	0.006	-1
57	-13.6	1.6	-12.0	1.4	0.2	0.006	-2
58	-10.3	1.9	-8.5	1.4	0.2	0.006	-3
59	-4.8	2.3	-2.5	1.4	0.2	0.006	-10
60	-4.3	3.1	-1.2	1.4	0.2	0.006	-13

TABLE D.3. Results and performance data for ceiling panel tests with Re = 65.

Test	T_{down} [°C]	RH_{down} [% RH]	W_{down} [g_w/kg_{air}]	ε_{lat} [-]	ε_{sens} [-]	ε_{tot} [-]	q'' [W/m^2]	m'' [$g_w/(s \cdot m^2)$]	NTU_{exp} [-]	$NTU_{m,ex}$ [-]
1	22.6	50.1	9.0	0.51	0.11	0.41	-5.4	-0.029	0.1	0.7
2	22.8	21.2	3.8	0.45	0.15	3.21	-7.3	0.010	0.2	0.6
3	25.0	62.2	13.1	0.41	0.06	-2.00	2.9	-0.007	0.1	0.5
4	24.9	33.7	7.0	0.26	0.06	0.22	2.9	0.025	0.1	0.3
5	24.0	56.0	11.0	0.42	0.20	0.44	-0.5	-0.017	0.2	0.6
6	24.8	23.1	4.7	0.28	1.75	0.30	--	0.014	--	0.3
7	22.1	32.0	5.6	0.20	0.59	0.18	-4.5	0.012	0.8	0.2
8	23.5	17.6	3.3	0.17	0.57	0.23	3.6	0.002	0.8	0.2
9	23.3	56.7	10.7	0.24	0.47	0.21	3.4	-0.007	0.6	0.3
10	20.8	53.6	8.7	0.26	0.08	0.20	-4.3	-0.011	0.1	0.3
11	24.2	18.6	3.7	0.21	0.11	0.17	9.9	0.011	0.1	0.2
12	24.2	30.0	5.9	0.21	0.44	0.20	-3.9	0.017	0.6	0.2
13	24.7	58.0	11.9	0.22	0.25	0.22	1.5	-0.012	0.3	0.3
14	22.6	26.2	4.7	0.19	0.07	0.27	1.0	0.005	0.1	0.2
15	22.5	26.2	4.7	0.25	0.05	0.36	-1.0	0.006	0.0	0.3
16	23.9	43.0	8.4	0.40	0.07	0.31	1.5	-0.013	0.1	0.5
17	23.4	41.7	7.9	0.37	0.04	0.27	1.0	-0.011	0.0	0.5
18	25.7	56.3	12.3	0.25	0.25	0.25	7.3	-0.006	0.3	0.3
19	20.8	49.7	8.0	0.38	0.09	0.26	-6.4	-0.016	0.1	0.5
20	21.0	51.2	8.4	0.37	0.09	0.27	-5.9	-0.016	0.1	0.5
21	21.2	51.7	8.6	0.40	0.10	0.30	-5.4	-0.017	0.1	0.5
22	21.6	51.2	8.7	0.42	0.07	0.31	-3.4	-0.017	0.1	0.5
23	22.0	50.6	8.8	0.47	0.06	0.37	-2.5	-0.020	0.1	0.6
24	22.1	53.5	9.4	0.49	0.02	0.40	-0.5	-0.021	0.0	0.7
25	22.4	54.3	9.7	0.48	0.06	0.40	1.0	-0.019	0.1	0.6
26	21.2	51.2	8.5	0.22	0.07	0.16	-5.4	-0.008	0.1	0.2
27	21.6	53.4	9.1	0.28	0.08	0.21	-4.4	-0.011	0.1	0.3
28	21.4	52.9	8.9	0.24	0.09	0.18	-6.9	-0.010	0.1	0.3
29	21.9	52.0	9.0	0.37	0.09	0.27	-6.9	-0.018	0.1	0.5
30	21.4	58.8	9.9	0.27	0.10	0.21	-7.4	-0.013	0.1	0.3
31	26.1	67.1	15.1	0.40	0.19	0.03	10.2	-0.004	0.2	0.5

TABLE D.3. Results and performance data for ceiling panel tests with Re = 65 cont.

Test	T_{down} [°C]	RH_{down} [% RH]	W_{down} [g_w/kg_{air}]	ε_{lat} [-]	ε_{sens} [-]	ε_{tot} [-]	q'' [W/m^2]	m'' [$g_w/(s \cdot m^2)$]	NTU_{exp} [-]	$NTU_{m,ex}$ [-]
32	26.1	65.7	14.8	0.27	0.27	0.29	10.7	-0.005	0.3	0.3
33	25.9	64.9	14.4	0.27	0.36	0.22	9.3	-0.008	0.4	0.3
34	25.8	63.2	13.9	0.29	0.74	0.23	8.3	-0.011	1.4	0.3
35	25.7	58.1	12.7	0.41	5.00	0.34	--	-0.016	--	0.5
36	25.4	58.5	12.6	0.37	0.36	0.29	4.9	-0.017	0.3	0.5
37	25.0	56.1	11.8	0.40	0.09	0.32	2.4	-0.021	0.1	0.5
38	21.8	59.1	10.2	0.28	0.13	0.23	-10.3	-0.014	0.1	0.3
39	21.8	60.4	10.4	0.30	0.15	0.25	-9.3	-0.014	0.2	0.4
40	27.1	58.1	13.8	3.22	0.22	-0.18	11.2	-0.008	0.2	1.5
41	24.3	69.3	14.0	1.89	0.13	-0.09	8.2	-0.006	0.1	1.1
42	23.6	66.4	12.8	0.37	5.00	0.32	--	-0.014	--	0.5
43	24.3	72.0	14.5	0.74	0.17	-0.25	8.7	-0.006	0.2	1.3
44	21.9	64.1	11.1	0.30	0.07	0.24	-3.5	-0.015	0.1	0.4
45	21.9	65.0	11.3	0.29	0.06	0.23	-2.9	-0.014	0.1	0.3
46	21.7	64.7	11.1	0.28	0.06	0.21	-3.4	-0.014	0.1	0.3
47	21.2	64.6	10.7	0.26	0.08	0.20	-5.4	-0.013	0.1	0.3
48	20.8	63.4	10.3	0.26	0.09	0.19	-6.9	-0.012	0.1	0.3
49	20.4	61.8	9.8	0.25	0.10	0.19	-8.4	-0.011	0.1	0.3
50	22.2	60.9	10.8	0.41	0.03	0.33	-1.0	-0.017	0.0	0.5
51	21.9	59.6	10.3	0.41	0.04	0.32	-1.5	-0.017	0.0	0.5
52	21.7	61.2	10.5	0.39	0.05	0.30	-2.0	-0.017	0.1	0.5
53	21.5	61.1	10.3	0.38	0.07	0.29	-3.0	-0.017	0.1	0.5
54	22.1	61.7	10.8	0.45	0.02	0.37	-0.5	-0.019	0.0	0.6
55	24.1	68.9	13.7	0.63	0.18	7.33	6.4	-0.009	0.2	1.0
56	24.5	68.8	14.0	0.40	0.26	0.73	7.8	-0.007	0.3	0.5
57	24.7	67.3	13.9	0.34	0.33	0.35	7.8	-0.006	0.4	0.4
58	24.6	65.8	13.5	0.38	0.37	0.38	6.8	-0.008	0.5	0.5
59	22.9	52.0	9.6	0.37	0.33	52.33	2.4	-0.010	0.4	0.5
60	23.1	58.8	11.0	0.33	0.40	56.84	2.9	-0.012	0.5	0.4

TABLE D.4. Operating conditions for remaining ceiling panel tests.

Test	T_{up} [°C]	RH_{up} [% RH]	W_{up} [g_w/kg_{air}]	$T_{HAMP,1}$ [°C]	$T_{HAMP,2}$ [% RH]	ρ_{HAMP} [g_w/kg_{air}]	RH_{HAMP} [% RH]	$W_{HAMP,1}$ [g_w/kg_{air}]	$W_{HAMP,2}$ [g_w/kg_{air}]
61	22.4	2.8	0.5	21.3	21.0	997.2	100.0	16.9	16.6
62	22.5	2.8	0.5	29.3	29.2	995.2	100.0	27.6	27.5
63	21.5	2.9	0.5	8.1	7.7	999.3	100.0	7.1	6.9
64	21.9	3.6	0.6	21.4	21.6	1215.3	31.3	5.2	5.3
65	22.0	3.1	0.5	29.5	30.3	1215.3	31.0	8.4	8.8
66	21.1	2.9	0.5	8.1	8.3	1215.3	31.2	2.2	2.2
67	22.1	2.8	0.5	21.6	21.9	1142.1	60.4	10.3	10.5
68	22.1	2.8	0.5	28.7	29.2	1142.1	59.8	15.7	16.1
69	21.2	3.7	0.6	8.1	7.8	1142.1	61.0	4.3	4.2
70	25.1	12.4	2.6	23.0	23.1	1176.7	45.8	8.5	8.5

TABLE D.5. HAMP design parameters for remaining ceiling panel tests.

Test	Re [-]	Ra_h [$x10^5$]	Ra_m [$x10^5$]	Ra^+ [$x10^5$]	Cr [-]	H* [-]
61	113	4.2	-7.8	-3.6	0.007	-37
62	111	-21.3	-12.8	-34.2	0.007	10
63	117	48.9	-3.1	45.8	0.007	-1
64	113	1.7	-2.3	-0.5	0.011	-23
65	112	-24.7	-3.9	-28.6	0.010	3
66	117	46.5	-0.8	45.6	0.011	0
67	113	1.6	-5.0	-3.4	0.010	-49
68	112	-21.6	-7.5	-29.1	0.009	6
69	117	47.9	-1.8	46.1	0.010	-1
70	105	5.7	-2.6	3.1	0.009	-7

TABLE D.6. Results and performance data for remaining ceiling panel tests.

Test	T_{down} [°C]	RH_{down} [% RH]	W_{down} [g_w/kg_{air}]	ε_{lat} [-]	ε_{sens} [-]	ε_{tot} [-]	q'' [W/m^2]	m'' [$g_w/(s \cdot m^2)$]	NTU_{exp} [-]	$NTU_{m,ex}$ [-]
61	22.3	16.3	2.9	0.14	0.09	0.15	-0.9	0.021	0.1	0.2
62	23.2	18.5	3.4	0.11	0.10	0.11	6.2	0.026	0.1	0.1
63	20.1	12.9	2.0	0.23	0.10	0.74	-12.4	0.013	0.1	0.3
64	22.1	6.6	1.1	0.11	0.40	0.14	1.8	0.005	0.4	0.1
65	23.0	8.6	1.6	0.13	0.13	0.13	8.8	0.009	0.1	0.1
66	19.7	5.8	0.9	0.23	0.11	0.05	-12.4	0.003	0.1	0.3
67	22.3	6.4	1.1	0.06	0.40	0.07	1.8	0.006	0.5	0.1
68	22.9	10.6	1.9	0.09	0.12	0.10	7.1	0.013	0.1	0.1
69	19.9	8.9	1.3	0.20	0.10	-0.15	-11.5	0.007	0.1	0.2
70	24.4	21.1	4.2	0.28	0.33	0.27	-5.8	0.013	0.4	0.3

TABLE D.7. Operating conditions for floor panel tests.

Test	T_{up} [°C]	RH_{up} [% RH]	W_{up} [g_w/kg_{air}]	$T_{HAMP,1}$ [°C]	$T_{HAMP,2}$ [°C]	ρ_{HAMP} [kg/m^3]	RH_{HAMP} [% RH]	$W_{HAMP,1}$ [g_w/kg_{air}]	$W_{HAMP,2}$ [g_w/kg_{air}]
71	21.9	69.7	12.1	11.8	12.2	1216.9	30.7	2.6	2.7
72	23.2	23.5	4.4	35.3	35.1	1210.5	32.4	11.6	11.4
73	21.0	5.7	0.9	18.2	17.7	997.8	100.0	13.87	13.43
74	21.1	7.2	1.2	18.5	18.2	997.7	100.0	14.14	13.87
75	20.9	5.1	0.8	17.6	18.1	997.8	100.0	13.34	13.78
76	21.1	5.0	0.8	17.6	16.6	997.9	100.0	13.34	12.51
77	21.4	4.7	0.8	18.1	16.8	997.8	100.0	13.78	12.67
78	21.3	4.4	0.7	18.0	16.7	997.8	100.0	13.69	12.59
79	20.9	5.2	0.8	17.0	17.4	997.9	100.0	12.83	13.17
80	20.0	7.7	1.2	17.6	17.5	997.8	100.0	13.34	13.26
81	19.7	6.9	1.0	17.5	17.3	997.8	100.0	13.26	13.09
82	22.8	70.9	13.0	24.1	24.3	1214.2	31.6	5.9	6.0
83	22.4	14.1	2.5	24.1	24.2	1214.2	31.6	5.9	5.9

TABLE D.8. HAMP design parameters for floor panel tests.

Test	Re [-]	Ra_h [$x10^5$]	Ra_m [$x10^5$]	Ra^+ [$x10^5$]	Cr [-]	H* [-]
71	62	-33.0	-3.4	-36.4	0.006	2
72	60	34.9	3.3	38.1	0.006	1
73	959	-9.7	5.3	-4.5	--	-12
74	957	-9.0	5.3	-3.7	--	-12
75	959	-10.5	5.2	-5.3	--	-9
76	4798	-12.8	5.9	-6.9	--	-9
77	4784	-13.3	6.3	-6.9	--	-10
78	4787	-13.3	6.2	-7.1	--	-10
79	4802	-12.9	6.1	-6.8	--	-8
80	963	-8.4	5.3	-3.1	--	-13
81	964	-8.0	5.4	-2.7	--	-14
82	62	3.2	-2.8	0.5	0.006	-14
83	62	5.5	1.4	6.9	0.006	5

TABLE D.9. Results and performance data for floor panel tests.

Test	T_{down} [°C]	RH_{down} [% RH]	W_{down} [g_w/kg_{air}]	ε_{lat} [-]	ε_{sens} [-]	ε_{tot} [-]	q'' [W/m^2]	m'' [$g_w/(s \cdot m^2)$]	NTU_{exp} [-]	$NTU_{m,ex}$ [-]
71	21.0	58.6	9.6	0.265	0.089	0.213	-4.4	-0.012	0.1	0.3
72	25.3	32.6	6.9	0.351	0.174	0.279	10.1	0.012	0.2	0.4
73	20.3	40.1	6.3	0.413	0.250	0.428	-51.9	0.391	0.3	0.5
74	20.6	41.7	6.6	0.422	0.192	0.442	-37.1	0.399	0.2	0.6
75	20.6	40.1	6.4	0.444	0.091	0.486	-22.2	0.407	0.1	0.6
76	20.2	15.8	2.4	0.130	0.257	0.114	-333.5	0.596	0.3	0.1
77	20.9	9.1	1.5	0.053	0.152	0.042	-185.0	0.251	0.1	0.1
78	20.8	12.0	1.9	0.092	0.152	0.086	-185.0	0.438	0.1	0.1
79	20.6	13.1	2.1	0.103	0.077	0.107	-111.1	0.453	0.1	0.1
80	19.7	34.4	5.2	0.328	0.125	0.346	-22.3	0.293	0.1	0.4
81	19.5	32.4	4.8	0.309	0.091	0.326	-14.9	0.277	0.1	0.4
82	23.7	53.0	10.2	0.391	0.692	56.0	4.4	-0.013	1.1	0.5
83	22.7	24.7	4.5	0.576	0.176	28.7	1.5	0.009	0.2	0.9

APPENDIX E – CONVECTION HEAT TRANSFER INSIDE HAMP

In Section 4.1, the convection heat and mass transfer coefficients in the air (h and h_m, respectively) are calculated. The analysis presented neglects any heat transfer or mass diffusion in the liquid desiccant inside the HAMP. Only the heat transfer and mass diffusion through the membrane and the air are considered in the analysis. This assumption means that the temperature and concentration of the liquid desiccant do not change across the height of the liquid channel. This appendix analyses the heat and mass transfer through the liquid desiccant and discusses why this transfer can be neglected from the analysis used in Section 4.1.

To calculate the heat and mass transfer coefficients, the heat and mass transfer between the HAMP and the air stream are compared to the amount of heat and moisture transfer across the membrane. Figure E.1 shows a schematic of the test section, with the HAMP in the top of the duct. The three measurement locations are marked with boxes in the schematic. The heat and moisture transfer across the membrane is between the HAMP location (measured at the centre of the liquid desiccant channel) and the location marked AIR. The conditions at the AIR location are the average of the upstream and downstream air conditions. Figure E.1 shows the circuit of resistances that will impede heat and mass transfer between these two points. In order to show that the amount of heat and mass transfer through the liquid is negligible compared to the total amount of heat and mass transfer, the temperature and humidity ratio of the liquid desiccant on

the inside surface of the membrane must be calculated. This location is marked in the schematic as HAMP,surf.

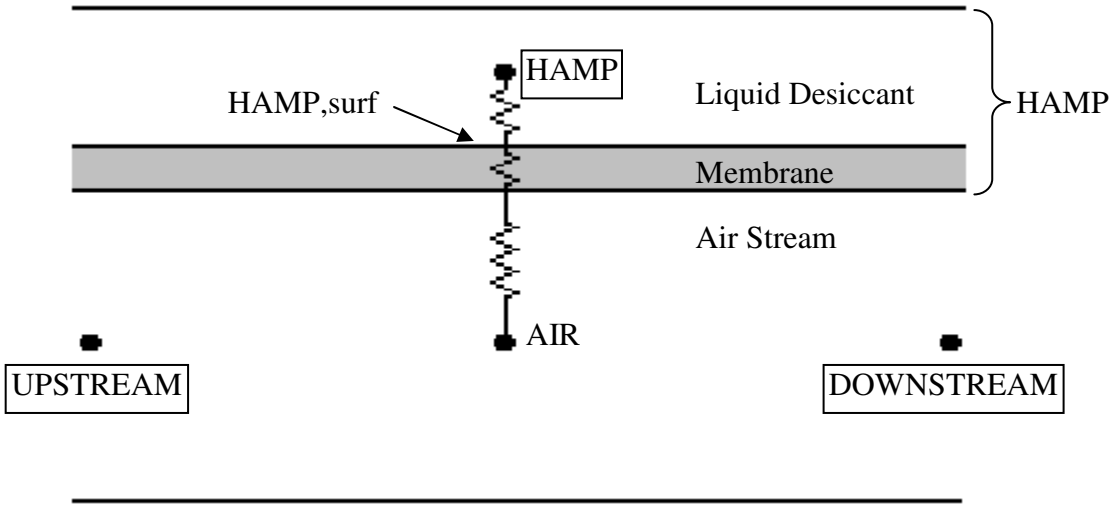

FIGURE E.1. Schematic of the heat and mass transfer resistance in the test section.

Assuming one-dimensional heat and mass transfer between the HAMP and the air stream with no losses to the surroundings, the following equations can be written

$$q_{HAMP\text{-}AIR}=q_{HAMP\text{-}HAMP,surf}=q_{UPSTREAM\text{-}DOWNSTREAM} \tag{E.1}$$

and $$\dot{m}_{w,HAMP\text{-}AIR}=\dot{m}_{w,HAMP\text{-}HAMP,surf}=\dot{m}_{w,UPSTREAM\text{-}DOWNSTREAM} \tag{E.2}$$

where q is the rate of heat transfer [W] and $\dot{m}_w$ is the rate of mass transfer [kg_w/s].

The heat transfer between the HAMP and the air is calculated from

$$q_{HAMP\text{-}AIR}=UA_{surface}\left(T_{HAMP}-T_{AIR}\right) \tag{E.3}$$

where U is the overall heat transfer coefficient [$W/(m^2 \cdot K)$], $A_{surface}$ is the surface area of the HAMP [m^2], T_{HAMP} is the measured temperature of the liquid desiccant [K] and T_{AIR} is the calculated average of the upstream and downstream temperatures [K].

The heat transfer across the HAMP is calculated from

$$q_{HAMP\text{-}HAMP,surf}=h_{sol}A_{surface}\left(T_{HAMP}-T_{HAMP,surf}\right) \quad (E.4)$$

where h_{sol} is the convection heat transfer coefficient of the liquid desiccant solution [W/(m^2·K)] and $T_{HAMP,surf}$ is the temperature at the surface between the membrane and the liquid desiccant, inside the HAMP [K].

The heat transfer added or removed from the air is calculated from

$$q_{UPSTREAM\text{-}DOWNSTREAM}=\dot{m}_{air}c_{p_{air}}\left(T_{DOWNSTREAM}-T_{UPSTREAM}\right) \quad (E.5)$$

where $\dot{m}_{air}$ is the mass flow rate of the air [kg$_{air}$/s], $c_{p_{air}}$ is the specific heat of the air [J/(kg$_{air}$·K)] and $T_{DOWNSTREAM}$ and $T_{UPSTREAM}$ are the measured temperatures at those two locations [K]. The heat transfer surface area of the prototype HAMP is 0.043 m^2. The specific heat of the air is taken from Incropera and DeWitt (2002) and the mass flow rate of the air is known from the experiments.

By combining equations (E.4) and (E.5) an expression is derived for the temperature of the liquid desiccant at the inside surface of the membrane

$$T_{HAMP,surf}=T_{HAMP}-\frac{\dot{m}_{air}c_{p_{air}}\left(T_{DOWNSTREAM}-T_{UPSTREAM}\right)}{h_{sol}A_{surface}}. \quad (E.6)$$

The only unknown in this equation is the convection heat transfer coefficient on the liquid side, h_{liquid}. This value can be approximated from a heat transfer correlation for flow through a rectangular channel with forced convection (Krishnamurty and Sambasiva Rao (1967)) as

$$Nu=0.93Re^{1/3}Pr^{1/3}\left(\frac{\mu_{avg}}{\mu_{bulk}}\right)^{0.14}\left(\frac{Z}{D_h}\right)^{-1/3}\int_0^1 \phi_x^{1/3}dr \qquad (E.7)$$

where Re = Reynolds number [-]
Pr = Prandtl number [-]
μ_{avg} = dynamic viscosity at the average air temperature [Pa·s]
μ_{bulk} = dynamic viscosity at the bulk air temperature [Pa·s]
Z = length of the heat transfer surface [m]
D_h = hydraulic diameter of the duct [m]
$\phi_x^{1/3}$ = a constant dependent on the aspect ratio of the duct

The length of the liquid desiccant channel is 1.14 m and the hydraulic diameter is 0.03 m. The aspect ratio of the channel is 0.71, which relates to a constant of 1.898 in equation (E.7). The average temperature of the fluid is the average of the inlet and outlet values. The bulk temperature of the fluid is the average of the inlet, outlet and surface values. At this time the surface values are not known so are neglected from the analysis. This means that the average and bulk temperature of the fluid are the same. The dynamic viscosity ratio then reduces to one.

The final two parameters that must be known to approximate the heat transfer coefficient in the liquid desiccant are the Reynolds number and Prandtl number. The Prandtl number is a function of specific heat, dynamic viscosity and thermal conductivity of the fluid, which vary with temperature and concentration for a salt solution. The Prandtl number will be different for each experiment, as the temperature and concentration vary from one test to another. For a lithium chloride solution at 20°C and a concentration of 35%, the Prandtl number is approximately 20. The Reynolds number is a function of the velocity of the fluid, the hydraulic diameter of the channel and the density and dynamic viscosity of the fluid. The velocity of the liquid desiccant is approximately 0.012 m/s for each test. The density and dynamic viscosity of the fluid will

vary for each test. The Reynolds number ranges between 80 and 100 for the range of tests. With these values, the Nusselt number is calculated from equation (E.7) and the convection heat transfer coefficient is calculated from the Nusselt number.

The mass transfer between the HAMP and the air is a bit more complicated. The mass transfer across the liquid desiccant channel is best described by the difference in concentration of the salt solution at the two locations. This is given by

$$\dot{m}_{w,HAMP\text{-}HAMP,surf}=h^{C}_{m,sol}A_{surface}\left(\gamma_{HAMP,surf}-\gamma_{HAMP}\right) \quad (E.8)$$

where $h^{C}_{m,sol}$ is the convection mass transfer coefficient in the liquid (based on concentration) [$kg_w/(m^2 \cdot s)$], $\gamma_{HAMP,surf}$ is the concentration of the salt solution at the surface of the membrane and γ_{HAMP} is the concentration of the salt solution in the middle of the liquid desiccant channel [-]. The amount of mass added or removed from the air is calculated based on the humidity ratio of the air as

$$\dot{m}_{w,UPSTREAM\text{-}DOWNSTREAM}=\dot{m}_{air}\left(W_{DOWNSTREAM}-W_{UPSTREAM}\right) \quad (E.9)$$

It should be noted when considering mass transfer from the HAMP to the air stream that moisture is being removed from the HAMP and added to the air. Therefore, the humidity ratio of the downstream air will be higher than the upstream air and the concentration of the salt solution at the surface of the membrane will be higher than the concentration of the salt solution in the middle of the channel. For this reason, the difference in concentration used in equation (E.8) is the opposite direction as the difference in temperature used in equation (E.4) for the heat transfer.

The concentration at the surface of the membrane inside the HAMP can be calculated by combining equations (E.8) and (E.9). The resulting equation is

$$\gamma_{HAMP,surf}=\gamma_{HAMP}+\frac{\dot{m}_{air}\left(W_{DOWNSTREAM}-W_{UPSTREAM}\right)}{h^{C}_{m,sol}A_{surface}}. \quad \text{(E.10)}$$

Using equations E.6 and E.10, the temperature and concentration at the inside surface of the membrane are calculated. The typical change in temperature from the centre of the channel to the inside surface of the membrane is 0.04°C, for all the tests. This value is less than the uncertainty that the temperature difference can be calculated at, which means that it cannot be accurately presented. It is also very small, which indicates that the resistance to heat transfer through the liquid desiccant is very small and therefore, can be neglected from the calculate of the overall heat transfer coefficient. The difference between the concentration at the inside surface of the membrane and the middle of the channel is also very small, so the resistance to mass transfer through the liquid desiccant can be neglected from the calculation of the overall mass transfer coefficient.

APPENDIX F – NUMERICAL MODELS

This appendix discusses the governing equations, assumptions and boundary conditions used in the two numerical models used to simulate the HAMP in Chapter 5. The numerical model used to predict the latent effectiveness of the HAMP was created by Mohit Bansal and the CFD model used to model the airflow through the test section was created by Prabal Talukdar.

F.1 NUMERICAL MODEL BY MOHIT BANSAL

A numerical model was created by Mohit Bansal to model the prototype HAMP using the commercial software program FLUENT (ANSYS, Canonsburg, PA). The geometry and mesh generation was performed in Gambit (Fluent Inc., Lebanon, NH). A schematic of the test section is shown in Figure F.1 with the HAMP in the floor panel configuration. The model is also performed with the HAMP in the ceiling panel configuration. A grid independency study was carried out and it was found that 100 grid points in each direction is sufficient to model the HAMP. The mesh is fine near the walls and coarser towards the inside of the duct. The computational domain is divided into two parts, a porous and a non-porous zone. The thickness of the porous zone is 0.16 mm, the thickness of the membrane. In the porous zone, 30 grid points were used in the Y-direction.

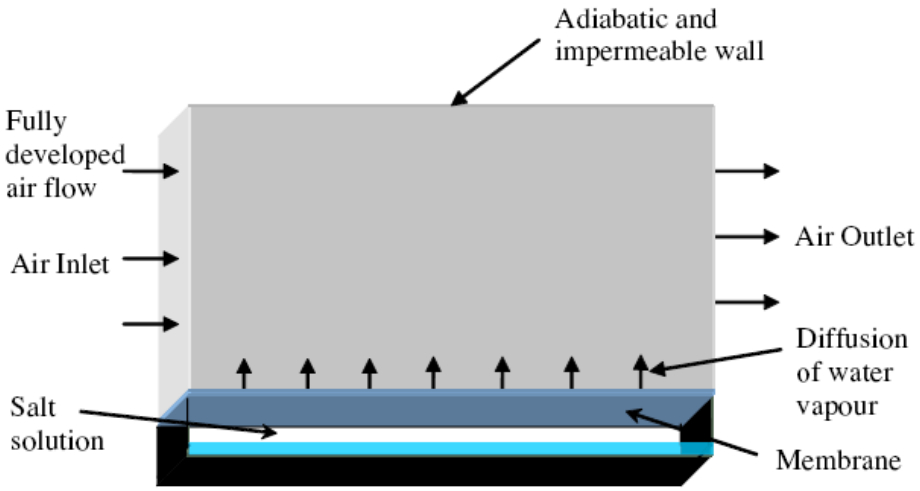

FIGURE F.1. The solution domain of the test section considered for the numerical model (Fauchoux et al. (2010)).

F.1.1 Assumptions

The following assumptions are made to simplify the governing equations:

- The surface temperature of the liquid is constant,
- The mass transfer through the membrane is by diffusion only,
- The thermo physical properties of the fluid are assumed to be constant and
- The secondary effects of concentration gradient on thermal diffusion and of thermal diffusion on mass transfer have been neglected.

F.1.2 Governing Equations

The governing equations for continuity, momentum, energy and species conservation for steady, incompressible flow, in 3D Cartesian coordinates are used in this model.

Continuity

$$\frac{\partial V_i}{\partial x_i}=0 \qquad \text{(F.1)}$$

Momentum

$$\rho \frac{\partial(V_i V_j)}{\partial x_j} = - \frac{\partial p}{\partial x_i} + \frac{\partial(2\mu s_{ij})}{\partial x_j} \tag{F.2}$$

where s_{ij} is the rate of strain tensor given by

$$s_{ij} = \frac{1}{2}\left(\frac{\partial V_i}{\partial x_j} + \frac{\partial V_j}{\partial x_i}\right) \tag{F.3}$$

Energy

$$\frac{\partial(V_i \rho E)}{\partial x_i} = \frac{\partial}{\partial x_i}\left(k_{eff} \frac{\partial T}{\partial x_i}\right) \tag{F.4}$$

where

$$E = h - \frac{p}{\rho} + \frac{V_i^2}{2} \tag{F.5}$$

$$k_{eff} = \varphi k_f + (1-\varphi) k_s \tag{F.6}$$

Concentration

$$\frac{\partial(\rho V_i Y_{i'})}{\partial x_i} = - \frac{\partial J_{i',i}}{\partial x_i} \tag{F.7}$$

where $J_{i'i}$ is the diffusion flux of species i' given by

$$J_{i'i} = -\rho D_{i',m} \frac{\partial Y_{i'}}{\partial x_i} \tag{F.8}$$

Variables

The variable in the above equations are:

V = velocity vector with respect to Cartesian coordinate x [m/s],
p = pressure [Pa],
T = temperature [K],
μ = dynamic viscosity [Pa·s],
ρ = density [kg_{air}/m^3],
k_{eff} = effective thermal conductivity [W/(m·K)],
h = enthalpy [J/kg],
φ = porosity of the medium [-],
k_f = thermal conductivity of the fluid [W/(m·K)],
k_s = thermal conductivity of the solid phase [W/(m·K)],
D = diffusion coefficient [m^2/s] and
Y = mass fraction [-].

F.1.3 Boundary Conditions

The following boundary conditions are used for the simulations:

- fully developed velocity profile at the inlet of the test section,
- a uniform temperature and concentration at the inlet,
- zero gradients for momentum, energy and concentration at the outlet,
- adiabatic and impermeable walls, except for the wall with the HAMP,
- zero heat and mass flux at the walls and
- surface of the HAMP has known temperature and mass fraction from the experiments.

F.2 CFD MODEL BY PRABAL TALUKDAR

The CFD simulation was created to model the specific HAMP used in the experiments, by Prabal Talukdar. The simulations are performed using an in-house CFD code called FASTEST3D. Four blocks were modeled; the inlet duct, the test section (below the HAMP), the outlet section

and the membrane (on top of the test section). The number of grids considered for each block are 30x50x50, 50x50x50, 60x50x50 and 50x50x10, respectively. Non-uniform grids are used with a grid size of 0.001 m at the wall. A commercial software program, ANSYS ICEM CFD (ANSYS, Canonsburg, PA) is used for the grid generation. The simulation is solved using an unsteady first order fully implicit scheme. A variable time step is used as it is computational faster than a small, uniform time step and gives very similar results.

(a)

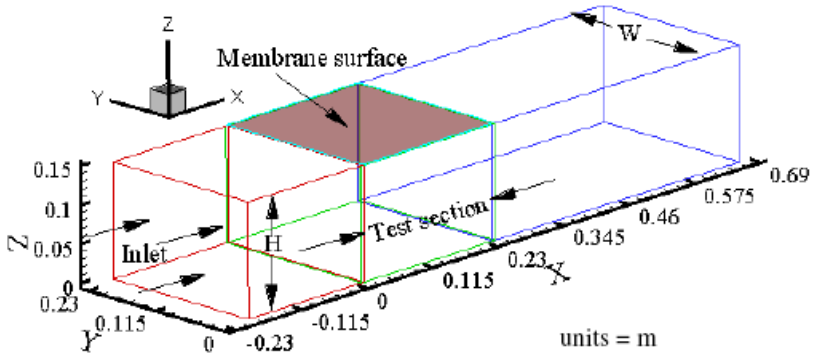

(b)

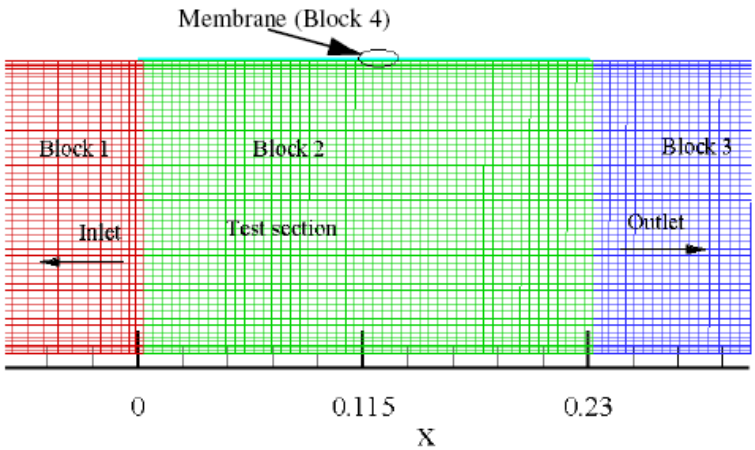

FIGURE F.2. Schematic of (a) the numerical domain and (b) a portion of the mesh in the xz-plane (Fauchoux et al. (2011)).

F.2.1 Assumptions

The following assumptions are made to simplify the governing transport equations:

- Viscous dissipation and compressibility effects in the energy equation are neglected,
- The thermo physical properties of the fluid are assumed to be constant except the density which is allowed to vary in the buoyancy term of the z-momentum equation,
- The secondary effects of concentration gradient on thermal diffusion and of thermal diffusion on mass transfer have been neglected and
- Mass transfer through the membrane is by diffusion only.

F.2.2 Governing Equations

The governing transport equations in 3-D Cartesian coordinates for fluid flow and heat and mass transfer are given in this section.

Continuity

$$\frac{\partial \rho}{\partial t} + \frac{\partial (\rho V_j)}{\partial x_j} = 0 \tag{F.9}$$

Momentum

$$\frac{\partial (\rho V_j)}{\partial t} + \frac{\partial}{\partial x_j}\left(\rho V_j V_i - \mu \frac{\partial V_j}{\partial x_j}\right) = -\frac{\partial P}{\partial x_i} + \frac{\partial}{\partial x_j}\left(\mu \frac{\partial V_j}{\partial x_i}\right) + \rho \beta g_i T + \rho \beta^* g_i C \tag{F.10}$$

Energy

$$\frac{\partial (\rho c_p T)}{\partial t} + \frac{\partial}{\partial x_j}\left(\rho V_j c_p T - k \frac{\partial T}{\partial x_j}\right) = 0 \tag{F.11}$$

Concentration

$$\frac{\partial C}{\partial t} + \frac{\partial}{\partial x_j}\left(V_j C - D \frac{\partial C}{\partial x_j}\right) = 0 \tag{F.12}$$

Variables

The variables in the above equations are:

V = velocity vector with respect to Cartesian coordinate x [m/s],
P = pressure [Pa],
T = temperature [K],
C = concentration of water vapour [-],
t = time [s],
ρ = total air density [kg_{air}/m^3],
μ = dynamic viscosity[Pa·s],
k = thermal conductivity [W/(m·K)],
g = gravity [m/s^2],
c_p = specific heat [J/(kg·K)] and
D = diffusion coefficient [m^2/s].

The volumetric coefficient of thermal expansion β [1/K] is given by

$$\beta = -\frac{1}{\rho}\frac{\partial \rho}{\partial T} = \frac{1}{T}. \quad \text{(F.13)}$$

The species expansion coefficient β^* [-] is given by

$$\beta^* = -\frac{1}{\rho}\frac{\partial \rho}{\partial C} = \frac{1}{\rho}\left[\frac{M_{air}}{M_w} - 1\right] \quad \text{(F.14)}$$

where M_{air} is the molecular weight of air [kg_{air}/mol] and M_w is the molecular weight of water vapour [kg_w/mol].

F.2.3 Boundary Conditions

The following boundary conditions are used for the simulations:

- a fully developed velocity profile for the air at the inlet,
- a uniform temperature and concentration at the inlet,
- no slip boundary conditions at the walls,

- adiabatic and impermeable boundary at the walls, except for the top of the test section, where the membrane is located,
- temperature and concentration boundary conditions are set at the surface of the membrane and
- zero gradients for momentum, energy and concentration at the outlet.